UNIVERSIDAD AUTÓNOMA DE MADRID

FACULTAD DE CIENCIAS

DEPARTAMENTO DE FÍSICA TEÓRICA

OBSERVATOIRE DE PARIS

LABORATOIRE D'ETUDES DU RAYONNEMENT ET DE LA MATIÈRE EN ASTROPHYSIQUE ET ATMOSPHÈRES

Dark matter distribution in the Universe with gravitational lensing: the distribution of Einstein radii as cosmological probes

Tesis presentada para aspirar al grado de Doctor en Astrofìsica

JESÚS VEGA FERRERO

DIRECTORES:

Gustavo YEPES (*FT-UAM*)

David VALLS-GABAUD (*LERMA-OBSPM*)

Madrid, 24 de Julio 2015

OBSERVATOIRE DE PARIS

École doctorale Astronomie et Astrophysique d'Île de France (ED 127)

THÈSE DE DOCTORAT

Spécialité

ASTRONOMIE ET ASTROPHYSIQUE

LA DISTRIBUTION DES RAYONS D'EINSTEIN COMME SONDES COSMOLOGIQUES

par

JESÚS VEGA FERRERO

Thèse dirigée par Gustavo YEPES et David VALLS-GABAUD

Soutenue publiquement le 24 juillet 2015
à l'Universidad Autónoma de Madrid
devant le jury composé de:

Evencio MEDIAVILLA	Président du jury
Jean-Paul KNEIB	Rapporteur
Prasenjit SAHA	Rapporteur
Eric JULLO	Examinateur
Raphael GAVAZZI	Examinateur

Universidad Autónoma de Madrid - Departamento de Física Teórica
Observatoire de Paris - Laboratoire d'etudes du rayonnement et de la matière en Astrophysique et Atmosphères

A mis padres.

Resumen

ESTA tesis de Doctorado ha sido realizada y escrita gracias a las Ayudas Predoctorales de Formación de Personal Investigador (Ayudas FPI) dentro del Programa Nacional de Formación de Recursos Humanos de Investigación, en el marco del Plan Nacional de Investigación Científica, Desarrollo e Innovación Tecnológica 2008-2011. La mayor parte de la tesis de Doctorado se ha realizado en el Departamento de Física Teórica en la Universidad Autónoma de Madrid (España), completándose con estancias en el departamento LERMA del Observatorio de París (Francia) y en el Observatorio de Bolonia, INAF-OABO (Italia). Dado que con esta tesis de Doctorado se pretende obtener el Título de Doctorado con Mención Internacional, ésta ha sido escrita en lengua inglesa. Complementariamente, presentamos un resumen con los principales contenidos y resultados de esta tesis en lengua española.

El efecto de lente gravitacional es una consecuencia directa de la teoría de la Relatividad General de Einstein (ver Bartelmann 2010 para más detalles). Básicamente, según esta teoría, la trayectoria de la luz puede ser desviada al pasar cerca del un objeto masivo a causa del campo gravitatorio creado por éste. El efecto de lente gravitacional es uno de los métodos más directos de que disponemos actualmente para medir la distribución de masa en cúmulos de galaxias. En particular, la abundancia de fenómenos denominados *lente gravitacional fuerte*, como por ejemplo la distorsión en forma de arco producida por el potencial gravitacional de los cúmulos de galaxias, pueden usarse para investigar los procesos de formación de estructuras a muy distintas escalas. Además, debido a que el número de arcos depende de la distribución de masa de los cúmulos de galaxias, así como de la abundancia cosmológica de los mismos, la estadística de eventos de *lente gravitacional fuerte* hace de este efecto una herramienta muy útil en Cosmología. Sin embargo, los intentos realizados por el momento para usar este

efecto de *lente gravitacional fuerte* como herramienta cosmológica han producido resultados controvertidos (Kneib & Natarajan, 2011; Meneghetti et al., 2013). Estudios recientes indican que algunos cúmulos de galaxias tienen anillos de Einstein muy extendidos, cuyas abundancias son difíciles de reproducir por el modelo cosmológico ΛCDM (Broadhurst & Barkana, 2008). Por otro lado, las observaciones de muy alta calidad sobre unos pocos cúmulos de galaxias han revelado que dichos cúmulos tienen concentraciones muy altas cuando se comparan con las estimaciones de los modelos teóricos (Zitrin et al., 2009). Esta discrepancia entre la estadística de lentes fuertes y los datos observacionales es lo que se conoce en inglés como *arc statistics problem*.

El trabajo expuesto en esta tesis está desarrollado con la intención de entender el origen de estas discrepancias. En este contexto, las simulaciones cosmológicas de N-cuerpos han sido esenciales para comprender cómo se forman las más grandes estructuras que se observan en el Universo. Concretamente, han sido cruciales en el estudio de las propiedades de los halos de materia oscura en en modelo ΛCDM. En los últimos años, gracias al desarrollo de nuevos códigos numéricos y al acceso a potentes supercomputadores, se han llevado a cabo grandes simulaciones cosmológicas con una elevada resolución en masa dentro de un gran volumen. Un buen ejemplo lo constituye la simulación *MultiDark* (Prada et al., 2012; Sembolini et al., 2013b). La simulación *MultiDark* contiene casi 9 mil millones de partículas en una caja cúbica de lado 1Gpc/h. Las estructuras más masivas que se forman en *MultiDark* han sido resimuladas, con mucha más resolución y considerando la contribución bariónica, por el grupo de Cosmología Numérica de la Universidad Autónoma de Madrid en el supercomputador *MareNostrum* del Centro Nacional de Supercomputación de Barcelona. Gracias a la gran resolución alcanzada por las simulaciones MUSIC (MUltidark SImulations of galaxy Clusters), hemos podido estimar los parámetros que caracterizan el perfil de densidad de los cúmulos de galaxias con una precisión sin precedentes y obtener una imagen consistente de la población de subestructuras dentro de ellos.

Los resultados descritos en esta tesis están basados en el estudio del catálogo de cúmulos de galaxias simulados MUSIC-MD (MUSIC *MultiDark*). En total, hemos analizado $\sim$ 1400 halos de materia oscura *disjuntos* (es decir, que no forman parte de un halo de mayor masa) con masas $M_{vir} \geqslant 2{\times}10^{14} h^{-1} M_{\odot}$ para los desplazamientos al rojo $z = (0.250, 0.333, 0.429, 0.667)$. Aprovechando las características de MUSIC-MD, hemos investigado importantes propiedades físicas de los cúmulos de galaxias,

tales como la masa y la concentración. Más concretamente, nuestro análisis está basado en los efectos de lente gravitacional producidos por los cúmulos de galaxias en MUSIC-MD. Para este propósito, MUSIC-MD constituye uno de los mejores catálogos de cúmulos de galaxias simulados, ya que muchos aspectos relevantes en el estudio de lentes gravitacionales pueden ser tratados con detalle. Por ejemplo, el efecto de la triaxialidad (y, por tanto, la variación producida por diferentes orientaciones) y el estado dinámico de los cúmulos de galaxias pueden ser abordados con una precisión única hasta la fecha.

El análisis realizado a partir de los perfiles de densidad esférica de los cúmulos de galaxias en MUSIC-MD nos ha permitido obtener resultados claves sobre la evolución con el desplazamiento al rojo en la relación concentración-masa ($c - M$). En el rango de masa estudiado la dependencia de la concentración con la masa es débil, mostrando una pendiente ligeramente negativa. Por otro lado, aunque la dependencia con el desplazamiento al rojo en la relación $c - M$ es prácticamente despreciable, ésta se hace más importante en cúmulos relajados. Además, los cúmulos más relajados son los que muestran concentraciones más elevadas.

Con la intención de incorporar en la relación $c - M$ los efectos producidos por la orientación de los cúmulos con respecto a un hipotético observador, hemos calculado los perfiles de densidad superficial (o proyectados) para 500 proyecciones aleatorias de cada cúmulo de galaxias en MUSIC-MD. A partir de dichos perfiles derivamos masas y concentraciones proyectadas, las cuales parecen ser inferiores a las derivadas de los perfiles de densidad esférica. La dependencia con la masa en la relación $c - M$ proyectada muestra una pendiente positiva, lo que implica que los halos más masivos presentan concentraciones proyectadas mayores que las esperadas con una relación $c - M$ en 3D.

Gracias a la elevada resolución de los cúmulos de galaxias en el catálogo MUSIC-MD hemos podido caracterizar los perfiles de masa hasta $\sim$ 15kpc y, por consiguiente, identificar anillos de Einstein de unos pocos segundos de arco ($\sim$ 3 arcsec para los desplazamientos al rojo considerados en este trabajo). Para el caso de una lente gravitacional con simetría axial, el anillo de Einstein puede ser estimado a partir de la posición de la línea tangencial crítica, definida ésta como $1 - \kappa - \gamma = 0$ (siendo κ y γ, la convergencia y el cizallamiento, respectivamente). En primer lugar, se calculan los perfiles de convergencia y cizallamiento para cada una de las 500 proyecciones de cada cúmulo de galaxias y, posteriormente, se determina el tamaño del anillo de Einstein. Alternativamente, usando un código de *ray-tracing*

(*Skylens*, ver Meneghetti et al. 2010a para más detalles), es posible obtener mapas de convergencia y cizallamiento en dos dimensiones para los cúmulos MUSIC-MD. A partir de dichos mapas hemos extraído información detallada sobre el tamaño del anillo de Einstein y la elipticidad de la línea tangencial crítica. El anillo de Einstein determinado de este modo se denomina comúnmente anillo de Einstein *efectivo* (Meneghetti et al., 2013) y se caracteriza por estar derivado sin considerar simetría axial para la lente gravitacional.

El objetivo central de esta tesis ha consistido en desarrollar un modelo semi-analítico (MAPLENS, MAdrid-Paris LENsing Semianalytics) especialmente diseñado para estimar la distribución de anillos de Einstein (y su evolución con el desplazamiento al rojo) para una muestra bien definida de cúmulos de galaxias. Las distribuciones de anillos de Einstein derivadas con MAPLENS incorporan adecuadamente posibles efectos de proyección, como la triaxialidad y la presencia de subestructuras en cúmulos de galaxias, por medio de la técnica denominada *kernel density estimate*. Siguiendo este procedimiento y a partir de la masa y el desplazamiento al rojo del cúmulo de galaxias, MAPLENS deriva la masa y concentración proyectadas, el tamaño del anillo de Einstein *efectivo* y la elipticidad de la línea crítica. Este método es muy efectivo en términos de recursos computacionales, ya que estas propiedades se derivan a partir de un modelo NFW, que está caracterizado únicamente por dos parámetros libres.

Las propiedades derivadas con MAPLENS pueden ser comparadas con muestras de cúmulos de galaxias observados para los cuales la función de selección es bien conocida. No obstante, estas propiedades no sólo dependen de los cúmulos que actúan como lentes gravitacionales. Otros aspectos determinantes son la masa y la distribución espacial de los cúmulos de galaxias. Con la intención de obtener predicciones sobre la distribución de anillos de Einstein en todo el Universo, hemos utilizado MAPLENS sobre una muestra de halos de materia oscura dentro del rango en masa de los cúmulos de galaxias obtenida a partir de la función de masa presentada por Tinker et al. (2008). Para obtener una precisión aceptable de los resultados generamos 1000 catálogos de halos considerando todo el cielo ($\sim$ 40000 grados cuadrados) con $z = [0.1 - 1.0]$. La comparación entre los resultados obtenidos con MAPLENS y los datos observaciones presentados en esta tesis se lleva a cabo por medio de dos estadísticos: la comparación de la distribución total de anillos de Einstein por un lado; y la distribución de valores extremos (EVS, *extreme value statistics*) de anillos de Einstein, por otro.

Finalmente, motivados por la reciente publicación de estudios sobre muestras de cúmulos de galaxias observados, hemos presentado una comparación detallada con la muestra CLASH obtenida con HST (Merten et al., 2015) y con el análisis presentado por (Oguri et al., 2012) para el catálogo SGAS de cúmulos de galaxias. La comparación entra la estadística de grandes anillos de Einstein teórica y la obtenida en estudios previos (Zitrin et al., 2012a; Waizmann et al., 2014; Redlich et al., 2014), evidencia todavía una pequeña discrepancia entre las predicciones teóricas y los datos observacionales. La conclusión general es que los cúmulos de galaxias observados a bajo desplazamiento al rojo ($z \lesssim 0.5$) son lentes gravitacionales más eficientes que los cúmulos simulados. No obstante, aunque estas diferencias pueden deberse a las incertidumbres del método usado por Zitrin et al. (2012a), la comparación entre los distintos modelos teóricos parece indicar que el método aplicado para derivar la triaxialidad de los cúmulos afecta considerablemente la distribución de grandes anillos de Einstein.

Résumé

L'EFFET de lentille gravitationnelle est une conséquence de la Relativité Générale, selon laquelle la trajectoire de la lumière peut être déviée par le champ gravitationnel d'un corps massif. Cet effet est le plus direct pour mesurer la distribution de masse des amas de galaxies. En effet, l'abondance de phénomènes comme les distortions en forme d'arc (un effet fort de lentille) peut être utilisé pour comprendre la formation de structures à des échelles très différentes. De plus, comme le nombre d'arcs dépend de la distribution de masse dans les amas, et de leur abondance cosmologique, ils deviennent un outil particulièrement utile en cosmologie. Cependant, les résultats obtenus jusqu'à présent sont assez controversés. Par exemple, certains amas de galaxies présentent des anneaux de grande dimension, dont l'abondance semble être en contradiction avec les prédictions du modèle cosmologique ΛCDM. Par ailleurs, des observations détaillées de quelques amas montrent des concentrations très élevées par rapport aux prédictions. Cette tension entre les observations et les prédictions est l'une des crises graves du paradigme de formation de structures cosmologiques.

Le travail développé dans le cadre de cette thèse traite de résoudre ce problème. Des re-simulations cosmologiques de très haute résolution ont été réalisées (MUSIC *MultiDark*, avec la meilleure résolution jamais atteinte jusqu'à présent) pour analyser de forme détaillée 1400 halos de matière noire isolés de masse viriel $M_{\rm vir} > 2 \times 10^{14}\ h^{-1}{\rm M}_{\odot}$ à des redshifts representatifs de $z = 0.250, 0.333, 0.429, 0.667$. La très haute résolution en masse et spatiale de ces amas simulés nous a permis d'obtenir une meilleure analyse de la relation masse-concentration des halos d'amas de galaxies en prenant en compte les effets de triaxialité, de projection selon des lignes de visée aléatoires (500 tirages distribués uniformèment sur la sphère), et de relaxation pour chacun de 1400 amas, ce qui constitue la plus grande base d'amas simulés à très haute résolution jamais établie.

Cette base est donc un outil unique pour étudier les propriétés de lentille gravitationnelle des amas tout en analysant les effets systématiques induits par les méthodes utilisées pour l'interprétation des observations. Par exemple, l'hypothèse d'une lentille avec symétrie axiale est souvent adoptée. Dans ce cas, la taille des anneaux est estimée à partir de la position de la ligne critique tangentielle donnée par $1 - \kappa - \gamma = 0$ avec κ et γ la convergence et le cisaillement du champ). Les profils de convergence et de cisaillement ont été calculés pour chacune des 500 projections des 1400 amas comme s'il s'agissait d'observations. La distribution résultante de la taille des anneaux et de leur ellipticité est comparée à celle obtenue par un code direct qui calcule les trajectoires réelles des rayons lumineux dans les amas (*Skylens*) et qui ne fait aucune hypothèse sur la symétrie de la distribution de masse des amas.

Avec ces éléments, un modèle semi-analytique a été développé (MAPLENS, *MAdrid-Paris LENsing Semianalytics*) pour prédire les distributions des propriétés de lentille gravitationnelle des amas, et leurs évolutions par la technique statistique bien connue d'estimation de densité par noyau (*kernel density estimate*). MAPLENS nous a permis de comparer les prédictions théoriques avec les observations en utilisant deux techniques complémentaires. D'une part la distribution de taille des anneaux et d'autre part la distribution de valeurs extrêmes (*extreme value statistics*). Il subsiste encore des différences entre les prédictions théoriques et les observations malgré la prise en compte des effets de méthode d'analyse. Nous avons montré en particulier que l'estimation de la triaxialité des amas est très sensible à la méthode utilisée et produit des reśultats très différents pour la distribution de taille des anneaux. Nous montrons également qu'il susbsiste d'une part des biais observationnels dans l'analyse de l'échantillon d'amas utilisé par Zitrin *et al.* (2012a), et, d'autre part, que les amas observés à bas redshifts $z < 0.5$ sont plus efficaces en tant que lentilles gravitationnelles que les amas simulés.

Par ailleurs nous avons également utilisé cet outil pour l'analyse détaillée de l'échantillon CLASH d'amas observés avec le Hubble Space Telescope, et le catalogue SGAS.

Contents

Thesis motivation and outline

STRONG lensing statistics can be as competitive as other cosmological probes for constraining cosmological parameters. However, previous attempts of using strong lensing statistics as a cosmological tool have produced controversial results. In particular, studying the lensing properties of a set of numerically simulated clusters, Bartelmann et al. (1998) argued that the ΛCDM cosmological model fails at reproducing the observed abundance of giant gravitational arcs reported in Le Fevre et al. (1994) by almost an order of magnitude. This inconsistency between expectations in the ΛCDM model, which is strongly supported by a number of powerful cosmological probes, and the observed abundance of gravitational arcs is knows as the *arc statistics problem*. Moreover, this discrepancy was also enforced by several other observations of strong lensing clusters, which seemed to indicate that: first, some galaxy clusters have very extended critical lines whose abundances can hardly be reproduced by cluster models in the framework of a ΛCDM cosmology (Broadhurst & Barkana, 2008; Tasitsiomi et al., 2004); and second, few clusters, for which high quality strong and weak lensing data became available, have concentrations which are way too large compared to numerical expectations (Broadhurst et al., 2008; Zitrin et al., 2009).

Understanding the origin of these mismatches between theoretical predictions and observations is fundamental, as these may evidence a lack of understanding of the cluster physics, which may be not well implemented in the simulations, or, conversely, highlight some inconsistencies between the ΛCDM scenario and the properties of the universe on small scales.

Until a few years ago a comparison between theoretical predictions and observations based on gravitational lensing was complicated by the lack of systematic arc surveys, but also by the fact that different approaches were used to analyze simulations and observations. This situation has been recently improved

thanks to the Cluster Lensing And Supernova Survey with Hubble (CLASH, Postman et al. 2012), which is a multi-cycle treasury program using 524 HST orbits to observe 25 galaxy clusters, largely drawn from the Abell and MACS cluster catalogs (Abell, 1958; Abell et al., 1989; Ebeling et al., 2001, 2007, 2010). One of the goals of CLASH is the measurement of accurate concentration parameters for massive X-ray bright clusters of galaxies. Each cluster reveals several multiple image systems and gravitational arcs, which are used to constrain mass models and to measure several properties of the clusters cores, including their Einstein radii (Zitrin et al., 2012b; Coe et al., 2012; Umetsu et al., 2012, 2014; Zitrin et al., 2015). In particular, twenty clusters of the CLASH sample were specifically selected by their largely unperturbed X-ray morphology with the goal of representing a sample of clusters with regular, unbiased density profiles. The CLASH sample is thus ideal for statistic studies of gravitational arcs.

Additionally, the Sloan Giant Arcs Survey (SGAS, Hennawi et al. 2008; Bayliss et al. 2011), which is a survey of strongly lensed giant arcs from the Sloan Digital Sky Survey (SDSS; York et al. 2000), has already discovered more than 30 bright giant arcs and therefore offers an ideal technique to expand the sample of clusters appropriate for detailed lensing analysis. In Oguri et al. (2012) the mass modeling of the strong lensing information of 28 clusters from the SGAS is combined with weak lensing measurements to obtain robust constraints on the concentration parameter and the shape of the mass distribution.

At the same time, thanks to the progress reached by computational astrophysics in the last two decades, N-body cosmological simulations of galaxy clusters are producing descriptions of the mass distributions very close to the observational results already mentioned.

The main motivation behind this thesis work is to use the state-of-the-art numerical simulations of galaxy clusters as a laboratory to test the general gravitational lensing properties of these objects that can then be incorporated into a semi-analityc model for the prediction of the statistical distribution of strong lens features in the universe. We present here the MUSIC (MUltidark Simulations of galaxy Clusters) dataset of hydrodynamical N-body+SPH simulations of clusters (see sec. 3.2 for a full description of the dataset). In particular, we restrict our analysis to the MUSIC-MultiDark dataset (thereafter, MUSIC-MD), which consists of a mass limited sample of re-simulated halos selected from the MultiDark cosmological simulation (Prada et al., 2012). The MultiDark simulation is a dark-matter only simulation

with 2048^3 particles in a $1h^{-1}$Gpc cubic box volume. The MUSIC-MD dataset allows us to estimate with unprecedented statistics the parameters characterizing mass distribution in galaxy clusters (such as the concentration) and to explore how these evolve with mass, redshift and morphology. In addition, the mass resolution of the re-simulated objects is high enough to take into account intrinsic selection effects, such as cluster triaxiality and/or substructures, and to accurately estimate the gravitational lensing properties of clusters of galaxies. For example, the MUSIC-MD will allow us to resolve the size of the Einstein radius down to $\sim$ 15 kpc.

Based on the results of the MUSIC-MD, we also present a semi-analytic model (*MAPLENS*, Madrid-Paris LENsing Semianalytics) that has been developed in order to estimate the Einstein radii distribution and its evolution with redshift for any well-defined sample of galaxy clusters. The model incorporates all the selection effects that could be accounted for in the MUSIC-MD dataset: triaxiality, substructures and mergers. We then compare the predictions of our model with recent observational data from CLASH and SGAS, aiming at checking whether the persistence of the *arc statistics problem* can be still questioned –both by theoreticians and by observers– in terms of the current ΛCDM cosmological model.

The scientific publications listed hereafter have been part of the result of the work presented in this thesis (see Appendix B).

Published papers

- CLASH: *The Concentration-Mass Relation of Galaxy Clusters*– Merten, J.; Meneghetti, M.; Postman, M.; Umetsu, K.; Zitrin, A. et al. 2015 (The Astrophysical Journal, 806, 4).
- *The* MUSIC *of* CLASH: *Predictions on the Concentration-Mass Relation*– Meneghetti M.; Rasia E.; Vega J.; Merten J.; Postman M. et al. 2014 (The Astrophysical Journal, 797, 34).
- CLASH: *The Enhanced Lensing Efficiency of the Highly Elongated Merging Cluster* MACS J0416.1-2403– Zitrin, A.; Meneghetti, M.; Umetsu, K.; Broadhurst, T.; Bartelmann, M. et al. 2013 (The Astrophysical Journal Letters, 762, L30).

Papers in preparation

- *Gravitational lensing analysis of* MUSIC *simulated clusters*– Vega J.; Valls-Gabaud D.; Yepes G.; Meneghetti, M.
- *The distribution function of Einstein radii with MAPLENS*– Vega J.; Valls-Gabaud D.; Yepes G.
- *Shapes of dark matter halos with Planck cosmology*– Vega J.; Yepes G.; Valls-Gabaud D.

Thesis outline

The thesis is organized as follows: In Chapter 1 we give a brief review of the theory of cluster formation, from the initial perturbations to the formation of most massive structures in the universe, while in Chapter 2 we summarize the main ingredients of the gravitational lensing theory to study the properties characterizing the mass distribution in clusters of galaxies. In Chapter 3 we present a detailed description of the MUSIC-MD dataset, enumerating the characteristics of the simulations. The main part of the thesis is devoted to the study of the mass distribution in cluster-size halos extracted from the MUSIC-MD dataset and the gravitational lensing techniques applied to the simulated clusters. (Chapter 4). In Chapter 5 we describe the semi-analytical model we have developed to estimate the Einstein radii distribution based on analysis of the MUSIC-MD clusters. We also present our predictions for the *all-sky* Einstein radii distribution in the redshift range $0.1 < z < 1.0$. In Chapter 6, we present a detailed comparison between our expectations and the most recent observations of galaxy clusters. We finalize this thesis dissertation with the main conclusions derived from our work and discussing some future prospects in Chapter 7.

CHAPTER 1

Clusters of galaxies in their cosmological context

CLUSTERS of galaxies are the most massive gravitationally bound structures in the universe. In the current paradigm of structure formation, they emerge in the cosmic web of large-scale structure as a result of the gravitational field seeded by quantum fluctuations during an early, inflationary epoch of the universe. Clusters of galaxies form in an hierarchical sequence of mergers and accretion of smaller systems driven by the dark matter that dominates the gravitational field. Although they were first recognised by Charles Messier and William Herschel at the end of the eighteenth century, the first evidence that the universe may contain dark matter came in 1933, when Zwicky studied the velocities in the Coma cluster. The masses implied by the measured velocity dispersions were found to exceed the mass of observed matter (hundreds of times the mass of all the stars) in the cluster.

Decades later, the dark matter hypothesis was reinforced by the discovery of extended hot intracluster medium (ICM) emitting X-ray energies filling the intergalactic space within the Coma Cluster (Cavaliere et al., 1971; Forman et al., 1972; Gursky et al., 1971; Kellogg et al., 1972; Meekins et al., 1971). Moreover, the measurement of the ICM temperature has also independently probed the large contribution of dark matter to the gravitational potential of clusters. More recently, measurements of the Sunyaev-Zeldovich effect, that arises from the interaction of CMB photons with the hot electrons in the ICM, corroborated the predominant role of a dark matter component in clusters of galaxies (Kosowsky, 2006; Marriage et al.,

2011; Vanderlinde et al., 2010; Carlstrom et al., 2011; Bartlett et al., 2008; Planck Collaboration et al., 2011).

After the discovery of gravitational arcs (Lynds & Petrosian, 1986; Soucail et al., 1987), these strong lensing effects have been widely used to constrain the structure of galaxy clusters on a variety of scales (e.g. Kovner, 1987; Bergmann et al., 1990; Kneib et al., 2003; Broadhurst et al., 2005c; Cacciato et al., 2006; Liesenborgs et al., 2009; Coe et al., 2010, for some examples). In addition, since the number of arcs depend both on the mass profile of the clusters and on their cosmological abundance, which in turn also depends on the cosmological scenario, the statistics of strong lensing events are also a useful tool for cosmology (e.g. Bartelmann et al., 1998).

1.1 The cosmological model

As cluster evolution is strictly coupled with the cosmological model, a clear description of the later is necessary to fully understand the former. Modern cosmology is based upon the *Cosmological Principle*, *i.e.* the hypothesis that the universe is spatially homogeneous and isotropic when looking at sufficiently large scales. The standard cosmological model can be described with a combination of the solution of the field equations of General Relativity and a theory for the formation of structures in a homogeneous and isotropic universe. There are many strong and independent observational evidences of the validity of these assumptions, such as the large-scale distribution of galaxies determined by surveys like 2 degree Field survey (2dF) and the near-uniformity of the Cosmic Microwave Background (CMB) temperature as revealed by the Cosmic Background explorer (COBE).

The metric tensor of the universe takes the form of the Robertson-Walker metric under the assumptions of homogeneity and isotropy (Weinberg, 1972):

$$ds^2 = c^2dt^2 - a(t)^2\left[\frac{dr^2}{1-kr^2} + r^2(d\theta^2 + \sin^2\theta d\varphi^2)\right] \tag{1.1}$$

where t is the cosmic time and r, θ and φ are the spherical co-moving coordinates. The curvature of space is defined by k, while c is the speed of light. The scale factor *a(t)* accounts for the expansion (or a possible contraction) of the universe as a function of the cosmic time. The scale factor is related to the cosmological redshift as:

$$a = \frac{1}{1+z} \tag{1.2}$$

The *Hubble parameter* is defined as the relative expansion rate as:

$$H(t) = \frac{\dot{a}}{a} \tag{1.3}$$

and its value at the present epoch $H_0 = H(t = t_0)$ has been measured by the CMB. Recent measurements indicate $H_0 = 67.8 \pm 0.9\ kms^{-1}Mpc^{-1}$ (PLANCK, Planck Collaboration et al. 2015) and $H_0 = 70.4^{+1.3}_{-1.4}\ kms^{-1}Mpc^{-1}$ (WMAP7, Komatsu et al. 2011). The inverse of the Hubble constant represents the time scale for the expansion of the universe, also called *Hubble time* ($t_H \approx H_0^{-1} 10^{12}$ years).

The dynamics of the metric is governed by Einstein's field equations, which relate the Einstein tensor ($G_{\mu\nu}$) to the stress-energy tensor ($T_{\mu\nu}$) of the matter contained in space-time:

$$G_{\mu\nu} = R_{\mu\nu} - \frac{1}{2} R g_{\mu\nu} = \frac{8\pi G}{c^2} T_{\mu\nu} + \Lambda_{\mu\nu} \tag{1.4}$$

Following the *Cosmological Principle*, Einstein's equations imply that $T_{\mu\nu}$ takes the form of the stress-energy tensor of a homogeneous perfect fluid, which is characterised by its density (ρ) and its pressure (p). In these terms and considering the stress-energy conservation law, the field equations can be simplified to the so-called Friedmann's equations:

$$\left(\frac{\dot{a}}{a}\right)^2 = \frac{8\pi G}{3}\rho + \frac{\Lambda}{3} + \frac{kc^2}{a^2} \tag{1.5}$$

$$\frac{\ddot{a}}{a} = -\frac{4\pi G}{3}\left(\rho + \frac{3p}{c^2}\right) + \frac{\Lambda}{3} \tag{1.6}$$

where G is Newton's gravitational constant and Λ is Einstein's cosmological constant. Those models, governed by Eq. 1.5 and Eq. 1.6 are known as Lemaître-Friedmann-Robertson-Walker (LFRW) universes.

1.2 Density Perturbations

Current theories of structure formation assume that clusters of galaxies grow gravitationally from density fluctuations at the very beginning of the universe. Although the origin of these fluctuations is yet unclear, they possibly originated from quantum fluctuations almost after the Big Bang, which were blown up during a later inflationary phase. In an expanding universe dominated by weakly interacting dark matter, perturbations grow with time. If we imagine an almost homogeneous universe with a slightly over-dense region, it is easy to understand that, due to gravitational forces, this region will attract matter slightly stronger that its surroundings, thus producing a denser region which has an ever stronger attraction effect. On the other hand, under-dense regions become less dense as matter flows away from them, and also expand quicker as the gravitational force opposing to the expansion of the universe is less strong in those regions.

The amplification of density perturbations is known as gravitational instability. Gravitational instability leads to a growth of the amplitudes of the density fluctuations, which are responsible for the formation of the structures that are observed in today's universe. The density fluctuations from the mean density can be quantified by the overdensity field at the co-moving position **x**:

$$\delta\left(\mathbf{x}\right) = \frac{\rho_M\left(\mathbf{x}\right) - < \rho_M >}{< \rho_M >} \tag{1.7}$$

The initial density fluctuations are predicted to be uncorrelated with amplitudes distributed as a gaussian random field. In the case that $\delta\left(\mathbf{x}\right)$ is isotropic, it can be characterised by an isotropic power spectrum, *P(k)*, which determines the amplitude of the fluctuations as a function of their spatial scale:

$$P(k) \equiv \quad < |\delta_k|^2 > \tag{1.8}$$

where δ_k is the Fourier transform of the overdensity field:

$$\delta_k(k) = \int \delta(\mathbf{x})\, e^{i\mathbf{kx}}\, d^3x \tag{1.9}$$

It is broadly assumed that the primordial power spectrum is a power-law, $P(k) \propto k^{n_p}$, and should be scale-invariant at the time the perturbations enter the horizon (the size of causally connected regions in the universe), which leads to a spectral index

$n_p = 1$. Under this assumptions, the power spectrum is called the *Harrison-Zel'dovich* spectrum (Harrison, 1970).

As the universe evolves, the initial power spectrum evolves too. This evolution can be accurately treated using a *scale-dependent* growth function (Eisenstein & Hu, 1999), defined as the transfer function *T(k)*, as follows:

$$P(k) \propto T(k)^2 \, P(k, z = 0) \tag{1.10}$$

To be complete in the description of the power spectrum, its normalisation should also be fixed. The normalisation of the power spectrum has been determined observationally by several methods. The first measurements of the current mass distribution of the universe were inferred by measuring the local variance of galaxy counts within certain volumes (Davis & Peebles, 1983). They found a variance of galaxy counts of $\sigma_8 \approx 1$ within spheres of 8 h^{-1}Mpc. As a result, the normalisation of the power spectrum is historically quantified in this term:

$$\sigma_8^2 = \frac{1}{8\pi^3} \int P(k) \, |W_k(R)|^2 \, d^3k \tag{1.11}$$

where $W_k(R)$ is the top-hat window function, with a constant value within a co-moving radius of 8 h^{-1}Mpc (otherwise, its value is zero).

On small scales, the growth of density fluctuations has no longer a linear behaviour. Generally, the non-linear evolution of $P(k)$ is too complex to be solved analytically and requires to be evaluated numerically using simulations of the large scale structure clustering process. In these simulations initially smooth matter evolves into a complex network of sheets, filaments and knots. The dense knots are often called dark matter halos. Simulations have been used to explore the abundance and spatial distribution of halos, and the distribution of mass in them, probing their close relation with the initial fluctuation field (Navarro et al., 1996; Moore et al., 1999; Colberg et al., 1999; Jenkins et al., 2001).

1.3 Cosmological parameters

In order to study the different terms contributing to the stress-energy tensor, it is useful to use the density parameters, which define the fraction of the critical density necessary for the universe to have a spatially flat geometry ($k = 0$):

$$\Omega_i(t) = \frac{\rho_i(t)}{\rho_c(t)} \tag{1.12}$$

where the *i-index* indicates the different components of the universe and $\rho_c(t)$ corresponds to critical density of the universe defined as:

$$\rho_c(t) = \frac{3H(t)^2}{8\pi G} \tag{1.13}$$

For a complete description of the expansion of the universe, an equation of state relating the pressure to the energy density of the matter is needed. Considering a equation of state in the form $p = w\rho c^2$, non-relativistic particles with a mass density ρ_M have negligible contribution to the total pressure, thus $w = 0$, while radiation and other forms of relativistic matter with an energy density $\rho_R c^2$ have a pressure with $w = 1/3$. Additionally, given the fact that Einstein's cosmological constant does not vary as the universe expands, it acts like an energy density $\rho_\Lambda c^2$ and exhibits a pressure with $w = -1$. The curvature parameter is defined as $\Omega_k = 1 - \Omega_0$, and is null in the case of $\Omega_0 = 1$. Accounting for these components, the first Friedmann equation is:

$$H^2(t) = H_0^2(t)\left[\Omega_M\,(1+z)^3 + \Omega_R\,(1+z)^4 + \Omega_\Lambda + (1-\Omega_0)\,(1+z)^2\right] \tag{1.14}$$

The matter density parameter Ω_M consists of a contribution of Ω_b from baryons and a contribution from non-baryonic, non-relativistic dark matter. The radiation density parameter includes contributions from the photons on the microwave background, and from relic neutrinos produced in the Big bang (Ω_ν), as long as they remain relativistic particles. The physical origin of the cosmological constant (Ω_Λ) is still unknown.

Different cosmological models correspond to different values of the cosmological parameters: a Standard Cold Dark Matter (SCDM) model, dominated by non-relativistic cold dark matter with $(\Omega_M,\ \Omega_\Lambda) = (1,\ 0)$; an open universe ($k < 0$, $\Omega_0 < 1$) with no cosmological constant may have $(\Omega_M,\ \Omega_\Lambda) = (0.3,\ 0)$; a flat universe with a Λ-term can be described by $(\Omega_M,\ \Omega_\Lambda) = (0.3,\ 0.7)$. Fig. 1.1 shows the evolution of energy densities with redshift for different cosmological models.

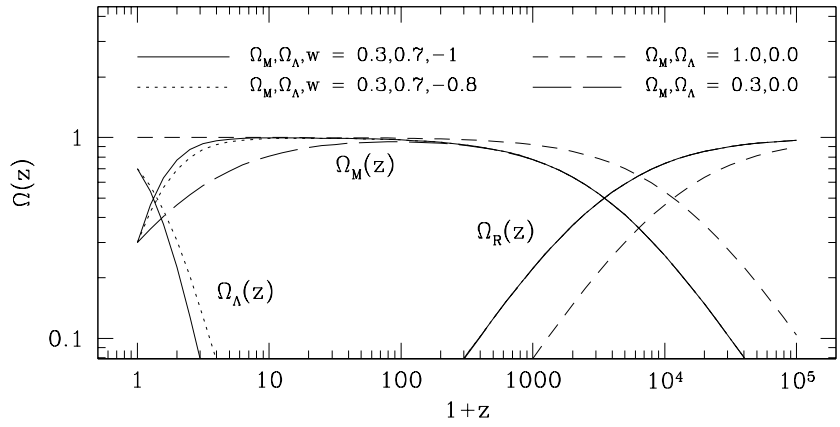

Figure 1.1: Evolution of energy densities with redshift for different cosmological models: solid lines, the concordance model with $\Omega_M = 0.3$, $\Omega_\Lambda = 0.7$ and $w = -1$; dotted lines, a dark energy model with $\Omega_M = 0.3$, $\Omega_\Lambda = 0.7$ and $w = -0.8$; long-dashed lines, an open-universe model with $\Omega_M = 0.3$ and $\Omega_\Lambda = 0$; short-dashed lines, a critical-universe model with $\Omega_M = 1$ and $\Omega_\Lambda = 0.7$. Figure taken from Voit (2005).

1.3.1 ΛCDM cosmological model

The overall cosmological parameters described in the previous sections can be divided into two different sets of parameters. The first set consists of H_0, Ω_M, Ω_b, Ω_R, Ω_Λ and w and governs the global behavior of the universe. The second set dominates the initial density perturbation spectrum and consists of σ_8 and n_p.

The measurement of the cosmological parameters has been addressed from an observational point of view using a wide range of techniques. Studies of the CMB, the large scale structure, the Type Ia supernovae and galaxy clusters have now placed strong constrains on the cosmological parameters supporting the concordance model, also known as ΛCDM (Cold Dark Matter model with a cosmological constant). Latest observations of the power spectrum in combination with lensing reconstructions (Planck Collaboration et al., 2015) indicate that the universe is flat and expanding, and the energy density is shared between dark energy ($\sim$ 70%), dark matter ($\sim$ 30%) and a small fraction of baryonic matter. Density perturbations seem to be well described by a scale-free initial power spectrum with a power-law index n_p and amplitude σ_8 (see Table 1.1 for further details on the cosmological parameters measured by Planck Collaboration et al. 2015). Combining the *Planck* results with Type Ia supernovae data, the equation of state of dark energy is constrained to $w = -1.006 \pm 0.045$, which is consistent with the

Table 1.1: Flat ΛCDM Parameters from Planck CMB+lensing (from Planck Collaboration et al. 2015).

Parameter	Value
H_0	67.81 ± 0.92
Ω_Λ	0.692 ± 0.012
Ω_M	0.308 ± 0.012
$\Omega_b h^2$	0.02226 ± 0.00023
n_p	0.9677 ± 0.0060
σ_8	0.8149 ± 0.0093

expected value for a cosmological constant.

1.4 Dark matter halos

The non-linear evolution of the density fluctuations yield to the formation of self-gravitating dark matter halos. In a hierarchical universe the first halos emerge from fluctuations on small scales and progressively merge to form later generations of more massive halos, where the groups and clusters of galaxies are thought to be hosted. Therefore, halos could be associated with the peaks in the primordial gaussian density field of dark matter, and their mass distributions can be derived in terms of the statistics of gaussian random fields. The differential mass function of dark matter halos can be defined by the Press-Schechter mass function as (Press & Schechter, 1974):

$$\frac{\mathrm{d}n}{\mathrm{d}M}(M,z) = \sqrt{\frac{2}{\pi}}\frac{\bar{\rho}}{M^2}\frac{\delta_c}{\sigma_M(z)}\left|\frac{\mathrm{d}\ln\sigma}{\mathrm{d}\ln M}\right|\exp\left[-\frac{\delta_c^2}{2\sigma_M^2(z)}\right] \tag{1.15}$$

where $\bar{\rho}$ is the current mean density of the universe, $\sigma_M(z)$ indicates the variance in the density field and δ_c is the critical linear overdensity for spherical top-hat collapse. The collapse criterion establishes that structures collapse if the amplitude of the *linearly-evolved* fluctuation reach a critical value, $\delta(z) = \delta_c$, with the widely accepted value $\delta_c = 1.686$. Applying this concept to the ΛCDM power spectrum, a characteristic mass scale, $M_*(z)$, can be defined by $\sigma[M_*(\mathrm{z}), \mathrm{z}] = \delta_c\ (\mathrm{z})$. Amplitudes of density fluctuations above the critical value δ_c will form halos with masses above $M_*(z)$.

Within the framework of ΛCDM cosmology, clusters of galaxies are placed in

large dark matter halos, which are the result of the merging processes of smaller halos which form first. The sequence of merging events and the masses of the halos involved in those events can be extracted using a similar formalism as the Press-Schechter approach (Lacey & Cole, 1993; Voit, 2005). Mergers of halos with smaller masses, while much more frequent, are more diffuse than mergers between halos with larger masses. When the merger involves a progenitor pair mass larger than 0.5, it is usually classified as a major merger. A major merger can drive the mass content of a halo considerably out of equilibrium. Moreover, major cluster-size mergers are the most energetic events in the universe since the Big Bang.

1.5 Properties of clusters of galaxies

Clusters of galaxies are the most massive virialised systems in the universe, which emerge at the intersection of dense filaments in the cosmic web of large scale structure. They typically contain tenths to hundreds of bright galaxies, and thousands of fainter galaxies, in a region with a radius of about ~2 Mpc. The most massive clusters can have a total mass larger than 10^{15} $M_{\odot}$.

Clusters of galaxies are multi-component systems consisting of dark matter and baryons (present in different phases: black holes, stars and gas). Dark matter represents the vast majority of the mass in clusters, approximately 85% of the total mass. As dark matter is supposed to be constituted mainly by non-relativistic particles that only interact via gravitation, it has not been directly observed.

On the other hand, although representing a small fraction of the cluster mass, galaxies are the main observable component of clusters in the optical wavebands. Clusters of galaxies primarily contain elliptical and lenticular *early-type* galaxies and are deficient in spiral galaxies, particularly near their centres. They often contain very large elliptical galaxies, which are located near the centres of relaxed clusters, refereed as *brightest cluster galaxies* (BCGs). BCGs are produced by the merger of smaller galaxies and contain significant masses of cooler gas and have large star formation rates.

The space within clusters, known as the intracluster medium (ICM), is filled by a mix of thermal plasma, magnetic field and relativistic particles. As revealed by X-ray observations, the ICM is a diffuse hot plasma with typical temperatures of $T \sim 10^7 - 10^8$ K (which correspond to thermal energy of $\sim 1 - 10$ keV). The

gas is mainly composed by hydrogen and helium, but also contains heavy elements (e.g. iron). This hot gas can extend out to the virial radius with typical masses of $\sim 10^{14} M_{\odot}$ (much larger than the sum of the masses of all rich galaxies in the cluster). Given the high temperature of the gas, the X-ray emission is the dominant radiation mechanism in the ICM, with typical luminosities $L_x \sim 10^{43} - 10^{45}$ erg s^{-1}.

1.5.1 Internal structure

In a universe dominated by dark matter, clusters of galaxies provide a unique source of information on the growth of structures and on the parameters governing their evolution. In this context, the internal structure of clusters is a key prediction of the ΛCMD paradigm. As found in numerical simulations, the matter distribution in clusters shows that the shape of the density profile tends to be steep, with a cusp centre. The steepness of the density profiles is still a matter of debate, but it is likely to be a flat power-law at small radii and power-law drop off at large radii.

Navarro et al. (1996) argued that density profiles of dark matter in galaxy clusters from N-body numerical simulations have an approximately universal form well described by a Navarro-Frenk-White (NFW) profile:

$$\rho(r) = \frac{\rho_s}{(r/r_s)\,(1 + r/r_s)^2} \tag{1.16}$$

where r_s is the characteristic scale radius (at which the logarithmic slope of the profile is equal to -2) and ρ_s is the density at $r = r_s$. Following numerical studies (see e.g. Navarro et al. 1997) confirmed that the NFW profile is adequate to describe the profiles of halos in *equilibrium*, and now is widely used to characterise the shape of cluster-sized halos both in observations and in simulations. The concentration of a NFW profile is defined as $c_\Delta = r_\Delta / r_s$ (where Δ denotes a certain overdensity above the critical density of the universe, $\rho_c(z)$). The characteristic density ρ_s is related to the concentration as follows:

$$\rho_s = \frac{M_\Delta}{4\pi r_s^3} \left[\ln(1 + c_\Delta) - \frac{c_\Delta}{1 + c_\Delta} \right]^{-1} \tag{1.17}$$

The most appropriate way to describe the size of an *equilibrium* halo is its virial radius, i.e. the radius within which the halo particles are gravitationally bound and settle into equilibrium orbits. The virial overdensity, $\Delta_{\rm vir}$, is a function of

redshift and cosmology. Accurate approximations for $\Delta_{\rm vir}$ in different cosmologies have been given by many several (Bryan & Norman, 1998; Eke et al., 1996). This overdensity corresponds to the virialised region of a dark matter halo with a viral radius:

$$r_{\rm vir} = \left(\frac{4\pi}{3} \frac{\Delta_{\rm vir}\, \rho_c(z)}{M_{\rm vir}} \right)^{-1/3} \tag{1.18}$$

Nevertheless, it is well known that a large fraction of halos formed in cosmological simulations are far from having reached virial equilibrium (Ludlow et al., 2012; Meneghetti & Rasia, 2013). In the case of non-equilibrium halos, the NFW function gives a less accurate description of the shape of the density profiles than other functions involving a larger flexibility (i.e. additional free parameters). One example is the generalised NFW profile (gNFW, Zhao 1996), which is given by:

$$\rho(r) = \frac{\rho_s}{(r/r_s)^{\beta}\,(1 + r/r_s)^{3-\beta}} \tag{1.19}$$

Compared to the NFW function, this profile is characterised by an additional parameter, namely the logarithmic inner slope β:

$$-\frac{\mathrm{d}\ln\rho}{\mathrm{d}\ln \mathrm{r}} = \beta \tag{1.20}$$

Recent results indicate that there is a systematic deviation of the dark matter halo profiles from the proposed NFW function (Merritt et al., 2005; Navarro et al., 2010). The function that fit best such profiles is the *Einasto* profile (Einasto & Haud, 1989; Retana-Montenegro et al., 2012):

$$\rho(r) = \rho_{-2} \exp\left(-\frac{2}{\alpha} \left[\left(\frac{r}{r_{-2}} \right)^{\alpha} - 1 \right] \right) \tag{1.21}$$

where r_{-2} is the characteristic radius and ρ_{-2} is the density at the radius r_{-2}, i.e. at the radius where the logarithmic slope of the density profile is -2. The index α is a parameter which controls how rapidly the logarithmic slope varies with radius.

$$-\frac{\mathrm{d}\ln\rho}{\mathrm{d}\ln \mathrm{r}} \propto r^{\alpha} \tag{1.22}$$

Massive clusters of galaxies at $z = 0$ are described by $\alpha \approx 0.2$ - 0.3, increasing with redshift by ~ 0.1 at $z \approx 3$ (Gao et al., 2008).

1.5.2 Shape

Within the ΛCDM paradigm, where clusters of galaxies form from the mergers of smaller objects, formation processes violates most of the assumptions that underlie the top-hat spherical collapse model of halo formation described in sec. 1.4. Besides, mass accretion in clusters come along a preferential direction (mostly along a filament) and tends to be clumpy. For these reasons, one should not expect clusters of galaxies to show a spherical shape if their relaxation times are longer than the time between mergers or their accretion events occur from a particular direction.

Numerical simulations indicate that matter distribution in galaxy clusters is well described by a triaxial model (Frenk et al., 1988; Dubinski & Carlberg, 1991; Cole & Lacey, 1996; Jing & Suto, 2002; Kasun & Evrard, 2005; Allgood et al., 2006). Clusters of galaxies seem to be less spherical towards their centers. Triaxiality of clusters increases with increasing both the mass or the redshift of the cluster (Jing & Suto, 2002; Allgood et al., 2006). It is confirmed by the predictions recently provided by Bonamigo et al. (2015) on the shape of simulated dark matter halos (with the updated Planck Cosmology) over six orders of magnitude in mass: dark matter haloes are triaxial objects and this effect is more prominent in clusters where the spherical model is quite far from being able to realistically represent the matter distribution .

Accounting for such triaxiality is particularly important in theoretical predictions and observations. In fact, the triaxiality of dark matter halos is supposed to play a central role in the X-ray morphologies of clusters and in observational weak and strong lensing analysis (Bartelmann et al., 1998; Meneghetti et al., 2000, 2001; Oguri et al., 2005).

1.6 Observations of clusters of galaxies

Since they were first discovered at the end of the nineteenth century, a variety of surveys have detected hundreds of galaxies clusters in the universe. Because of their multi-component nature, clusters of galaxies have been detected at different wavelengths.

The hot ICM strongly emits in the X-ray band via bremsstrahlung and line emission from ionised metals injected into the plasma by stripping and feedback processes.

Galaxy clusters therefore 'light up' at X-ray wavelengths as luminous, continuos, spatially-extended sources (Allen et al., 2011). Clusters have typical soft X-ray band luminosities of 10^{44} erg/s or more, and spatial extents of several arcmins or larger, even at higher redshifts. With modern X-ray satellites using deeper follow-up observations of individual clusters, it is possible to measure the density, temperature and metallicity profiles of the ICM. The first X-ray cluster catalog constructed for cosmological purposes (Edge et al., 1990) were based on the Ariel V and HEAO-1 all-sky surveys and pointed observations made with the Einstein Observatory and EXOSAT (see Lahav et al. 1989 for further details). These catalogs were used subsequently in a series of pioneering cosmological works (Viana & Liddle, 1996; Eke et al., 1998), providing the first early evidence of evolution in the luminosity function of clusters of galaxies (Edge et al., 1990). These catalogs were eventually extended by surveys carried out with the ROSAT satellite. Launched in 1990, this mission had two main parts: the ROSAT All-Sky Survey (RASS, Voges et al. 1999) and pointed observations. The most relevant cluster catalogs used in cosmological studies and constructed from the RASS were: the ROSAT Brigthest Cluster Sample (BCS, Ebeling et al. 1998); the ROSAT-ESO Flux-Limited X-ray Galaxy Cluster Survey (REFLEX, Böhringer et al. 2004); the HIFLUGCS sample (Reiprich & Böhringer, 2002) of the X-ray brightest clusters at high galactic latitudes; and the Massive Cluster Survey (MACS, Ebeling et al. 2010). Although many other cluster surveys have been constructed from the RASS, they have not yet been used to derive rigorous cosmological constraints. The present generation of X-ray satellites, XMM-Newton and Chandra, has considerably improved the observation in terms of resolution and sensitivity. In particular, XMM-Newton (Jansen et al., 2001) has produced catalogs with thousands of clusters detected in both soft and hard X-ray bands.

Stellar emission from galaxies and intracluster light dominate the optical and near-infrared emission from galaxy clusters. The main observables in the optical band are the richness, luminosity and colour. Observations of individual clusters have measured their galaxy number densities, luminosities and velocity dispersion profiles. The first extensive cluster catalog at optical wavelengths was constructed by George Abell (Abell, 1958) based on photographic plates from the Palomar Observatory Sky Survey. Abell identified clusters as concentrations of 50 or more galaxies in a magnitude range *m3* to *m3+2* (where *m3* is the magnitude of the third brightest cluster member) within a radius $R_A = 1.5$Mpc (based on the magnitude

of the tenth brightest galaxy). Abell's catalog was extended and updated to the southern sky by Abell et al. (1989). As the cores of galaxy clusters are dominated by red, early-type galaxies, it is useful to use colour information to select for over densities of red galaxies (Gladders & Yee 2005, and references therein). The Red-Sequence Cluster Survey (RCS), a sample of 956 clusters identified with a single $(R_c - z)$ color, provided the first modern cosmological constraints using optical selection (Gladders et al., 2007). The five-band photometry of the Sloan Digital Sky Survey (SDSS) was able to cover a broad range of redshifts by tracking the intrinsic 4000 angstrom breaks feature of the old stellar population as it reddens. The maxBCG catalog (Koester et al., 2007) contains almost 14000 clusters with optical richness $N_{gal} \geqslant 10$ at $0.1 < z < 0.3$. Recently, larger SDSS clusters samples have become available, identified using photo-z clustering (Wen et al., 2009) and a gaussian mixture modeling extension of the maxBCG method (GMBCG Galaxy Cluster catalog, Hao et al. 2010). The GMBCG contains 55,424 rich clusters spanning $z \lesssim 0.6$ extracted from the SDSS, which covers roughly 8000 deg^2 of sky.

The Sunyaev-Zel'dovich effect (SZ, Sunyaev & Zeldovich 1970) arises from the interaction of CMB photons with the hot electrons of the ICM, and it is observed in the microwave band. The first SZ catalogs, containing hundreds of clusters, were created at the beginning of this century taking advantage of the new generation of radiotelescopes and microwave detectors. The most important SZ observations have been performed by the radiotelescopes ACT (Atacama Cosmology Telescope, Kosowsky 2006; Marriage et al. 2011) and SPT (South Pole Telescope, Vanderlinde et al. 2010; Carlstrom et al. 2011), along with the results presented by Bartlett et al. (2008) and Planck Collaboration et al. (2011). See Carlstrom et al. (2002) for a review on the SZ effect and its use for cosmological studies.

According to general relativity, light rays passing close to a mass concentration will bend in a phenomenon know as gravitational lensing. Gravitational lensing can both magnify and distort the images of background galaxies. Therefore, it can be detected by studying the statistical appearance of background galaxies (*weak lensing*) and the strong distortions and multiple images of individual sources (*strong lensing*). Gravitational lensing offers a unique probe into the total matter distributions in clusters that does not depend on assumptions regarding the dynamical state of the gravitating matter (Bartelmann, 2010; Kneib & Natarajan, 2011). The combination of weak and strong lensing measurements can strongly

constrain the cluster total mass estimates. So far, gravitational lensing have been used to explore the distribution and nature of dark matter that provides the dominant component of mass in the universe. But additionally, it provides an unique insight into the mysterious dark energy.

Finally, foreground clusters of galaxies can also be used as natural 'telescopes', providing unique information about magnified galaxies seen at early cosmic times. (Frye & Broadhurst, 1998; Pelló et al., 1999) identified sources at $z = 4.04$ lensed by the cluster A2390. A few years later, Kneib et al. (2004) found an object with $z \simeq 7$ lensed by the clusters A2218, and Pelló et al. (2004) claim to have detected an object with $z = 10.0$ magnified by the cluster A1835. The magnification by galaxy clusters as *cosmic telescopes* has also been used in systematic searches for galaxies at very high redshift (Bradac et al., 2009; Richard et al., 2008; Smail et al., 2007; Stark et al., 2007) and for increasing the resolution in detailed studies of sit ant galaxies (Swinbank et al., 2006, 2007).

Being the main topic discussed in this thesis, it is worth dedicating the next Chapter to gravitational lensing theory and its applications in cosmology.

CHAPTER 2

Gravitational lensing by clusters of galaxies

GRAVITATIONAL lensing is a direct consequence of Einstein's theory of General Relativity (see e.g. Bartelmann 2010; Kneib & Natarajan 2011 for a complete description) and constitutes a powerful method to investigate the distribution of matter (either dark or barionic) in galaxy clusters. In the ΛCDM cosmological model, where structure grows hierarchically from small objects that merge together to form larger, gravitational lensing by massive clusters of galaxies is one most direct probes of the rarest high density peaks of the initial density perturbations in the primordial universe. Being the largest and latest collapsed objects in the universe, clusters of galaxies are a small scale reproduction of the universe in terms of composition. Besides, they are often undergoing violent dynamical processes, which allows us to study in detail how structure formation takes place.

For these reasons, galaxy clusters are expected to act as the most powerful lenses in the universe. Gravitational lensing is a purely geometric effect, independent on the wavelength of the emitted light and on the dynamical state of the matter that produced the gravitational field. The lensing effects by clusters of galaxies are spectacular, occasionally producing multiple-images of the same single background galaxy and the formation of giant gravitational arcs. This regime is often called *strong lensing* and occurs when a background galaxy lays at a small angular distance of the cluster centre. Strongly lensed distant objects will thus appear distorted and highly magnified. A massive cluster of galaxies such as that in Fig. 2.1 produces

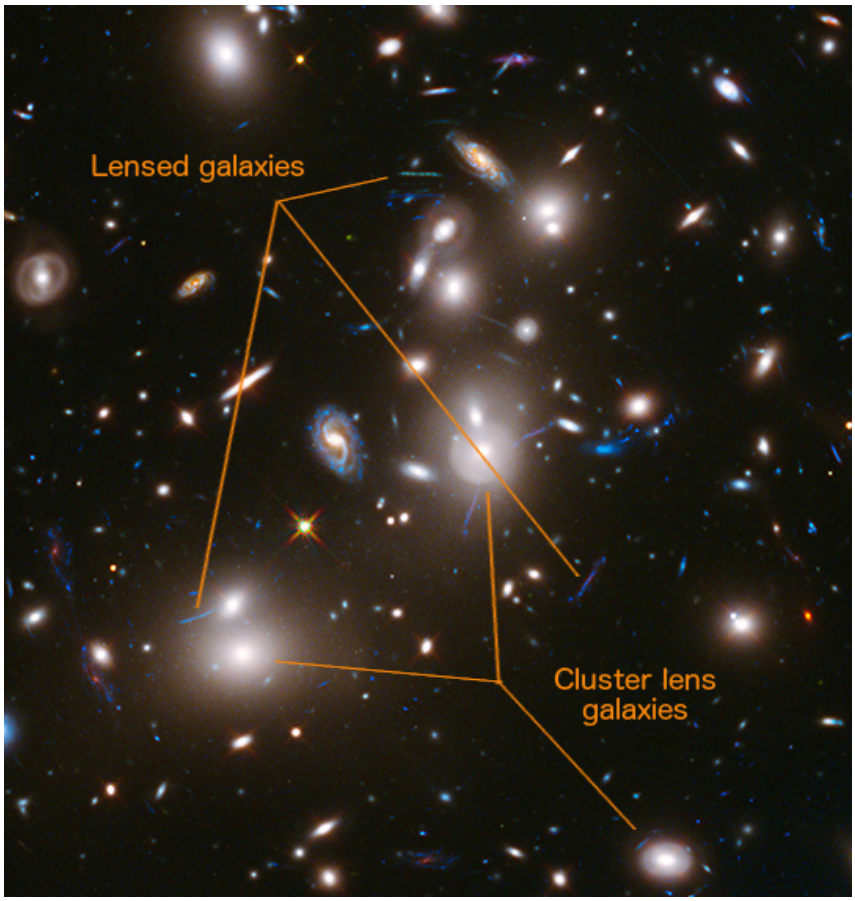

Figure 2.1: Hubble Space Telescope false colour image of Abell2744 taken as part of the Frontier Fields programme. The image reveals many luminous members (white/yellow colour), but also numerous background galaxies (typically blue) stretched and distorted by the gravitating mass in the cluster, which is mainly dominated by dark matter. Credits: NASA/ESA.

striking distorted images of background galaxies which appear to swirl around the cluster core.

However, even when the angular distances of the background objects are large, the shape of background galaxies is weakly distorted (*weak lensing*). In the weak lensing regime, where the shape of background galaxies are dominated by their intrinsic ellipticities, statistical methods are required to detect the weak lensing signal. Furthermore, the observed images of these galaxies are also distorted by the image camera optics and the imaging point spread function (PSF).

2.1 Gravitational lensing theory

For cluster size lenses, the lens mapping can be described by the thin lens equation

$$\vec{\beta} = \vec{\theta} - \vec{\alpha}\left(\vec{\theta}\right) \tag{2.1}$$

This equation describes the shift in the original angular position in the source plane $\vec{\beta} = (\beta_1, \beta_2)$ by a deflection angle $\vec{\alpha} = (\alpha_1, \alpha_2)$ to the angular coordinates $\vec{\theta} = (\theta_1, \theta_2)$ in the lens plane (Fig. 2.2). As the lens equation can have more than one solution for a fixed $\vec{\beta}$, the lens can produce multiple images of the same source at $\vec{\beta}$. The thin lens approximation is valid only when the distances from the observer to the lens and source are significantly larger than the physical extend of the lens, which is true for clusters of galaxies. Because of the expanding nature of the universe, there are many ways to specify the distance between two points in cosmology. The angular diameter distance, frequently used in gravitational lensing, is defined as the ratio of an object's physical size to its observed angular size and depends on the assumed cosmology. For a ΛCDM cosmology with $\Omega_k = 0$, the angular diameter distance is expressed as:

$$D_A = \frac{c\, H_0}{(1+z)} \int_0^z \frac{dz'}{E(z')} \tag{2.2}$$

with $E(z') = \sqrt{\Omega_M(1+z)^3 + \Omega_k(1+z)^2 + \Omega_\Lambda}$.

By applying the Fermat principle, which states that light follows the path with a stationary travel time, the deflection angle can be related to a lensing potential:

$$\psi\left(\vec{\theta}\right) = \frac{1}{\pi} \int \mathrm{d}^2\theta' \frac{\Sigma\left(D_L\vec{\theta}\right)}{\Sigma_{cr}} \ln|\vec{\theta} - \vec{\theta}'| \tag{2.3}$$

which is a line-of-sight projected and rescaled version of the gravitational Newtonian potential. The critical surface mass density for lensing (Σ_{cr}) introduced here is given by:

$$\Sigma_{cr} = \frac{c^2}{4\pi G} \frac{D_S}{D_L\, D_{LS}} \tag{2.4}$$

and depends on the angular diameter distances between the observer and the lens (D_L), between the observer and the source (D_S) and between the lens and the source (D_{LS}).

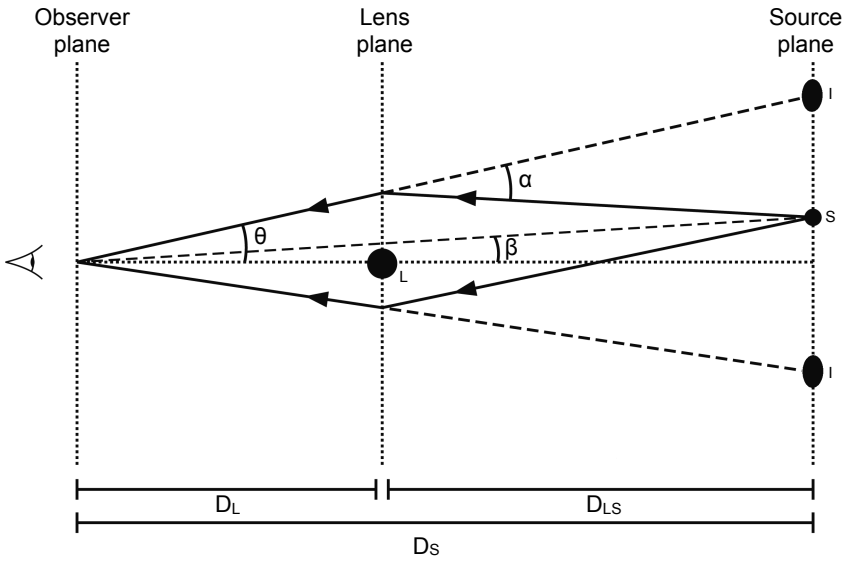

Figure 2.2: Geometry of a simple thin lens configuration. Due to the gravitational field of the lens (L), the true source position in the source plane (S) is deflected by an angle (α) producing an image (I) with an angle θ (instead of β) with respect to the observer (O). The angular diameter distance between the observer and the lens, between the observer and the source and between the lens and the source are denoted D_L, D_S and D_{LS}, respectively.

The deflection angle depends on the surface-mass density distributions of the lens $\Sigma\left(D_L\vec{\theta}\right)$ and can be written as the gradient of the lensing potential as:

$$\vec{\alpha}\left(\vec{\theta}\right) = \nabla\psi\left(\vec{\theta}\right) = \frac{1}{\pi}\int \mathrm{d}^2\theta' \frac{\Sigma\left(D_L\vec{\theta}\right)}{\Sigma_{cr}} \frac{\vec{\theta}-\vec{\theta'}}{|\vec{\theta}-\vec{\theta'}|^2} \tag{2.5}$$

As a result of the gravitational lensing effect, the position of the images can be calculated from the solutions $\vec{\theta}$ of the lens equation for a source at $\vec{\beta}$. The original shape of the source will be distorted because light bundles are deflected differentially, leading to the occurrence of giant gravitational arcs in clusters of galaxies. In the case of a source much smaller than the angular scale on which lens properties change, the lens equation can be locally linearised and the distortion of images can be then described by the Jacobian matrix (also referred as magnification matrix):

$$\mathcal{A}^{-1}(\vec{\theta}) = \frac{\partial\vec{\beta}}{\partial\vec{\theta}} = \left(\delta_{ij} - \frac{\partial^2\psi(\vec{\theta})}{\partial\theta_i\partial\theta_j}\right) = \begin{pmatrix} 1-\kappa-\gamma_1 & -\gamma_2 \\ -\gamma_2 & 1-\kappa+\gamma_1 \end{pmatrix} \tag{2.6}$$

where the *convergence* κ is related to the lensing potential ψ through the Poison's equation as:

$$\kappa(\vec{\theta}) = \frac{1}{2}\nabla^2\psi(\vec{\theta}) = \frac{\Sigma(D_L\vec{\theta})}{\Sigma_{cr}} \tag{2.7}$$

and the *shear* vector (often expressed as a complex number $\vec{\gamma} = \gamma_1 + \mathrm{i}\gamma_2$) is defined as:

$$\gamma_1 = \frac{1}{2}\left(\partial^2/\partial^2\theta_1 - \partial^2/\partial^2\theta_2\right)\,\psi(\vec{\theta}) \tag{2.8}$$

$$\gamma_2 = \frac{\partial^2\psi(\vec{\theta})}{\partial\theta_1\,\partial\theta_2} \tag{2.9}$$

As the magnification matrix is real and symmetric, it can be diagolalised and expressed in terms of its principal axes as follows:

$$\mathcal{A}^{-1} = (1-\kappa)\left[\begin{pmatrix} 1 & 0 \\ 0 & 1 \end{pmatrix} + \frac{\gamma}{1-\kappa}\begin{pmatrix} 1 & 0 \\ 0 & -1 \end{pmatrix}\right] \tag{2.10}$$

Gravitational lensed images will be observed as distorted images in shape and size of the original source image. The shape distortion is due to the tidal gravitational

field, which is described by the shear γ. When relating the shear to observables, the most directly measured quantity is the reduced shear defined as $g = \gamma/(1-\kappa)$. On the other hand, $1-\kappa$ describes an isotropic deformation caused by the local matter density κ of the lens.

In addition to the distortion of the images, by which the reduced shear can be measured locally, gravitational lensing also magnifies the images. According to Liouville's theorem, gravitational lensing conserves the surface brightness. Hence, for a surface brightness distribution in the source plane $I_S\ (\vec{\beta})$, the observed surface brightness distributions is given by:

$$I(\vec{\theta}) = I_S\left[\vec{\beta}(\vec{\theta})\right] \tag{2.11}$$

Using the locally linearised lens equation, the observed surface brightness of a point at $\vec{\theta}_0$ within an image is:

$$I(\vec{\theta}) = I_S\left[\vec{\beta}_0 + \mathcal{A}(\vec{\theta}_0)\ \cdot\ (\vec{\theta} - \vec{\theta}_0)\right] \tag{2.12}$$

with $\vec{\beta}_0 = \vec{\beta}\,(\vec{\theta}_0)$ the corresponding point within the source. The ratio of the observed flux $I(\vec{\theta})$ to the unlensed source flux $I_S(\vec{\beta})$ is defined as the *magnification* μ:

$$\mu = \frac{1}{\det \mathcal{A}} = \frac{1}{(1-\kappa)^2 - |\gamma|^2} = \frac{1}{(1-\kappa)^2 - (1-g)^2} \tag{2.13}$$

Sources in the lens plane where the lens equation becomes singular, i.e. where its Jacobian determinant vanishes ($\det \mathcal{A} = 0$), will define two closed curves called *critical lines*. The corresponding lines in the source plane are called *caustic lines*. Sources near caustics can be strongly magnified and distorted, producing luminous arcs and multiple images of the same source (*strong lensing* regime).

Although not always realistic, strong lensing with galaxy clusters is most easily illustrated with axially symmetric lens models. Under this assumption, the most important quantities for lensing in clusters of galaxies (the deflection angle α, the convergence κ, and the shear γ) can be expressed in terms of the projected surface mass density as:

$$\begin{aligned} \kappa(r) &= \frac{\Sigma(r)}{\Sigma_{cr}} \\ \gamma(r) &= \frac{\bar{\Sigma}(r) - \Sigma(r)}{\Sigma_{cr}} \\ \vec{\alpha}(r) &= \theta \, \frac{\bar{\Sigma}(r)}{\Sigma_{cr}} \end{aligned} \tag{2.14}$$

where $\bar{\Sigma}(R)$, defined as mean surface mass density inside the radius R, is given by:

$$\bar{\Sigma}(R) = \frac{1}{\pi R^2} \int_0^R 2\pi r \Sigma(r) dr \tag{2.15}$$

with $R = \theta D_L$ is the physical radius spanned by the angular radius θ.

In the same way, the total projected mass inside an aperture radius R can be expressed as follows:

$$M(R) = 2\pi \int_0^R \Sigma(r) r dr \tag{2.16}$$

In the idealised case of axially symmetric lenses, both the critical and caustic lines form circles and are easy to distinguish: the internal critical line where the deformations are radial, and the external critical line where the deformations are tangential. The position of the tangential critical line is denoted as the *Einstein radius* $R_E = \theta_E D_L$ and has been defined in different ways in literature. For example, the *equivalent* Einstein radius is defined as the radius enclosing a mean convergence of one (Zitrin et al., 2011; Richard et al., 2010):

$$\bar{\kappa}(R_{E,\,eqv}) = \frac{\bar{\Sigma}(R_{E,\,eqv})}{\Sigma_{cr}} = 1 \tag{2.17}$$

Meneghetti et al. (2011) proposed to quantify the size of the Einstein radius by taking the median distance of the tangential critical points from the clusters centre (denoted as $\theta_{E,\,med}$). The lensing cross section correlates better with $\theta_{E,\,med}$ than with $\theta_{E,\,eqv}$ due to the fact that $\theta_{E,\,med}$ captures better the important effect of shear caused by the cluster substructures: elongating the tangential critical lines along preferred directions and pushing critical points to distances where the convergence κ is below to unity (Meneghetti et al., 2011; Bartelmann, 1995). Redlich et al. (2012) found that $\theta_{E,\,med}$ and $\theta_{E,\,eff}$ are tightly correlated, being $\theta_{E,\,eff}$ the *effective* Einstein radius defined as the radius of the circle having the area (A) enclosed by the tangential critical line:

$$\theta_{E,\,eff} \equiv \sqrt{\frac{A}{\pi}} \tag{2.18}$$

The mass enclosed by the tangential critical line (also denoted as the Einstein radius r_E) is:

$$M(R_E) = \pi \Sigma_{cr} R_E^2 \tag{2.19}$$

while the position of the radial critical line, which depends on the gradient of the mass profile, is defined as:

$$\frac{\mathrm{d}}{\mathrm{d}R}\left(\frac{M(R)}{\pi \Sigma_{cr} R}\right) = 1 \tag{2.20}$$

Given Eqs. 2.19 - 2.20, the presence of tangential and radial arcs indicates that clusters of galaxies have dense cores with fairly flat density profiles. The position of the tangential critical line allows estimates of the total enclosed lens mass, while the radial critical line constrains the slope of the mass profile near the cluster centre. Therefore, identifying the sizes of the critical lines (both radial and tangential) in observed clusters is a crucial step towards measuring the mass and its distribution in the inner regions. These are profound, qualitative conclusions quite independent of the detailed mass distribution on lensing clusters of galaxies. However, for an accurate estimate of the enclosed mass, the redshifts of the lensing cluster and the arcs need to be known precisely. Furthermore, the determination of the critical lines for non-symmetric lenses cannot be addressed analytically in most of the cases.

2.2 Mass distribution in clusters of galaxies

Cluster mass distribution in the strong lensing regime is commonly modeled using *parametric* models (e.g. Kneib et al. 1996; Natarajan & Kneib 1997; Broadhurst et al. 2005b). In this approach the mass distribution of the lens is described by a combination of different mass components: small scale perturbations (galaxy components) and some large scale components (resembling the dark matter, X-ray gas and ICM). Each component is characterized by a set of parameters, which are optimised individually to fit the observed strong lensing features. In order to obtain an accurate best-fit model, the number of model parameters needs to be balanced to the number of observational constrains available.

However, given the few constrains generally available to optimize the model, the Bayesian approach is well-suited to strong lens modeling. In the context of a fully Bayesian framework, Jullo et al. (2007) developed LENSTOOL for modeling strong lensing in clusters of galaxies with parametric methods.

At the same time, there has been a considerable progress in developing *non-parametric* techniques to model the cluster mass distribution from strong lensing in the last years (Abdelsalam et al., 1998; Saha & Williams, 1997; Diego et al., 2005a,b; Jullo & Kneib, 2009; Coe et al., 2010; Zitrin A. et al., 2010). Although the mass distribution is generally tessellated into a regular grid of small mass elements, recent studies (Coe et al., 2008, 2010; Deb et al., 2008) use the actual distribution of images as an irregular grid. In this context, non-parametric methods are clearly favored to model extremely complex mass distributions and have become more popular with the increase of the discovery of numerous multiple images (Zitrin et al., 2012b; Zitrin et al., 2013; Jauzac et al., 2014a,b; Grillo et al., 2015; Merten et al., 2015). Indeed, one of the most important results of these schemes is the discovery of the dissociation between the dark matter distribution and the ICM in the 'Bullet cluster' (Bradac et al., 2006).

Although the parametric methods have demonstrated that small mass clumps do substantially affect the positions of the observed images, galaxy mass scales are usually not taken into account in the non-parametric approach. Nevertheless, combining strong and weak lensing observations of clusters naturally probe complementary regimes, as strong lensing information can accurately constraint the matter distribution in the cluster centre whereas weak lensing traces mass out to the cluster outskirts. Current methods that combine strong and weak lensing information have been proposed by Bradac et al. (2005); Cacciato et al. (2006); Diego et al. (2007); Merten et al. (2009).

The large number of multiple images identified in the last decade has increased rapidly the number of constraints for modeling the mass distribution in cluster of galaxies. For instance, approximately 200 multiple image systems have been identified in the cluster MACSJ0416.1-2403 by Jauzac et al. (2014a) based on *HST Frontier Fields* (HFF) imagine data (Fig. 2.3). This increase in the number of observational constraints has allowed to describe the mass distributions by a larger number of mass components (which can also be more complex) and hence with unprecedented accuracy.

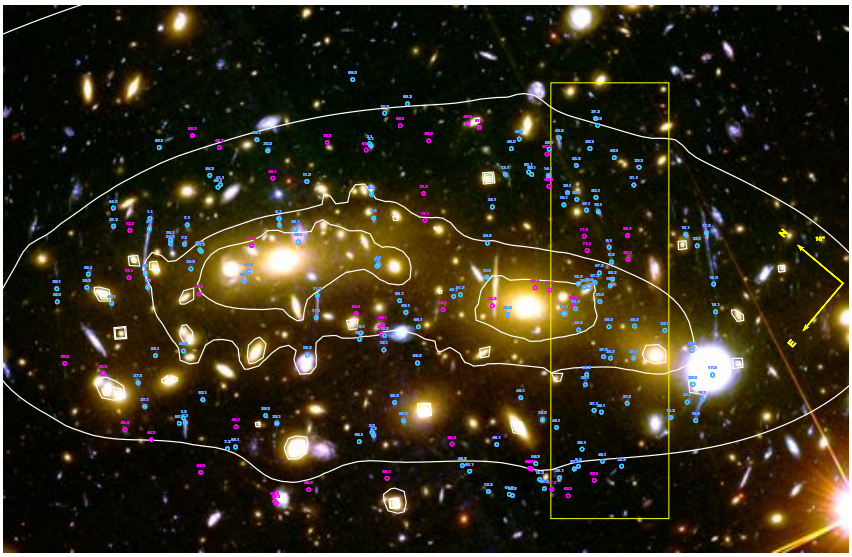

Figure 2.3: Overview of all multiple-image systems in the cluster MACSJ0416.1-2403. The most secure identifications, used to optimise the lens model in the image plane (149 images) are shown in cyan; the less secure candidates (45 images) are shown in magenta. The underlying colour image is a composite created from HST/ACS images in the F814W, F606W, and F435W passbands. Mass contours of the best-fit strong-lensing model are shown in white. Image taken from Jauzac et al. (2014a).

2.2.1 Cluster mass estimates

As previously demonstrated, gravitational lensing provides important information on the distribution of matter in clusters of galaxies. Cluster masses obtained in this way are very close to mass estimates derived from X-ray observations. However, gravitational lensing is sensitive to the projected mass regardless of its physical state, while the interpretations of X-ray data requires assumptions on symmetry and hydrostatic equilibrium of the gas trapped by the gravitational potential well. Although there is a qualitative, overall agreement between these entirely different mass estimates, recent examples have found substantially discrepant mass estimates based on X-ray and strong lensing observations (Pratt et al., 2005; Gitti et al., 2007; Miranda et al., 2008; Halkola et al., 2008; Ebeling et al., 2009), while a good agreement is nevertheless found in other galaxy clusters (Rzepecki et al., 2007; Bradac et al., 2008; Israel et al., 2010).

The reasons for these discrepancies are still under debate. However, a good agreement is achieved in clusters for which equilibrium can be assumed, while unrelaxed clusters usually show different mass estimates with different methods.

X-ray mass estimates from numerical simulations are generally bias (Bartelmann & Steinmetz, 1996; Rasia et al., 2006), particularly in the case of merging clusters because their X-ray gas is still cooler than expected from their total mass, which is already seen by the lensing effect. Allen (1998) found an appreciable mass discrepancy in clusters without cooling flows, but a good agreement of X-ray and lensing mass estimates in clusters with cooling flows. This supports the concept that well-relaxed clusters which had sufficient unperturbed time to develop a cooling flow are well-described by simple, axially-symmetric models for lensing and the X-ray emission, while dynamically more active clusters tend to give discrepant mass estimates (as confirmed by Wu 2000). Meneghetti et al. (2014) recently found that simulated halos with X-ray morphologies similar to those of the CLASH clusters are modestly affected by strong lensing bias. Therefore, intracluster gas in an incomplete or perturbed hydrostatic equilibrium seems to explain the observed discrepancy in some clusters.

Given the fact that gravitational lensing accounts for the projected mass along the line of sight, the triaxiality of cluster lenses and the presence of substructures also play an important role. For example, asymmetries and substructures in galaxy clusters affect the lensing efficiency at a given mass. The most efficient lenses tend to be prolate halos whose longest axis is well aligned with the optical axis (Hennawi et al., 2007; Oguri & Blandford, 2009; Meneghetti et al., 2010a; Waizmann et al., 2012). Mass estimates based on axially symmetric models are thus systematically too high (Bartelmann, 1995; Hasinger et al., 1998). As found by Giocoli et al. (2012b), the main contribution to the bias in mass and in concentration is due to the halo triaxiality and second to the presence of substructures within the host halo virial radius.

Consequently, it appears that mass discrepancies can commonly be traced back to the dynamical activity in unrelaxed clusters (see also Smith et al. 2005), but at least part of the disagreement also occurs because of model restrictions which, if removed, generally lead to better agreement (Gavazzi, 2005; Donnarumma et al., 2009).

2.2.2 Cluster mass profiles

Being much closer to the cluster cores than tangential arcs, radial arcs are also more likely to be confused with, or hidden by, the light of the cluster galaxies. For

these reasons, although the positions and relative abundances of radial compared to tangential arcs in clusters of galaxies provide important constrains on their central density profiles, results based on radial arcs have not been exploded successfully yet. Assuming mass profiles with cores, tangential arcs require small core radii as described above, but the existence of radial arcs requires finite cores of some sort (Le Fevre et al., 1994; Luppino et al., 1999). However, numerical simulations of dark matter halos show that density profiles flatten toward the core, but do not develop flat cores (Navarro et al., 1996, 1997). Simultaneously, Bartelmann (1996) showed that radial arcs can also be formed by halos such *cuspy* density cores, provided the central cusp is not too steep. Applying the same technique as Miralda-Escude (1995), Sand et al. (2005) demonstrated that, assuming axially-symmetric mass distributions, central density profiles have to be substantially flatter than those found in CDM simulations. However, small deviations from axial symmetry can invalidate this conclusion and establish agreement between these observations and CDM density profiles (Bartelmann & Meneghetti, 2004; Meneghetti et al., 2007). Conducting a similar analysis, Gavazzi et al. (2003) found that an isothermal core profile for the cluster MS2137 is preferred compared to the NFW profile. Using X-ray, weak and strong lensing data, Smith et al. (2001) constrained the core density profile in A383 and found it more peaked than the NFW profile, but argued that this may be due to the density profile of the cD galaxy. It must be stressed that baryons, in particular by cooling and star formation, can affect cluster density profiles where the gas density is high enough for cooling times to fall below the Hubble time. In fact, the presence of baryons in cluster cores can significantly influence and steepen the innermost cluster density profiles (Barkana & Loeb, 2010).

2.3 Arc abundances and statistics

The description of the mass distribution in clusters of galaxies can also be addressed statistically (see Meneghetti et al. 2013 for a complete review). The probability for a cluster to be a strong lens depends sensitively on the lens properties which characterise its mass distribution. In addition, since both lens properties and geometry of the universe depend on cosmology, the statistics of strong lensing events is a potential tool for constraining the average structural properties of clusters of galaxies and the cosmological parameters. In particular, strong gravitational lensing by clusters of galaxies is one of the most important test of the cosmological

model in the sense that it probes the rarest high density peaks in the universe and is extremely sensitive to the properties of the clusters cores.

The abundance of strong lensing events, such as gravitational arcs and multiple images, depends on cosmology through the angular-diameter distances of the lens and the source and through the structure formation (given that the mass function of dark matter halos and the internal properties of the lenses are related to the cosmological parameters). Massive and compact clusters of galaxies at $0.2 \lesssim z_l \lesssim 0.4$ (for sources at redshifts $z_s \gtrsim 1$) are the most efficient lenses on producing gravitational arcs. The number of potential lenses that populates the universe at high redshift is expected to be higher in cosmological models where the growth of the cosmic structures is faster at earlier epochs, such as models where some dynamical dark energy starts dominating the expansion of the universe at earlier epochs (Bartelmann et al., 2003; Macciò, 2005; Meneghetti et al., 2005). As reported by Bartelmann et al. (1998), the probability of producing gravitational arcs from simulated clusters changes by orders of magnitude in different cosmological models.

Under the assumption of a constant number density of clusters of galaxies and given that the volume per unit redshift is larger in low-density than in high-density cosmological models, the number of possible efficient lenses is thus higher in the former than in the later models.

The cluster concentrations are found in numerical simulations to reflect the density of the universe at the epoch of cluster formation. Clusters forming earlier have higher concentrations (Dolag et al., 2004) and are expected to be more efficient lenses. Strong lensing is a highly non linear effect and the number of strong lensing events depends sensitively on the number of cusps in, and the length of, the caustic lines of the lenses. Cusps directly implies asymmetric lenses. Asymmetric and substructured clusters are thus more efficient in producing large arcs than symmetric clusters (assuming that the individual clusters subclumps are compact enough).

2.3.1 Arc statistics problem

Strong lensing statistics can be as competitive as other cosmological probes for constraining cosmological parameters. However, previous attempts of using strong lensing statistics as a cosmological tool have produced controversial results. In particular, studying the lensing properties of a set of numerically simulated

clusters, Bartelmann et al. (1998) argued that the ΛCDM cosmological model (with $\Omega_M = 0.3$ and $\Omega_\Lambda = 0.7$) fails at reproducing the observed abundance of giant gravitational arcs reported in Le Fevre et al. (1994) by almost an order of magnitude. This inconsistency between expectations in the ΛCDM model, which is strongly supported by a number of powerful cosmological probes, and the observed abundance of gravitational arcs is knows as the *arc statistics problem*.

A long series of papers have tried to minimize the discrepancy found by Bartelmann et al. (1998). Despite the asymmetry, Meneghetti et al. (2003) found that analytic models are inadequate for quantitative arc statistics, demonstrating the importance of taking into account substructures in these models. Because of the triaxiality and substructure of ΛCDM halos, Dalal et al. (2004) found that the cross section for gravitational arcs in individual clusters varies by more than an order of magnitude as a function of viewing angle and evidenced a possible excess of arcs observed in clusters at $z \gtrsim 0.6$. Oguri et al. (2004) studied the strong lensing properties of triaxial halos and found that they may well explain the high arc abundance, provided their central density slopes are steep enough, with a logarithmic slope close to 1.5. Bartelmann et al. (2003) estimated the effect of higher cluster concentrations and found that dark energy may in fact increase arc abundances substantially, but not sufficient for solving the arc statistics problem. Cluster mergers significantly increase the lensing efficiency (Torri et al., 2004; Redlich et al., 2012).

All these limitations found in numerical simulations, including cooling in cluster cores (Puchwein et al., 2005; Wambsganss et al., 2004) and line-of-sight projections effects (Puchwein & Hilbert, 2009), returned moderate enhancements of the expected arc abundance. Killedar et al. (2012) showed that, while gas cooling and stat formations alone increase the number of expected giant arcs, the inclusion of AGN feedback brings the strong lensing cross sections back to values very similar to those measured in dark matter only simulations.

The impact of several sources properties on the efficiency of numerically simulated clusters to produce giant arcs was extensively discussed in Gao et al. (2004). They found that the source size and clustering only have a small effect on the abundance of gravitational arcs. Additionally, they noted that $\sim$ 30% of galaxies with very elongated shapes ($e = 1 - b/a > 0.5$) increases the productions of giant arcs by a factor of 2, compared to simulations where the galaxy ellipticities were uniformly distributed in the range $0 < e < 0.5$.

The value of the normalization parameter for the dark matter power spectrum (σ_8) was found to affect significantly the lensing efficiency (Li et al., 2005; Fedeli et al., 2008). However, recent measurements converge on a low normalization parameter ($\sigma_8 \simeq 0.81$, see Table 1.1), which drastically lowers the expected abundance of gravitational arcs.

This evidence pushed in the same direction of the *arc statistics problem*, in the sense that they both suggested that observed galaxy clusters are too strong lenses compared to numerically simulated clusters (Fig. 2.4). Moreover, as it was also enforced by several other observations of strong lensing clusters, which seemed to indicate that: first, some galaxy clusters have very extended critical lines whose abundances can hardly be reproduced by cluster models in the framework of a ΛCDM cosmology (Broadhurst & Barkana, 2008; Tasitsiomi et al., 2004); and second, few clusters, for which high quality strong and weak lensing data became available, have concentrations which are too large compared to numerical expectations (Broadhurst et al., 2008; Zitrin et al., 2009).

Understanding the origin of these mismatches between theoretical predictions and observations is fundamental, as these may evidence a lack of understanding of the cluster physics, which may be not well implemented in the simulations, or, conversely, highlight some inconsistencies between the ΛCDM scenario and the properties of the universe on small scales.

So far the comparison between theoretical predictions and observations has been complicated by the lack of systematic arc surveys but also by the fact that different approaches were used to analyze simulations and observations. In this context, the Einstein radius defines characteristic scale of strong lensing mainly related to the aperture mass it encloses. Therefore it is expected that the largest Einstein radii in the universe probe the structure and abundance of the most massive clusters. This enables a test of the ΛCDM model at the upper mass tail of the halo mass function in terms of the Einstein radius statistics. An advantage of this test is the simple and straightforward determination of the Einstein radius in observations and its correspondence to identify large lenses. Besides, this approach is computationally less demanding than explicitly calculating individual lensing cross sections, since the computation of Einstein radii can be implemented in a particularly efficient way. Therefore, studying Einstein radii statistics rather than arc statistics, may be seriously considered as a more efficient method to constrain cosmological parameters and structure formation with strong lensing in clusters of galaxies.

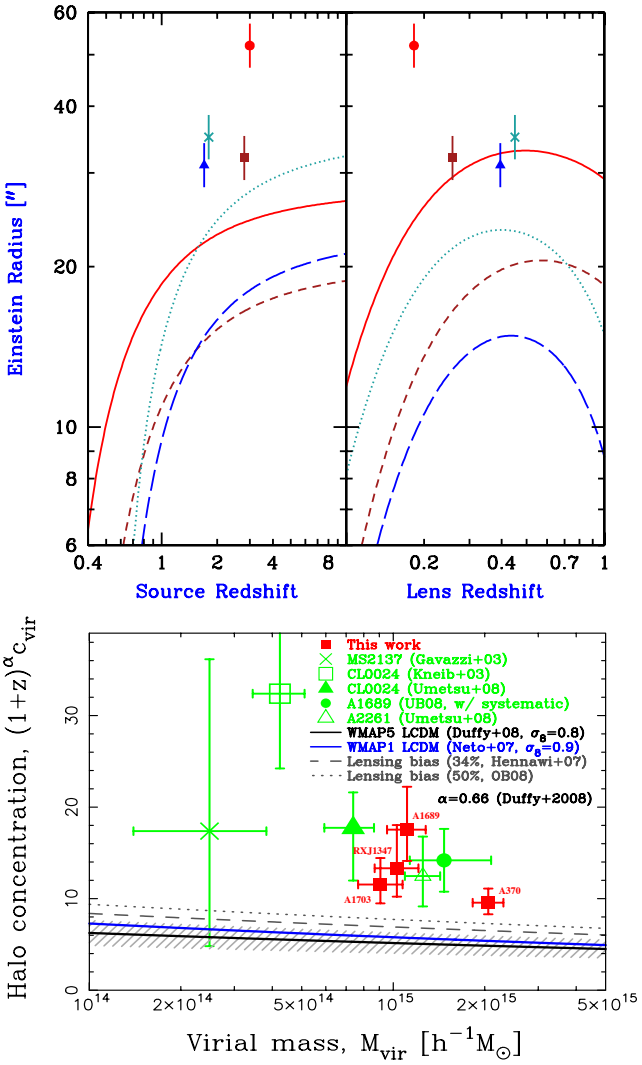

Figure 2.4: Upper panel: Dependence of the Einstein radius θ_E on the source redshift z_s and lens redshift z_l. The points correspond to the observed clusters, while the curves show the predicted θ_E based on the median c_{200} of relaxed simulated halos as measured by Neto et al. (2007), after correction for lensing and projection bias: A1689, solid curves and circles; A1703, short-dashed curves and squares; Cl0024, long-dashed curves and triangles; RXJ1347, dotted curves and crosses. Image taken from Broadhurst & Barkana (2008). Bottom panel: Comparison of observations with the ΛCDM model, based on N-body simulations for the $c_{\rm vir} - M_{\rm vir}$ relation derived at $z = 0$. The data points are derived from a lensing analysis, and are multiplied by $(1 + z)^{0.66}$ at the cluster redshift, for consistency with the evolution of $c_{\rm vir}(M_{\rm vir})$ derived from ΛCDM simulations by Duffy et al. (2008). The predictions of Duffy et al. (2008) ($\sigma_8 = 0.8$, WMAP5) and Neto et al. (2007) ($\sigma_8 = 0.9$, WMAP1) are shown as solid curves. Image taken from Broadhurst et al. (2008).

However, first attempts to compare the observed Einstein radii statistics to simulations were controversial, probably due to the limited number of strong lenses available. Meneghetti et al. (2011) compared the statistics of Einstein radii in the *MareNostrum Universe* to those in a sample of 12 MACS clusters at redshift $z > 0.5$ (Ebeling et al., 2007). The distributions of the observed Einstein radii is characterised by an excess of clusters toward the large values of θ_E. The medians of the Einstein radii in the two samples differ by $\sim 25\%$. Comparing the MACS clusters to semi-analytical models considering WMAP7 cosmological parameters, Zitrin et al. (2011) reported a difference of $\sim 40\%$ between the observed and the theoretical Einstein radii distributions.

2.3.2 Semi-analytic models

Several theoretical studies have proved that strong lensing clusters are particularly complex systems, which cannot be described by means of simple analytical models like axially symmetric or even elliptical lenses. As discussed before, various cluster properties contribute to the strong lensing efficiency: clusters galaxies, substructures, asymmetries and triaxiality of the mass distributions, mergers, effects of baryons, etc. Given this, N-body cosmological simulations have been essential for reliable arc statistics studies. In recent years, the development of numerical codes (i.e. ray-tracing methods) and the advent of increasingly faster supercomputers have made possible to perform cosmological simulations with high mass resolution over large volumes (minimizing the impact of cosmic variance). Large cosmological simulations can be used to construct realistic mass distributions in combination with analytical mass components (*semi-analytic* methods). The code MOKA (Giocoli et al., 2012a) is an example of this kind of approaches. The code constructs realizations of clusters lenses combining: 1) a smooth halo component, resembling the dark matter halo of the cluster; 2) a central concentration of 'stars', resembling the presence of a massive galaxy dominating the mass distribution in the cluster centre; 3) a number of substructures, which constitute the clumpy component of the cluster mass distribution. Giocoli et al. (2012a) found that halos simulated with MOKA reproduce very well the lensing cross sections of halos in the *MareNostrum Universe*.

Also using a semi-analytic approach, Redlich et al. (2012) implemented an interesting method to account for the impact of mergers in the distribution of

Einstein radii. Based on this method, Waizmann et al. (2012) evaluated the occurrence probability of the Einstein radius of MACSJ0717.5+3745 in terms of the extreme value statistics of the largest Einstein radius in a ΛCDM cosmology. Using triaxial NFW halo models and generating cluster distributions from mass functions calibrated on numerical simulations, Waizmann et al. (2012) concluded that MACSJ0717.5+3745 is not in tension with ΛCDM (see also Oguri & Blandford 2009). Based on the same statistical approach, Waizmann et al. (2014) showed that the twelve Einstein radius reported by Zitrin et al. (2011) are consistent with the expectations of the ΛCDM model. Moreover, Redlich et al. (2014) demonstrated that cluster mergers increased the expected values of the largest Einstein radius by $\sim 10\%$. They found no evidence for a tension between the strength of the observed gravitational lenses at $z > 0.5$ and the theoretical predictions of the ΛCDM model. At redshifts $z < 0.5$, the situation is more complicated. By comparing the largest Einstein radii of the 10,000 SDSS clusters analysed by Zitrin et al. (2012a) to the theoretical distributions, Redlich et al. (2014) found that the observed gravitational lenses at $z < 0.5$ appear to be stronger than expected, but not reliable statistical evidence for claiming that these observations seriously challenge the predictions of the standard cosmological model. Besides, the general conclusion is that the distribution of the largest Einstein radius is particularly sensitive to the precise choice of the halo mass function, lens triaxiality, the inner slope of the halo density profile and the mass-concentration relation. We will analyze these effects in more detail in the following sections.

2.3.3 Projection effects and selection bias

Combined strong and weak lensing analysis of galaxy clusters have found in many cases that NFW density profiles well reproduce the lensing observables, but with concentration parameters that are substantially larger than expected from numerical simulations (Broadhurst et al., 2005a; Comerford & Natarajan, 2007; Umetsu & Broadhurst, 2008; Broadhurst et al., 2008; Umetsu et al., 2010; Sereno et al., 2010). The concentration in this case is defined as the ratio between the virial radius and the scale radius of the profile, which is the radius where the central shallower slope turns into the steeper slope farther out (Sec. 1.5.1). Due to selection biases and projection effects, strongly lensing clusters should be among the most concentrated clusters, in the sense that concentrations inferred from their projected

mass distribution, c_{2D}, should be significantly higher than in three dimensions c_{3D}. Meneghetti et al. (2010a) found that the concentration bias is heavily conditioned by the lens redshifts and strong lensing cross sections. For the strongest lenses, the concentration bias c_{2D}/c_{3D} can be of the order of 50% - 70% even for clusters with mass $M > 7 \times 10^{14} h^{-1} M_{\odot}$.

Other studies suggest that the extreme concentrations of some galaxy clusters derived from the lensing analysis can be explained by means of clusters elongation along the line of sight (see the review by Limousin et al. (2013) and references therein). Different studies based on numerical simulations showed that the dark matter halo shapes are triaxial (Sec. 1.5.1). Besides, various observations of clusters of galaxies, both in optical and in X-ray, have confirmed this picture and have revealed that a discrete number of X-ray selected clusters present also their major axis elongated along the line of sight. Elongated clusters can produce very distorted gravitational arcs and large Einstein radii, and also a discrepancy between cluster masses and concentrations determined from X-ray and gravitational lensing observations.

The triaxiality of lensing clusters has a substantial impact on the distribution of the largest Einstein radii. For instance, a very elongated cluster with its major axis projected along the line of sight can lead to a highly concentrated, projected surface mass density profile which can produce a large tangential critical curve (Oguri et al., 2004; Dalal et al., 2004; Meneghetti et al., 2007, 2010a). Besides, the largest Einstein radii either are produced by lower concentrated very elongated halos or by less elongated but higher concentrated ones, which indicated that the impact of triaxiality should always be discussed together with the one of the concentration. Giocoli et al. (2012b) found that elongated halos generated with MOKA lead to large differences both in mass (M_{2D}/M_{3D}) and concentration (c_{2D}/c_{3D}) of about 35% - 40%, even up to 50% in the case of very massive clusters. These results can lead to very important systematics when trying to recover cosmological information from the mass and concentration estimates based on lensing analysis without taking into account possible projection effects (Sereno & Zitrin, 2012; Coe et al., 2012).

Additionally, as discussed in Sect. 2.3.1, the cluster's ability to produce strong lensing events is boosted by dynamical processes such as mergers or, more generally, by substructures orbiting around their host halo and occasionally crossing the cluster cores in projections (Bayliss et al., 2014). For these reasons, the selection of clusters based on their ability to produce strong lensing features is likely to

generate a sample affected by biases. Given that lensing is sensitive to the total mass projected on the lens plane, the cluster structural parameters inferred from the lensing analysis of clusters affected by a projection bias will be biased as well. To avoid this, a selection based on the cluster X-ray morphology is often advocated. For example, comparing halos from the *MareNostrum Universe* to MACS clusters, which constitute a sample of X-ray selected clusters, Meneghetti et al. (2011) estimated that the median concentration bias of the MACS sample is only $\sim 11\%$, and for $\sim 20\%$ of the sample the concentration bias is expected to be $> 40\%$. Giocoli et al. (2012b) pointed out that, from randomly selected cluster samples, the concentration-mass relation derived from a 2D lensing analysis is expected to have a lower amplitude, compared to the 3D concentration-mass relation. Rasia et al. (2013) showed that selecting clusters according to their X-ray luminosity not only increases the normalization of the concentration-mass relation with respect to a control sample, but also returns a steeper slope.

Thanks to the progress reached by computational astrophysics in the last two decades, N-body cosmological simulations of galaxy clusters are producing descriptions of the mass distributions very close to the observational results before mentioned. Therefore, the state-of-the-art numerical simulations of galaxy clusters has become a powerful tool for characterizing the general gravitational lensing properties of these objects at the level required for precision cosmology.

CHAPTER 3

Simulations of galaxy clusters

NUMERICAL simulations have been used to study clusters of galaxies for more than four decades. In 1970 Peebles was the first to test gravitational instability as the dominant process of cluster formation, by modelling the Coma cluster using 300 particles of the same mass (Peebles, 1970). In the following decades also the baryon component was included in cluster simulations (Evrard, 1988; Thomas & Couchman, 1992; Katz & White, 1993; Bryan et al., 1994; Navarro et al., 1995), under the assumption that radiative losses of the diffuse gas could be neglected, as cooling time for the bulk is generally longer than a the cluster age. Numerical simulations including baryons were able to reproduce the morphological characteristics of the X-ray observation performed at that time, and succeeded in predicting properties of clusters in X-ray observations.

In the following years, the advances made in both simulations and observations have also shown that a more complicated description of physical processes is required to fully describe the formation and evolution of galaxy clusters, especially regarding the cluster core. For distances to the cluster centre larger than 10% of the virial radius, simulations have accurately reproduced the nearly self-similar behaviour of the gas, while for the inner regions the numerical predictions showed a high discrepancy with observations. The modelling of the radiative physical processes occurring in the cluster core, particularly the energy injection by the central AGN, has been therefore one of the most active topics in cluster simulations.

Numerical simulations of three-dimensional self-gravitating fluids have become an indispensable tool in Cosmology. They have been essential for understanding the growth of structure in the Universe, and, in particular, for studying the properties

of dark matter halos in the ΛCDM cosmology. Numerical simulations are also an invaluable tool for analyzing galaxy surveys, for studying the abundance evolution of clusters of galaxies, and for semi-analytical models of galaxy formation. In recent years, the access to powerful supercomputers and the development of numerical codes (with high level of parallelism) have made possible to perform Grand Challenge cosmological simulations with high mass resolution over a large volume, which provide the basis to explore many problems in cosmology.

3.1 Numerical methods for cosmological simulations

The first attempts of simulating clusters were largely based on the direct summation method for the gravitational N-body problem. This method is not efficient for cosmological simulations –that usually have large values of N– given that the computational costs increase rapidly with N (see e.g. Yepes 1997 for a review of numerical methods for cosmological simulations).

As mentioned in Chapter 1, the dynamical processes of galaxy clusters are driven by dark matter. The dynamics of dark matter is collision less and it is governed by the Boltzmann equation:

$$\frac{\partial f}{\partial t} + \mathbf{v}\frac{\partial f}{\partial r} - \nabla\Phi\frac{\partial f}{\partial \mathbf{v}} = 0 \tag{3.1}$$

where f is the distribution function, $\mathbf{v}$ the velocity, r the position and Φ the gravitational potential. The Boltzmann equation defines the continuity equation of the coarse-grained phase space density on the six dimensional space of velocity and coordinates. The classical method to solve this equation is known as the N-body method.

The problem of direct summation in N-body methods was overcome thanks to the development of new techniques for collision less dynamics that compute the large-scale gravitational field on a regular or irregular grid. The simplest implementation of grid-based N-body methods is the *Particle – Mesh* (PM) N-body technique (e.g. Hockney & Eastwood 1981), where the Poisson equation is solved using *Fast Fourier Transform* (FFT) in a regular grid of the density filed, that is constructed by interpolations from the particle positions to the grid nodes. In this kind of methods the time of the force computations scales as $O(N \log N)$, which makes them able to handle large number of particles.

However, PM methods are limited by the lack of resolutions below the grid-size, so hybrid schemes were developed to increase the numerical resolution. Hockney et al. (1974) proposed an algorithm called P^3M that decomposes the force acting on each particle into a long-term force, computed by the particle-mesh, and a short range force due to nearby particles. A different approach to increase the resolution of PM methods consist of using non-uniform grids and algorithms to adapt the computational mesh to the structures formed by gravitational clustering. The Poisson equation can be solved on a hierarchically refined mesh by means of finite-difference relaxation methods, as in the *Adaptive Refinement Tree* (ART) code proposed by Kravtsov et al. (1997) or the RAMSES AMR code (Teyssier, 2002).

An alternative method is to use tree algorithms that arrange particles in a hierarchy of groups, and compute the gravitational field at a given point by summing over multiple expansion of these groups, reducing the computational costs of a complete force evaluation to a $O(N \log N)$ scaling.

On the other hand, the baryonic component of the universe can typically be described as an ideal monoatomic gas fluid. Therefore, to trace the evolution of that fluid, it is necessary to solve the Euler equations:

$$\begin{aligned} \frac{\mathrm{d}\mathbf{v}}{\mathrm{dt}} &= -\frac{\nabla P}{\rho} - \nabla\Phi \\ \frac{\mathrm{d}\rho}{\mathrm{dt}} &+ \rho\nabla\mathbf{v} = 0 \\ \frac{\mathrm{du}}{\mathrm{dt}} &- \frac{P}{\rho}\nabla\mathbf{v} = 0 \end{aligned} \tag{3.2}$$

which represent the conservation of mass, momentum and energy (neglecting radiative losses).

The numerical schemes developed in the last decades for solving this coupled system of collisional baryonic matter and collisionless dark matter fall into two main categories: particles methods, which have Lagrangian nature and discretize mass; and grid-based methods, which have an Eulerian nature and discretize space. The above mentioned ART and RAMSES AMR codes are two examples of grid-based mesh refinement codes. Separately, particles codes usually employ Smoothed Particles Hydrodynamics (SPH) to describe the gas. This technique, introduced by Lucy (1977); Gingold & Monaghan (1977), has the advantage of adapting to any given geometry. The Lagrangian nature of this method also allows for a

changing resolution that follows the local gas density. In addition, SPH codes adjust naturally to the N-body approach for self-gravity and can be easily implemented in three dimensions. For these reasons, SPH codes have become the most popular hydrodynamical codes employed in cosmological simulations.

Alternatively, Springel (2010) developed the code AREPO using a Godunov scheme on an unconstructed moving Voronoi mesh. The main differences to Eulerian AMR codes consist in the AREPO is almost Lagrangian and it is Galilean invariant by construction. Furthermore, AREPO has automatic refinement for hydrodynamics and gravity, and uses a Tree-PM gravity solver. The main difference to SPH codes is that the hydrodynamic equations are solved with a finite-volume Godunov scheme.

A comparison study between the SPH and grid-based codes can be found in Frenk et al. (1999). The major differences were found in the central part of the radial entropy and temperature profiles of the galaxy clusters used for the comparison (the so called *Santa Barbara Cluster*). The AMR codes tend to produce an isentropic gas profile in the inner regions, while SPH codes predict an isothermal profile with a decreasing entropy towards the centre of cluster halos. In a recent work, Power et al. (2014) studied the formation and evolution of a simulated massive galaxy cluster with non-radiative physics comparing three different approaches: one based on the classical SPH method; one based on a novel SPH algorithm with a higher order dissipation switch (SPHS, Read et al. 2010); and the last based on the RAMSES AMR method. SPHS and RAMSES codes appear to be in excellent agreement with ash other. In both cases, the spherically averaged entropy profile forms a well-defined entropy core that rapidly converges with increasing mass and force resolution. By contrast, in agreement with what was observed in the *Santa Barbara Cluster*, standard SPH exhibits a rather different behavior, especially at low redshift.

Sembolini et al. (2015) revisited the idea of the *Santa Barbara Cluster* fifteen years later. Using twelve modern cosmological simulations codes, Sembolini et al. (2015) studied the formation and evolution of a large galaxy cluster. All the codes employed in Sembolini et al. (2015) succeed in recovering the global properties and most of the radial profiles of a simulated large galaxy cluster with much greater accuracy and significantly smaller scatter than those presented in Frenk et al. (1999); this highlights the enormous strides in the development of astro- physical hydrodynamical simulation codes over the last decade.

3.1.1 Describing the ICM in hydrodynamical simulations

The simplest way to perform a hydrodynamical simulation is to include only non-radiative physics. In this way, reliable predictions on some properties of the ICM can be derived, even when using a relatively low resolutions. Nevertheless, although gravity plays the main dynamical role in the evolution of galaxy clusters, other important effects on the properties of the ICM arise from feedback processes, related to star formation and accretion onto supermassive black holes. Adding feedback effects to the simulations implies to include a very large number of different processes, such as injection of energy and heavy elements via stellar winds and supernovae, secular mass loss by stars, stellar winds, etc. The parametrization of these effects is led both by observations and by results from stellar models.

The non-gravitational heating was the first radiative mechanism added into hydrodynamical simulations (Evrard & Henry, 1991; Kaiser, 1991), as observations seem to point out that significant amounts of energy are injected to the ICM already at early epochs ($z > 1$) by galactic wind and AGN (see Voit 2005 for a complete review). The increment of entropy prevents the gas from falling to the centre of dark matter halos. Simulations adding heating to the ICM via supernovae-driven winds (Metzler & Evrard, 1994; Borgani et al., 2004) or from pre-heating at early epochs (Borgani & Guzzo, 2001; Mohr & Evrard, 1997) sensibly raised the matching with X-ray observations, but the amount of energy needed to heat the ICM was too high to be provided by these factors alone. Radiative cooling is another effect which has been proposed as responsible of suppressing the hot X-ray emitting gas content of poor systems (Bryan, 2000; Bryan & Voit, 2001). Radiative hydrodynamical simulations confirmed the analytical prediction that radiative cooling removes low-entropy gas from the hot phase, leaving only gas with relatively high entropy to be observed as X-ray emitter. However, radiative cooling tends to convert a too large fraction of gas into stars. Observationally, only $10-15\%$ of the baryon component is supposed to be in the stellar phase (Gonzalez et al., 2007), but radiative simulations usually convert into stars $\sim 35\%$ of the gas inside the virial radius of the cluster (Borgani & Kravtsov, 2011). Although there has been many attempts to remove this cold gas from cluster cores by mechanism associated to supernovae feedback, they have been unable to reconcile the amount of stars formed with the observed values. In recent simulations, AGN feedback have been the most popular candidate to solve this discrepancy. Heating from AGN feedback is produced by the release of energy

during the accretion of the ICM gas onto a supermassive black hole hosted by the central galaxy cluster. The effect of AGN has been observed in many galaxy clusters (McNamara & Nulsen, 2007) and the energy provided by AGNs is sufficiently high to suppress star formation at the inner regions of the clusters (Duffy et al., 2010; McCarthy et al., 2011; Rasia et al., 2013; Planelles et al., 2014). However, AGN feedback still does not seem to produce the correct luminosity of central cD galaxies in clusters (Ragone-Figueroa et al., 2013).

3.2 The MUSIC dataset

Due to the computational effort requested to add radiative feedbacks to hydrodynamical simulations, it is not trivial to find a good compromise between reproducing the ICM of galaxy clusters including radiative processes with a good mass resolution, and at the same time ensure a large statistics on the number of simulated objects. The main goal of the MUSIC (MUltidark Simulations of galaxy Clusters) project is to overcome the problem of limited statistic on radiative hydrodynamical simulations, providing a dataset of hundreds of massive clusters ($M_{vir} > 5 \times 10^{14}\ h^{-1}M_{\odot}$) simulated with a large number of radiative processes and keeping a good resolution in mass and space.

The MUSIC project consists of two sets of resimulated galaxy clusters extracted from two large volume simulations:

- The *MareNostrum Universe*, a non-radiative SPH simulation with 2 billion particles (2×1024^3 gas and dark matter) in a 500 h^{-1}Mpc cubic box (Gottlöber & Yepes, 2007).
- The *MultiDark Simulation*, a dark-matter only N-body simulation with 2048^3 particles in a 1 h^{-1}Gpc box volume (Prada et al., 2012).

The two simulations have slightly different cosmologies. The *MareNostrum Universe* was made with the cosmological parameters compatible with WMAP1 results ($\Omega_M = 0.3$, $\Omega_b = 0.045$, $\Omega_\Lambda = 0.7$, $\sigma_8 = 0.9$, $n = 1.0$, $h = 0.7$), while the *MultiDark Simulation* was performed using the best-fit cosmological parameters to WMAP7 + BAO + SNI ($\Omega_M = 0.27$, $\Omega_b = 0.0469$, $\Omega_\Lambda = 0.73$, $\sigma_8 = 0.82$, $n = 0.95$, $h = 0.7$) presented by Komatsu et al. (2011).

A complete description of the MUSIC project and the resimulations therein is given in Sembolini et al. (2013b). The database of MUSIC clusters is publicly available in a SQL query format through the website: `http://music.ft.uam.es`. The database comprehends also the initial conditions of all MUSIC objects, in order to give the possibility to resimulate the clusters with other hydro codes and/or with different modeling for the radiative processes (e.g. AGN feedback, MHD, cosmic ray pressure, etc.).

For the purposes of this thesis, we focus our analysis on the non-radiative run of the *MultiDark Simulation* (thereafter referred as MUSIC-MD). This choice is based on the fact that radiative simulations without a proper description of energy feedback from AGNs generally produces artificial dense cores (see sec. 2.3.1).

3.2.1 MUSIC-MD: MultiDark resimulated clusters

The MUSIC-MD dataset consists of a mass limited sample of re-simulated clusters selected from the *MultiDark Simulation*. This simulation is dark-matter only and contains 2048^3 particles in a $(1\ h^{-1}\mathrm{Gpc})^3$ cube. It was performed in 2010 using ART (Klypin et al., 2001) at the NASA Ames Research centre. All the data of this simulation are available from the online *MultiDark Database* (`www.multidark.org`).

Using a low resolution (256^3 particles) version of the MultiDark simulation, we selected a total of 282 objects more massive than $10^{15}\ h^{-1}\mathrm{M}_\odot$ at $z = 0$. We first found all particles within a sphere of 6 Mpc radius (which roughly corresponds to 3 times the virial radius of a $10^{15}\ h^{-1}\mathrm{M}_\odot$ cluster) around the center of each selected object. This set of particles was then mapped back to the initial conditions to find out the Lagrangian region corresponding to a $6\ h^{-1}Mpc$ radius sphere centered at the cluster centre of mass at $z = 0$. To avoid problems with periodic conditions, each resimulated cluster is always located at the center of the corresponding $6\ h^{-1}Mpc$ box. In order to reduce the computational effort, the initial conditions of the resimulated clusters are produced using the zooming technique (Klypin et al., 2001). The initial conditions of the original simulations were generated in a finer mesh of 4096^3 sizes. Therefore, the mass resolution of the resimulated objects is increased by a factor of 8 with respect to the original simulation. The highest mass-refinement level is kept within the Lagrangian region of each cluster and the rest is covered with shells of increasing mass particles down to the lower resolution level of 256^3.

Given that, resimulated clusters contain dark matter particles of 5 different mass refinements (from 4096^3 to 256^3). The gas SPH particles were added only to the highest refinement level. The SPH particles were given the same initial velocity as their dark matter counterparts, with their positions slightly displaced (0.4 times the mean inter-particle distance).

The resimulations have been performed using the parallel TreePM+SPH GADGET-2 (Springel, 2005) code. In this code, both collisionless dark matter and the gaseous fluid, as well as stars are represented as particles, allowing self-gravity of all components to be computed. GADGET-2 solves the Poisson equation fro gravitational forces by using a hybrid method called TREEPM algorithm. The potential is split into two different terms (long and short-range) that are solved independently. The long-range term can be efficient and accurately solved with a Particle-Mesh algorithm, while the short-range term is computed by a TREE algorithm which divides the space into smaller computational cells.

The most important feature of the GADGET-2 code is the highly efficient work-load balance on different tasks, which makes of it a massively parallel code. Such parallel programs have the potential to be scalable up to very large number of processes although, in practice, it is only possible when all processors have the similar work.load and the communication between them is minimized. A commonly taken approach is to decompose the computational volume into a set of domains, each one assigned to one processor. GADGET-2 uses a space-filling fractal curve to map 3D space onto a 1D function, the so-called Peano-Hilbert curve. This results in a highly scalable and customizable parallel algorithm, allowing to perform simulations with a very large number of particles and volumes using many processors. Besides, it is fully adaptive both in force computation and in time stepping (i.e. each particles can have its own mass and time step).

Although the 282 massive clusters were resimulated with and without radiative physics, we focus our analysis on the non-radiative version of these simulations. In the non-radiative run, baryons were added to the dark matter distributions extracted from the the parent *MultiDark Simulation* and their physics was simulated via SPH techniques, without including radiative processes. The mass resolution for these simulations corresponds to $m_{DM} = 9.01{\times}10^8\ h^{-1}\mathrm{M}_\odot$ and to $m_{SPH} = 1.9{\times}10^8\ h^{-1}\mathrm{M}_\odot$. The gravitational softening was set to $6\ h^{-1}$kpc for the SPH and dark matter particles in the high-resolution areas.

The identification of halos and sub-halos in the MUSIC-MD dataset is performed using the hybrid MPI-OpenMP parallel halo finder AHF (see Knollmann & Knebe 2009 for a detailed description of the code). AHF is the successor of the MHF halo finder (Gill et al., 2004) and identifies structures (and substructures) by finding peaks in the density field generated in a hierarchy of grids as AMR codes do. The grid hierarchy is build in such a way that the grid is refined in high-density regions and hence naturally traces density contours. Moreover, as the algorithm is based on particles, AHF easily supports multi-mass collisionless particles and also SPH gas particles. It has been proven that it can reality recover substructures containing at least 20 particles (Knebe et al., 2011).

In each resimulated box, several low mass clusters have been found close to the massive ones but not overlapping with them. Thus, the total number of resimulated objects is considerably larger: 535 clusters with $M_{vir} > 10^{14}\ h^{-1}M_{\odot}$ at $z = 0$ and more than 2000 group-like objects with masses in the range $10^{13}\ h^{-1}M_{\odot} < M_{vir} < 10^{14}\ h^{-1}M_{\odot}$. For each resimulated object, we have stored snapshots for 15 different redshifts in the range $0 \leqslant z \leqslant 9$. Consequently, the MUSIC-MD dataset constitutes the larger database of massive clusters from high resolution hydrodynamical simulations (a factor of 10 larger than the most recent simulations, as for instance the *Dianoga* dataset, Fabjan et al. 2011).

3.2.2 General properties of MUSIC-MD clusters

Given the motivations of this thesis and that the most efficient lenses on producing gravitation arcs are expected to be massive and compact galaxy clusters at $0.2 \lesssim z_l \lesssim 0.4$, we select four snapshots at $z = (0.250, 0.333, 0.429, 0.667)$ from the MUSIC-MD database.

The MUSIC-MD dataset is built to be a volume limited complete sample of the parent *MultiDark Simulation* above a given mass threshold (here denoted as completeness mass, M_c). In other words, all the halos that formed in the cosmological comoving volume of $(1\ h^{-1}Gpc)^3$, corresponding to the volume of the parent *MultiDark Simulation* above M_c have been resimulated in the MUSIC-MD dataset. The completeness of the MUSIC-MD dataset permits to avoid selection effects having at the same time large statistics and achieving a better accuracy than any previous works employing simulations. Moreover, the clusters selected in this way are the best resolved ones, which contain millions of particles, allowing us to

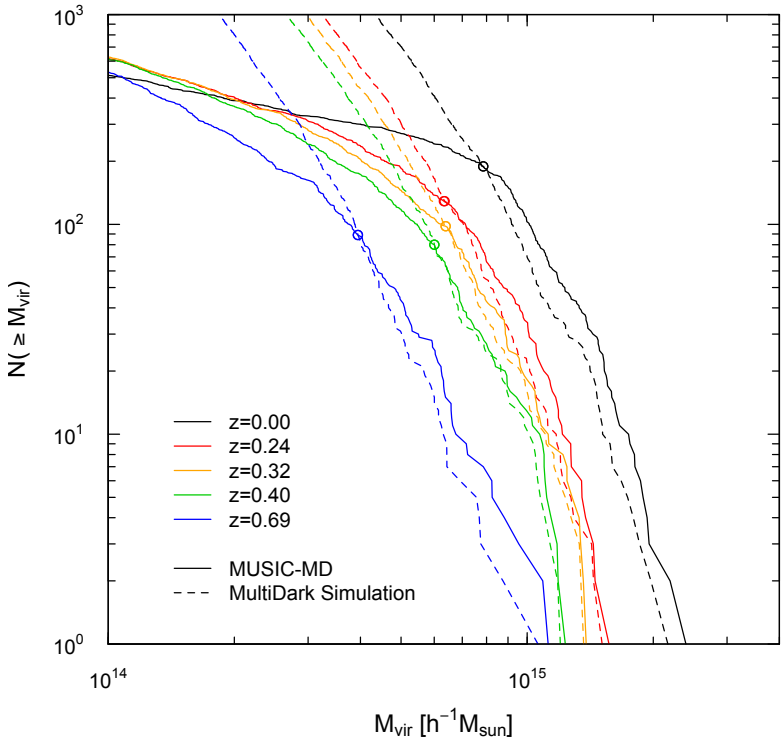

Figure 3.1: Comparison of the cumulative mass functions of MUSIC-MD and MultiDark simulations at z =0.000, 0.250, 0.333, 0.429 and 0.667. The open circles indicate the completeness mass beyond which the MUSIC-MD dataset constitutes a volume limited complete sample.

extend the analysis towards the inner regions of the clusters. To extend our analysis towards smaller masses and being able to constrain the lensing properties over a wider range mass range, we analyse also halos with masses below the completeness limits. In particular, we include all halos with mass above the minimum mass $\mathrm{M_{min}} = 2 \times 10^{14}\ h^{-1}\mathrm{M_{\odot}}$.

In order to give a first classification of the halos based on the dynamical state, we differentiate between relaxed and unrelaxed halos following the selection criteria proposed by Neto et al. (2007). We consider as super-relaxed halos the halos satisfying the following properties:

1. their centre of mass displacement, defined as the offset between the centre of mass (determined using all the particles within the virial radius) and the minimum of the potential, in units of the virial radius, is $s = (\vec{r}_{cm} - \vec{r}_{\phi})/r_{vir} <$ 0.07;

Table 3.1: Completeness mass (M_c, in units of 10^{14} $h^{-1}M_\odot$); number of halos above the completeness mass; number of halos above the minimum mass (M_{min} = 2×10^{14} $h^{-1}M_\odot$); fraction of halos according to their relaxation state: unrelaxed (f_{un}), relaxed (f_{rel}) and super-relaxed (f_{sup}) halos.

Redshift	0.250	0.333	0.429	0.667
M_c	6.34	6.39	6.00	3.94
$N(\geqslant M_c)$	128	97	80	89
$N(\geqslant M_{min})$	403	393	365	258
f_{un}	0.39	0.41	0.47	0.48
f_{rel}	0.46	0.47	0.42	0.42
f_{sup}	0.15	0.12	0.10	0.09

2. their virial ratio is $\eta = 2T/|U| < 1.35$, where T is the kinetic energy and U is the gravitational energy, computed using the particles within the virial radius;

3. their substructure mass fraction computed as the mass in resolved substructures within the virial radius, is $f_{sub} < 0.1$.

The halos satisfying only the first condition are consider as relaxed halos. The cumulative mass function of MUSIC-MD clusters is shown in Fig. 3.1. The number of halos above the completeness and the minimum mass along with the fractions of relaxed halos at each redshift analyzed in this work is reported in Tab. 3.1. The fractions of unrelaxed, relaxed and super-relaxed halos (averaged for all the redshifts) in the MUSIC-MD dataset are 0.44, 0.45 and 0.11, respectively.

MUSIC-MD clusters are free from contamination of low resolution particles, as the distance between the center of the cluster and the closest low resolution particle is at least 2 times the virial radius at z=0 and more than 3 times the virial radius at higher redshifts. Besides, MUSIC-MD clusters are *distinct* objects, halos which are not subhalos of more massive halos.

CHAPTER 4

Lensing properties of the MUSIC-MD clusters

The MUSIC-MD dataset is by far the best sample ever devised of simulated galaxy clusters, as many aspects are taken into account, from the triaxiality (and hence the variability in properties produced by different orientations), to the lack of spherical symmetry through projection effects in their properties. Therefore, MUSIC-MD dataset allows us to study in detail not only the lensing properties, but also other key aspects of galaxy clusters, such as the evolution with redshift of the concentration-mass relation (*c-M* relation). Taking advantage of the high-resolution MUSIC-MD simulated clusters, we aim to improve the comparison between observations and theoretical expectations in terms of the Einstein radii distribution and the abundance of giant gravitational arcs.

In this Chapter, we study all cluster-sized distinct halos in the MUSIC-MD dataset to model their structural properties and to derive the size of the Einstein radius produced by these halos when acting as gravitational lenses. In order to increase the statistics and to take into account possible projections effects, we study each cluster-sized halo under a large number of line-of-sight. More precisely, we investigate 500 random lines of sight for all the halos with $M_{vir} \geqslant 2 \times 10^{14}\ h^{-1}M_{\odot}$. We examine the shapes of both their density and surface density profiles by fitting them with the most common functions (NFW, gNFW and Einasto profiles, see sec. 1.5.1). We derive the concentration-mass relations from the NFW fits and investigate their evolution with redshift and halo relaxation. In addition, we also produce two-dimensional convergence and shear maps by means of ray-tracing techniques to

derive the properties characterizing the tangential critical lines, such as its *effective* Einstein radius and its ellipticity.

The fitting procedure to analytical models is based on the assumption that mass is spherically distributed in clusters, while the ray-tracing accounts for the two-dimensional mass distribution of the clusters, so the difference between the two procedures could give us hints on the projection effects (cluster triaxiality, substructures and mergers).

Finally, we present the Einstein radii distribution of the MUSIC-MD dataset at the four different redshifts above mentioned, z =0.250, 0.333, 0.429 and 0.667.

4.1 Density profiles of MUSIC-MD clusters

In order to describe the structural properties of the galaxy clusters in the MUSIC-MD dataset, we perform an analysis of their three-dimensional density profiles based un the functional forms introduced in sec. 1.5.1. Such an analysis is done by fitting the NFW, gNFW and *Einasto* profiles (Eqs. 1.16, 1.19 and 1.21, respectively) to the azimuthally averaged density profiles of the simulated clusters. As is common practice in the literature, to perform this analysis we minimize the function:

$$R^2_{3D}\left(\mathrm{M_{3D}}, \mathrm{c_{3D}}\right) = \frac{1}{N_{\mathrm{dof}}} \sum_i \left[\log \rho_i - \log \rho\left(\mathrm{r}_i \mid \mathrm{M_{3D}}, \mathrm{c_{3D}}\right)\right]^2 \tag{4.1}$$

where ρ_i is the density measured in the *i-th* radial shell and N_{dof} is the number of degrees of freedom, i.e. the number of radii at which the profiles are evaluated minus the number of free parameters in the fit. The free parameters are the cluster mass and concentration ($\mathrm{M_{3D}}$ and $\mathrm{c_{3D}}$). Thereafter, we adopt the round number $\Delta = 200$ for the overdensity as proposed by Navarro et al. (1996), which is commonly used in literature independently on the assumed cosmological model. In this regard, we also define the size of the halos as r_{200}, which is the radius enclosing a means density $\bar{\rho} = 200\rho_c(z)$. As recently shown by Diemer & Kravtsov (2014), rescaling clusters to this radius returns a self-similar inner density profile. By definition, the concentration parameter (c_{200}) for the NFW and gNFW profiles is defined as the ratio between r_{200} and the scale radius, r_s. We adopt the same definition also for the *Einasto* profiles, $c_{200} \equiv r_{200}/r_{-2}$.

We perform a similar analysis on the two-dimensional profiles, i.e. on the

azimuthally averaged surface-density profile (Σ_i) corresponding to an arbitrary line-of-sight to the MUSIC-MD cluster. The surface mass density, $\Sigma(R)$ is obtained by integrating the density profile along the line-of-sight:

$$\Sigma(R) = 2 \int_0^{r_t} \rho(r = \sqrt{R^2 + \xi^2}) \mathrm{d}\xi \tag{4.2}$$

where ξ indicates the spatial coordinate along the line-of-sight and R is the projected radius. In the formula above, r_t is a truncation radius, which is introduced to take into account that our halos are at the center of a cube with side-length $r_t = 6\,h^{-1}$Mpc comoving.

In the case of these two-dimensional profiles, the fitting parameters are labeled as M_{2D} and c_{2D}. The function to be minimized is:

$$R^2_{2D}(\mathrm{M_{2D}}, \mathrm{c_{2D}}) = \frac{1}{\mathrm{N_{dof}}} \sum_{\mathrm{i}} \left[\log \Sigma_{\mathrm{i}} - \log \Sigma(\mathrm{R_i} \mid \mathrm{M_{2D}}, \mathrm{c_{2D}})\right]^2 \tag{4.3}$$

The three-dimensional fits are performed over the radial range $[\tilde{r}_{min},\ \tilde{r}_{200}]$, where $\tilde{r}_{min} = 0.02 r_{\mathrm{vir}}$, and $\tilde{r}_{200}$ is the true r_{200} of the halo. When analyzing the surface density profiles, we perform the fits over the radial range $[20h^{-1}\mathrm{kpc},\ \tilde{r}_{200}]$. The procedure used to perform this analysis is a general-purpose optimization based on Nelder & Mead (1965) algorithm. The results derived in this way are in perfect agreement with the results of the code used by Merten et al. (2015) on the CLASH clusters, which is based on the open-source library *Levmar*. Besides, masses and concentrations (M_{2D} and c_{2D}) estimated in this way are the *equivalent* to the values derived from a comprehensive lensing analysis of real observations.

Although only based on the results derived from the first 100 projections (instead of 500) of the MUSIC-MD dataset here presented, Meneghetti et al. (2014) quantified the goodness of the different fitting functions by means of the residuals given in Eqs. 4.1 and 4.3. We found that the NFW profile is the model with the largest residuals (see also Meneghetti & Rasia 2013). This is not surprising given that the NFW model has one free parameter less than the gNFW or the *Einasto* profiles. Restricting the analysis to the relaxed halos reduces the differences between the residuals distributions of the NFW and gNFW or *Einasto* fits (see Fig. 4.1).

As we will described in sec. 5.2, we aim at producing *all-sky* predictions on the Einstein radii distribution, that implies to sample large number of halos. The NFW model is one of the simplest functions proposed (i.e. one less

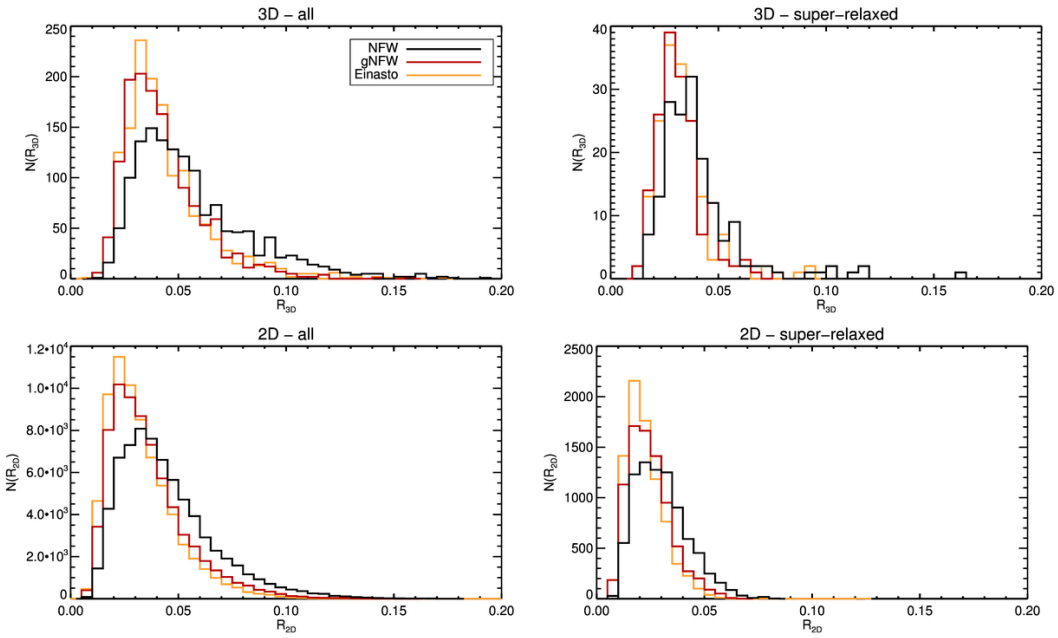

Figure 4.1: Distributions of the fit residuals. Results are shown for the fits of the density (upper panels) and of the surface density profiles (bottom panels). The left and the right panels refer to the whole sample and to the subsample of super-relaxed halos, respectively. The black, red, and yellow histograms show the results for the NFW, gNFW, and *Einasto* models. Figure taken from Meneghetti et al. (2014).

free parameter), therefore lensing models based on this functional are less-time demanding. Moreover, combining the information based on the analysis of the density (and surface density) profiles and the convergence (and shear) maps, we are able to quantify the systematics affecting the Einstein radii distribution by the NFW model and by the assumption of spherical symmetry. For these reasons, we consider the NFW profile to be sufficiently accurate to constrain the Einstein radii distribution al the level required for the purpose of this thesis.

Thereafter, we present the results for the NFW fits to the azimuthally averaged density and surface density profiles of 500 projections of the MUSIC-MD dataset. We refer the reader to Meneghetti et al. (2014) for a detailed analysis using gNFW and *Einasto* models based on the first 100 projections of the MUSIC-MD presented in this work.

4.1.1 Cluster masses

As explained above, we fit the density profiles of the MUSIC-MD halos by minimizing the functions in Eqs. 4.1 and 4.3. From the fits to the density profiles we obtain the three-dimensional masses and concentrations. Both estimates are obtained under the assumption of spherical symmetry, hence the results do not depend on the orientation of the halo. On the other hand, the two-dimensional masses and concentrations are different for each projection of the same halo configuration, depending on the morphology of the halo and on the presence of substructures along the line of sight. This implies that, for each cluster, we have a catalog containing one measurement of $\{M_{3D}, c_{3D}\}$, and 500 measurements of the projected mass and concentration $\{M_{2D}, c_{2D}\}$.

The ratios between the three-dimensional masses (M_{3D}) and the true halo masses (M_{true}) are shown in Fig. 4.2. The halo true masses have been derived by interpolating the density profile at $r = r_{200}$, thus $M_{true} = M_{200}$. The results are shown for the three types of halos depending on their relaxation state (black, orange and red points) as described in sec.3.2.1. The masses recovered from the fits to the density profiles are in good agreement with the true masses. As expected, the M_{3D} of un-relaxed halos deviate more from the true masses than the relaxed (or super-relaxed) halos. The mean ratios M_{3D}/M_{true} are ~ 0.98 (with $\sigma = 0.06$) and ~ 0.95 (with $\sigma = 0.12$) for super-relaxed and un-relaxed halos, respectively.

In the case of the mass and concentration derived from the surface density profiles, for each cluster, we compute the median rescaled mass $Q_M = M_{2D}/M_{true}$ and concentration $Q_c = c_{2D}/c_{3D}$ as a function of the M_{true}, and including the 500 projections per cluster. In Fig. 4.3 we show the median (points) and the first and third quartiles (error bars) of the rescaled mass and concentration for each cluster. We also show the bets-fit to our data points (see Table 4.1), which can be written as:

$$\log(Q_M) = A_M \log(M_{vir}) - B_M \tag{4.4}$$

$$\log(Q_c) = A_c \log(M_{vir}) - B_c \tag{4.5}$$

The estimates based on the fit to the surface density profiles show a larger scatter than the ones derived from the density profiles. The larger scatter is expected, given that M_{2D} and c_{2D} are derived under the assumption of spherical symmetry. Halos are generally triaxial and projections effects can easily cause the mass and

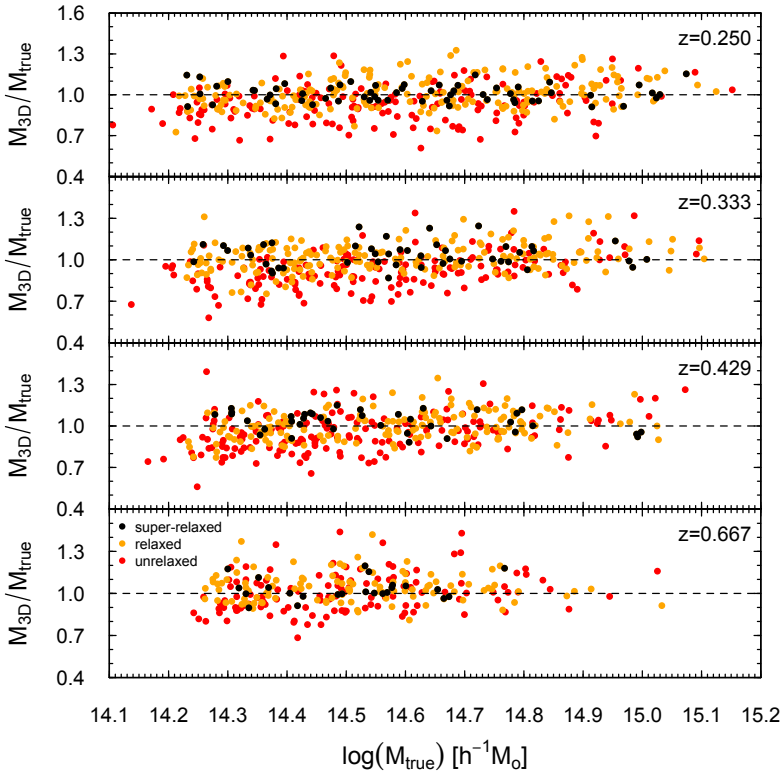

Figure 4.2: Ratios between the three-dimensional and true masses for all the halos at the four redshifts analyzed. The M_{3D} are obtained by fitting the spherical mass profiles, while the M_{true} is computed by interpolating the mass profile at $r = r_{200}$. Halos are classified according to their dynamical state in: super-relaxed (black points), relaxed (orange points) and un-relaxed halos (red points).

concentration to be over or underestimated, depending on the halo orientation (see e.g. Meneghetti et al. 2010b). Besides, as it has been demonstrated (Jing & Suto, 2002; Allgood et al., 2006), massive haloes are on average more elongated than low mass haloes, since they form at later times and thus still retain memory of their original shape which is influenced by the direction of the surrounding filaments or of the last major merger. From Fig. 4.3, we expect a modest negative bias of $\sim 5\%$ on the mass estimates from the fit to the surface density (or convergence) profiles of galaxy clusters. This is again due to the prolate shape of the clusters, which are more probably elongated on the plane of the sky than along the line of sight. The two-dimensional masses of the halos in equilibrium are in good agreement with the true masses (Fig. 4.4). The best agreement is obtained for the super-relaxed halos with a negative bias $\lesssim 2\%$. As halos deviate from the equilibrium, the two-dimensional masses deviates from the true masses, also increasing the scatter of the data.

The trend with halo mass is inverted when looking at the rescaled concentration Q_c in Fig.4.3. The c_{2D} are over-estimated for halos with larger true masses (especially un-relaxed halos), while under-estimated for less massive halos. Nevertheless, for relaxed systems, c_{2D} is well recovered without any bias ($< 1\%$). The best-fit parameters to Eqs. 4.4 and 4.5 reported by Giocoli et al. (2012b) (Eqs. 18 and 19 therein) are also shown in Fig. 4.3. The differences reported here can be argued in terms of the triaxial model assumed by Giocoli et al. (2012b), which is based on the findings of Jing & Suto (2002). The analysis of Jing & Suto (2002) was based on simulations with 512^3 particles in a $100h^{-1}$Mpc box, which contained hardly any halo above $10^{14}h^{-1}\mathrm{M}_\odot$ and some higher resolution runs which provided only 12 haloes with more than 10^6 particles.

Moreover, we also notice that the concentration estimate is more biased than the mass estimate, therefore the concentration estimate is more influenced by the triaxiality and the presence of substructures when projecting the cluster mass along the line-of-sight, as already reported by Giocoli et al. (2012b). The scatter of the rescaled concentration is larger than the scatter of the rescaled mass (see σ_M and σ_c columns in Table 4.1).

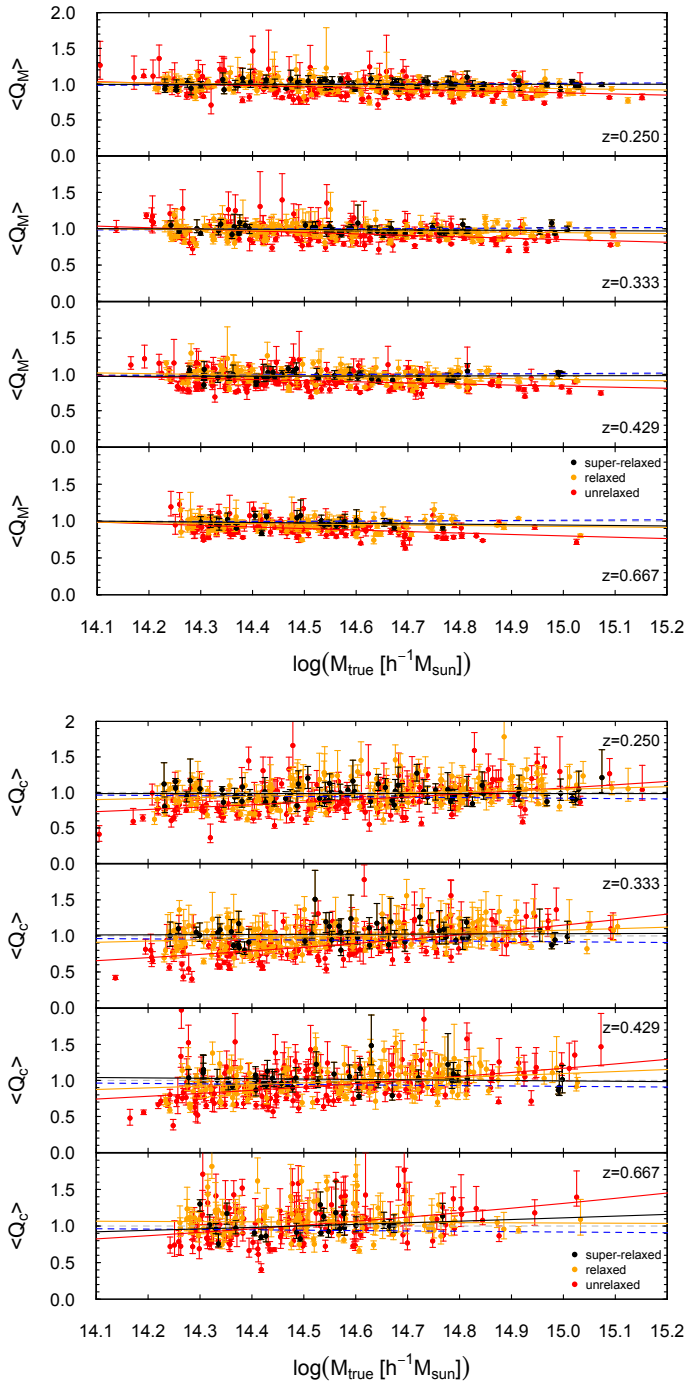

Figure 4.3: Median rescaled mass (upper panels) and concentration (bottom panels) estimates as a function of the true masses. The error bars enclose the first and the third quartiles. The solid lines show the linear fits to the data points (see Table 4.1) with color coding according to the relaxation criteria. Blue dashed lines correspond to the results of Giocoli et al. (2012b) once corrected for elongation.

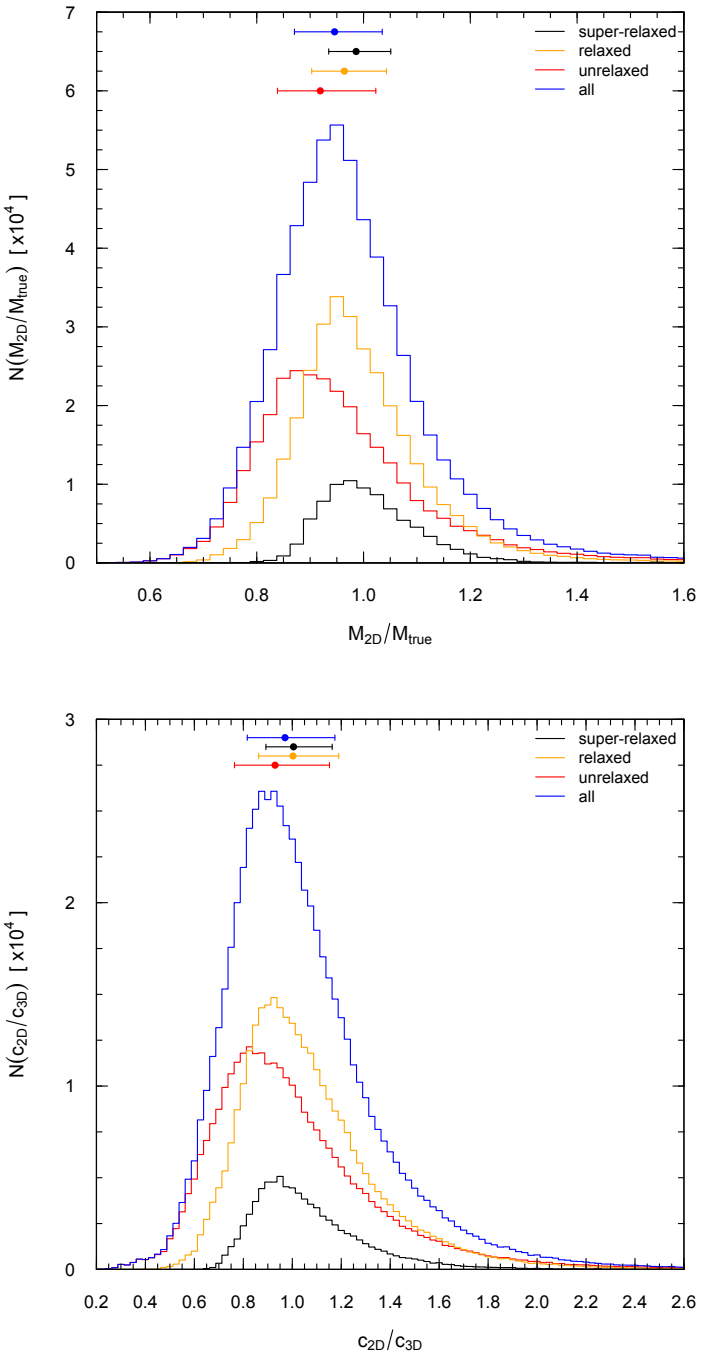

Figure 4.4: Upper panel: Distributions of the ratios between the M_{2D}, obtained by fitting the surface mass density profiles, and true masses for all the halos at the four redshift analyzed. Bottom panel: Distributions of the concentration ratio, c_{2D}/c_{3D}. Different colors show the relaxing criteria (super-relaxed, relaxed and un-relaxed halos) and the full sample (blue histogram). The data points indicate the median and the error bars correspond to the first and third quartile of each distribution.

Table 4.1: Fitting parameters for the rescaled mass and concentration showed in Eq. 4.4 and 4.5 at the four different redshift considered. The r.m.s. values of both fitting functions are shown in columns σ_M and σ_c.

z	relax.	A_M	B_M	σ_M	A_c	B_c	σ_c
0.250	un	2.800	-0.192	0.006	-3.520	0.239	0.007
0.250	rel	1.597	-0.110	0.002	-1.577	0.107	0.004
0.250	srel	0.135	-0.010	0.001	-0.272	0.018	0.002
0.333	un	3.531	-0.242	0.004	4.301	0.292	0.006
0.333	rel	1.426	-0.099	0.003	-1.702	0.117	0.004
0.333	srel	0.645	-0.046	0.002	-0.678	0.047	0.003
0.429	un	3.303	-0.229	0.005	-4.053	0.277	0.008
0.429	rel	1.738	-0.120	0.003	-2.301	0.157	0.005
0.429	srel	-0.531	0.035	0.001	-0.010	0.007	0.003
0.667	un	4.248	-0.296	0.006	-4.765	0.329	0.009
0.667	rel	1.266	-0.089	0.003	-1.218	0.085	0.006
0.667	srel	1.534	-0.107	0.001	-2.412	0.166	0.003

4.1.2 Concentration-mass relation

The concentration-mass ($c - M - z$) relation is derived by a nonlinear least-square fitting using a Levenberg-Marquardt algorithm. We used the fitting function proposed in Meneghetti et al. (2014),

$$c(M,z) = A\left(\frac{1.34}{1+z}\right)^B \left(\frac{M}{8\times 10^{14}h^{-1}M_\odot}\right)^C , \tag{4.6}$$

which has been also used by Duffy et al. (2008) and De Boni et al. (2013) but with a different pivot mass and redshift. Using this equation, we derive the $c - M - z$ relation for all the MUSIC-MD clusters from the fitting parameters presented in the previous section. In Fig. 4.5, we show the 3D concentration-mass relations at the four redshift analyzed . We present separately the three subsamples according to the relaxation state of the halos (full, relaxed and super-relaxed). The corresponding best fit parameters and errors of the $c - M - z$ relation are reported in Table 4.2. In all cases we find that the dependency of the concentration on mass is very shallow. The 3D concentration-mass relation for the full sample scales with mass as $c \propto M^{-0.081\pm0.014}$. Besides, we find a much stronger dependence of concentration on

the halo dynamical state. The normalization of our $c - M - z$ relation increases by $\sim 9\%$ between the relaxed and the full sample. However, Bhattacharya et al. (2013) found that concentration of relaxed halos increase only by $\sim 3\%$. As pointed out by Meneghetti et al. (2014), for the full sample a good agreement is found with the results of Bhattacharya et al. (2013). Nevertheless, their $c-M$ relation has a slightly stronger redshift evolution. Using the new suite of MultiDark simulations, Klypin et al. (2014) studied the evolution of concentration covering a large range of masses and volumes. For comparison, we included their results for WMAP7 cosmology derived by Einasto and NFW approximations. We do not find any upturn in the concentration of massive halos at high redshifts. As pointed out by Klypin et al. (2014), this can be due to the NFW fitting procedure, which is known to predict too low concentrations for the most massive halos at high redshifts. The $c - M$ relation for the full MUSIC-MD dataset is flatter than the one reported in Klypin et al. (2014) for the NFW approximation. Concentrations derived with the Einasto approximation at $z = 0$ in Klypin et al. (2014) are $\sim 10\%$ lower than the MUSIC-MD halos at $z = 0.250$, but the $c - M$ relations show a similar trend with mass.

For comparison, in the bottom panel in Fig. 4.5 we also show the $c - M$ relation presented by Ludlow et al. (2014) for redshifts $z = 0$ and $z = 1$ (grey region). We find a good agreement for the relaxed subsamples, while super-relaxed halos deviate from the Ludlow et al. (2014) estimates, showing higher concentrations at higher masses. However, the analysis performed in Ludlow et al. (2014) implies only super-relaxed halos, there are important differences between our and Ludlow et al. (2014) analysis: 1) our simulations include baryons, while the halos studied by Ludlow et al. (2014) are made only of dark-matter; 2) our analysis focusses on a limited mass range and the volume we sample is smaller compared to the simulations employed by Ludlow et al. (2014); 3) the mass resolution of our simulations is roughly two orders of magnitude better; 4) Ludlow et al. (2014) fit their halos over a different radial range, $[0.05\text{-}0.6]r_{200}$. As our MUSIC-MD dataset is a non-radiative run of the MultiDark simulation, we do not expect that the differences between the $c - M$ relations arise from baryonic effects. De Boni et al. (2013) show that concentrations are higher by $5-15\%$ in radiative simulations compared to dark-matter only simulations. Besides, as it has been shown by other authors, halos in adiabatic simulations develop density profiles pretty similar to those of pure dark-matter halos (Killedar et al., 2012). We also include the results of Klypin et al. (2014) for a relaxed sample of the MultiDark simulations with

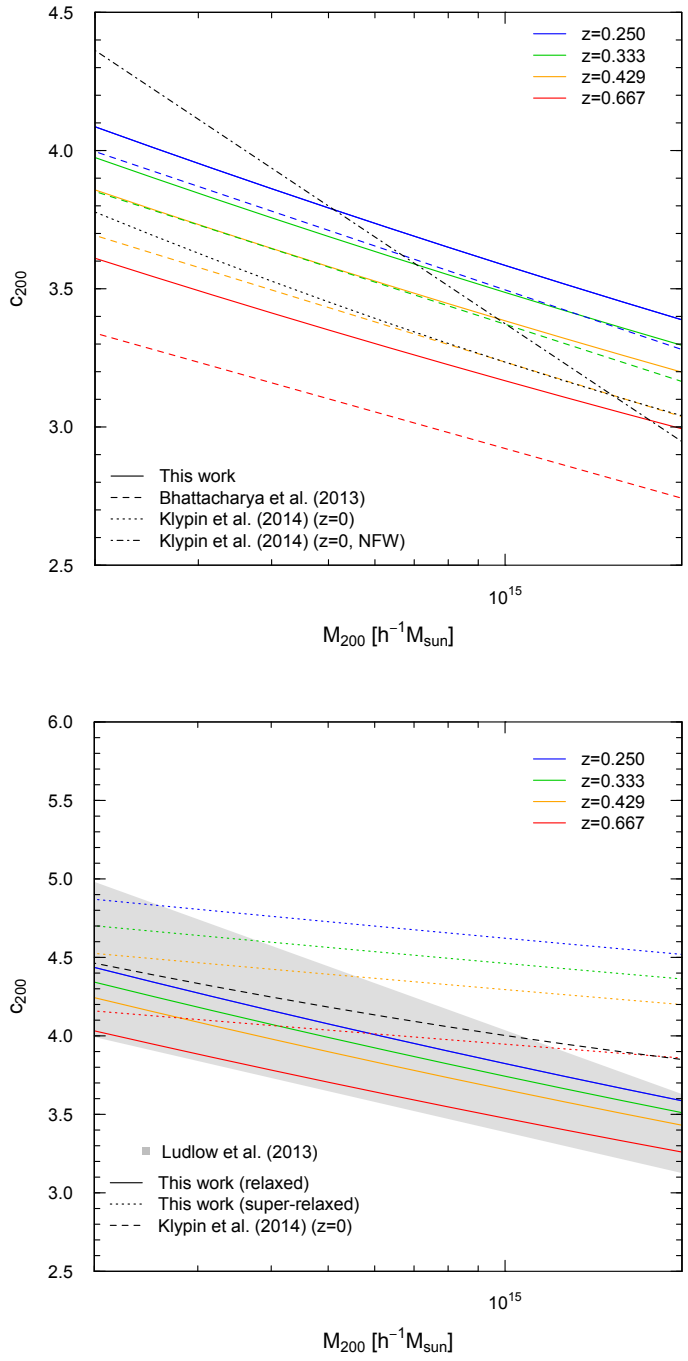

Figure 4.5: Concentration-mass relation and its evolution with redshift as obtained from fitting the halo density profiles with a NFW model. The results of this analysis are compared with the work of Bhattacharya et al. (2013), Ludlow et al. (2014) and Klypin et al. (2014). The redshift evolution is illustrated by different colours. The upper and the bottom panels show the results for the whole sample and for the subsamples of relaxed and super-relaxed halos. Note that Bhattacharya et al. (2013) only distinguish between relaxed and un-relaxed halos, while Ludlow et al. (2014) analyzed only super-relaxed halos.

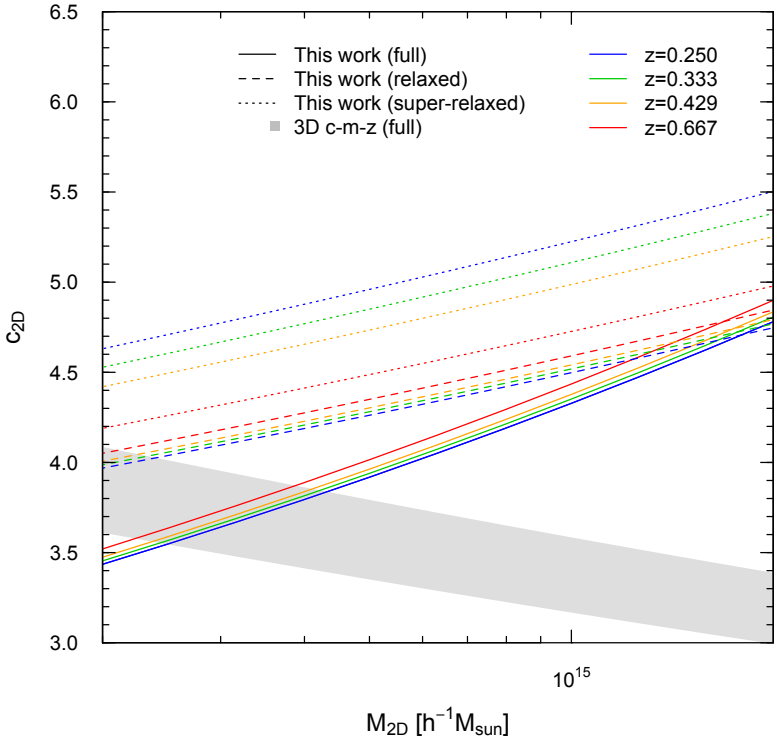

Figure 4.6: Concentration-mass relation (in 2D) and its evolution with redshift as obtained from fitting the halo surface density profiles with a NFW model. The lines indicate the results obtained for the halos in the full, relaxed and super-relaxed samples (solid, dashed and dotted lines, respectively). For comparison, the 3D $c - M$ relation derived for the full sample is shown in grey. The redshift evolution is illustrated by different colours.

WMAP7 cosmology at $z = 0$ and $z = 1$. Although comparing different redshifts, we find a good agreement for halos low mass halos, but deviating $\gtrsim 5\%$ for halos with $M_{200} \gtrsim 10^{15} h^{-1} M_{\odot}$. These differences can be explained again in terms of the different mass resolutions between the resimulated MUSIC-MD clusters and the MultiDark simulations used in Klypin et al. (2014). Moreover, the criteria used to select relaxed halos in Klypin et al. (2014) are also based on different considerations.

On the contrary, as we reported in Meneghetti et al. (2014), the 2D concentration-mass relation shows a slightly positive logarithmic slope (see Fig 4.6 and Table 4.2). For the full sample, we obtain $C = -0.081$ for the 3D and $C = 0.144$ for the 2D $c-M$ relation (Eq. 4.6), respectively. One possible explanation for the positive slope

could be that the halo triaxiality is somehow biased below the completeness mass listed in Table 3.2.2. However, we checked that the $c - M$ relation obtained only from halos above the completeness limits does not differ significantly from what we obtain using the full sample. In this context, Giocoli et al. (2012b) also found indicators for a 2D concentration decreasing with mass. The redshift dependence of the 2D $c - M$ relations is almost negligible. However, it appears to be stronger for the un-relaxed and super-relaxed systems. In particular, for the super-relaxed halos we find that 2D $c - M$ relation scales with redshift as $c \propto (1 + z)^{-0.35}$. One difference to notice is that we extend the MUSIC-MD over a total of 500 random projections for each halo, while in Meneghetti et al. (2014) the results arise from 100 projections of the complete sample (and only 30 projections for halos below the completeness mass and above $2 \times 10^{14} h^{-1} \mathrm{M}_{\odot}$). Therefore, we account for a larger number of projections with masses below the completeness mass than in Meneghetti et al. (2014). Besides, as already described, the $\mathrm{c}_{2\mathrm{D}}$ are underestimated for low mass halos ($\mathrm{M}_{200} \leqslant$ 3-4 $\times 10^{14} h^{-1} \mathrm{M}_{\odot}$) compared to the $\mathrm{c}_{3\mathrm{D}}$. In conclusion, this increase in the number of projections may lead to a 2D $c - M - z$ relation slightly steeper than found by Meneghetti et al. (2014). However, we checked that the $c - M - z$ relation obtained from 500 projections does not differ significantly from what we obtain using only 100 projections.

Projections effects do affect the derived concentrations, as it has been also discussed in Giocoli et al. (2012b). We illustrate these effects in Fig. 4.7, where we show the distribution of the MUSIC-MD halos in the $(\mathrm{c}_{2\mathrm{D}} - \mathrm{c}_{3\mathrm{D}})/\mathrm{c}_{3\mathrm{D}}$ vs $(\mathrm{M}_{2\mathrm{D}} - \mathrm{M}_{3\mathrm{D}})/\mathrm{M}_{3\mathrm{D}}$ plane. The 2D distributions show that, at the four redshift bins, the masses and concentrations derived from fitting the surface density profiles tend to be smaller than measured from fitting the density profiles. The trend is qualitative agreement with the findings of Giocoli et al. (2012b), although the amplitude of both the concentration and mass biases found here is smaller. The solid grey contours denote the the 10%, 50% and 90% intensity levels of the probability peak of the distributions in Fig. 4.7. The dashed grey contours overlapped in the figure indicate the same intensity levels for the super-relaxed subsample. As discussed in sec. 4.1.1, the bias is clearly reduced for the relaxed halos, because these systems are typically more spherical than un-relaxed halos. The concentration bias is reduced for massive halos (red contours), with 2D concentrations larger that the 3D ones (bottom panel in Fig. 4.3). As the largest Einstein radii are expected to be produced by massive and high-concentrated clusters, this result can shed light on the *arc statistics problem*.

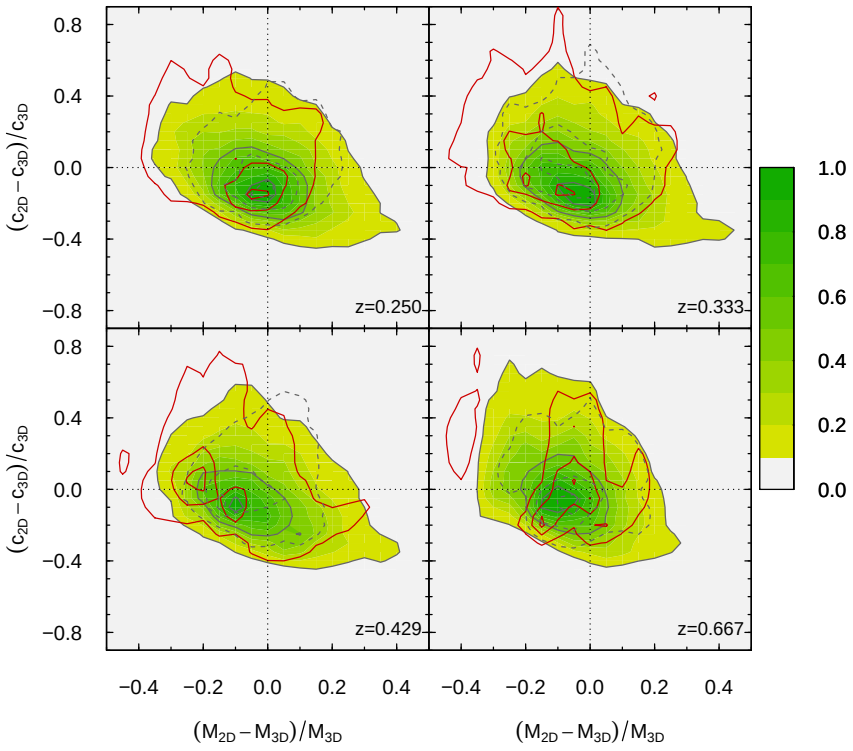

Figure 4.7: Distributions of halos in the plane $(c_{2D} - c_{3D})/c_{3D}$ vs $(M_{2D} - M_{3D})/M_{3D}$. The two-dimensional distributions show the results for the whole sample. The grey contours overlaid to the image show the intensity levels corresponding to 10%, 50% and 90% of the probability peak, while the grey dashed contours indicate the same levels for the super-relaxed sample. The red contours correspond to the same levels of the distribution only for halos with $M_{true} \geqslant 7 \times 10^{14} h^{-1} M_{\odot}$.

Table 4.2: Best fit parameters for the 3D and 2D $c-M-z$ relations. First column: 3D or 2D analysis; second column: selection function (full=full sample; str=strong lensing selection); third column: relaxation state (all=all halos; un=un-relaxed; rlx=relaxed; sup=super-relaxed); columns 4,5,6: $c-M-z$ parameters (see Eq. 4.6)

3D/2D	sel.	relax.	A	B	C
3D	full	un	2.980 ± 0.068	0.428 ± 0.109	-0.137 ± 0.020
3D	full	rlx	3.814 ± 0.059	0.332 ± 0.088	-0.092 ± 0.017
3D	full	sup	4.482 ± 0.128	0.549 ± 0.171	-0.032 ± 0.033
3D	full	all	3.543 ± 0.048	0.430 ± 0.074	-0.081 ± 0.014
2D	full	un	3.694 ± 0.005	-0.250 ± 0.006	0.174 ± 0.001
2D	full	rlx	4.442 ± 0.004	-0.071 ± 0.005	0.078 ± 0.001
2D	full	sup	5.015 ± 0.007	0.348 ± 0.009	0.075 ± 0.002
2D	full	all	4.216 ± 0.003	-0.085 ± 0.004	0.144 ± 0.001
2D	str	un	4.063 ± 0.007	0.115 ± 0.014	-0.060 ± 0.005
2D	str	rlx	4.626 ± 0.005	0.062 ± 0.010	-0.007 ± 0.003
2D	str	sup	5.040 ± 0.009	0.344 ± 0.019	0.096 ± 0.005
2D	str	all	4.473 ± 0.004	0.115 ± 0.008	-0.014 ± 0.003

4.2 Lensing analysis

The lensing analysis of the MUSIC-MD clusters is based on the estimates of the Einstein radii. We address the derivation of the Einstein radii in two different ways: on one hand, we compute the *equivalent* Einstein radius from the mean convergence profiles; on the other hand, we estimate the *effective* Einstein radius using a ray-tracing code to compute convergence and shear maps. The derivation of the *equivalent* Einstein radius is based in the assumption that mass in clusters is spherically distributed, as the mean convergence profiles are computed by averaging the projected mass in circular shells. In contrast, estimations of the *effective* Einstein radius computed in terms of the convergence and shear maps, account for the two-dimensional projected mass distribution. By comparing these two independent estimations, we aim to characterize the systematics affecting the lens models based on analytic functions derived for axially symmetric lenses.

Thereafter, all the lensing properties are computed considering a source redshift $z_s = 2$.

4.2.1 Ray-tracing procedure

In this thesis we follow the lensing simulation pipeline described in Meneghetti et al. (2014), for which the following steps are involved:

- all the particles belonging to each individual halo are projected along the line of sight on the *lens plane*;
- starting from the position of the virtual observer, a bundle of light-rays is traced through a regular grid of 2048×2048 covering a region of $3.0 \times 3.0\ h^{-1}$Mpc around the halo center on the lens plane;
- the deflection $\vec{\alpha}(\vec{x})$ at each light-ray position $\vec{x}$ is computed accounting for the contributions from all particles on the lens plane;
- the deflection field is used to derive several lensing quantities. From this analysis, we obtain the convergence, $\kappa(\vec{x})$, and the shear, $\vec{\gamma} = (\gamma_1, \gamma_2)$, maps.

As described in sec. 2.1, the lens critical lines are defined as the curves along which the determinant of the lensing Jacobien is zero (det $\mathcal{A} = 0$, see Eq. 2.13). In particular, the *tangential* critical line is defined by the condition $(1 - \kappa - |\gamma|) = (1 - \bar{\kappa}) = 0$. Using Eq. 2.18, we obtain the *effective* Einstein radius in terms of the area enclosed by the tangential critical line. Moreover, we also fit the critical line by an ellipse, recovering an estimate of the ellipticity of the critical line (ϵ_θ). This additional information of the shape of the critical lines cannot be recovered from the mean convergence profiles alone, as critical lines of axially symmetric lenses are consequently circles.

4.2.2 MUSIC-MD Einstein radii distribution

As already mentioned, the *equivalent* Einstein radius is defined as the radius enclosing a mean convergence equal to one. Therefore, we first compute the mean convergence profiles of the MUSIC-MD clusters in terms of the surface density profile using Eq. 2.15 and then, we derive the size of the projected Einstein radius (labeled here as θ_{proj}) using Eq. 2.17. In addition, we derive the NFW approximation to the size of the Einstein radius (identified by θ_{NFW}) using the best fit parameters, M_{2D} and c_{2D}, to the surface density profiles.

We also run the ray-tracing pipeline described in the previous section over the full MUSIC-MD dataset. For each projection we produce mean convergence maps ($\bar{\kappa}$-maps) and compute the contour of the tangential critical line ($1-\bar{\kappa}=0$). The surface covered by the tangential critical line allows us to estimate the *equivalent* Einstein radius, thereafter θ_E, with Eq. 2.18.

Therefore, we have three different estimators of the Einstein radius, along with the mass and concentration derived from both fits to the density and surface density profiles, for 500 projections of each MUSIC-MD cluster. Given the spatial resolution in MUSIC-MD ($\sim\ 15h^{-1}$kpc), we are able to resolve critical lines with *effective* Einstein radius, $\theta_E = 15h^{-1}\mathrm{kpc}/D_L$. At the redshift here analyzed, $z \in [0.250, 0.667]$, this roughly corresponds to an Einstein radius of $\theta_E \approx 3-5$".

The cumulative Einstein radii distributions of the MUSIC-MD sample are shown in Fig. 4.8 (only projections with $\theta_E \geqslant 10$"). The results are shown for the complete subsample, so only halos with masses above the completeness mass are considered (see Table 3.1). By doing this, the Einstein radii distributions here presented give a fiducial representation of a $1h^{-1}$Gpc box volume at four different redshifts analyzed. The different lines show the mean values of the cumulative distribution of Einstein radii over the 500 random orientations produced. The dashed lines correspond to the Einstein radii distribution of θ_{NFW}. The solid lines show the *effective* Einstein radii distribution, θ_E, while the shaded regions correspond to the 2 and 98 percentiles of the distribution of θ_E. The Einstein radii statistics for the low-mass, the complete and the full samples are shown in Table 4.3. The low-mass subsample is composed by the halos below the completeness at each redshift and above the minimum mass ($2\times10^{14}h^{-1}\mathrm{M}_\odot$). The fraction of halos within the low-mass subsample that are capable of producing critical lines (i.e. with $\theta_E \gtrsim 3$") is below 3%. Therefore, the MUSIC-MD halos below the completeness mass are not too effective in producing strong lensing events. However, depending on the morphology and the orientation along the line of sight, we find low-mass halos producing $\theta_E \gtrsim 20$". In particular, 35 projections at $z = 0.429$ are due to halos below the completeness mass.

In the $\bar{\kappa}$-maps, all the tangential critical lines are best-fitted by an ellipse, which centre coincides with the halo centre. We define this ellipticity as $\epsilon_\theta = 1 - a/b$, with a and b the minor and mayor axis of the tangential critical line, respectively. In Fig. 4.9 we show the boxplots for the ϵ_θ at the four redshifts analyzed. We divided the sample according to θ_E in three subsamples with θ_E greater than 10, 20 and 30 arcsec, respectively. The mean values for the ellipticity show almost

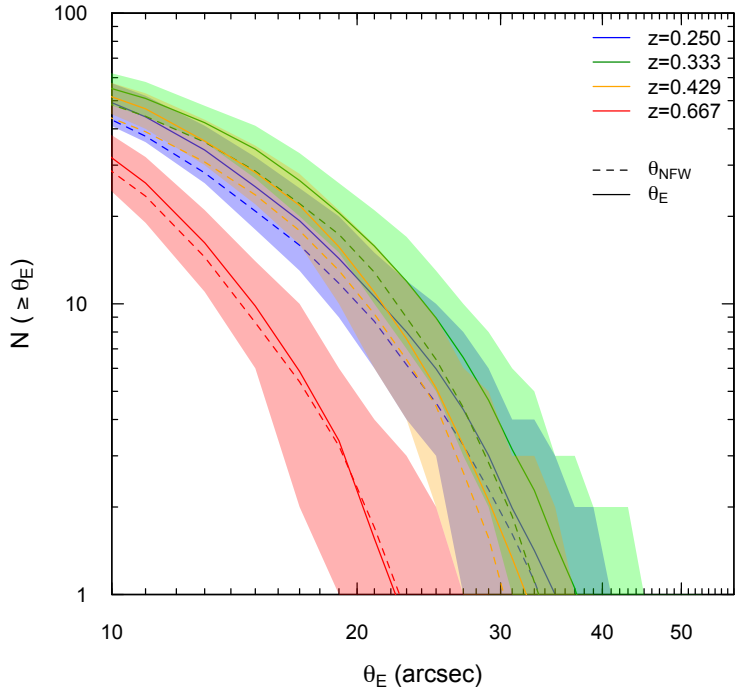

Figure 4.8: Cumulative Einstein radii distribution of $1h^{-1}$Gpc box volume at four different redshifts. Only the halos with masses above the completeness mass are considered. Mean values of the size of the Einstein radius: by fitting by the convergence profiles to a NFW (θ_{NFW}, dashed lines), and by computing the area within the tangential critical line (θ_E, solid lines). The shaded regions show the 2 and 98 percentile of the θ_E statistics for the 500 random orientations produced. Only the results for $\theta_E \geqslant 10$ arcsec are shown.

Dataset	Redshift	N_{halos}	N_{proj}	$N(\theta_E \geqslant 3'')$	$N(\theta_E \geqslant 10'')$	$N(\theta_E \geqslant 20'')$	$N(\theta_E \geqslant 30'')$
all	0.250	403	201500	42983 (21%)	22292 (11%)	5297 (3%)	993 (< 1%)
all	0.333	393	196500	43614 (22%)	25992 (13%)	7904 (4%)	1577 (< 1%)
all	0.429	365	182500	39857 (22%)	24089 (13%)	5520 (3%)	667 (< 1%)
all	0.667	258	129000	38429 (30%)	13223 (10%)	779 (1%)	0 (0%)
com	0.250	128	64000	41305 (65%)	21993 (34%)	5294 (8%)	991 (2%)
com	0.333	97	48500	40679 (83%)	25443 (52%)	7900 (16%)	1577 (3%)
com	0.429	80	40000	36305 (91%)	23437 (59%)	5485 (14%)	667 (2%)
com	0.667	89	44500	36231 (81%)	13019 (29%)	779 (2%)	0 (0%)
low	0.250	275	137500	1678 (1%)	299 (< 1%)	3 (< 1%)	2 (< 1%)
low	0.333	296	148000	2935 (2%)	549 (< 1%)	4 (< 1%)	0 (0%)
low	0.429	285	142500	3552 (2%)	652 (< 1%)	35 (< 1%)	0 (0%)
low	0.667	169	84500	2198 (3%)	204 (< 1%)	0 (0%)	0 (0%)

Table 4.3: Einstein radii statistics. First column: selected dataset (com=complete sample; low=low-mass halos; all=full sample); second column: redshift bin; columns 3,4: number of halos and number of projections (500 times the number of halos); columns 5,6,7,8: number of projections producing an Einstein radius greater than a given value (0, 10, 20 and 30 arcsec, respectively), along with the fraction of lenses ($N(\theta_E)/N_{proj}$, in %).

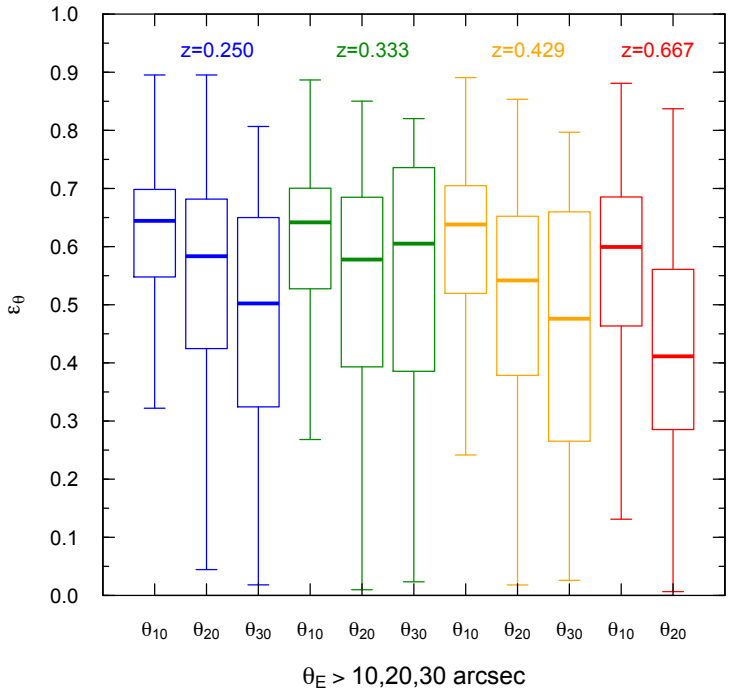

Figure 4.9: Boxplots for the ellipticity of the tangential critical lines of 500 projections of each of the MUSIC-MD clusters in a $1h^{-1}$Gpc box volume at four different redshifts. We divided the whole sample into three subsamples with θ_E greater than 10, 20 and 30 arcsec. Thick lines denote the median of each distribution, the boxes correspond to the interquartile range (IQR) and the errors bars enclosed the 2 and 98-percentil. We used different colors for each redshift analyzed.

no evolution with redshift (between 0.60-0.65 for all the projections with $\theta_E \geqslant$ 10 arcsec). However, when we selected projections with θ_E greater than 20 or 30 arcsec, the mean ellipticity tends to be smaller at high redshift. From this figure, we can also conclude that projections with larger θ_E show, on average, smaller ellipticities. The largest Einstein radii are found when a prolate, massive and/or concentrated halo is seen along its mayor axis, producing almost circular tangential critical lines. This correlation between the ellipticity and the size of the critical line can be clearly seen in the bottom-right panels of Fig. 4.12 and 4.13 for a super-relaxed and an un-relaxed halo.

Both estimates of the Einstein radius, θ_{proj} and θ_{NFW}, are derived by assuming

that the halos are axially symmetric lenses, while the θ_E give us the *real* size of the Einstein radius. Thus, the differences between θ_{proj} and θ_E are mainly due to the projections effects (such as triaxiality and substructures along the line of sight). To illustrate that, in Fig. 4.10 we show the distribution of halos in the plane $(\theta_E - \theta_{proj})/\theta_E$ vs ϵ_θ for all the redshifts analyzed. Elongated critical lines have the largest differences between the θ_{proj} and θ_E estimates. For the critical lines with an $\epsilon_\theta \geqslant 0.60$, the assumption of spherical symmetry starts to fail, the average projected mass within θ_E tend to be less than the mass within the surface covered by a elongated tangential critical line in the $\bar{\kappa}$-maps. The largest differences (almost 60%) are reported for critical lines with $\epsilon_\theta \geqslant 0.70$. In contrast, we find that θ_{proj} is over-estimated respect to θ_E, with differences on average of $\sim 5\%$ for projections with $\epsilon_\theta \leqslant 0.60$. This discrepancy is mainly due to the radial binning used to compute the projected mass in circular shells.

In addition, as the largest Einstein radii tend to have less elongated critical lines, we expect a 5% positive bias in θ_{proj} for projections with $\theta_E \gtrsim 20$". This can be understood by combining the information showed in Fig. 4.10 and Fig. 4.11. We find that 90% projections with $\theta_E \gtrsim 20$" are well recovered by both θ_{proj} (and θ_{NFW}) estimates, with $\lesssim 10\%$ bias. This situation drastically changes for projections with smaller θ_E, for which the estimation of the Einstein radius from the convergence profiles can lead to $> 50\%$ bias.

On the other hand, the θ_{NFW} estimate is computed by interpolating the mean convergence NFW profile at

$$\bar{\kappa}_{NFW}\,(R_E, \mathrm{M_{2D}}, \mathrm{c_{2D}}) = 1 \tag{4.7}$$

with $R_E = \theta_E D_L$, and $\mathrm{M_{2D}}$ and $\mathrm{c_{2D}}$ the best fit parameters to the surface density profiles. As the fitting procedure is performed over a broad radial range (going up to the virial radius, R_{200}), the best fit parameters account for the distribution of the mass within R_{200}. Therefore, the differences between θ_{NFW} and θ_E are due not only to projection effects, but also to the residuals of the NFW fit to the surface density profiles at $R \approx R_E$.

In the case of non-equilibrium halos, the NFW profile fails on giving a good description of the shape of the surface density profiles. Hence we expect larger differences between θ_{proj} and θ_{NFW} (and consequently between θ_{NFW} and θ_E) for un-relaxed halos. In Fig. 4.12 and Fig. 4.13 we show the results for a super-relaxed

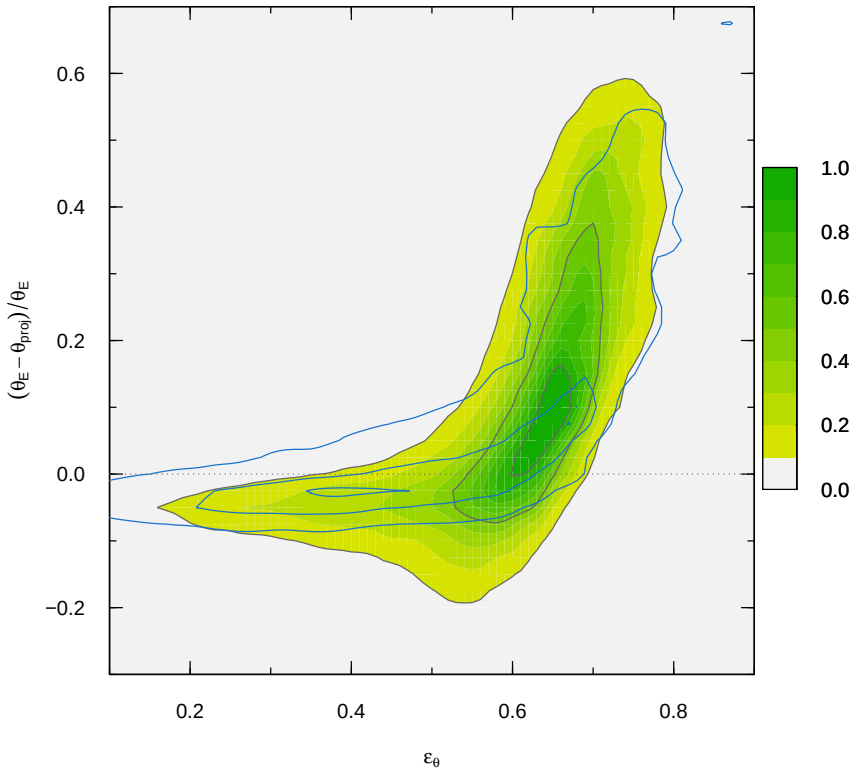

Figure 4.10: Distribution of halos in the plane $(\theta_E - \theta_{proj})/\theta_E$ vs ϵ_θ for all the redshifts analyzed. The two-dimensional distributions show the results for the 500 projections of the halos in $1h^{-1}$Gpc box volume at the four redshifts analyzed. The grey contours overlaid to the image show the intensity levels corresponding to 10%, 50% and 90% of the probability peak. The blue contours correspond to the same levels of the distribution for projections with $\theta_E \geqslant 20$ arcsec.

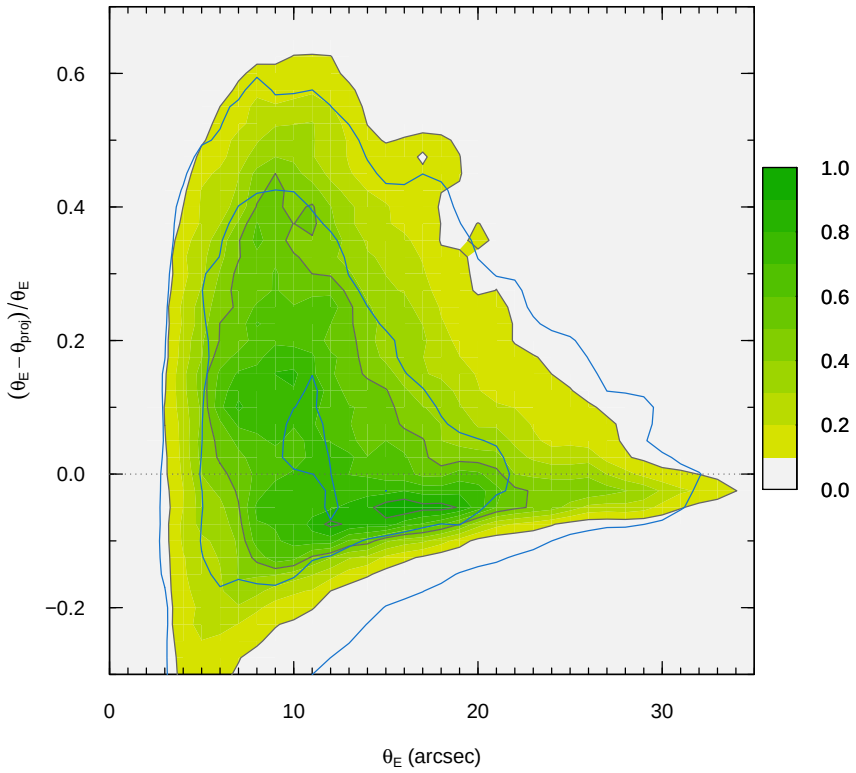

Figure 4.11: Distribution of halos in the plane $(\theta_E - \theta_{proj})/\theta_E$ vs θ_E for all the redshifts analyzed. The two-dimensional distributions show the results for the 500 projections of the halos in $1h^{-1}$Gpc box volume at the four redshifts analyzed. The grey contours overlaid to the image show the intensity levels corresponding to 10%, 50% and 90% of the probability peak. The blue contours correspond to the same levels of the distribution for projections in the plane $(\theta_E - \theta_{NFW})/\theta_E$ vs θ_E.

and an un-relaxed halo at $z = 0.250$ and $z = 0.333$, respectively. The super-relaxed halo has $M_{true} = 1.07 \times 10^{15}\, h^{-1}\, M_\odot$ and $c_{200} = 5.69$, while the un-relaxed halo has $M_{true} = 1.25 \times 10^{15}\, h^{-1}\, M_\odot$ and $c_{200} = 4.27$. The different panels show: the convergence profiles for 500 random orientations and the residuals of the NFW fit to the mean convergence profiles, with the red region indicating the positions of the tangential critical lines (R_E); the best-fitted M_{2D} and c_{2D} parameters to the surface density profile, with the 3D mass and concentration highlighted in red; the *effective* Einstein radii distribution, along with the θ_{NFW} estimates from best-fitted M_{2D} and c_{2D} parameters (previous panel); the ellipticity of the critical lines as function of θ_E for each projection. From these two figures, we can clearly observe how the NFW model is more appropriate to describe the profiles of *equilibrium* halos, such as our super-relaxed halo in Fig. 4.12. Therefore, the estimation of the Einstein radius considering a NFW model is more accurate for a relaxed halo, when comparing it with the *effective* Einstein radius. We observe the wide spread in the sizes of Einstein radius depending on the projection for the same halo configuration. In the un-relaxed case, the minimum and maximum sizes are 18" and 56", respectively. The latest value corresponds to the largest Einstein radius found in the MUSIC-MD dataset. The spread in the lensing parameters is a direct proof of the projection effects that we are accounting for in this work.

To illustrate this idea, in Fig. 4.14 we show the convergence maps for four projections of the super-relaxed halo above mentioned: two projections with intermediate-to-high concentrations, the projections with the maximum and minimum θ_E for this halo. For each projection we show the contour corresponding to the tangential critical line (and the fit to an ellipse), along with the θ_{NFW} and θ_E estimates. The panel showing the largest Einstein radius $\theta_E = 41$" also have the less elongated critical line, indicating that the halo is projected with its major axis along the line of sight. In this case, the lensing efficiency is boosted by more than 50% by projections effects when looking at the Einstein radii distribution.

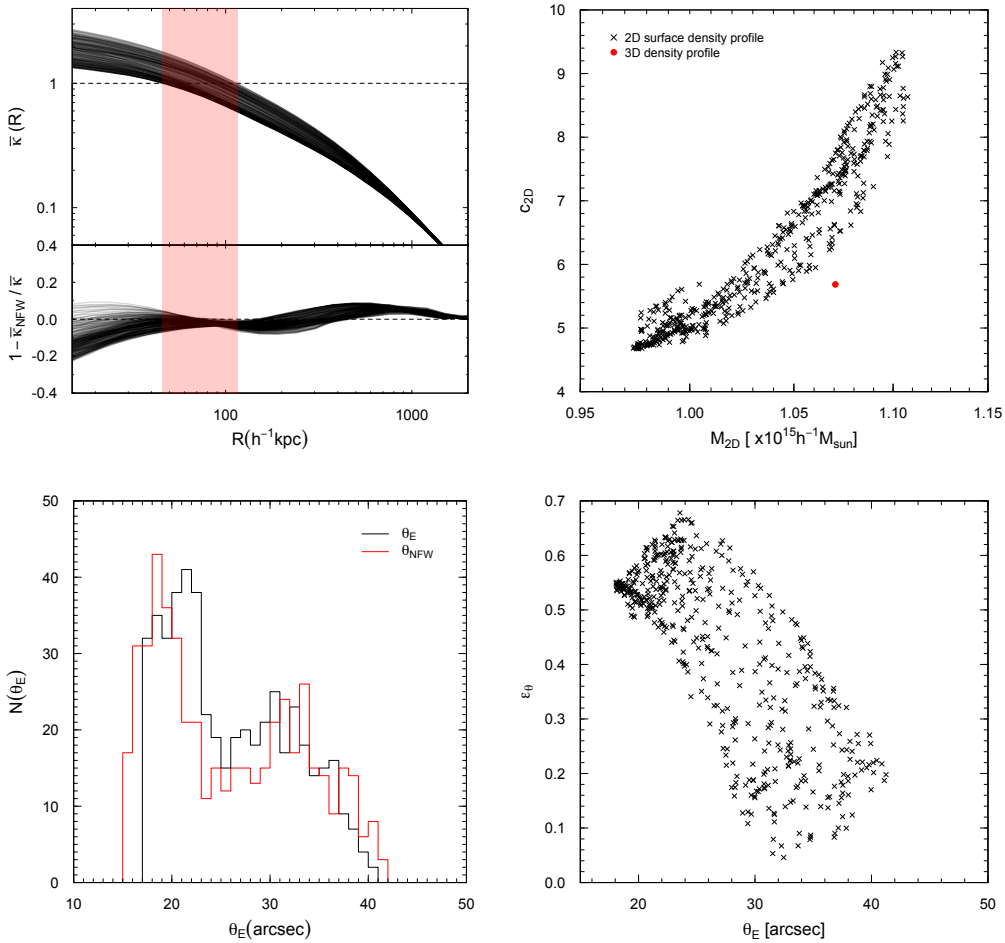

Figure 4.12: Left upper panel: Mean convergence NFW profiles for 500 different projections of a super-relaxed halo ($M_{true} = 1.07 \times 10^{15} h^{-1} M_{\odot}$ at $z = 0.250$) and the residuals of the residuals of the NFW fit. The horizontal dashed line shows the $\bar{\kappa} = 1$. Upper right panel: NFW fitting parameters, c_{2D} vs M_{2D}, for each projection (black crosses). The red circle represents the mass and concentration derived from the density mass profile. Bottom left panel: Einstein radii distribution (in arcsec) for each projection: θ_E in grey; θ_{NFW} in red. Bottom right panel: Ellipticity of the critical line as function of θ_E.

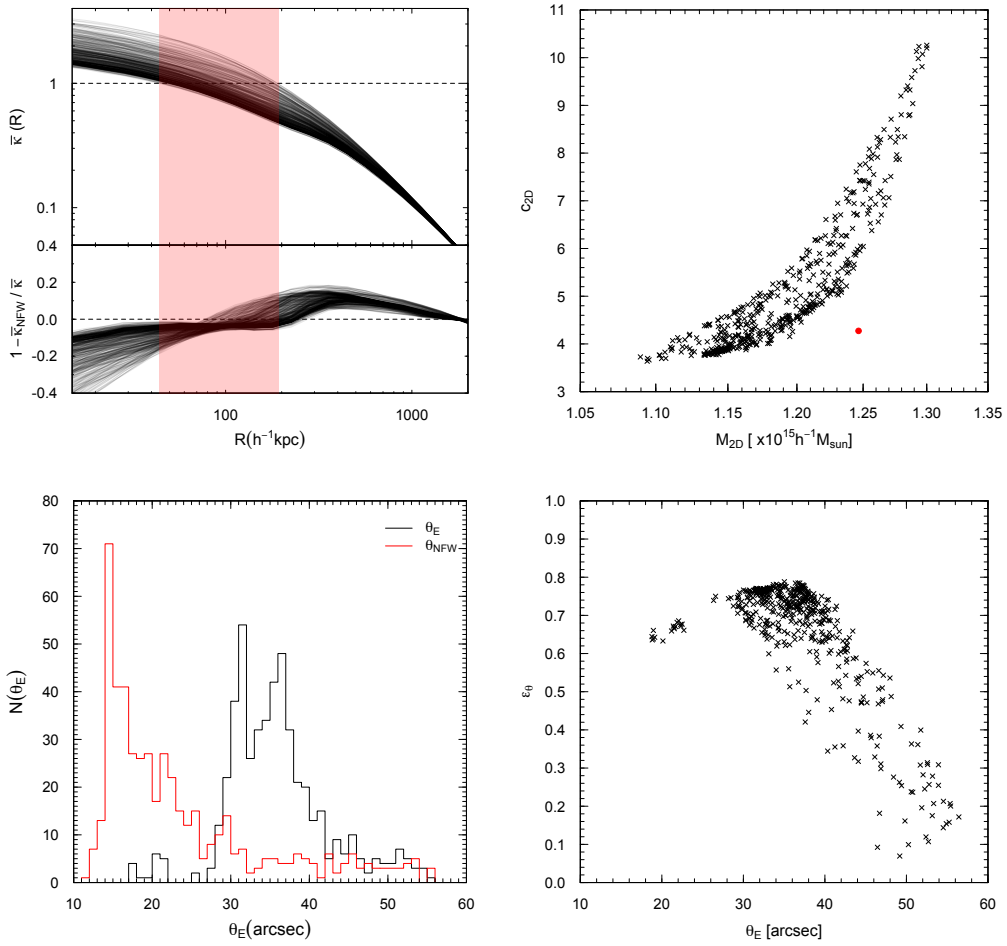

Figure 4.13: Left upper panel: Mean convergence NFW profiles for 500 different projections of a un-relaxed halo ($M_{true} = 1.25 \times 10^{15} h^{-1} M_{\odot}$ at $z = 0.333$) and the residuals of the residuals of the NFW fit. The horizontal dashed line shows the $\bar{\kappa} = 1$. Upper right panel: NFW fitting parameters, c_{2D} vs M_{2D}, for each projection (black crosses). The red circle represents the mass and concentration derived from the density mass profile. Bottom left panel: Einstein radii distribution (in arcsec) for each projection: θ_E in grey; θ_{NFW} in red. Bottom right panel: Ellipticity of the critical line as function of θ_E.

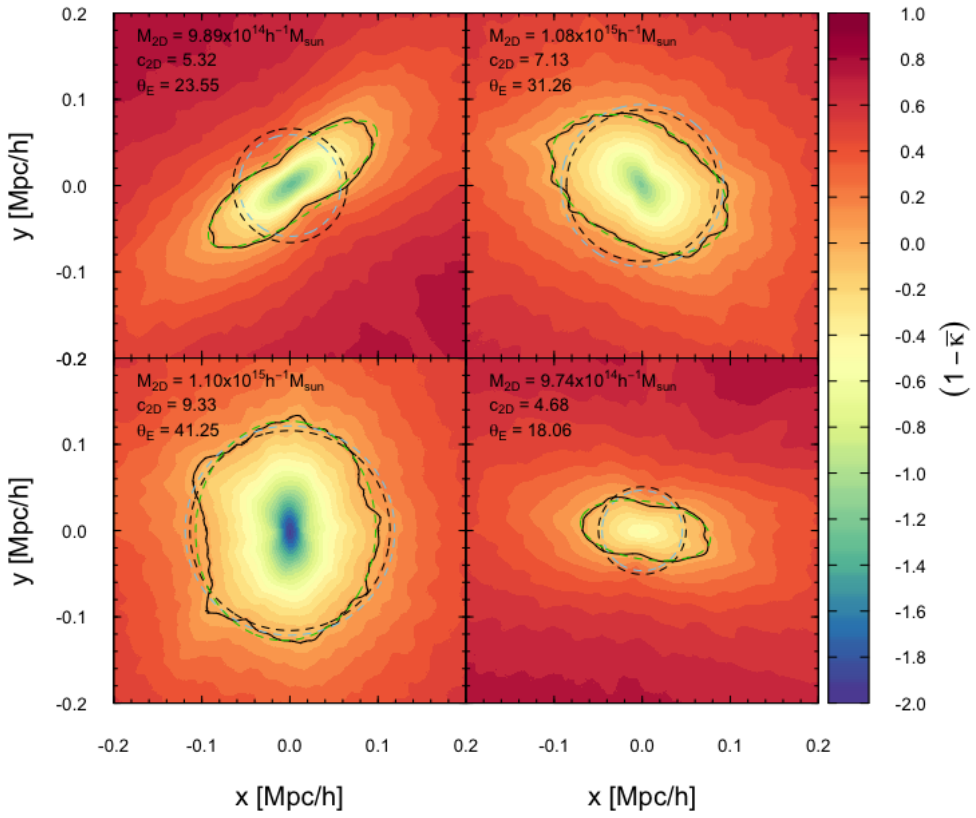

Figure 4.14: Convergence maps $(1 - \bar{\kappa})$ for four different projections of the super-relaxed halo presented in Fig. 4.12. Black contours indicate the position of the tangential critical lines (i.e. $1 - \bar{\kappa} = 0$). Black dashed lines correspond to the circle enclosing the same area as the critical line, while blue dashed lines indicates the θ_{NFW} estimates. The green dashed ellipses are the best-fit to the critical lines. We show in each panel the derived 2D mass and concentration along with the the size of the Einstein radii (θ_E).

CHAPTER 5

MAPLENS: MAdrid-Paris LENsing Semianalytics

In this Chapter, we describe the procedure to build up the *MAPLENS* semi-analytic model to infer the Einstein radii distribution and its evolution with redshift from a sample of dark matter halos. The name comes from the acronym *MAdrid-Paris LENsing Semianalytics*. *MAPLENS* is based on the analysis of cluster-sized distinct halos ($M \geqslant 2 \times 10^{14} h^{-1} M_{\odot}$) from the MUSIC-MD dataset at $z = (0.250, 0.333, 0.429, 0.667)$ (as detailed in Chapter 4). By comparing the Einstein radii distribution obtained by the NFW approximation and the *effective* Einstein radius, we incorporate the projections effects (triaxiality and presence of substructures) to our model with the aim to recover more realistic estimates of the Einstein radii distribution. With this objective, we generate a set of kernel density estimates to account for the distribution of the main properties of MUSIC-MD clusters (such as projected mass and concentration, θ_{NFW}, θ_E and ϵ_θ). Based on these kernel density estimates, *MAPLENS* allow us to derive the lensing properties of a sample of dark matter halos, once the mass and the redshift of each halo are known. Therefore, by construction, we can infer the Einstein radii distributions of a catalog of dark matter halos generated from an arbitrary mass function.

5.1 Kernel density estimation

Kernel density estimation is a non-parametric way to estimate the probability density function of a random variable directly from the data, without assuming

a particular form for the underlying distribution. For a d-variate random sample $\mathbf{X}_1, \mathbf{X}_2, \ldots, \mathbf{X}_n$ drawn from a density f, the kernel density estimate is defined by:

$$\hat{f}(\mathbf{x}; \mathbf{H}) = n^{-1} \sum_{i=1}^{n} K_{\mathbf{H}} (\mathbf{x} - \mathbf{X}_i) \tag{5.1}$$

where $\mathbf{x} = (\mathbf{x}_1, \mathbf{x}_2, \ldots, \mathbf{x}_d)^t$ and $\mathbf{X}_i = (\mathbf{X}_{i1}, \mathbf{X}_{i2}, \ldots, \mathbf{X}_{id})^t$ with $i = 1, 2, \ldots, n$. Here $K(\mathbf{x})$ is the kernel which is a symmetric probability density function and $\mathbf{H}$ is the bandwidth matrix which is symmetric and positive-definite, with $K_H(\mathbf{x}) = |H|^{-1/2} K(H^{-1/2}\mathbf{x})$. We evaluate the 3D-kernel density estimates using a Gaussian kernel for $K(\mathbf{x})$, with diagonal covariance matrix on a regular grid over the $\mathbf{x}$ variates. The diagonal bandwidth matrix constrains the smoothing to be performed in directions parallel to the co-ordinate axes, so it is not able to apply accurate levels of smoothing to the obliquely oriented central portion. We use a diagonal plug-in selector with a *SAMSE* pilot estimation to compute the bandwidth matrix $\mathbf{H}$ of the kernels (see Duong 2007 for more details).

As presented in Chapter 4, there is a large spread of the MUSIC-MD lensing parameters depending on the halo redshift, the halo mass and its dynamical state. In addition, the same halo configuration can yield very different projected masses and concentrations, and Einstein radii (as can be see in Fig. 4.12 and Fig. 4.13). The kernel density estimation method is ideal in these situations, where the underlying distributions between variates –which are also correlated– are not well described by the usual analytical distributions. The largest Einstein radii are produced by massive and/or concentrated clusters seen with its major axis projected along the line of sight. These statistically unlikely configurations are difficult to account when sampling from scaling relations (such as a *c-M* relation). In contrast, kernel density estimates fit the data points accounting for non-smoothed density distributions in the whole parameter space.

Taken advantage of this method, we compute two different 3D-kernel density estimates from the analysis of the 500 projections of each cluster in the MUSIC-MD dataset at redshifts $z = (0.250, 0.333, 0.429, 0.667)$:

- the first kernel density estimate, labeled as $\hat{f}_p$, contains the information derived from the fits to the density profiles, with variates $\mathbf{x} = (\mathrm{M_{200}}, \mathrm{M_{2D}}, \mathrm{c_{2D}})$ and a bandwidth matrix $\mathbf{H}_p$.
- the second one, labeled as $\hat{f}_\theta$, includes the lensing properties with variates

$\mathbf{x} = (\theta_{NFW}, \theta_E, \epsilon_\theta)$ and $\mathbf{H}_\theta$ the bandwidth matrix.

In total, we have 8 kernel density estimates: a $\hat{f}_p$ and a $\hat{f}_\theta$ at each of the four redshifts analyzed. These kernel density estimates can be used to sample the lensing properties (in particular, the *effective* Einstein radii). Given a hypothetical halo with redshift z and mass $\mathrm{M_{200}}$, we estimate the projected mass and concentration ($\mathrm{M_{200}}$ and $\mathrm{c_{200}}$) from the kernel density estimate $\hat{f}_p$ by means of *Monte Carlo* (MC) sampling with the conditional probabilities $p(\mathrm{M_{2D}} \mid \mathrm{M_{200}})$ and $p(\mathrm{c_{2D}} \mid \mathrm{M_{200}}, \mathrm{M_{2D}})$.

Using Eq. 4.7, we derive the Einstein radius by a NFW approximation (θ_{NFW}) considering a redshift z, and the $\mathrm{M_{2D}}$ and $\mathrm{c_{2D}}$ sampled above. Finally, given the redshift z and the θ_{NFW} of the halo, we estimate the corresponding *effective* Einstein radius (θ_E) using the kernel density $\hat{f}_\theta$. In this case, the conditional probabilities considered are $p(\epsilon_\theta \mid \theta_{NFW})$ and $p(\theta_E \mid \theta_{NFW}, \epsilon_\theta)$.

As a test to the procedure described above, we perform 500 MC realizations for the clusters in the MUSIC-MD dataset with mass above the completeness mass at each redshift. By doing this, we can assure that the predictions made from this mass-selected sample are representative of those produced in a $(1h^{-1}\mathrm{Gpc})^3$ box volume at each redshift, $z = (0.250, 0.333, 0.429, 0.667)$. The true masses measured at $\bar{\rho} = 200\rho_c(z)$, therefore M_{200}, and the redshifts of the halos are considered as inputs in our model. Given that we are producing the same number of realizations that the number of projections of each cluster in the MUSIC-MD, the results are expected to be very accurate.

In Fig. 5.1 we show the projection in the plane $\mathrm{M_{2D}}$ vs $\mathrm{M_{2D}}$ for 500 MC realizations performed over the $(1h^{-1}\mathrm{Gpc})^3$ box volume. The 2D histograms show the results of the MC sampling based on the $\hat{f}_p$ kernel density estimates at each redshift, with grey contours report the intensity levels for 10%, 50% and 90% of the probability peak. The dashed contours correspond to the same levels for the original MUSIC-MD dataset. As can be seen, the sampled parameters $\mathrm{M_{2D}}$ and $\mathrm{c_{2D}}$ are in excellent agreement with the simulated MUSIC-MD dataset. This demonstrates the utility of the kernel density method on recovering non-smoothed, asymmetric distributions.

From the sampled $\mathrm{M_{2D}}$ and $\mathrm{c_{2D}}$ and using the second set of kernel density estimates ($\hat{f}_\theta$), we derive the *effective* Einstein radii (θ_E) and the ellipticity of the tangential critical lines (ϵ_θ) for 500 MC realizations. In Fig. 5.2 we show the distribution of halos in the θ_E vs ϵ_θ plane at the four different redshifts analyzed. The 2D histograms show the results of the MC sampling, with the grey contours indicating

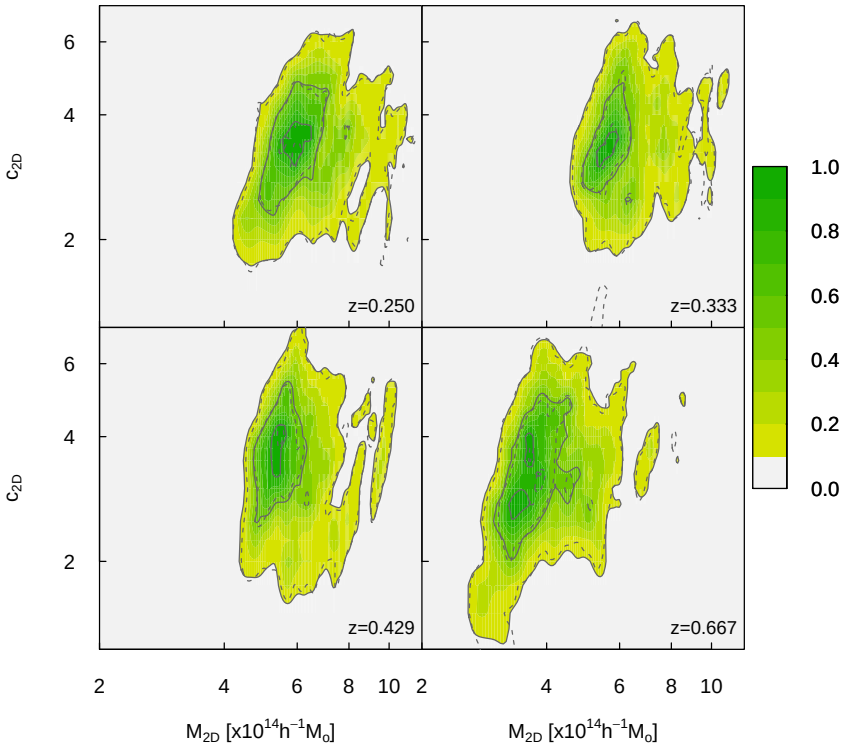

Figure 5.1: Distributions of halos in the plane c_{2D} vs M_{2D}. The two-dimensional histograms show the results for the 500 MC realizations of the halos in $(1h^{-1}\text{Gpc})^3$ box volume at the four redshifts analyzed. The grey contours overlaid to the image show the intensity levels corresponding to 10%, 50% and 90% of the probability peak. The dashed contours correspond to the same levels of the distribution of the original MUSIC-MD sample.

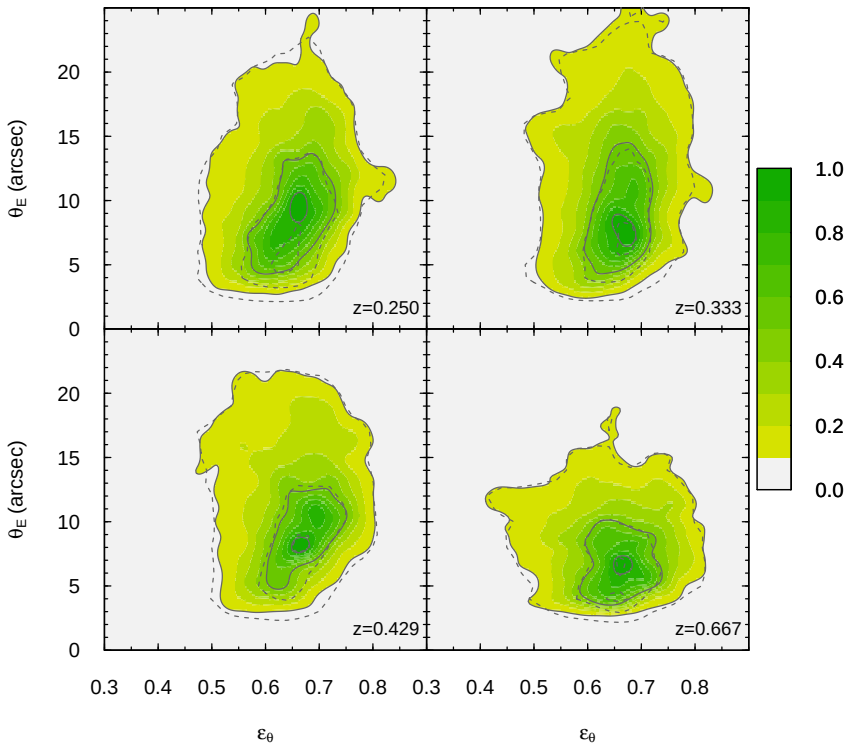

Figure 5.2: Distributions of halos in the plane θ_E vs ϵ_θ. The two-dimensional histograms show the results for the 500 MC realizations of the halos in $(1h^{-1}\text{Gpc})^3$ box volume at the four redshifts analyzed. The grey contours overlaid to the image show the intensity levels corresponding to 10%, 50% and 90% of the probability peak. The dashed contours correspond to the same levels of the distribution of the original MUSIC-MD sample.

the intensity levels (10%, 50% and 90%) of the probability peak, while the dashed contours show the original MUSIC-MD dataset (500 projections of the $(1h^{-1}\text{Gpc})^3$ box volume). A good agreement is clearly seen for all the redshifts with the exception of the first redshift, $z = 0.250$, where we find an offset of 10% levels between the original and the sampled distributions.

Besides, an appropriate selection of the bandwidths (or the smooth of the kernel density estimates) allows us to recover the peaks of the original distribution with a good accuracy, and to introduce some scatter where the intensity of the original distribution is lower. This can be noticed by comparing the sampling 2 and 98-percentile in Fig 5.3 and the same levels for the MUSIC-MD dataset shown in Fig. 4.8. The Einstein radii distributions obtained with *MAPLENS* are at the percent level for $\theta_E > 10$", probing the validity of the kernel density estimates

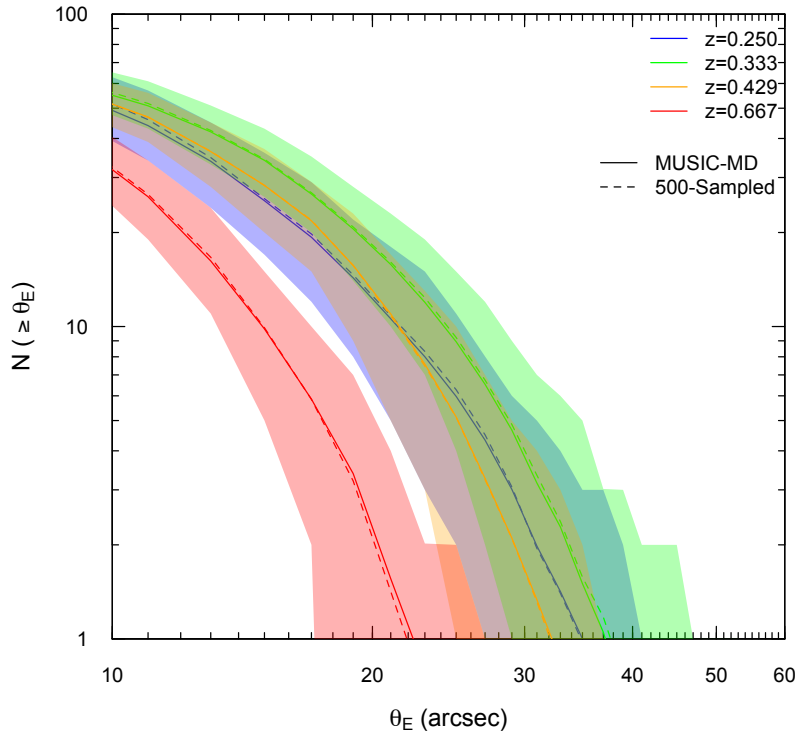

Figure 5.3: Distributions of the size of the Einstein radii at the four redshifts analyzed. The solid line show the mean values for 500 MC realizations of the original dataset ($(1h^{-1}\mathrm{Gpc})^3$ box volume) The dashed line show the mean values of the sampling for 500 projections of the original MUSIC-MD sample. Shaded regions show the 2 and 98 percentile of the 500 MC realizations (almost identical to the contours in Fig. 4.8).

on recovering correlated variates (such as the *effective* Einstein radius) by means of MC realizations.

One important aspect to notice is that we do not assume any scaling function relating the properties of the dark matter halos as input in our model (such as c-M relation or the triaxial shape as function of the halo mass and redshift). Therefore, the lensing properties of galaxy clusters obtained with *MAPLENS* account for the overall distribution in the parameter space at which the kernel density estimates are constructed. Besides, although there is no *a priori* information on the dynamical state of the halos in our model, the sampled Einstein radii distributions reflect the impact of the projection effects: the intrinsic triaxial shape, the presence of substructures along the line of sight and mergers in the MUSIC-MD dataset.

5.2 Einstein radii distribution: all-sky statistics

Following the procedure described in sec. 5.1, we extend our predictions on the Einstein radii distribution over a realization of dark matter halos generated with a analytic mass function of dark matter halos and considering *full-sky* coverage. Based on these expectations, we attempt a comparison between our theoretical results and the most recent observations of galaxy clusters (such as the CLASH and the SDSS surveys).

We generate mock halo catalogs according to the Tinker et al. (2008) mass function using the same cosmological parameters as the MUSIC-MD dataset. The Tinker et al. (2008) mass function is broadly accepted as a more accurate representation of the mass function determined from N-body simulations than the Press & Schechter (1974) or the Sheth & Tormen (1999) mass functions. In particular, this choice is preferential for a *strong-lensing* analysis, as described in Waizmann et al. (2012).

The mock catalogs are randomly created with the Poisson distribution of the expected mean number of dark matter haloes as follows:

$$\bar{N}(z, M) \; = \frac{\mathrm{d}\, n(z, M)}{\mathrm{d}\, M\, \mathrm{d}\, z}\, \Delta\, M\, \Delta\, z \times V_c \tag{5.2}$$

where V_c is the integrated comoving volume per solid angle Ω (Hogg, 1999) and M is the viral mass (defined as the mass at which the average density inside a spherical region is $\bar{\rho} = 200\rho_c$. The mean number of halos is computed using the code 'hmf v1.6.2' (see Murray et al. 2013 for more details), and assuming Δz=0.01 and $\Delta(\log \mathrm{M})$=0.01. We run 1000 realizations of dark matter haloes on Ω=40000 square degree, which roughly corresponds to *all-sky* excluding the galactic plane. In the previous section, we limited our analysis to a complete subsample of MUSIC-MD dataset, i.e., clusters more massive than the completeness mass limit defined at each redshift. Here, we extend our limits in mass by including all the MUSIC-MD halos with $\mathrm{M} \geqslant 2 \times 10^{14} h^{-1} \mathrm{M}_{\odot}$ when generating the kernel density estimates. Again, we account for 500 projections of each halo in the MUSIC-MD sample. The catalogues are thus generated in the range of cluster masses ($\mathrm{M} \geqslant 2 \times 10^{14} h^{-1} \mathrm{M}_{\odot}$) within $z \in [0.10, 1.0]$. The mean number of halos above the minimum mass for the 1000 realizations is $\tilde{N}$ = 46,290 with a standard deviation of σ_N = 203.

Given that the kernel density estimates are computed at discrete redshifts, mock halos at a different redshift than the redshifts of the kernel density estimates are

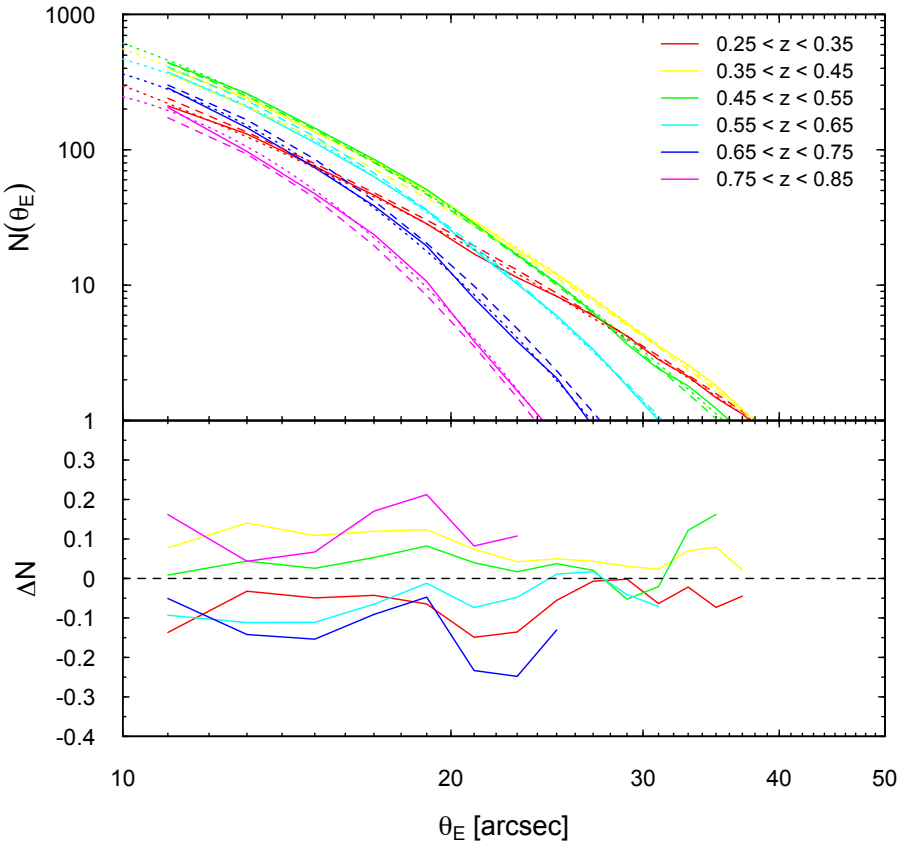

Figure 5.4: Differential Einstein radii distribution in different redshift bins (upper panel). Solid lines show the mean all-sky distribution in 1000 realizations; dotted lines correspond to the individual best-fit to the all-sky distribution in each redshift bin; dashed lines indicate the expected distribution using the *universal* function given by Eq. 5.3.

sampled using a linear interpolation of the kernel density estimates.

5.3 A universal distribution function of Einstein radii

We derive now the *effective* Einstein radii for 1000 all-sky mock catalogs based on the kernel density estimates generated from the MUSIC-MD dataset. In Fig 5.4 we show the differential all-sky Einstein radii distributions from $z = 0.25$ to $z = 0.85$ with $\Delta z = 0.1$ and $\Delta\theta_E = 2$ arcsec.

We propose as simple fitting formula to the *all-sky* Einstein radii distribution as follows:

$$N\,(z+\Delta z,\theta_E+\Delta\theta_E) = 10^{\,n(z,\theta_E)}\,\Delta z\,\Delta\theta_E \tag{5.3}$$

with $n\,(z,\theta_E)$ well described by a parabolic function in $\log\,\theta_E$ of the form:

$$n\,(z,\theta_E) = a(z) + b(z)\,\log\,\theta_E + c(z)\,\log^2\theta_E \tag{5.4}$$

The redshift dependence is described by:

$$\begin{aligned} a(z) &= a_0 + a_1\,z + a_2\,z^2 \\ b(z) &= b_0 + b_1\,z + b_2\,z^2 \\ c(z) &= c_0 + c_1\,z + c_2\,z^2 \end{aligned} \tag{5.5}$$

where a_i, b_i and c_i are determined using a weighted least-squares minimization to a parabolic function at each redshift bin. The results of the fitting function (Eq. 5.3) are also shown in Fig 5.4. The relative error in the number of lenses is constrain within $\lesssim$ 20% for lenses with $\theta_E \geqslant 10$ arcsec, and it is reduced to $\lesssim$ 10% for lenses with $\theta_E \geqslant 25$ arcsec The fitting functions governing the redshift dependence are presented in Fig. 5.5 for the best fitting parameters reported in Table 5.1. The measured dispersion in the number of Einstein radii in Eq. 5.3 is $\sigma_N = \sqrt{N}$.

The *universal* distribution function of Einstein radii given by Eq. 5.3 enable us to simply estimate the all-sky Einstein radii distribution produced by clusters of galaxies at a given redshift z. The predictions obtained in this way can be straightforward compared with the observed Einstein radii statistics. With this in mind, in sec. 6.3 we present a detailed comparison of our theoretical expectations with the observational data of 10000 SDSS galaxy clusters.

Table 5.1: Best-fit parameters to the differential Einstein radii distribution as a function of redshift (Eq. 5.5).

	$i=1$	$i=2$	$i=3$
a_i	3.26 ± 1.74	12.33 ± 6.99	-30.00 ± 6.54
b_i	1.12 ± 2.53	-14.75 ± 10.15	48.28 ± 9.49
c_i	-2.33 ± 0.96	7.93 ± 3.86	-23.60 ± 3.61

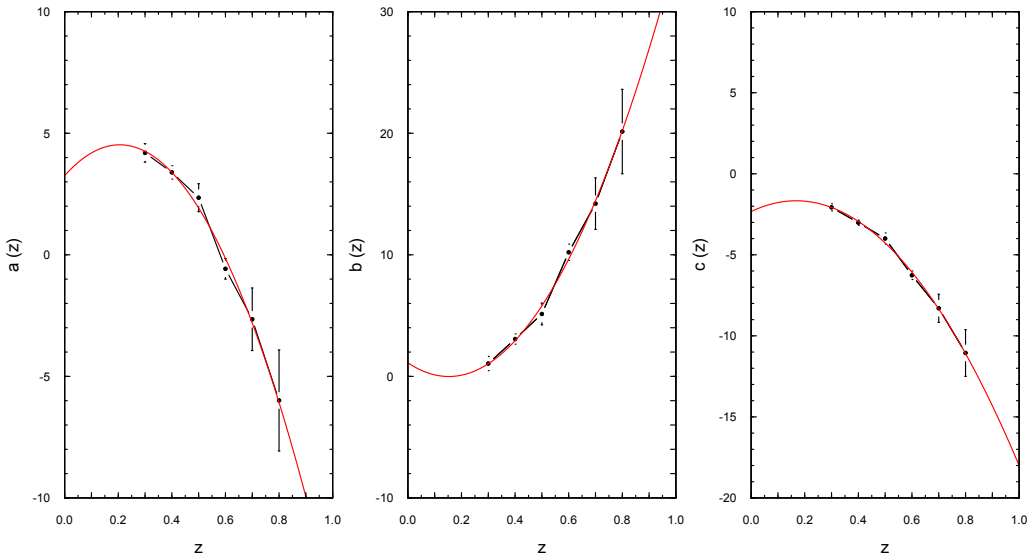

Figure 5.5: Fitting functions to the differential Einstein radii distribution as a function of redshift. Black points and error bars are derived by best-fitting the number of lenses within a given redshift bin to Eq. 5.4. The best-fits to data points correspond to the red lines in each panel. The best-fit parameters for Eq. 5.5 can be found in Table 5.1.

5.4 What is the largest Einstein radius: extreme value statistics

To better understand the Einstein radii distribution of both the theoretical and observed estimates, we perform an analysis based on the extreme value statistics (EVS) of the distribution of Einstein radii. The EVS describes the stochastic behavior of extremes and provides a rigorous framework for determining the likelihood of rare events (Gumbel, 2004). Since we are interested in the study of the distribution of the largest Einstein radii, the method developed in this work is based on the so-called Gnedenko approach (Fisher & Tippett, 1928; Gnedenko, 1943), which models the distribution of block maxima, M_n, of independent identically distributed random variates, X_i, which are defined as:

$$M_n = max(X_1, \ldots, X_n) \tag{5.6}$$

As already shown (Fisher & Tippett, 1928; Gnedenko, 1943), for $n \rightarrow \infty$, the cumulative distribution function (CDF) of these maxima converges to the general extreme value (GEV) distribution:

$$G_{\gamma,\beta,\alpha}(x) = \begin{cases} \exp\left\{-\left[1+\gamma\left(\frac{x-\alpha}{\beta}\right)\right]^{-1/\gamma}\right\}, & \text{for} \quad \gamma \neq 0, \\ \exp\left\{e^{-\left(\frac{x-\alpha}{\beta}\right)}\right\}, & \text{for} \quad \gamma = 0, \end{cases} \tag{5.7}$$

with α, β and γ being the location, the scale and the shape parameters. The mode of the GEV distribution –which is the most likely value– is given by:

$$x_0 = \alpha + \frac{\beta}{\gamma}\left[(1+\gamma)^{-\gamma} - 1\right], \tag{5.8}$$

The expectation value of the GEV distribution reads:

$$\mathrm{E_{GEV}} = \alpha - \frac{\beta}{\gamma} + \frac{\beta}{\gamma}\Gamma(1-\gamma) \tag{5.9}$$

where Γ denotes the Gamma function.

We use the GEV distribution from Eq. 5.7 to fit the sampled distributions of the largest Einstein radii extracted from the 1000 *all-sky* MC realizations. Basically, for each realization we select the clusters producing the n largest Einstein radii, $M = \left(\theta_E^1, \ldots, \theta_E^n\right)$. For convenience, we divide our mock cluster catalogs according to their redshifts into two different catalogs: low-redshift (for clusters with $0.1 < z < 0.55$) and high-redshift (for clusters with $0.5 < z < 1.0$). Thereafter, we refer to the former as the *low-z* catalog and the later as the *high-z* catalog.

The upper panel in Fig. 5.6 shows the cumulative distribution functions of the 12 largest Einstein radii extracted from the *low-z* catalog. The CDFs steepen with increasing order. The red dashed line indicates the fit to the general extreme value (GEV of the Gnedenko approach) to the CDF of the 1000 maxima sampled. The best fitting parameters of the GEV distribution are given by (α, β, γ) = (51.66 ± 0.10, 5.1 ± 0.15, 0.00 ± 0.03). The mode of the GEV distribution, which is the most likely value, is 51.7". The expectation value of the GEV distribution is 54.6". On the other hand, the bottom panel in Fig. 5.6 shows the cumulative distribution functions of the 12 largest Einstein radii extracted from the *high-z* catalog. The best fitting parameters of the GEV distribution are given by (α, β, γ) = (36.25 ± 0.05, 2.54 ± 0.07, 0.03 ± 0.03). The mode and the expectation values of the GEV distribution are 36.2"and 37.8",respectively. For comparison, Redlich et al. (2014) found 50.4" and 55.4" considering the same redshift range and including the impact of cluster mergers.

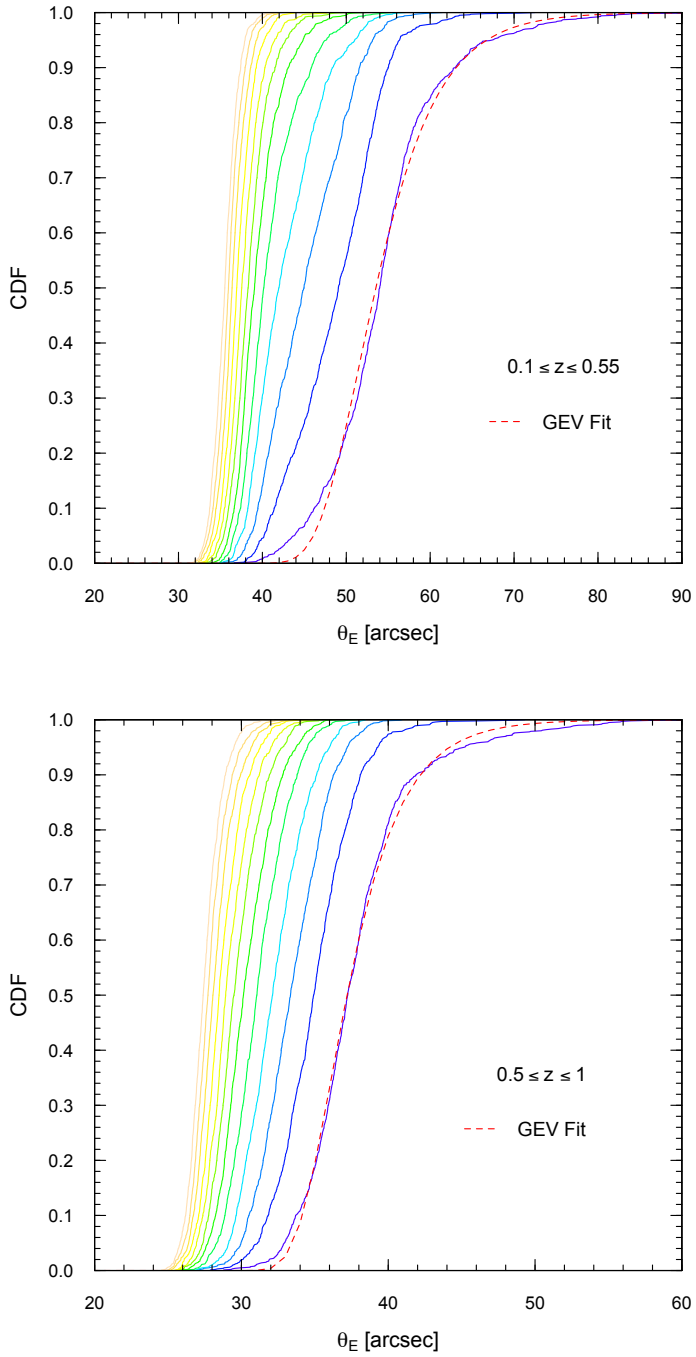

Figure 5.6: Cumulative distribution functions (CDF) of the 12 largest Einstein radii. The CDFs were extracted from the *low-z* catalog (upper panel) and the *high-z* catalog (bottom panel). The red dashed lines indicate the fit of the GEV distribution to the CDF of the largest Einstein radii.

In Fig. 5.7, we show the distributions of virial mass (M_{200}) and redshift for the 12 largest Einstein radii in the 1000 all-sky realizations for the *low-z* catalog. As expected, all the largest Einstein radii ($\theta_E \geqslant 45$") are produced by massive clusters with $M_{200} > 10^{15} h^{-1} M_\odot$. This figure also reveals the optimum redshift where to find the strongest lenses, between $0.35 < z < 0.4$. At lower orders, the minimum mass to produce strong lenses ($\theta_E \geqslant 30$") is shifted towards lower masses. Only a few clusters with masses $M_{200} = 2\text{-}4 \times 10^{14} h^{-1} M_\odot$ are strong enough to produce lenses with $\theta_E \geqslant 30$".

The distribution of the redshift, mass, projected concentration and ellipticity of the critical line for halos in the *low-z* catalog at the different order statistics is shown in Fig. 5.8. All orders extend over a wide range of masses and concentrations. It can be seen that the mean mass drops by a factor of ~ 2 from the 1st to the 12th order. The mean concentrations also decrease with increasing order. In particular, mean concentrations are $c_{2D} \gtrsim 8$ for the 1st order, while $c_{2D} \lesssim 7$ for the 12th order statistic. Therefore, the largest Einstein radii are produced by massive and/or concentrated clusters at redshift $z \approx (0.35 - 0.40)$. Moreover, the mean ellipticity of the critical lines increases from 0.25 to 0.55 with increasing order. This image reinforces the impact of the triaxiality on the largest Einstein radii statistics, as the strongest lenses are found to be produced by prolate clusters with their major axis projected along the line of sight. Consequently, in these cases, most of the mass of the halo is projected along the line of sight, and the critical line tend to be circular (with low ϵ_θ).

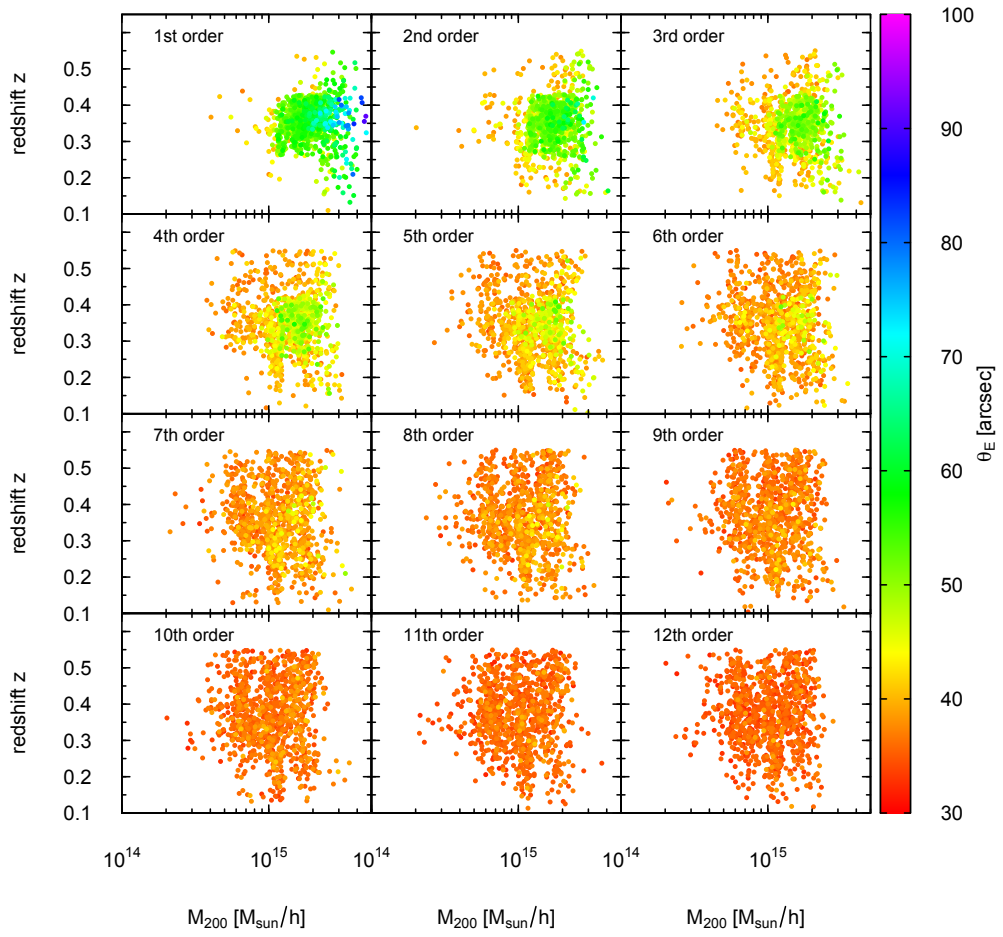

Figure 5.7: Distribution in mass and redshift of 1000 sampled values of the effective Einstein radii of the 12 largest orders in the *low-z* catalog ($0.1 < z < 0.55$). The colour encodes the size of the individual effective Einstein radii of a given order from each realization.

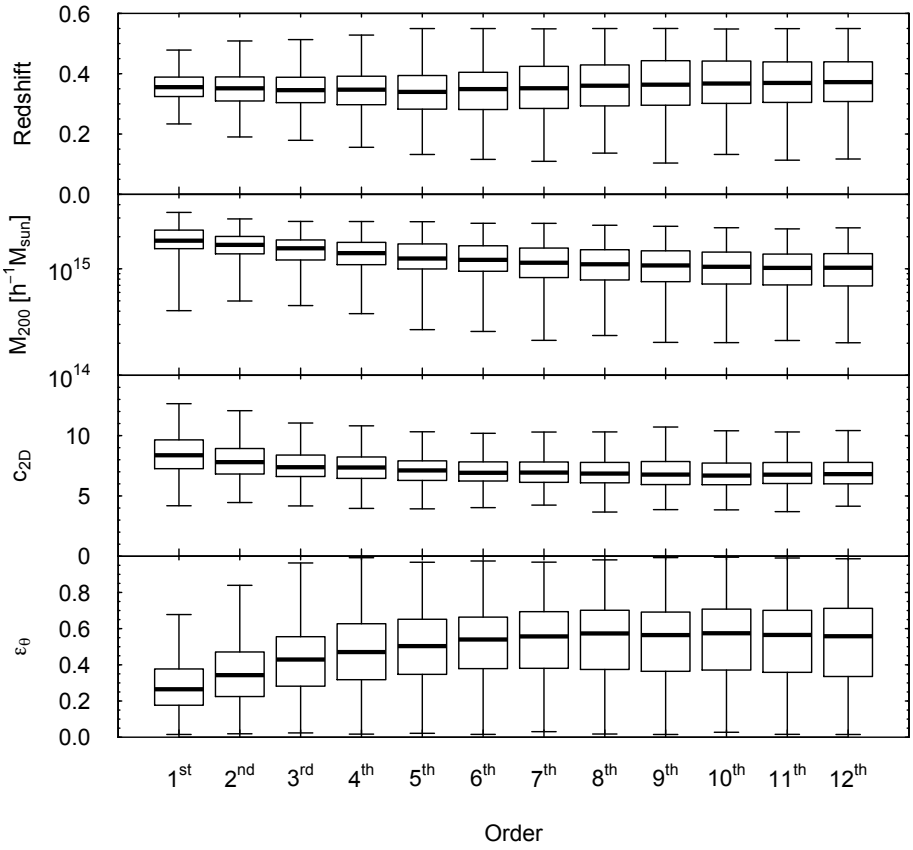

Figure 5.8: Boxplot containing the redshift, the mass, the projected concentration and the ellipticity of the critical line for the halos in the *low-z* catalog ($0.1 < z < 0.55$) as a function of the 12 largest orders. Boxes correspond to the inter-quartile-range (IQR), thick lines denote the 50-percentile (i.e. the median) and whiskers mark the range between the 2 and 98-percentile (Q2 and Q98, respectively).

CHAPTER 6

Comparison with observations

In the past few years the identified clusters have considerably increased, not only in number, but also the quality of its observations. The observations have provided enough accuracy on the mass density profiles to measure the *c*-*M* relation using gravitational lensing and to estimate the Einstein radii down to a few arcsec. The relation between mass and concentration in galaxy clusters is an important probe of the formation and evolution of dark matter halos in the framework of the ΛCDM cosmological model.

As described in Sec. 2.3.1, a significant number of observed galaxy clusters are over-concentrated (Broadhurst et al., 2008; Oguri et al., 2009; Umetsu et al., 2011), showing a $c - M$ relation which is steeper than predicted by theoretical models (Comerford & Natarajan, 2007; Fedeli, 2012). Orientation and cluster triaxiality partially explain the over-concentration problem, as the lensing strength is boosted by prolate clusters elongated towards the observer (Hennawi et al., 2007; Oguri & Blandford, 2009).

As we discussed in Sec. 2.2.1, selection effects play a major role, leading to stepper $c - M$ relations (Giocoli et al., 2014). The observed $c - M$ relation is usually determined in samples which are neither statistical significant nor complete, which might constitute a biased population (Sereno & Zitrin, 2012). Using the same MUSIC-MD simulation dataset, in Meneghetti et al. (2014) we have shown that the concentrations of CLASH clusters derived by Merten et al. (2015) are in good agreement with theoretical predictions after accounting for projections and selection effects (in terms of the X-ray morphologies). In Meneghetti et al. (2014) we found that simulated halos which resemble the X-ray morphologies of the CLASH clusters

is composed mainly by relaxed halos ($\sim$ 70%), but it also contains a significant fraction of unrelaxed systems. Fur such sample, the average 2D concentration is $\sim$ 11% higher than found for the full MUSIC-MD dataset. However, after accounting for projections and selection effects, the average NFW concentrations recovered from the lensing analysis are expected to be somewhat in between those predicted in 3D for a relaxed and the super-relaxed subsamples of the MUSIC-MD dataset. Besides, Merten et al. (2015) found an excellent 4% agreement between the CLASH concentrations and the expectations from the lensing analysis of the MUSIC-MD dataset after using the same selection criteria of CLASH based on x-ray morphologies.

In this chapter, we investigate whether the tension between observed $c-M$ relations in lensing cluster samples and the ΛCDM paradigm may be reconciled with a proper treatment of the projection and selection effects. As described in the previous chapter, we derived $c-M$ relations for *all-sky* realizations based on the MUSIC-MD dataset. The kernel density technique accounts for the distributions of the lensing properties of the simulated clusters, but no scaling relation is applied to sample them. The scaling relations (as the $c-M$ relation) presented in this chapter are obtained *a posteriori* from the sampled mass and concentrations of the *all-sky* realizations. The $c-M$ relations derived from *all-sky* realizations are expected to differ from the MUSIC-MD relations presented in sec. 4.1.2, as the later were derived for an incomplete sample of MUSIC-MD clusters. Besides, sampled $c-M$ relations are obtained by taking into account the expected number of halos between $0.1 < z < 1.0$, and not only at four different redshifts (as in the case of the MUSIC-MD relations).

In the following sections, we present a detailed comparison between our theoretical *all-sky* predictions and the most recent observations of galaxy clusters from literature for which projected mass, projected concentration and size of the Einstein radii are available. We present separately the comparison for two different set of observations. On one hand, we compare the order statistics of the largest Einstein radii taken from the analysis of 10000 Sloan Digital Sky Survey (SDSS) clusters presented by Zitrin et al. (2012a) and the $c-M$ relations of 28 SGAS lensing clusters by combining the results of Oguri et al. (2012) and Sereno et al. (2015b). On the other hand, we perform a similar comparison over the 19 X-ray galaxy clusters from the CLASH cluster sample based on the results presented by Merten et al. (2015). We also compare the order statistics of the Einstein radii for a *high-z* strong lensing

cluster sample analyzed in Zitrin et al. (2011).

6.1 The SGAS clusters

Oguri et al. (2012) presented a combined strong and weak lensing analysis for a subsample of 28 clusters from the Sloan Giant Arcs Survey (SGAS) in the redshift range $0.27 \lesssim z \lesssim 0.68$, based on a follow-up imaging observations with Subaru/Suprime-cam. Recently, Sereno et al. (2015b) re-analyzed the shear profiles of these 28 clusters with the additional constraints on the effective Einstein radii (Oguri et al. 2012, table 2) and derived the mass and concentration using uniform linear priors. For a direct comparison with these observations, we construct a θ_E-selected sample by considering galaxy clusters in the 1000 *all-sky* realizations within $0.25 \lesssim z \lesssim 0.70$ with $\theta_E \gtrsim 3$".

For each *all-sky* realization, we propose a fitting function to the projected $c - M - \theta_E$ relation as follows:

$$c(M, \theta) = A\ \theta^B \left(\frac{M}{8 \times 10^{14} h^{-1} M_\odot} \right)^C , \tag{6.1}$$

We perform a least-squares minimization of both the sampled data and the SGAS $c - M - \theta_E$ relations. The best-fitted parameters can be found in Table 6.1. In Fig. 6.1 we show the M_{200} and c_{200} reported in Sereno et al. (2015b) combined with the Einstein radii measured by Oguri et al. (2012). We also show the observed and theoretical $c - M - \theta_E$ relations at $\theta_E = (3, 14, 40)$ arcsec, which correspond to the minimum, the median and the maximum θ_E of the SGAS sample, respectively. We find a similar trend with mass in the observed and the theoretical $c - M - \theta_E$, with $C_{SGAS} = -0.3$ and $C_{all-sky} \simeq 0.27$, respectively. However, the dependence with θ_E seems to be stronger in the observed $c - M - \theta_E$ than predicted with *MAPLENS*. The normalization of the theoretical $c - M - \theta_E$ relation is higher than the observed relation. We also show the results of the stacked analysis of the shear measurements presented by Sereno et al. (2015b) for the SGAS sample (black contour). The observed $c - M - \theta_E$ at the mean $\theta_E = 14$" of SGAS clusters (green dashed line) crosses the 1σ contour from the stacked analysis. The predicted $c - M - \theta_E$ at $\theta_E = 14$" (green solid line) is slightly flatter than the observed relation, with $\lesssim 12\%$ slightly over-estimated concentrations for the mass range considered

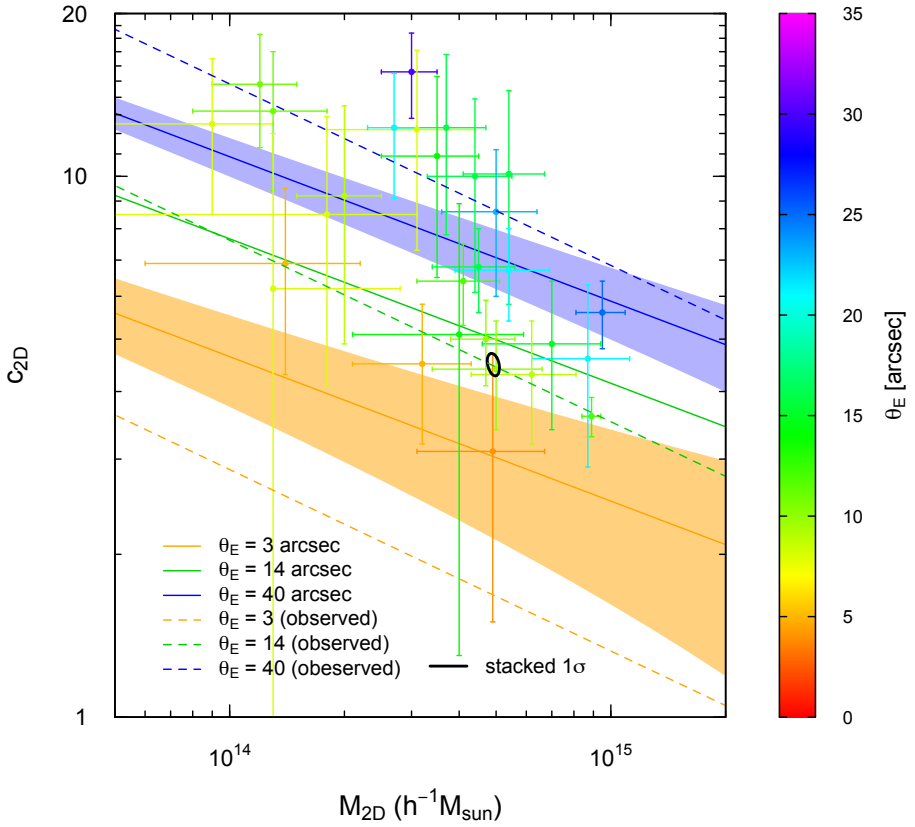

Figure 6.1: A comparison between the SGAS clusters and the $c - M - \theta_E$ relations of the 1000 *all-sky* realizations. The points and error bars correspond to the results presented by Oguri et al. (2012). Solid lines represent the expected $c - M - \theta_E$ relations of a θ_E-selected sample. The shaded contours indicate the 1σ-level in the theoretical $c - M - \theta_E$ relations. Dashed lines denote the best-fit $c - M - \theta_E$ relations to the SGAS sample. The relations are shown for $\theta_E = (3, 14, 40)$ arcsec, which correspond to the minimum, median and the maximum θ_E of the SGAS clusters. The thick black contour denote the results of the stacked analysis presented by Sereno et al. (2015b).

Table 6.1: Fitting parameters for the observed and theoretical $c - M - \theta_E$ relation in Eq. 6.1.

sample	A	B	C	σ
SGAS	0.7 ± 0.3	0.6 ± 0.1	-0.3 ± 0.1	2.1
all-sky	1.83 ± 0.03	0.333 ± 0.006	-0.267 ± 0.005	0.90

Therefore, we can conclude that the SGAS sample is slightly over-concentrated but still consistent, within the errors, with the theoretical predictions for a strong lensing sample of dark matter halos in the redshift range $0.25 \lesssim z \lesssim 0.70$, considering *full-sky* coverage. From the stacked analysis, the overall agreement is even better.

6.2 The CLASH sample

In Merten et al. (2015) we presented a new determination of the *c-M* relation for galaxy clusters based on a lensing analysis of 19 X-ray selected galaxy clusters from the CLASH cluster sample. New multiple images have been identified in most of the clusters in that work, so they present better constraints on the cluster mass distribution from a strong and weak lensing analysis. We take their mass and concentrations estimates, which have been derived by best-fitting the surface mass profiles of the clusters to a NFW model, along with the estimation of the median Einstein radius (defined as the median distance of the tangential critical points from the clusters centre).

Out theoretical $c - M - z$ relations are derived by means of nonlinear least-square fitting of Eq. 4.6. We select clusters from our 1000 all-sky realizations within the redshift range of the CLASH sample ($0.19 < z < 0.89$). In Fig. 6.2 we show the $c - M$ relation for the *all-sky* full sample (black solid line). Data points in the figure correspond to the CLASH estimates derived in Merten et al. (2015), while the color coding represents the size of the Einstein radius of each cluster. We also report the $c - M - z$ relation of a *all-sky* θ_E-selected sample, by selecting clusters with $\theta_E \gtrsim 3$ arcsec from the full sample. For a direct comparison, we also show the observed $c-M-z$ relation obtained by Merten et al. (2015) and the expected relation for a X-ray selected sample extracted from the MUSIC-MD dataset presented by Meneghetti et al. (2014). The best-fitted parameters are reported in Table 6.2. Note that Merten et al. (2015) used a fitting function with a different normalization in redshift.

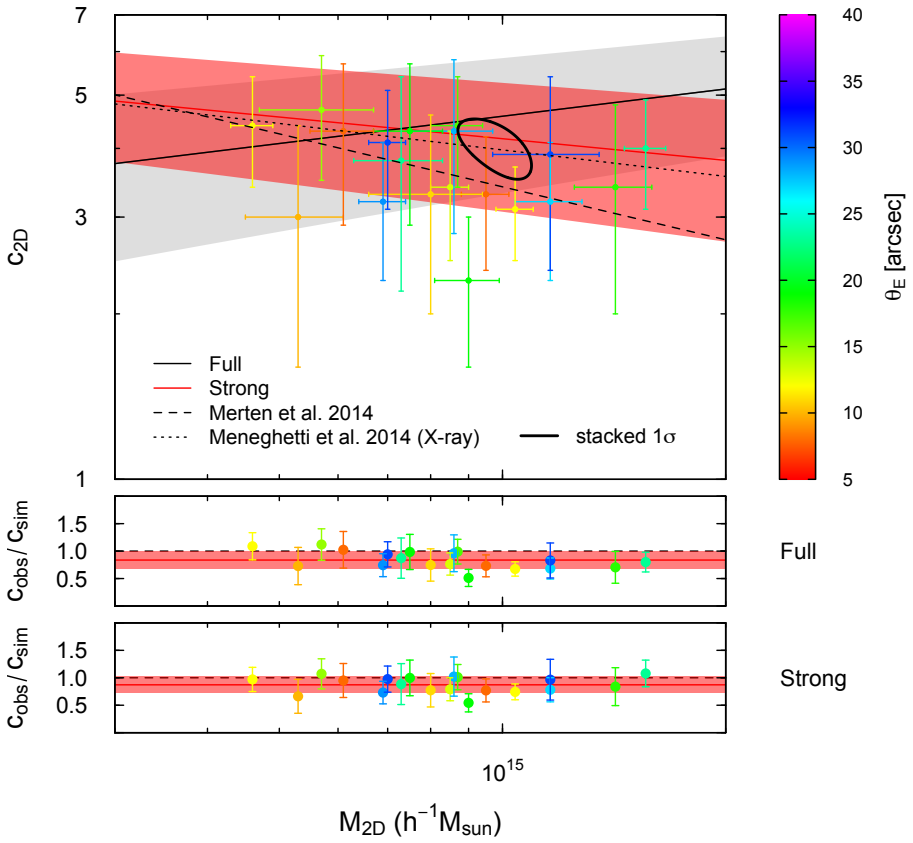

Figure 6.2: A comparison between the CLASH clusters and the $c - M - z$ relations of the 1000 *all-sky* realizations. The points and error bars represent the concentration-mass analysis presented by Merten et al. (2015) with color coding according to the measured θ_E. The black solid line corresponds to the $c - M - z$ relation of the *all-sky* full sample, while the red solid line corresponds to the relation of a *all-sky* θ_E-selected sample. The grey and red contours indicate the 1σ level of the full and strong samples, respectively. The $c - M - z$ relation obtained by Merten et al. (2015) over the CLASH clusters is shown by the dashed black line. The $c - M - z$ relation derived by Meneghetti et al. (2014) for a X-ray selected sample from the MUSIC-MD dataset correspond to the dotted black line. The black thick contours encircle the 68% confidence level of the concentration-mass analysis of Umetsu et al. (2014) for a redshift of $z \simeq 0.35$. The bottom panels shows the ratio between the observed concentration value and the value predicted by the $c - M - z$ relations of the *all-sky* full and the θ_E-selected samples. The red lines indicate the mean of this ratio and the red shaded region defines the 1σ level of confidence.

Table 6.2: Fitting parameters for the $c - M - z$ relation in Eq. 4.6 of the different samples: *all-sky* full sample, *all-sky* θ_E-selected sample and the observed data from Merten et al. 2015.

sample	A	B	C	σ
full	4.41 ± 0.02	-0.05 ± 0.01	0.165 ± 0.004	1.26
strong	4.30 ± 0.03	0.18 ± 0.02	-0.131 ± 0.005	1.10
CLASH	3.66 ± 0.16	-0.14 ± 0.52	-0.32 ± 0.18	1.17

To statistically quantify the agreement with the different subsamples we calculate the mean ratio $\langle c_{obs}/c_{sim} \rangle$. For the full sample, the mean ratio is $\langle c_{obs}/c_{sim} \rangle = 0.84 \pm 0.16$. In the case of the strong lensing, the mean ratio is slightly higher, with $\langle c_{obs}/c_{sim} \rangle = 0.87 \pm 0.15$. Therefore, after taking into account projection and selection effects, we do not evidence any disagreement between the observed and the theoretical $c - M - z$ relations. Overall, the $c - M - z$ relation for the strong lensing selected sample is in better agreement with the CLASH $c - M - z$ relation derived by Merten et al. (2015) than the $c - M - z$ relation for the full sample. This is not surprising given that X-ray selected halos of the MUSIC-MD dataset are frequently efficient strong lenses, with only $\sim 8\%$ of them which do not have an extended critical line (see Meneghetti et al. 2014 for further details on the X-ray election criteria). Besides, the strong lensing $c - M - z$ relation shows a declining shape, but slightly flatter than the observed relation.

To confirm our results with another concentration-mass analysis, which is not fully independent but different in its methodology, we over plot in Fig. 6.2 the $c - M$ contour at the 1σ confidence level from Umetsu et al. (2014). This contour is derived from the stacked analysis of 16 CLASH X-ray selected clusters. Although the stacked result lies slightly above the value from our full $c - M - z$ relation, it is in good agreement with our results for the strong lensing $c - M - z$ relation given the uncertainties in both analysis.

6.3 The SDSS Clusters

Zitrin et al. (2012a) presented the results from the strong lensing modeling of 10000 SDSS clusters in the range $0.1 < z < 0.5$, finding that the observed gravitational lenses might be stronger than theoretically expected. The method proposed

by Zitrin et al. (2012a) is based on the assumption that the light distribution observed in galaxy clusters generally traces their mass distribution. The red cluster member galaxies represent the galaxy component of the mass distribution, while the dark matter component is constructed by smoothing the distribution of galaxies with a two-dimensional cubic spline interpolation. The contribution of the two components serves as an indicator for the total projected matter density map of the cluster. The crucial point of the method is the calibration of the mass-to-light ratio, which is based on a subsample of ten well-studied SDSS galaxy clusters that were covered by high-quality HST images. Using this procedure, Zitrin et al. (2012a) blindly processed the 10000 SDSS clusters, derived simple lens models from the photometry of the cluster member galaxies and estimated the corresponding Einstein radii for sources at redshift $z_s = 2.0$.

In Fig. 6.3 the green region shows the redshift distribution of the 10000 SDSS clusters analyzed in Zitrin et al. (2012a). We also show the number of halos with $M_{200} \geqslant 2{\times}10^{14}h^{-1}M_{\odot}$ for the *low-z* catalog ($0.1 < z < 0.55$). The black line shows the mean number of halos, while the grey shaded region indicates the 2 and 98 percentile. The shaded vertical lines show the redshift analyzed from the MUSIC-MD sample, where the kernel density estimates have been computed. The redshift distribution of the SDSS clusters clearly exceeds the expectations of the mass function integration. This is notable since the SDSS DR7 covered approximately one fourth of the full sky and only 20% of the discovered clusters were analyzed in Zitrin et al. (2012a). This corresponds to 1/20 of the expected number of clusters in the considered redshift. This discrepancy could be explained in terms of the minimum mass threshold ($2{\times}10^{14}h^{-1}M_{\odot}$) adopted to produce the catalogs. However, as we have shown in sec. 4.2.2, clusters with $M_{200} \lesssim 2{\times}10^{14}h^{-1}M_{\odot}$ are not strong enough to produce large Einstein radius and should not strongly impact the Einstein radii distributions. Nevertheless, our estimates should in principle exceed the distribution of Einstein radii of the subsample of SDSS clusters.

We compare the results presented by Zitrin et al. (2012a) with the theoretically expected order statistics of the largest Einstein radii in the *low-z* catalog, which contains clusters within the same redshift range as the 10000 SDSS clusters ($0.1 < z < 0.55$). In Fig. 6.4, we show a boxplot which contains information on the Einstein radii distribution of each order statistics obtained with our model for the *low-z* catalog. We present the same order statistics obtained for the 10000 SDSS clusters in Zitrin et al. (2012a), along with the recent results obtained analytically

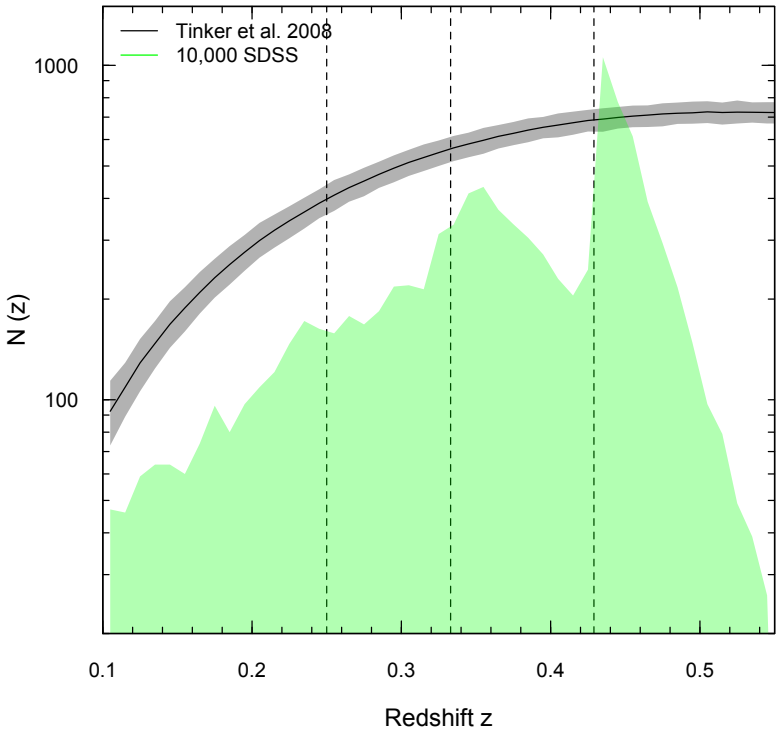

Figure 6.3: Mean number of halos (above $M_{200} \geqslant 2{\times}10^{14} h^{-1} M_{\odot}$) as a function of redshift for the *low-z* catalog (black line). The shaded region in grey corresponds to the 2 and 98 percentile of the 1,000 realizations. The green shaded region shows the redshift distribution of the 10000 SDSS clusters from Zitrin et al. (2012a). Note that the total number of clusters analyzed in that work correspond to approximately 1/20 of the full-sky coverage (black line). The vertical dashed lines show the redshift where the kernels have been computed (see sect. 5.1).

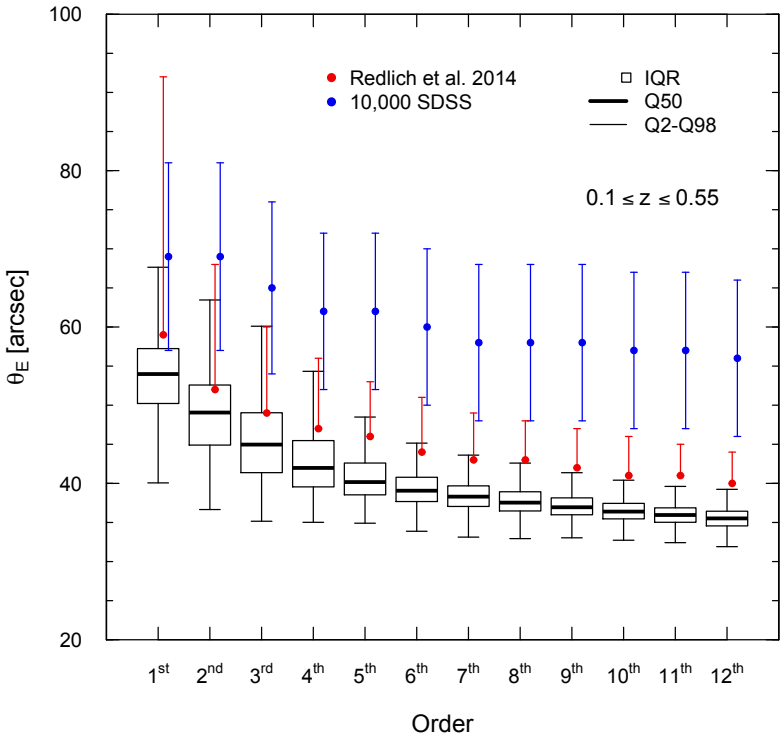

Figure 6.4: Boxplot comparing the expected order statistics of the 12 largest Einstein radii en the *low-z* catalog. Black boxes correspond with the results obtained in this work, while red and blue points correspond to the results reported in Redlich et al. (2014) and Zitrin et al. (2012a), respectively.

by Redlich et al. 2014 (see Sec. 2.3.2). Although the uncertainties of the method used by Zitrin et al. (2012a) are significant (at least $\sim$ 17% for the 1σ boundary), the gravitational lenses observed at low redshifts are stronger than our expectations.

As can be clearly seen in Fig. 6.4, the distribution of the largest Einstein radii obtained with *MAPLENS* is below the distribution presented by Redlich et al. (2014) ($\sim$ 10% lower for all the 12 orders analyzed), but showing a similar trend. In particular, the 98 percentile of the 1st order statistics presented by Redlich et al. (2014) is $\sim$ 90 arcsec, while we expect the 98 percentile to be $\sim$ 68 arcsec. We will investigate the impact of the halo triaxiality on the order statistics of Einstein radii derived with semi-analytic models in Sec. 6.3.1.

For a more detailed comparison, in Fig. 6.5 we present the Einstein radii distributions in different redshift bins. The blue histograms correspond to the

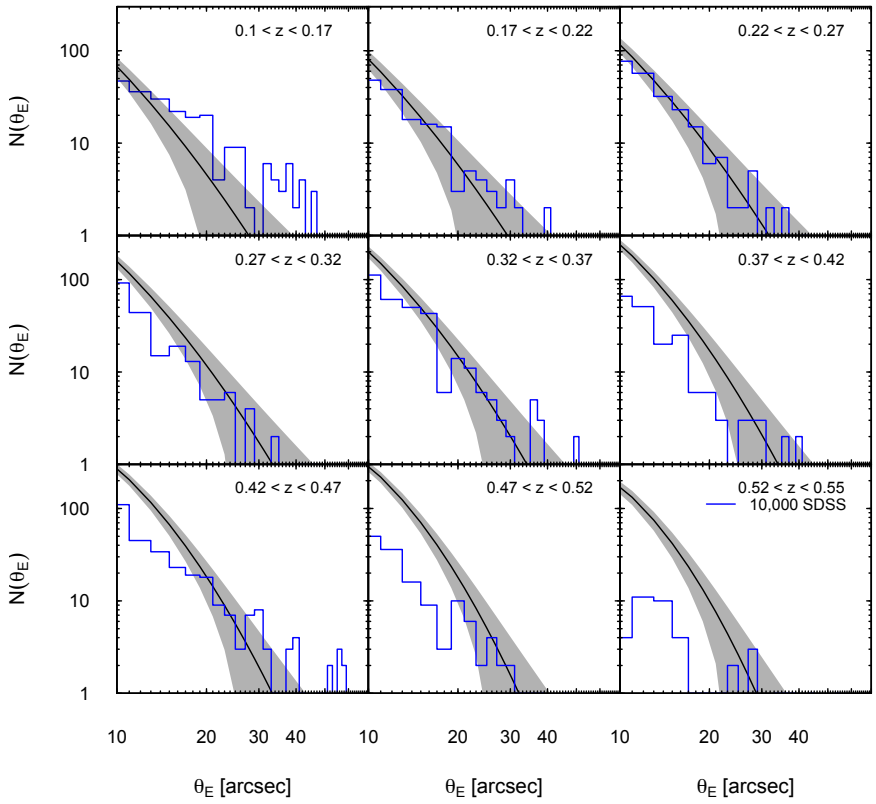

Figure 6.5: *All-sky* Einstein radii distributions ($z_s = 2.0$) for clusters with $0.1 < z < 0.55$ in different redshift bins. Black lines correspond to the mean number of Einstein radii as function of θ_E, while the shaded regions show the 2-σ levels of the distribution. In each frame, we also show the Einstein radii distributions of the 10000 SDSS clusters (blue histograms).

10000 SDSS clusters, while the black lines are the expectations of the Einstein radii distributions obtained with the *universal* distribution given by Eq. 5.3. The largest discrepancies are found for clusters at the lowest redshift bin ($0.1 < z < 0.17$). At this redshift bin, there is large number of strong lenses in the SDSS with $\theta_E \gtrsim 30$". Despite the lowest redshift bin, there is a good overall agreement between observed and theoretical Einstein radii distributions. After accounting for projections effects and including the mass variance through the 1000 *all-sky* realizations, we did not find statistical evidences for claiming that the Einstein radii distribution of the 10000 SDSS clusters exceed the theoretical expectations of the ΛCDM cosmological model. Given the large uncertainties of the method used by Zitrin et al. (2012a), it could be interesting to carefully re-analyze the SDSS sample, particularly focusing on the strongest lenses in this sample.

6.3.1 Impact of triaxiality on the largest Einstein radii

The discrepancy between theoretical and observed order statistics of Einstein radii may be reconciled with a more detail characterization of galaxy clusters. As already described in Sec. 5.4, the triaxiality of lensing galaxy clusters has a substantial impact on the distribution of the largest Einstein radii (also discussed in Waizmann et al. 2012, 2014). For clusters with $0.1 < z < 0.55$, we find that the mean ellipticity of the critical lines of the 12 order statistics of the largest Einstein radii is below ~ 0.55. In particular, the maxima Einstein radii (1st order) have critical lines with $\epsilon_\theta \lesssim 0.3$ on average, indicating that large tangential critical curves are due to elongated (also massive and concentrated) clusters, which their major axis directly points towards the observer (Fig. 5.8).

The semi-analytic models designed to derive the Einstein radii distribution by galaxy clusters (as those describes in Sec. 2.3.2) generally described the mass distribution by a triaxial model as proposed by Jing & Suto (2002) (thereafter JS02). The results presented in JS02 are based on simulations with 512^3 particles in a 100 Mpch^{-1} box, which contained hardly any halo above $10^{14}h^{-1}\mathrm{M}_\odot$, and some higher resolutions runs which provided only 12 halos with more than 10^6 particles. Therefore, arc statistics of galaxy clusters inferred by the methods proposed by Giocoli et al. (2012a) and Redlich et al. (2012) rely on extrapolations from lower mass halos. In particular, small values of the sampled axis ratios from the JS02 procedure will potentially propagate into extreme strong lensing events. In order

to study the impact of the triaxiality, Waizmann et al. (2012) introduced a cut-off in the distribution of axis ratios of JS02 to remove extreme axis ratios. Waizmann et al. (2012) found that the impact of the tail of the axis ratio distribution on the largest Einstein radii distribution is substantial. Besides, highly elongated halos exhibit small values of the concentration parameter. Thus, the largest Einstein radii either stem from lowly concentrated very elongated halos or from lies elongated but higher concentrated ones. However, due to the limited knowledge of the statistics of extremely small axis ratios, it is not possible to clearly define a proper choice of the cut-off (if present) until the triaxiality distributions of large halo samples (up to cluster masses) are studied in numerical simulations.

More recent works have analyzed larger simulated datasets like the Millennium XXL simulation (Bonamigo et al., 2015) using an halo mass cut $M > 10^{14} h^{-1} M_{\odot}$. Dark matter haloes are triaxial with a tendency of being prolate and, in particular, that more massive objects are less spherical. In addition, Bonamigo et al. (2015) found that unrelaxed halos have the effect of artificially increasing the axis ratios. In order to obtain accurate strong leasing estimates, we consider essential to implement the semi-analytic models with these updated prescriptions on the triaxial shape of dark matter halos, particularly in the cluster mass range.

In Fig. 6.6, we show the minor-to-major axis ratios s_{2500} for the MUSIC-MD clusters measured at an overdensity of $\Delta = 2500\rho_{crit}$ as a function of the virial mass. As we compute the axis ratio from the inertia tensor with a spherical window, we convert between spherical axis ratios using Eq. A.4 (see Appendix A for a description of the methods used for determining the halo shapes). From this figure, we conclude that MUSIC-MD clusters are slightly more spherical than predicted by JS02. Besides, the dispersion in the axis ratio distribution of the MUSIC-MD dataset is smaller than the JS02 value of $\sigma_s = 0.113$. We find only a small fraction of clusters exceeding the 1σ levels derived by JS02. Therefore, extending the axis ratio probability distributions derived by JS02 to higher masses will produced very elongated halos that strongly affect the order statistics of the largest Einstein radii. The differences observed in Fig. 6.4 for the largest Einstein radii between this work and the results presented in Redlich et al. (2014), are probably due to the different axis ratios distributions in both works. Besides, the impact of the triaxiality should always be discussed together with that of the concentration, as the concentration used in semi-analytic models is strictly related to the axis ratio of the halos (Jing & Suto, 2002).

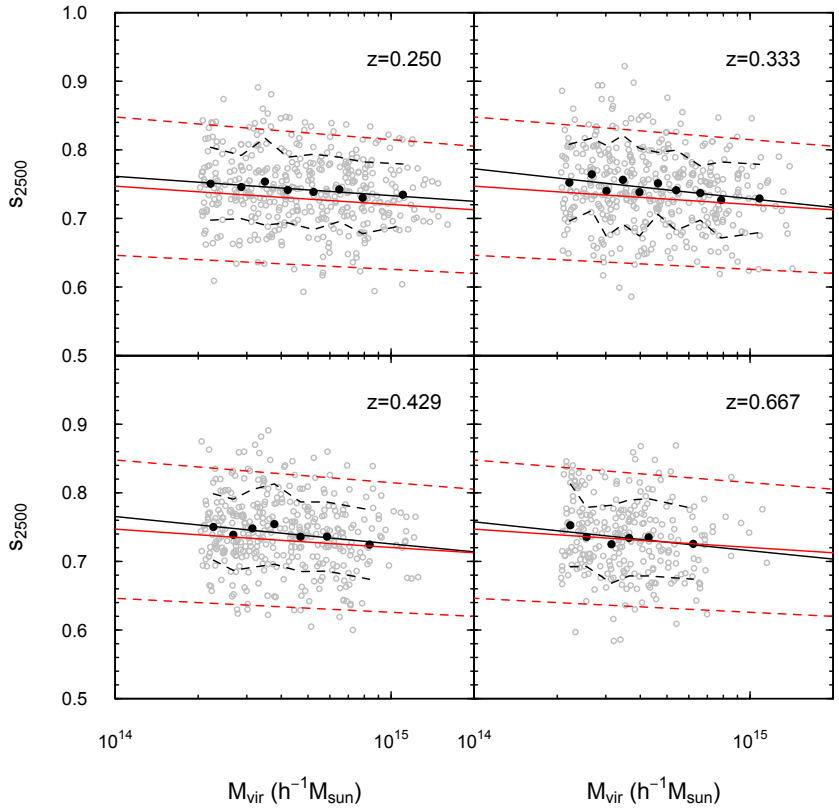

Figure 6.6: Axis ratio s_{2500} measured at $\Delta = 2500\rho_{crit}$ as a function of the virial mass for all the halos in the MUSIC-MD dataset. The grey open circles show the individual axis ratios of the MUSIC-MD clusters. The black solid circles correspond to the running means in different mass bins, while the dashed black lines indicate the 1σ level in each mass bin. The black lines show the linear best-fit to the data points in the different redshifts bins. The red lines show the relation found by JS02 with the 1σ dispersion (dashed red lines).

CHAPTER 7

Conclusions and future projects

In this thesis we have reported a study of galaxy clusters employing high resolution hydrodynamical simulations, the MUSIC dataset. The MUSIC sample is at present the largest available dataset of high resolution SPH hydrodynamical simulations of clusters, comprehending more than 700 clusters and 2000 groups. We focused our analysis on the MUSIC-MD dataset, a sample including more than 500 objects with $M_{vir} > 10^{14}\ h^{-1}M_{\odot}$ at $z = 0$, simulated using WMAP7 + BAO + SNI cosmological parameters ($\Omega_M = 0.27$, $\Omega_b = 0.0469$, $\Omega_\Lambda = 0.73$, $\sigma_8 = 0.82$, $n = 0.95$, $h = 0.7$, Komatsu et al. 2011). Although MUSIC-MD clusters have been simulated using radiative and non-radiative physics, we specifically investigate the properties of cluster-size halos extracted from the non-radiative run of the MUSIC-MD dataset.

We have taken advantage of the large statistics and of the high resolutions provided by our simulated dataset to explore many global properties of galaxy clusters, particularly those derived from a gravitational leasing analysis. We investigated the mass distribution in galaxy clusters and its evolution with redshift through their density and surface-density profiles. In order to increase the statistics and to take into account projections effects, we analyzed 500 line-of-sight for each each galaxy cluster in the MUSIC-MD dataset. From the NFW fits to the density and surface-density profiles, we derived the concentration-mass relations in 3D and 2D, respectively, and investigated their evolution with redshift. Under the assumption of spherical symmetry, we computed the *equivalent* Einstein radii. In addition, we produced two-dimensional convergence and shear maps for each line-of-sight using the *Skylens* lensing simulation pipeline described in Meneghetti et al. (2014).

We computed the tangential critical line and derived the *effective* Einstein radius and the its ellipticity from these maps. We presented Einstein radii distributions of the MUSIC-MD dataset and characterized the systematics affecting the models for axially symmetric lenses, such as the NFW model.

The main topic of this thesis has been the development of MAPLENS, a semi-analytic model to infer the Einstein radii distribution from a sample of dark matter halos. MAPLENS is based on the analysis of distinct cluster-size halos from the MUSIC-MD dataset. By means of kernel density estimates, MAPLENS accounts for projections effects to derive realistic Einstein radius. As a test to the procedure, we presented the results of the Einstein radii distribution for 500 *Monte Carlo* realizations of the halos in $(1h^{-1}\mathrm{Gpc})^3$ box volume, equivalent to the MUSIC-MD simulated volume.

Using MAPLENS, we extended our predictions on the Einstein radii distributions and the concentration-mass relations for a realization of dark matter halos considering *full-sky* coverage. The halo mock catalogs are generated in the redshift range $0.1 < z < 1.0$ using a Tinker et al. (2008) mass function and the same cosmological parameters as for the MUSIC-MD dataset. We derived the *effective* Einstein radii for 1000 *all-sky* realizations and presented a fitting function to the *all-sky* Einstein radii distribution. To better understand the Einstein radii distribution from both theoretical and observed estimates, we described an analysis based on the extreme value statistics (EVS) of Einstein radii.

Finally, we investigated whether the tension between observed $c - M$ relations in lensing cluster samples and the ΛCDM paradigm may be reconciled with a proper treatment of the projection and selection effects. We presented a detailed comparison between our theoretical predictions and the most recent observations of galaxy clusters, such as the SGAS survey and the CLASH sample. In addition, we compared the order statistics of the largest Einstein radii of 10000 SDSS clusters and the *all-sky* realizations obtained with MAPLENS.

Our main results are summarized as follows:

- The NFW model is sufficiently accurate to constrain the Einstein radii distribution when combining the results derived from the surface density profiles with the convergence and shear maps obtained by ray-tracing techniques.

- The masses recovered from the fits to the density profiles are in good agreement with the true masses. The M_{3D} of un-relaxed halos deviate more from the true masses than the relaxed (or super-relaxed) halos. The mean ratios M_{3D}/M_{true} are ~ 0.98 (with $\sigma = 0.06$) and ~ 0.95 (with $\sigma = 0.12$) for super-relaxed and un-relaxed halos. respectively.

- We found a modest negative bias of $\sim 5\%$ on the mass estimates from the fit to the surface-density profiles of galaxy clusters from the MUSIC-MD dataset. This is due to the prolate shape of the clusters, which are more frequently elongated on the plane of the sky than along the line of sight. The two-dimensional masses of the halos in equilibrium are in good agreement with the true masses. The best agreement is obtained for the super-relaxed halos with a negative bias $\lesssim 2\%$. As halos deviate from the equilibrium, the two-dimensional masses deviates from the true masses, also increasing the scatter of the data.

- The c_{2D} are over-estimated with respect to the c_{3D} for halos with larger true masses (especially un-relaxed halos), while they under-estimated for less massive halos. For relaxed systems c_{2D} is well recovered without any bias ($< 1\%$). The concentration is more influenced than the mass by the triaxiality and the presence of substructures when projecting the cluster mass along the line-of-sight.

- The 3D concentration-mass relation for the full MUSIC-MD sample scales with mass as $c \propto M^{-0.081\pm0.014}$. This relation is also depends on the halo dynamical state. The normalization of our $c - M - z$ relation increases by $\sim 9\%$ for the relaxed subsample with respect to the full sample.

- The 2D concentration-mass relation for MUSIC-MD clusters shows a slightly positive logarithmic slope ($C = 0.144$ for the full sample). The redshift dependence of the 2D $c - M$ relations is almost negligible, but larger for the un-relaxed and super-relaxed systems.

- The masses and concentrations derived by fitting the surface density profiles tend to be smaller than those directly measured by fitting the density profiles of the MUSIC-MD clusters. The concentration bias is reduced for massive halos, with 2D concentrations taking larger values than the 3D ones.

- The largest Einstein radii are found when a prolate, massive and/or concentrated halo is seen along its mayor axis, producing almost circular tangential critical lines. θ_{proj} is over-estimated with respect to θ_E with average differences $\sim$ 5% for projections with $\epsilon_\theta \leqslant 0.60$. In contrast, elongated critical lines ($\epsilon_\theta \geqslant 0.60$) have the largest differences between the θ_{proj} and θ_E estimates, as the assumption of spherical symmetry starts to fail. In the case of no-equilibrium halos, we found larger differences between θ_{proj} and θ_{NFW} (and consequently between θ_{NFW} and θ_E) for un-relaxed halos, as the NFW profile fails on giving a good description of the mass distribution in these objects.

- The sampled parameters, M_{2D} and c_{2D}, obtained with MAPLENS are in excellent agreement with the simulated MUSIC-MD dataset. Einstein radii distributions obtained with MAPLENS are at 1% level for $\theta_E > 10$", probing the validity of the kernel density estimates on recovering correlated variates (such as the *effective* Einstein radius) by means of MC realizations.

- The lensing properties of galaxy clusters obtained with MAPLENS account for the overall distribution in the parameter space at which the kernel density estimates are constructed. This happens even without assuming any scaling function relating the properties of the input halos. The sampled Einstein radii distributions recovered with MAPLENS account for the projection effects (i.e., the intrinsic triaxial shape, the presence of substructures along the line of sight and mergers) in the MUSIC-MD dataset, even though there is no explicit information on the dynamical state of the input halos.

- The fitting function to the *all-sky* Einstein radii distribution shows a maximum separation to the fitted data of $\lesssim$ 20% for $\theta_E \geqslant 10$" and $\lesssim$ 10% for lenses with $\theta_E \geqslant 25$". The measured dispersion in the number of Einstein radii is gaussian, i.e. $\sigma_N = \sqrt{N}$.

- The best fitting parameters of the *all-sky* general extreme value (GEV) distribution (Eq. 5.7) for clusters at $0.1 < z < 0.55$ are given by (α, β, γ) = (51.66 ± 0.10, 5.1 ± 0.15, 0.00 ± 0.03). For clusters at $0.5 < z < 1.0$ the best fitting parameters of the GEV distribution are given by (α, β, γ) = (36.25 ± 0.05, 2.54 ± 0.07, 0.03 ± 0.03). As expected, all the largest Einstein radii ($\theta_E \geqslant 45$") are produced by massive clusters with $M_{200} > 10^{15} h^{-1} M_\odot$ at 0.35

< z < 0.4. The mean ellipticity of the critical lines increases from 0.25 to 0.55 with increasing the order statistics.

- In Meneghetti et al. (2014) we showed that the concentrations of CLASH clusters derived by Merten et al. (2015) are in good agreement with theoretical predictions from the MUSIC-MD dataset, after accounting for projections and selection effects. In that work we found that simulated halos which resemble the X-ray morphologies of the CLASH clusters are composed mainly by relaxed halos ($\sim$ 70%). Merten et al. (2015) found an excellent agreement between the CLASH concentrations and the results derived from the lensing analysis of the MUSIC-MD dataset.

- The SGAS sample (Oguri et al., 2012), although slightly over-concentrated, is consistent within errors with the theoretical predictions of MAPLENS for a strong lensing selected sample of halos in the redshift range $0.25 \lesssim z \lesssim 0.70$.

- We did not find any significant disagreement between the observed $c - M$ relation for the CLASH sample (Merten et al., 2015) and the theoretical relations of MAPLENS, after accounting for projections and selection effects. For the full *all-sky* sample the mean ratio is $\langle c_{obs}/c_{sim} \rangle = 0.84 \pm 0.16$. In the case of the *all-sky* θ_E-selected sample the mean ratio is slightly higher, with $\langle c_{obs}/c_{sim} \rangle = 0.87 \pm 0.15$. The strong lensing sample is in better agreement with the observed $c - M$ relation because the X-ray selected halos of the MUSIC-MD dataset are frequently efficient strong lenses (Meneghetti et al., 2014).

- The gravitational lenses analyzed by Zitrin et al. (2012a) over 10000 SDSS clusters are stronger than our expectations for clusters at $0.1 < z < 0.55$. The largest discrepancies are found for clusters at the lowest redshift bin ($0.1 < z < 0.17$). After accounting for projections effects and including the mass variance through the 1000 *all-sky* realizations, we did not find statistical evidences for claiming that the Einstein radii distribution of the 10000 SDSS clusters exceed the theoretical expectations of the ΛCDM cosmological model. Given the large uncertainties of the method used by Zitrin et al. (2012a), it could be interesting to carefully re-analyze the SDSS sample, particularly focusing on the strongest lenses in their sample.

- The triaxial shape of lensing galaxy clusters has a substantial impact on the distribution of the largest Einstein radii. For clusters with $0.1 < z < 0.55$ we

find that the mean ellipticity of the critical lines of the 12 order statistics of the largest Einstein radii is below $\epsilon_\theta \lesssim 0.55$. In particular, the maxima Einstein radii (first order) have critical lines with $\epsilon_\theta \approx 0.3$ on average.

- The clusters in the MUSIC-MD dataset are (on average) slightly more spherical and show smaller dispersion in the axis ratio distribution than the results of JS02. Therefore, extending the axis ratio probability distributions derived by JS02 to higher masses, as it has been done in previous semi-analytic models, will produced very elongated halos, which strongly affect the order statistics of the largest Einstein radii.

- The discrepancy between the *all-sky* expectations of MAPLENS for clusters at $0.1 < z < 0.55$ and the results presented in Redlich et al. (2014) on the largest Einstein radii can be explained in terms of the different axis ratio distributions of the clusters assumed in each work.

7.1 Future projects

As the implementation of baryonic physics in simulations will not lead to a significant change in the gravitational lensing properties (Killedar et al., 2012), the work presented in this thesis was based on the non-radiative run of the *MultiDark Simulation*. Nevertheless, baryonic physics contributes to shape the cluster density profile in the inner regions due to to the competing effects of cooling and feedback processes (Rozo et al., 2008; Duffy et al., 2010; De Boni et al., 2013). The cooling of baryons consequently leads to more concentrated halos in the inner regions. Therefore, the $c - M$ relation after this adiabatic contraction is steeper than the theoretical expectations for dark-matter only simulations. On the other hand, other baryonic processes mitigate the effects of contraction. As demonstrated by other hydrodynamical simulations (see Planelles et al. 2013 for a good example), the introduction of AGN feedback in the simulations prevents the gas to be excessively convert into stars and, at the same time, lowers the baryon fraction in the inner region of clusters. The counter-balancing actions of cooling and feedback are still under debate. They have to be included in a consistent way that accounts at the same time for a steep $c - M$ relation and for the observed stellar fraction in clusters of galaxies (Duffy et al., 2008).

To this scope, the MUSIC-MD clusters have been resimulated including AGN

feedback in collaboration with the Numerical Cosmology group of the University of Trieste (Italy). The model for AGN feedback is based on the original implementation presented by (Springel et al., 2005), with some technical modifications described in Planelles et al. (2013). In an ongoing project, we plan to implement the MAPLENS code presented in this thesis with the new simulations of the MUSIC-MD dataset including AGN feedback.

In a recent paper, Sereno et al. (2015a) estimated the systematic errors in the measurement of mass and concentration made by fitting Einasto-like shear profiles with NFW models. Even though the NFW fits of observed tangential shear profiles can be excellent, viral masses and concentrations of very massive halos ($\gtrsim 10^{15} h^{-1}\mathrm{M}_{\odot}$) can be over- and under-estimated by $\sim 10\%$, respectively. Therefore, we will increased MAPLENS flexibility by including in the kernel density procedure the masses and concentrations derived from the fit to the mass (and surface mass) density profiles with a *Einasto* profiles.

As we have repeatedly mentioned in the work presented in this thesis, the abundance of gravitational lensing events, such as gravitational arc and multiple images, depends on cosmology through the angular-diameter distances and throughout structure formation, Moreover, as a consequence of the link with the halo assembly history, the $c - M$ relation strongly depends on the cosmological framework. The normalization of the power spectrum σ_8 and dark matter content strongly affect the overall amplitude and shape of the $c - M$ relation (Diemer & Kravtsov, 2014). Therefore, the accurate knowledge of cosmological parameters is crucial to predict the relation between masses and concentration, and to estimate the arc statistics by galaxy clusters at the level requires for precision cosmology. At the time of writing this thesis dissertation, a new dataset of galaxy clusters with the updated Planck cosmology (Planck Collaboration et al., 2015) is almost completely resimulated. Following the same procedure as described in this thesis, we will explored the lensing properties of simulated galaxy clusters in the Planck era for cosmology based on this new dataset.

In a ongoing project, the triaxial shape of dark matter halos will be investigated over five orders of magnitude in mass. For this purpose, we will analyze cluster-size halos extracted from the *Huge-MultiDark* simulation (a dark-matter only simulation in a $(4h^{-1}\mathrm{Gpc})^3$, see Appendix A for a brief description). In order to extend our limits on mass, we will use a set of three simulations with smaller simulated volumes: $(0.4, 1.0, 2.5\ h^{-1}\mathrm{Gpc})^3$. From these simulations, we aim to

provide predictions for the shape of dark matter halos from $\sim 10^{11}h^{-1}\mathrm{M}_{\odot}$ to $\sim 4\times10^{15}h^{-1}\mathrm{M}_{\odot}$. The simulations investigated in this work have been performed with Planck cosmological parameters (Table 1.1).

In addition, the huge potential of the MUSIC-MD dataset have been source of a lot of other applications. In Sembolini et al. (2013b,a), the MUSIC-MD dataset were used to explore the baryon budget and the calibration of scaling relations. Motivated by the most recent SZ surveys (such as ACT, SPT and Planck), they particularly focused on the study of the validity of the self-similar model and the calibration of the $Y - M$ scaling relation. X-ray temperatures and luminosities were used to investigate the relation to the total cluster mass and the SZ properties. Moreover, Sembolini et al. (2014) extended this analysis to protoclusters, the high redshift progenitors of the present massive clusters in the MUSIC-MD dataset.

Conclusiones y proyectos futuros

En esta tesis de Doctorado hemos presentado un estudio de cúmulos de galaxias utilizando para ello la base de datos MUSIC de simulaciones hidrodinámicas de alta resolución. MUSIC constituye el conjunto de simulaciones numéricas hidrodinámicas de cúmulos de galaxias más grande realizado hasta la fecha, comprendiendo más de 700 cúmulos y mas de 2000 grupos de galaxias. En concreto, en este trabajo nos hemos centrado en el análisis de los cúmulos dentro de la base de datos MUSIC-MD, la cual incluye más de 500 objetos con masas $M_{vir} > 10^{14}\ h^{-1}M_{\odot}$ a $z = 0$, simulados con los parámetros cosmológicos que mejor ajustan a WMAP7 + BAO + SNI ($\Omega_M = 0.27$, $\Omega_b = 0.0469$, $\Omega_\Lambda = 0.73$, $\sigma_8 = 0.82$, $n = 0.95$, $h = 0.7$, Komatsu et al. 2011). Los cúmulos de galaxias extraídos de MUSIC-MD han sido resimulados, por una parte, asumiendo únicamente calentamiento radiativo del gas por efecto gravitacional y, por otra, incluyendo procesos físicos radiativos (tales como enfriamiento radiativo, formación estelar, etc.). No obstante, hemos investigado específicamente las propiedades de los cúmulos de galaxias extraídos de la simulación no-radiativa (o adiabática).

Aprovechando la enorme estadística y la alta resolución de las simulaciones MUSIC-MD, hemos explorado las propiedades globales de cúmulos de galaxias, en particular, las que se derivan de un análisis basado en el efecto de lente gravitacional. Hemos estudiado la distribución en masa en cúmulos de galaxias y su evolución con el desplazamiento al rojo a partir de los perfiles de densidad de masa y de masa superficial. Con el objetivo de incorporar posibles efectos de proyección, hemos analizado 500 proyecciones aleatorias a lo largo de la línea de visión para cada cúmulo de galaxias en MUSIC-MD. Por medio de un ajuste de los perfiles con un modelo NFW es posible derivar las relaciones concentración-masa en 3D y 2D, así como su evolución con el desplazamiento al rojo. Bajo la aproximación de

simetría esférica axial, hemos estimado el tamaño del anillo de Einstein *equivalente*. Adicionalmente, creamos mapas en 2D de convergencia y *shear* para cada una de las 500 proyecciones haciendo uso del código de *ray-tracing*. En concreto, hemos utilizado *Skylens*, un código fundamentalmente pensado para reproducir los efectos de lente gravitacional en cúmulos de galaxias simulados (Meneghetti et al., 2014). A partir de los mapas producidos con *Skylens* hemos calculado la posición de la línea tangencial crítica, su elipticidad y el tamaño del anillo de Einstein *efectivo*. Para concluir la primera parte de esta tesis, hemos presentado las distribuciones de anillos de Einstein de MUSIC-MD y caracterizado los errores sistemáticos debidos los modelos de lentes con simetría axial, como el modelo NFW.

El tema principal de esta tesis ha sido el desarrollo del modelo MAPLENS, un código semi-analítico especialmente construido para estimar la distribución de anillos de Einstein a partir de una muestra de cúmulos de galaxias. MAPLENS está basado en el análisis de los cúmulos de galaxias identificados en el catálogo MUSIC-MD. Haciendo uso de la técnica denominada *kernel density estimates*, MAPLENS incorpora los efectos de proyección para obtener una estimación más realista del tamaño del anillo de Einstein. A modo de prueba, hemos presentado los resultados obtenidos con MAPLENS para la distribución de anillos de Einstein en una caja con un volumen igual a $(1h^{-1}\mathrm{Gpc})^3$, equivalente al volumen simulado a partir del cual se extraen los cúmulos de MUSIC-MD.

En la segunda parte de esta tesis hemos presentado los resultados obtenidos con MAPLENS sobre la distribución de anillos de Einstein y las relaciones concentración-masa para una muestra de halos de materia oscura obtenida a partir de la función de masa propuesta por Tinker et al. (2008). Más concretamente, hemos generado 1000 muestras con el número de halos medio en todo el cielo (con masas en el rango de los cúmulos de galaxias y $0.1 < z < 1.0$) y con los mismos parámetros cosmológicos que los usados para generar las simulaciones MUSIC-MD. Hemos derivado las distribuciones de anillos de Einstein para todo el cielo y presentado una función *universal* que reproduce dichas distribuciones con errores inferiores al 20% en todo el rango en desplazamiento al rojo analizado. Complementariamente, con la intención de comparar la distribución de anillos de Einstein teórica y observada, hemos presentado un análisis basado en la estadística de valores extremos (EVS) de las distribuciones de anillos de Einstein.

Finalmente, en la última parte de esta tesis, hemos investigado hasta qué punto la tensión entre las relaciones $c - M$ observadas en catálogos de cúmulos de galaxias

y las obtenidas teóricamente dentro del modelo cosmológico ΛCDM puede ser mitigada cuando se tienen en cuenta tanto los efectos de proyección, como los de selección de un modo apropiado. Hemos presentado una comparación detallada entre nuestras predicciones teóricas y las observaciones de cúmulos de galaxias más recientes, tales como la muestra SGAS y el catálogo CLASH. Asimismo, hemos comparado la estadística de grandes anillos de Einstein para la muestra de 10000 cúmulos de galaxias del SDSS y para las estimaciones obtenidas con MAPLENS para todo el cielo.

A continuación enumeramos los principales resultados derivados de este trabajo de tesis:

- El modelo NFW es lo suficientemente preciso para describir la distribución de anillos de Einstein al nivel requerido para por este trabajo, cuando se combinan los resultados obtenidos a partir de los perfiles de densidad superficial de masa con los mapas de convergencia y *shear* producidos con la técnica de *ray-tracing*,

- Las masas obtenidas de los ajustes a los perfiles de densidad concuerdan con las masas *reales* de los cúmulos de galaxias. La masas (M_{3D}) de halos no relajados derivadas de este modo difieren más de las masas reales que las masas de halos relajados o super-relajados. El cociente medio de estas masas (M_{3D}/M_{true}) es ~ 0.98 (con $\sigma = 0.06$) y ~ 0.95 (con $\sigma = 0.12$) para halos super-relajados y halos no relajados, respectivamente.

- Hemos encontrado un sesgo ligeramente negativo ($\sim 5\%$) en las estimaciones de las masas a partir del ajuste de los perfiles de densidad superficial de masa. Esta diferencia es debida principalmente a la forma triaxial de los cúmulos de galaxias, los cuales se encuentran frecuentemente proyectados con su eje mayor apuntando lejos de la línea de visión. Las masas M_{2D} derivadas para halos en equilibrio concuerdan con las masas reales. La desviación mínima de los datos se obtiene para los halos super-relajados con un sesgo negativo $\lesssim 2\%$. A medida que los halos se alejan del equilibrio, las masas M_{2D} difieren de las masas reales, incrementándose al mismo tiempo la dispersión de los datos.

- Las concentraciones c_{2D} están sobrestimadas respecto de las c_{3D} para halos de elevada masa (en particular, para halos no relajados), mientras que están

subestimadas para los halos menos masivos. La concentración se ve más afectada que la masa por los efectos producidos por la triaxialidad de los halos y por la presencia de subestructuras cuando se proyecta la masa a lo largo de la línea de visión.

- La relación concentración-masa en 3D para la muestra MUSIC-MD depende de la masa según $c \propto M^{-0.081\pm0.014}$. La normalización de dicha relación depende de estado dinámico del halo, incrementándose en $\sim 9\%$ cuando se tienen en cuenta sólo halos relajados.

- La relación concentración-masa en 2D de los cúmulos en MUSIC-MD muestra una pendiente logarítmica ligeramente positiva ($C = 0.144$, para la muestra completa). La dependencia con el desplazamiento al rojo en esta relación es prácticamente despreciable. No obstante, dicha dependencia es mayor en las muestras de halos no relajados y super-relajados.

- Las masas y las concentraciones proyectadas (o 2D) son en media inferiores que las obtenidas con los perfiles de densidad de masa (o 3D). El sesgo en la determinación de la concentración se reduce para halos masivos, mostrando concentraciones c_{2D} más elevadas que las correspondientes c_{3D}.

- Los anillos de Einstein más grandes encontrados en MUSIC-MD están producidos por halos oblongos, masivos y/o concentrados, cuyo eje mayor está proyectado a lo largo de la línea de visión y con líneas críticas tangenciales casi circulares. La estimación del anillo de Einstein según θ_{proj} está sobrestimada con respecto a θ_E con una diferencia media de $\sim 5\%$ para proyecciones con $\epsilon_\theta \leqslant 0.60$. Por otro lado, la líneas críticas más elongadas ($\epsilon_\theta \geqslant 0.60$) presentas las mayores diferencias entre las estimaciones de θ_{proj} y θ_E. Estas diferencias son debidas a que la aproximación de simetría axial considerada en el cálculo de θ_{proj} falla en el caso de líneas críticas elongadas. En el caso de halos alejados del equilibrio, las diferencias entre θ_{proj} y θ_{NFW} son todavía mayores y, por consiguiente, también lo son las diferencias entre θ_{NFW} y θ_E. Esta discrepancia se debe principalmente que el modelo NFW no reproduce adecuadamente la distribución en masa para halos no relajados.

- Las masas y las concentraciones, M_{2D} y c_{2D}, obtenidas con MAPLENS para los halos en una volumen de $(1h^{-1}\mathrm{Gpc})^3$ están en perfecto acuerdo con las estimaciones de la muestra MUSIC-MD. Las estimaciones sobre las

distribuciones de anillos de Einstein derivadas con MAPLENS difieren en menos de 1% para anillos con $\theta_E > 10$". En conclusión, estos resultados demuestran la eficacia de la técnica *kernel density estimates* para reproducir distribuciones de variables correlacionadas (como, por ejemplo, el anillo de Einstein *efectivo*) para muestras generadas según el método de *Monte Carlo*.

- MAPLENS incorpora los efectos de lente gravitacional en cúmulos de galaxias teniendo en cuenta la distribución global en el espacio de parámetros en el que se generan los *kernel density estimates*. Esta metodología elimina la necesidad de considerar *a priori* algún tipo de relación de escala que vincule las propiedades de los halos analizados con MAPLENS, diferenciando este modelo semi-analítico del resto de modelos desarrollados bata el momento. Además, las distribuciones de anillos de Einstein obtenidas con MAPLENS incorporan efectos de proyección (tales como la triaxialidad, la presencia de subestructuras y la fusión de cúmulos de galaxias).

- La función *universal* de anillos de Einstein para todo el cielo reproduce los datos con errores $\lesssim 20\%$ para $\theta_E \geqslant 10$" y $\lesssim 10\%$ para lentes con $\theta_E \geqslant 25$". La dispersion medida en el número de anillos de Einstein es de naturaleza gaussiana, es decir, $\sigma_N = \sqrt{N}$.

- El mejor ajuste a la distribución general de valores extremos (GEV) en todo el cielo (Eq. 5.7) para cúmulos de galaxias a $0.1 < z < 0.55$ se obtiene con los siguientes parámetros: $(\alpha, \beta, \gamma) = (51.66 \pm 0.10, 5.1 \pm 0.15, 0.00 \pm 0.03)$. En el caso de cúmulos a $0.5 < z < 1.0$, el mejor ajuste a la distribución GEV se obtiene para $(\alpha, \beta, \gamma) = (36.25 \pm 0.05, 2.54 \pm 0.07, 0.03 \pm 0.03)$. Como era de esperar, los anillos de Einstein más grandes ($\theta_E \geqslant 45''$) están producidos por cúmulos masivos con masas $M_{200} > 10^{15} h^{-1} M_\odot$ y desplazamientos al rojo en el rango $0.35 < z < 0.4$. La elipticidad media de las líneas críticas tangenciales aumenta a medida que aumenta el orden de la estadística de extremos, de 0.25 a 0.55 para el primer y el duodécimo ordenes, respectivamente.

- En Meneghetti et al. (2014) hemos mostrado que las concentraciones de los cúmulos CLASH son compatibles con las predicciones teóricas derivadas del análisis de los cúmulos en MUSIC-MD, una vez que se han tenido en cuenta los efectos de proyección y de selección. En Meneghetti et al. (2014) hemos encontrado que los halos simulados con morfologías en rayos X similares a los cúmulos CLASH están compuestos principalmente por halos relajados

($\sim$ 70%). Por otro lado, Merten et al. (2015) encontró un acuerdo excelente entre las concentraciones de los cúmulos CLASH y los resultados derivados del análisis del catálogo MUSIC-MD.

- La muestra SGAS (Oguri et al., 2012), aunque con concentraciones ligeramente superiores, es consistente con las predicciones teóricas obtenidas con MAPLENS para una muestra de halos seleccionados por θ_E con $0.25 \lesssim z \lesssim 0.70$.

- No hemos encontrado discrepancias significativas entre la relación $c - M$ observada para la muestra CLASH analizada por Merten et al. (2015) y las relaciones teóricas derivadas con MAPLENS. Para la muestra completa de todo el cielo, hemos estimado el valor medio del cociente $\langle c_{obs}/c_{sim} \rangle = 0.84 \pm 0.16$. Este cociente es ligeramente mayor en el caso de una muestra seleccionada por θ_E, con $\langle c_{obs}/c_{sim} \rangle = 0.87 \pm 0.15$. Esto se explica porque los cúmulos en MUSIC-MD seleccionados por la morfología en rayos X son, con frecuencia, lentes gravitacionales muy eficientes (Meneghetti et al., 2014).

- Las lentes gravitacionales analizadas por Zitrin et al. (2012a) para 10000 cúmulos de galaxias observados en el SDSS son más eficientes que las predicciones para cúmulos con $0.1 < z < 0.55$. Las mayores discrepancias se deben a los cúmulos con los desplazamientos al rojo más bajos ($0.1 < z < 0.17$). Una vez que se tienen en cuenta los efectos de proyección y la varianza en masa (por medio de las 1000 realizaciones para todo el cielo), no hemos encontrado ninguna evidencia estadística para concluir que existe una discrepancia entre la distribución de anillos de Einstein de los 10000 cúmulos de la muestra SDSS y las predicciones teóricas para el modelo cosmológico ΛCDM. No obstante, dadas las grandes incertidumbres del método utilizado por Zitrin et al. (2012a), consideramos que sería interesante re-analizar cuidadosamente la muestra SDSS, prestando particular atención en las lentes más fuertes dentro de dicha muestra.

- La morfología triaxial de los cúmulos de galaxias que actúan como lentes gravitacionales tiene un impacto considerable en la distribución de grandes anillos de Einstein. Para cúmulos con $0.1 < z < 0.55$, hemos encontrado que la elipticidad media de las líneas críticas tangenciales para los 12 órdenes de la estadística de grandes anillos es $\epsilon_\theta \lesssim 0.55$. En concreto, los anillos más grandes (primer orden) tienen líneas críticas con $\epsilon_\theta \approx 0.3$ en media.

- Los cúmulos de galaxias en el catálogo MUSIC-MD son en media ligeramente más esféricos (y con una dispersión menor en el cociente de los ejes) que lo esperado por Jing & Suto (2002). Por lo tanto, extrapolar las distribuciones del cociente de los ejes derivadas por Jing & Suto (2002) al rango de masa de los cúmulos de galaxias (como se hace en otros modelos semi-analíticos) puede producir cúmulos muy elongados que contribuyen considerablemente a la estadística de grandes anillos de Einstein.

- La discrepancia entre las predicciones para todo el cielo en la distribución de anillos de Einstein obtenidas con MAPLENS para cúmulos de galaxias con $0.1 < z < 0.55$ y los resultados presentados por Redlich et al. (2014) pueden ser explicadas en términos de la diferencia de los modelos triaxiales empleados en cada trabajo.

Proyectos futuros

Dado que la implementación de la física bariónica en simulaciones no produce cambios significativos en las propiedades de cúmulos de galaxias derivados por medio del efecto de lente gravitacional (Killedar et al., 2012), el trabajo presentado en esta tesis está basado en la versión no radiativa de la simulación *MultiDark*. No obstante, debido a la combinación de los efectos producidos por los procesos de enfriamiento y retroalimentación, la física bariónica puede modificar los perfiles de masa en las regiones más internas de los cúmulos de galaxias (Rozo et al., 2008; Duffy et al., 2010; De Boni et al., 2013). Por consiguiente, el enfriamiento de los bariones produce cúmulos de galaxias más concentrados en el núcleo. Por el contrario, otros procesos que influyen en la física bariónica pueden mitigar estos efectos de contracción. Como ha sido demostrado por medio de otras simulaciones hidrodinámicas (ver, por ejemplo, Planelles et al. 2013), la introducción de retroalimentación por AGN en las simulaciones evita que excesivas cantidades de gas se conviertan en estrellas y, al mismo tiempo, disminuye la fracción de bariones en las regiones internas de cúmulos de galaxias. Los efectos producidos por el enfriamiento radiativo y la retroalimentación están en debate todavía en la actualidad. Estos efectos deben ser incluidos de un modo consistente para reproducir una relación $c - M$ con más pendiente y la fracción de estrellas en cúmulos de galaxias (Duffy et al., 2008).

Con este objetivo en mente, los cúmulos en MUSIC-MD han sido resimulados incluyendo retroalimentación por AGN en colaboración con el grupo de Cosmología Numérica de la Universidad de Trieste (Italia). El modelo que describe la retroalimentación por AGN está basado en en la implementación original presentada por Springel et al. (2005), que incluye algunas modificaciones técnicas descritas en Planelles et al. (2013). En este sentido, estamos desarrollando un nuevo proyecto con la intención de incluir en MAPLENS las propiedades de las nuevas simulaciones MUSIC-MD con retroalimentación por AGN.

En un trabajo reciente, los autores de Sereno et al. (2015a) estimaron los errores sistemáticos en la medida de la masa y la concentración derivadas con los perfiles del tipo *Einasto* y NFW. Las masas viriales y las concentraciones de halos masivos ($\gtrsim 10^{15}h^{-1}\mathrm{M}_{\odot}$) pueden ser sobrestimadas y subestimadas en $\sim$ 10%, respectivamente. Por lo tanto, pretendemos mejorar la flexibilidad de MAPLENS incluyendo en el método basado en *kernel density* las masas y las concentraciones derivadas con perfiles del tipo *Einasto*.

Como hemos mencionado en este trabajo de tesis, la abundancia de eventos de lente gravitacional (como arcos gravitacionales y múltiples imágenes) depende de la cosmología a través de las distancias diámetro-angulares y la teoría de formación de estructuras. Además, la relación $c - M$ depende fuertemente del modelo cosmológico debido a la relación de ésta con la historia de formación de los halos (MAH). La normalización del espectro de potencia (σ_8) y el contenido de materia oscura en el universo influye considerablemente en la amplitud y la forma de la relación $c - M$ (Diemer & Kravtsov, 2014). Por consiguiente, una determinación rigurosa de los parámetros cosmológicos es crucial para predecir la relación $c - M$ y para estimar la estadística de arcos al nivel requerido por la cosmología actual.

En paralelo a la escritura de esta tesis, la simulación de un nuevo catálogo de cúmulos de galaxias con cosmología Planck (Planck Collaboration et al., 2015) ha sido casi completada. Siguiendo el mismo procedimiento al expuesto en esta tesis, pretendemos investigar las propiedades de cúmulos de galaxias simulados con está nueva cosmología basados en el mencionado catálogo.

Simultáneamente, estamos desarrollando un nuevo proyecto para estudiar la triaxialidad de halos de materia oscura para cinco órdenes de magnitud en masa. Con este objetivo, analizaremos halos con masas en el rango de los cúmulos de galaxias identificados en la simulación *Huge-MultiDark* (ver Apéndice A para

más detalles). Para extender los límites en masa, identificamos halos en tres simulaciones con volúmenes más reducidos: $(0.4, 1.0, 2.5\ h^{-1}\mathrm{Gpc})^3$. Basados en en análisis de estas simulaciones, pretendemos obtener predicciones sobre la morfología de halos de materia oscura con masas desde $\sim\ 10^{11}h^{-1}\mathrm{M}_{\odot}$ hasta $\sim\ 4 \times 10^{15}h^{-1}\mathrm{M}_{\odot}$. Todas las simulaciones analizadas en este proyecto han sido realizadas con los parámetros cosmológicos obtenidos por Planck Collaboration et al. (2015) que se describen en la Tabla 1.1.

Además, el enorme potencial que ofrece la muestra MUSIC-MD ha sido fuente de numerosas aplicaciones. Un buen ejemplo lo constituye el estudio del contenido bariónico y la calibración de relaciones de escala derivadas por el efecto SZ en cúmulos de galaxias presentado por Sembolini et al. (2013a,b, 2014).

APPENDIX A

Shapes of galaxy clusters in the *Huge-Multidark* simulation

The common procedure to determine the shape of halos is to model them as ellipsoids. Most of the methods found in the literature model halos using the eigenvectors from some form of the inertia tensor. The eigenvectors correspond to the direction of the axes, and the eigenvalues to the length of the axes ($c \leqslant b \leqslant a$) of the ellipsoid. The minor-to-major and intermediate-to-major axis ratios are defined as $s \equiv c/a$ and $q \equiv b/a$, respectively.

The two forms of the inertia tensor commonly used in the literature to determine the shape of halos are the unweighted inertia tensor

$$I_{ij} \equiv \sum_n x_{i,n} x_{j,n} \tag{A.1}$$

and the weighted (or reduced) inertia tensor

$$\tilde{I}_{ij} \equiv \sum_n \frac{x_{i,n} x_{j,n}}{r_n^2} \tag{A.2}$$

where

$$r_n = \sqrt{x_n^2 + y_n^2/q^2 + z_n^2/s^2}, \tag{A.3}$$

is the elliptical distance in the eigenvector coordinate system from the centre to the nth particle.

In this Appendix we present the axis ratio distributions for the MUSIC-MD clusters

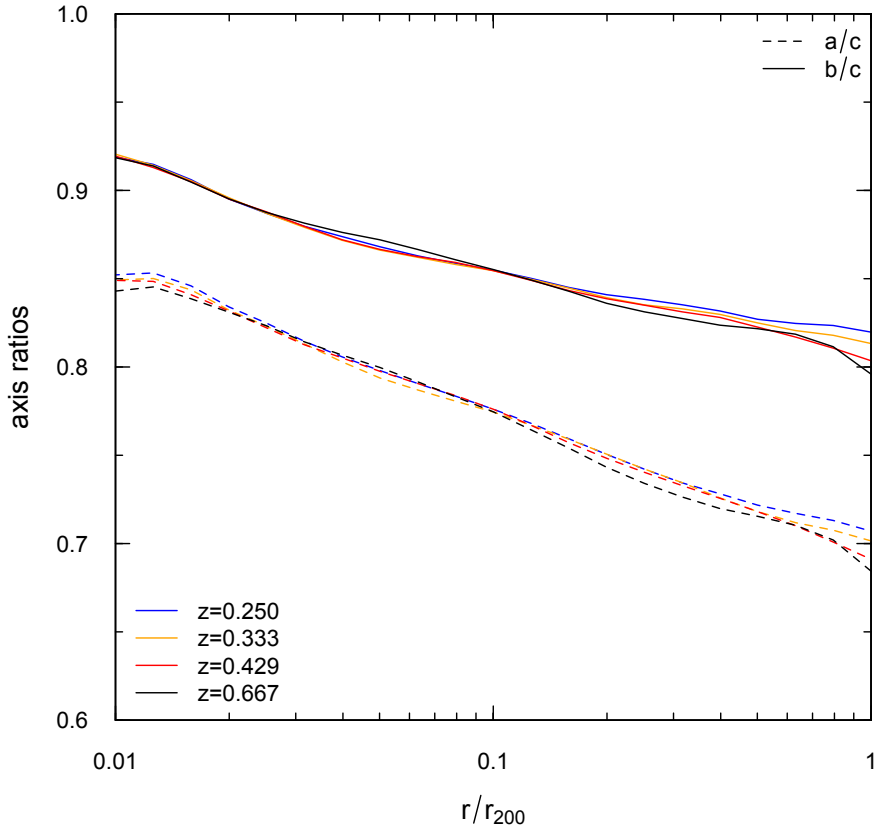

Figure A.1: Stacked profiles of the axis ratios (a/c and b/c) for all the MUSIC-MD halos at the four different redshifts analyzed.

with masses above $2 \times 10^{14} h^{-1} \mathrm{M}_{\odot}$. The axis ($c < b < a$) of the MUSIC-MD clusters have been computed by diagonalizing the inertia tensor of each halo using a spherical window (i.e., by determining the inertia tensor with $s = 1$ and $q = 1$ and including all particles within a given radius). In Fig. A.1 we show the stacked axis ratio profiles for the 1419 MUSIC-MD clusters at the four different redshifts analyzed. The profiles show almost no evolution with redshift and converge to $s \equiv c/a \sim 0.8$ and $q \equiv b/a \sim 0.7$ for $r = r_{200}$. From this figure we can also conclude that haloes tend to be more circular towards the center, with axis ratios growing up to $s \sim 0.9$ and $q \sim 0.85$ for $r = 0.01 r_{200}$.

The axis ratios in JS02 were derived at an overdensity of $\Delta = 2500 \rho_{crit}$ and using a iterative weighted inertia tensor method. For a direct comparison between the axis ratios of the MUSIC-MD dataset and the analysis presented by JS02, we

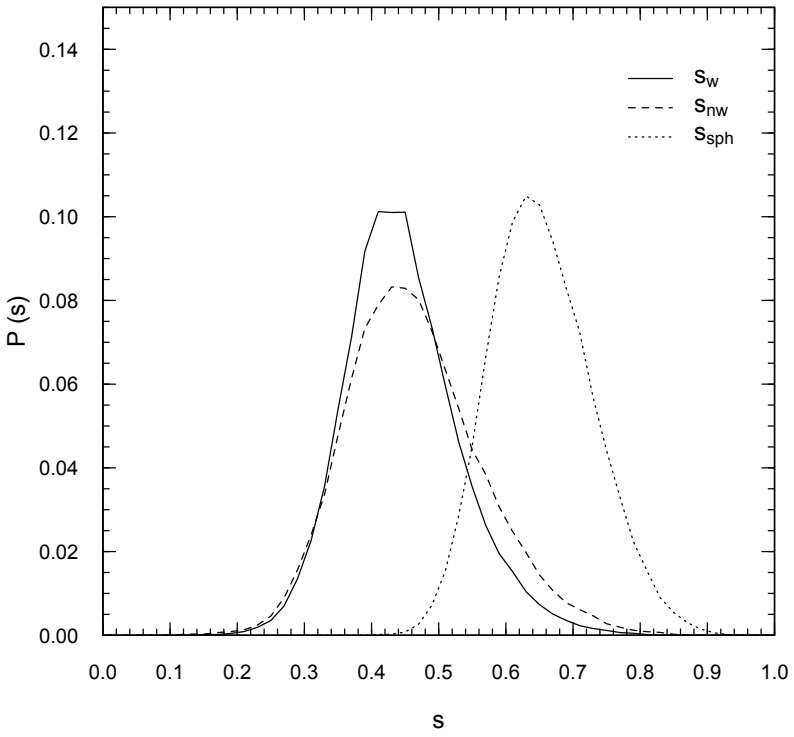

Figure A.2: Probability distribution of virial axis ratios s for the different methods used to determine the shape of the halos. The distributions are derived for halos at $z = 0.00$ in the HMD simulation with $N_p \geqslant 5{,}000$.

therefore need to convert from axis ratios derived with a spherical window to iterative methods (see Allgood et al. 2006 and Bonamigo et al. 2015 for a detailed description between different methods). We do so by computing the axis ratios of a sample of galaxy clusters extracted from a large volume dark matter only simulation (the *Huge-MultiDark* simulation) considering: a) weighted inertia tensor in a spherical window; b) iterative weighted inertia tensor; c) iterative unweighted inertia tensor. We label the axis ratios according to the method used as s_{sph}, s_w and s_{nw}, respectively.

The *Huge MultiDark* (HMD) is a dark-matter only simulation with 4096^3 particles in a $4h^{-1}$Gpc box volume and with mass resolution $m_p = 7.9 \times 10^{10} h^{-1} M_\odot$. The HMD simulation were performed within the ΛCDM cosmological model with Planck cosmological parameters: (Ω_M, Ω_b, Ω_Λ, σ_8, n_s, h) = (0.307, 0.048, 0.693, 0.829, 0.96, 0.677). The halos in the HMD simulation have been identified using

the ROCKSTAR phase-space halo finder (Behroozi et al., 2012), which allows to compute the shape parameters for the different cases considered here. To ensure a good resolution we limited our analysis to distinct halos with more than 1,000 particles within R_{vir}. Given the mass per particle in the HMD simulation, the minimum halo mass is $M_{min} = 7.9 \times 10^{13} h^{-1} M_{\odot}$.

In Fig. A.2, we show the probability distributions of the virial axis ratios for the three methods considered. The axis ratio distribution for s_{nw} is flatter than the s_w, showing more extended wings (both positive and negative). There is a clear shift to higher axis ratios when comparing the s_{sph} with the iterative methods s_w and s_{nw}. In Fig. A.3, we show the scatter plot for the axis ratios s_w vs s_{sph}. We perform a power-law fit to the data finding $s_w = s_{sph}^{\gamma}$ with $\gamma = 1.77 \pm 0.10$ and dispersion $\sigma = 0.08$. A similar result was found in Bailin & Steinmetz (2005) with $\alpha = \sqrt{3} \approx 1.73$. However, data points are best-fitted by a linear relation

$$s_w = (-0.147 \pm 0.019) + (0.920 \pm 0.027) s_{sph} \tag{A.4}$$

with a lower dispersion $\sigma = 0.06$. As the slope is almost equal to unity, the use of the iterative weighted inertia tensor results on a shift to lower axis ratios in ~0.15 when comparing with the weighted inertia tensor in a spherical window.

We also examined the difference in the determination of the virial axis ratios derived with the weighted (s_w) and the unweighted (s_{nw}) iterative inertia tensor (Fig. A.4). Both methods give similar results

$$s_{nw} = (0.109 \pm 0.009) + (0.735 \pm 0.016) s_w \tag{A.5}$$

with a dispersion of $\sigma = 0.06$.

A more detailed analysis on the distribution of the shape parameters for dark matter halos, spanning more than 4 orders of magnitude in mass, from the combined sample of halos from all the *MultiDark* simulations (Klypin et al., 2014), and a comparison with previous results will be published elsewhere (Vega et al., 2015).

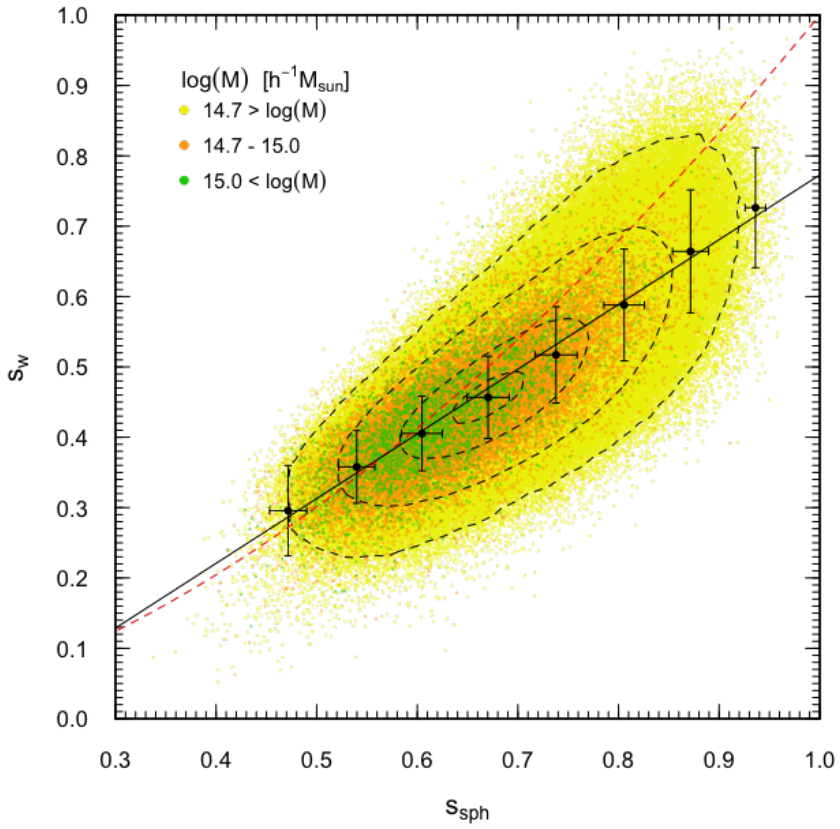

Figure A.3: Distribution of virial axis ratios in the plane s_w vs s_{sph} for halos with $M_{vir} \gtrsim 4{\times}10^{14}$ $h^{-1}M_{\odot}$ in the HMD simulation at $z = 0.00$. The black circles and error bars are the running means and 1σ levels in eight bins in s_{sph}. The black contours overlaid to the image show the intensity levels corresponding to 1%, 10%, 50% and 90% of the probability peak. The red dashed line indicates the result of the fit with a power-law to the data points ($s_w \simeq s_{sph}^{1.93}$), while the black dashed line corresponds to the linear best-fitted to the data points.

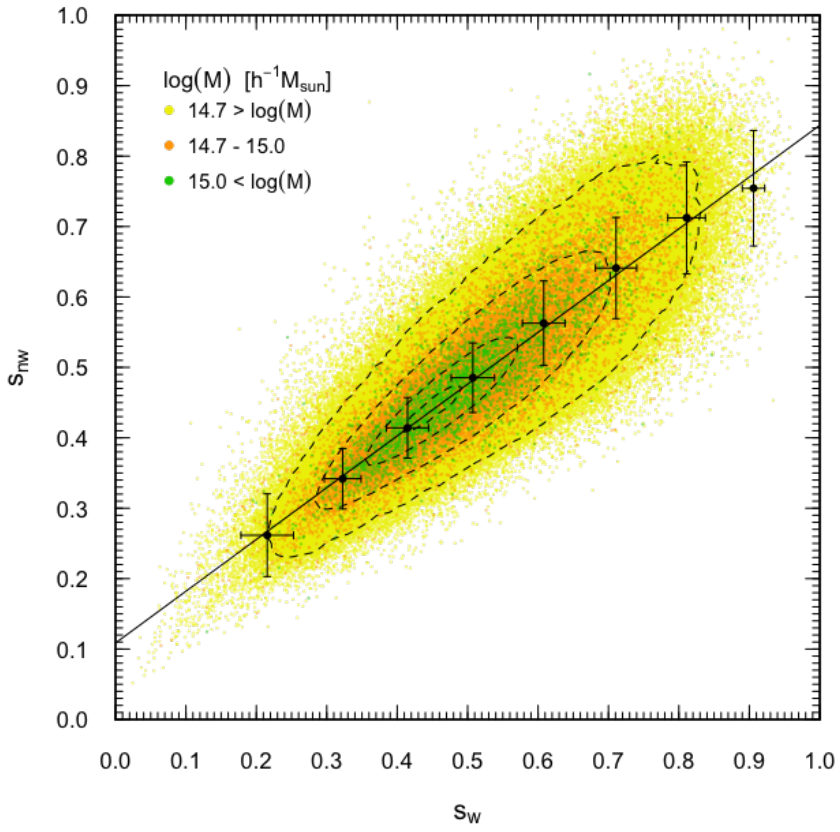

Figure A.4: Distribution of virial axis ratios in the plane s_{nw} vs s_w for halos with $M_{vir} \gtrsim 4{\times}10^{14}$ $h^{-1}M_{\odot}$ in the HMD simulation at $z = 0.00$. The black circles and error bars are the running means and 1σ levels in eight bins in s_w. The black dashed line corresponds to the linear best-fitted to the data points.

APPENDIX B

Publications

- CLASH: *The Concentration-Mass Relation of Galaxy Clusters*– Merten, J.; Meneghetti, M.; Postman, M.; Umetsu, K.; Zitrin, A. et al. 2015 (The Astrophysical Journal, 806, 4).
- *The* MUSIC *of* CLASH: *Predictions on the Concentration-Mass Relation*– Meneghetti M.; Rasia E.; Vega J.; Merten J.; Postman M. et al. 2014 (The Astrophysical Journal, 797, 34).
- CLASH: *The Enhanced Lensing Efficiency of the Highly Elongated Merging Cluster* MACS J0416.1-2403– Zitrin, A.; Meneghetti, M.; Umetsu, K.; Broadhurst, T.; Bartelmann, M. et al. 2013 (The Astrophysical Journal Letters, 762, L30).

The Astrophysical Journal, 806:4 (26pp), 2015 June 10 doi:10.1088/0004-637X/806/1/4

CLASH: THE CONCENTRATION-MASS RELATION OF GALAXY CLUSTERS

J. Merten[1,2,3], M. Meneghetti[1,4,5], M. Postman[6], K. Umetsu[7], A. Zitrin[2,32], E. Medezinski[8], M. Nonino[9], A. Koekemoer[6], P. Melchior[10], D. Gruen[11,12], L. A. Moustakas[1], M. Bartelmann[13], O. Host[14], M. Donahue[15], D. Coe[6], A. Molino[16], S. Jouvel[17,18], A. Monna[11,12], S. Seitz[11,12], N. Czakon[7], D. Lemze[8], J. Sayers[2], I. Balestra[9,19], P. Rosati[20], N. Benítez[15], A. Biviano[9], R. Bouwens[21], L. Bradley[6], T. Broadhurst[22,23], M. Carrasco[13,24], H. Ford[8], C. Grillo[14], L. Infante[25], D. Kelson[26], O. Lahav[17], R. Massey[27], J. Moustakas[28], E. Rasia[29], J. Rhodes[1,2], J. Vega[30,31], and W. Zheng[6]

[1] Jet Propulsion Laboratory, California Institute of Technology, 4800 Oak Grove Drive, Pasadena, CA 91109, USA; jmerten@caltech.edu
[2] California Institute of Technology, MC 249-17, Pasadena, CA 91125, USA
[3] Department of Physics, University of Oxford, Keble Road, Oxford OX1 3RH, UK
[4] INAF, Osservatorio Astronomico di Bologna, via Ranzani 1, I-40127 Bologna, Italy
[5] INFN, Sezione di Bologna, Viale Berti Pichat 6/2, I-40127 Bologna, Italy
[6] Space Telescope Science Institute, 3700 San Martin Drive, Baltimore, MD 21208, USA
[7] Institute of Astronomy and Astrophysics, Academia Sinica, P.O. Box 23-141, Taipei 10617, Taiwan
[8] Department of Physics and Astronomy, The Johns Hopkins University, 3400 North Charles Street, Baltimore, MD 21218, USA
[9] INAF/Osservatorio Astronomico di Trieste, via G.B. Tiepolo 11, I-34143 Trieste, Italy
[10] Center for Cosmology and Astro-Particle Physics and Department of Physics, The Ohio State University, Columbus, OH 43210, USA
[11] Universitäts-Sternwarte München, Scheinerstr. 1, D-81679 München, Germany
[12] Max-Planck-Institute für extraterrestrische Physik, Giessenbachstr. 1, D-85748 Garching, Germany
[13] Universität Heidelberg, Zentrum für Astronomie, Institut für Theoretische Astrophysik, Philosophenweg 12, D-69120 Heidelberg, Germany
[14] Dark Cosmology Centre, Niels Bohr Institute, University of Copenhagen, Juliane Maries Vej 30, DK-2100 Copenhagen, Denmark
[15] Department of Physics and Astronomy, Michigan State University, East Lansing, MI 48824, USA
[16] Instituto de Astrofísica de Andalucía (CSIC), E-18080 Granada, Spain
[17] Institut de Ciéncies de l'Espai (IEEC-CSIC), E-08193 Bellaterra (Barcelona), Spain
[18] Department of Physics and Astronomy, University College London, London WC1E 6BT, UK
[19] INAF—Osservatorio Astronomico di Capodimonte, Via Moiariello 16, I-80131 Napoli, Italy
[20] Dipartimento di Fisica e Scienze della Terra, Università degli Studi di Ferrara, Via Saragat 1, I-44122 Ferrara, Italy
[21] Leiden Observatory, Leiden University, P. O. Box 9513, NL-2333 Leiden, The Netherlands
[22] Department of Theoretical Physics and History of Science, University of the Basque Country UPV/EHU, P.O. Box 644, E-48080 Bilbao, Spain
[23] Ikerbasque, Basque Foundation for Science, Alameda Urquijo, 36-5 Plaza Bizkaia, E-48011 Bilbao, Spain
[24] Instituto de Astrofsica, Facultad de Física, Pontificia Universidad Católica de Chile, Casilla 306, Santiago 22, Chile
[25] Centro de Astro-Ingeniería, Departamento de Astronomía y Astrofísica, Pontificia Universidad Catolica de Chile, V. Mackenna 4860, Santiago, Chile
[26] Observatories of the Carnegie Institution of Washington, Pasadena, CA 91101, USA
[27] Institute for Computational Cosmology, Durham University, South Road, Durham DH1 3LE, UK
[28] Department of Physics and Astronomy, Siena College, 515 Loudon Road, Loudonville, NY 12211, USA
[29] Physics Dept., University of Michigan, 450 Church Ave, Ann Arbor, MI 48109, USA
[30] Departamento de Física Teórica, Universidad Autónoma de Madrid, Cantoblanco, E-28049 Madrid, Spain
[31] LERMA, CNRS UMR 8112, Observatoire de Paris, 61 Avenue de l'Observatoire, F-75014 Paris, France
Received 2014 April 8; accepted 2015 April 2; published 2015 June 3

ABSTRACT

We present a new determination of the concentration–mass (c–M) relation for galaxy clusters based on our comprehensive lensing analysis of 19 X-ray selected galaxy clusters from the Cluster Lensing and Supernova Survey with Hubble (CLASH). Our sample spans a redshift range between 0.19 and 0.89. We combine weak-lensing constraints from the *Hubble Space Telescope* (*HST*) and from ground-based wide-field data with strong lensing constraints from *HST*. The results are reconstructions of the surface-mass density for all CLASH clusters on multi-scale grids. Our derivation of Navarro–Frenk–White parameters yields virial masses between $0.53 \times 10^{15}\, M_{\odot}/h$ and $1.76 \times 10^{15}\, M_{\odot}/h$ and the halo concentrations are distributed around $c_{200c} \sim 3.7$ with a 1σ significant negative slope with cluster mass. We find an excellent 4% agreement in the median ratio of our measured concentrations for each cluster and the respective expectation from numerical simulations after accounting for the CLASH selection function based on X-ray morphology. The simulations are analyzed in two dimensions to account for possible biases in the lensing reconstructions due to projection effects. The theoretical c–M relation from our X-ray selected set of simulated clusters and the c–M relation derived directly from the CLASH data agree at the 90% confidence level.

Key words: dark matter – galaxies: clusters: general – gravitational lensing: strong – gravitational lensing: weak

1. INTRODUCTION

The standard model of cosmology (ΛCDM) is extremely successful in explaining the observed large-scale structure of the universe (see, e.g., Anderson et al. 2012; Planck Collaboration et al. 2014). However, when moving to progressively smaller length scales, inconsistencies between theoretical predictions and real observations have emerged. Examples include the cored mass-density profiles of dwarf-spheroidal galaxies (Walker & Peñarrubia 2011), the abundance of Milky Way satellites (Boylan-Kolchin et al. 2012), and the flat dark matter density profiles in the cores of galaxy clusters (Sand et al. 2002; Newman et al. 2013).

Galaxy clusters are unique tracers of cosmological structure formation (e.g., Voit 2005; Borgani & Kravtsov 2011). As the

[32] Hubble Fellow.

largest collapsed objects in the observable universe, clusters form the bridge between the large-scale structure of the universe and the astrophysical regime of individual halos. From an observational point of view, all main mass components of a cluster, hot ionized gas, dark matter, and luminous stars, are directly or indirectly observable with the help of X-ray observatories (e.g., Rosati et al. 2002; Ettori et al. 2013), gravitational lensing (e.g., Bartelmann & Schneider 2001; Bartelmann 2010), or optical observations.

As shown by numerical simulations (Navarro et al. 1996), dark matter tends to arrange itself following a specific, spherically symmetric density profile

$$\rho_{\rm NFW}(r) = \frac{\rho_s}{r/r_s\left(1 + r/r_s\right)^2}, \quad (1)$$

where the only two parameters ρ_s and r_s are a scale density and a scale radius. This functional form is now commonly called the Navarro–Frenk–White (NFW) density profile. It was found to fit well the dark matter distribution of halos in numerical simulations, independent of halo mass, cosmological parameters, or formation time (Navarro et al. 1997; Bullock et al. 2001).

A specific parametrization of the NFW profile uses the total mass enclosed within a certain radius r_Δ

$$M_\Delta = 4\pi\rho_s r_s^3\left(\ln\left(1 + c_\Delta\right) - \frac{c_\Delta}{1 + c_\Delta}\right), \quad (2)$$

and the concentration parameter

$$c_\Delta = \frac{r_\Delta}{r_s}. \quad (3)$$

When applying the relations above to a specific analysis, the radius r_Δ is chosen such that it describes the halo on the scale of interest. An example is the radius at which the average density of the halo is 200 times the critical density of the universe at this redshift ($\Delta = 200c$). Cosmological simulations show that there is a correlation between mass and concentration for dark matter structures, although with significant scatter. This defines the concentration–mass (c–M) relation which is a mild function of formation redshift and halo mass (Bullock et al. 2001; Eke et al. 2001; Zhao et al. 2003; Duffy et al. 2008; Gao et al. 2008; Klypin et al. 2011; Prada et al. 2012; Bhattacharya et al. 2013).

Observational efforts have been undertaken to measure the c–M relation either using gravitational lensing (Comerford & Natarajan 2007; Oguri et al. 2012; Okabe et al. 2013), X-ray observations (Buote et al. 2007; Schmidt & Allen 2007; Ettori et al. 2010), or dynamical analysis of cluster members (Lemze et al. 2009; Wojtak & Łokas 2010; Biviano et al. 2013). Some of the observed relations are in tension with the predictions of numerical simulations (Duffy et al. 2008; Fedeli 2012). The most prominent example of such tension is the cluster Abell 1689 (Broadhurst et al. 2005; Peng et al. 2009, and references therein), with a concentration parameter up to a factor of three higher than predicted. In a follow-up study, Broadhurst et al. (2008) compared a larger sample of five clusters to the prediction from ΛCDM and found the derived c–M relation in tension with the theoretical expectations (see also Broadhurst & Barkana 2008a; Zitrin et al. 2010; Meneghetti et al. 2011). Possible explanations for these discrepancies include a selection-bias of the cluster sample since these clusters were known strong lenses, paired with the assumption of spherical symmetry for these systems (Hennawi et al. 2007; Meneghetti et al. 2010a). Moreover, the influence of baryons on the cluster core (Fedeli 2012; Killedar et al. 2012) and even the effects of early dark energy (Fedeli & Bartelmann 2007; Sadeh & Rephaeli 2008; Francis et al. 2009; Grossi & Springel 2009) have been introduced as possible explanations. Ultimately, a new set of high-quality observations of an unbiased ensemble of clusters was needed to answer the question if observed galaxy clusters are indeed in tension with our cosmological standard model.

The Cluster Lensing And Supernova Survey with Hubble (CLASH; Postman et al. 2012a) is a multi-cycle treasury program, using 524 *Hubble Space Telescope* (*HST*) orbits to target 25 galaxy clusters, largely drawn from the Abell and MACS cluster catalogs (Abell 1958; Abell et al. 1989; Ebeling et al. 2001, 2007, 2010). Twenty clusters were specifically selected by their largely unperturbed X-ray morphology with the goal of representing a sample of clusters with regular, unbiased density profiles that allow for an optimal comparison to models of cosmological structure formation. As reported in Postman et al. (2012a) all clusters of the sample are fairly X-ray luminous with X-ray temperatures $T_x \geqslant 5$ keV and show a smooth morphology in their X-ray surface brightness. For all systems the separation between the brightest cluster galaxy (BCG) and the X-ray luminosity centroid is <20 kpc. An overview of the basic properties of the sample can be found in Table 1. In the following we will use these X-ray selected clusters to derive the observed c–M relation for CLASH clusters based on weak and strong lensing and perform a thorough comparison to the theoretical expectation from numerical simulations. This study has two companion papers. The weak-lensing and magnification analysis of CLASH clusters by Umetsu et al. (2014) and the detailed characterization of numerical simulations of CLASH clusters by Meneghetti et al. (2014).

This paper is structured as follows. Section 2 provides a basic introduction to gravitational lensing and introduces the method used to recover the dark matter distribution from the observational data. The respective input data is described in Section 3 and the resulting mass maps and density profiles of the CLASH clusters are presented in Section 4. We interpret our results by a detailed comparison to theoretical c–M relations from the literature in Section 5 and use our own tailored set of simulations to derive a CLASH-like c–M relation in Section 6. We conclude in Section 7. Throughout this work we assume a flat cosmological model similar to a WMAP7 cosmology (Komatsu et al. 2011) with $\Omega_m = 0.27$, $\Omega_\Lambda = 0.73$, and a Hubble constant of $h = 0.7$. For the redshift range of our cluster sample this translates to physical distance scales of 3.156–7.897 kpc/″.

2. CLUSTER MASS PROFILES FROM GRAVITATIONAL LENSING

We use gravitational lensing to recover the distribution of matter in galaxy clusters from imaging data. Lensing is particularly well-suited for this purpose since it is sensitive to the lens' total matter content, independent of its composition and under a minimum number of assumptions. After we discussed the basics of this powerful technique we will present a non-parametric inversion algorithm which maps the dark matter mass distribution over a wide range of angular scales.

Table 1
The CLASH X-Ray Selected Cluster Sample

Name	z	R.A. (deg/J2000)	Decl. (deg/J2000)	k T_x[a] (keV)	L_{bol}[a] (10^{44} erg s^{-1})	$''\rightarrow$ kpc[b]
Abell 383	0.188	42.014090	−3.5292641	6.5	6.7	3.156
Abell 209	0.206	22.968952	−13.611272	7.3	12.7	3.392
Abell 1423	0.213	179.32234	33.610973	7.1	7.8	3.482
Abell 2261	0.225	260.61336	32.132465	7.6	18.0	3.632
RX J2129+0005	0.234	322.41649	0.0892232	5.8	11.4	3.742
Abell 611	0.288	120.23674	36.056565	7.9	11.7	4.357
MS 2137−2353	0.313	325.06313	−23.661136	5.9	9.9	4.617
RXC J2248−4431	0.348	342.18322	−44.530908	12.4	69.5	4.959
MACS J1115+0129	0.352	168.96627	1.4986116	8.0	21.1	4.996
MACS J1931−26	0.352	292.95608	−26.575857	6.7	20.9	4.996
RX J1532.8+3021	0.363	233.22410	30.349844	5.5	20.5	4.931
MACS J1720+3536	0.391	260.06980	35.607266	6.6	13.3	5.343
MACS J0429−02	0.399	67.400028	−2.8852066	6.0	11.2	5.411
MACS J1206−08	0.439	181.55065	−8.8009395	10.8	43.0	5.732
MACS J0329−02	0.450	52.423199	−2.1962279	8.0	17.0	5.815
RX J1347−1145	0.451	206.87756	−11.752610	15.5	90.8	5.822
MACS J1311−03	0.494	197.75751	−3.1777029	5.9	9.4	6.128
MACS J1423+24	0.545	215.94949	24.078459	6.5	14.5	6.455
MACS J0744+39	0.686	116.22000	39.457408	8.9	29.1	7.186
CL J1226+3332	0.890	186.74270	33.546834	13.8	34.4	7.897

[a] From Postman et al. (2012a) and references therein.
[b] Conversion factor to convert arcseconds to kpc at the cluster's redshift and given the cosmological background model.

The CLASH data were designed to provide a unique combination of angular resolution, depth and multi-wavelength coverage that allows many new multiply lensed galaxies to be identified and their redshifts to be accurately estimated. These data are ideal for use with the `SaWLens` algorithm, which makes no a priori assumptions about the distribution of matter in a galaxy cluster.

2.1. Gravitational Lensing

Gravitational lensing is a direct consequence of Einstein's theory of general relativity (see, e.g., Bartelmann 2010, for a complete derivation). For cluster-sized lenses the lens mapping can be described by the lens equation

$$\boldsymbol{\beta} = \boldsymbol{\theta} - \boldsymbol{\alpha}(\boldsymbol{\theta}). \tag{4}$$

This lens equation describes how the original 2D angular position in the source plane $\boldsymbol{\beta} = (\beta_1, \beta_2)$ is shifted by a deflection angle $\boldsymbol{\alpha} = (\alpha_1, \alpha_2)$ to the angular coordinates $\boldsymbol{\theta} = (\theta_1, \theta_2)$ in the lens plane. From now on we denote the angular diameter distance between observer and lens as D_l, between observer and source as D_s, and between lens and source as D_{ls}. The deflection angle depends on the surface-mass density distribution of the lens $\Sigma(D_d\boldsymbol{\theta})$ and can be related to a lensing potential

$$\psi(\boldsymbol{\theta}) := \frac{1}{\pi}\int d^2\theta' \frac{\Sigma(D_l\boldsymbol{\theta})}{\Sigma_{cr}} \ln|\boldsymbol{\theta} - \boldsymbol{\theta}'|, \tag{5}$$

which is a line of sight projected and rescaled version of the Newtonian potential. The cosmological background model enters this equation through the critical surface mass density for lensing given by

$$\Sigma_{cr} = \frac{c^2}{4\pi G}\frac{D_s}{D_l D_{ls}}, \tag{6}$$

where c is the speed of light and G is Newton's constant. By introducing the complex lensing operators (e.g., Bacon et al. 2006; Schneider & Er 2008) $\partial := \left(\frac{\partial}{\partial\theta_1} + i\frac{\partial}{\partial\theta_2}\right)$ and $\partial^* := \left(\frac{\partial}{\partial\theta_1} - i\frac{\partial}{\partial\theta_2}\right)$ one can derive important lensing quantities as derivatives of the lensing potential

$$\begin{aligned} \alpha &:= \partial\psi \quad s = 1 \\ 2\gamma &:= \partial\partial\psi \quad s = 2 \\ 2\kappa &:= \partial\partial^*\psi \quad s = 0 \end{aligned} \tag{7}$$

where α is the complex form of the already known deflection angle, γ is called the complex shear, and the scalar quantity κ is called convergence. The behavior of each quantity under rotations of the coordinate frame is given by the spin-parameter s.

When relating these basic lens quantities to observables one distinguishes two specific regimes. In the case of weak lensing the distortions induced by the lens mapping are small and due to the intrinsic ellipticity of galaxies, localized averages over an ensemble of sources are used to separate the lensing signal from the random orientation caused by the intrinsic ellipticity. These local averages of ellipticity measurements can be related to Equation (7) by the reduced shear g

$$\langle\epsilon\rangle = g := \frac{\gamma}{1-\kappa}, \tag{8}$$

where we defined the ellipticity of a galaxy as $|\epsilon|:=\frac{a-b}{a+b}$ with the two axes of the ellipse fulfilling $a > b$. This relation between the measured ellipticities and the properties applies only in the regime where $|g| < 1$ and assumes that the shear is constant across a galaxy (Schneider & Er 2008). To mitigate this, we exclude shear measurements inside the region where $|g| > 1$ (see also Section 3.2). For the combination of galaxy shape moments used in the RRG method, the constant shear approximation remains correct (to within 1% for a singular isothermal sphere lens) outside 1.07 times the Einstein radius (Massey & Goldberg 2008). This potential source of bias is far smaller than other sources of statistical error in our current analysis. For completeness we note that for $|g| > 1$, the relation between the measured ellipticities and the properties of the lens switches to

$$\langle \epsilon \rangle = \frac{1-\kappa}{\gamma^*}. \quad (9)$$

For a more thorough description of the relation between the measured shapes of galaxy images and the lens properties in the weak lensing regime we refer to the review by (Bartelmann & Schneider 2001, and references therein). We also do not discuss here the many systematic effects to be taken into account during such a shape measurement but refer to, e.g., Kitching et al. (2012), Massey et al. (2013), or Mandelbaum et al. (2014).

In the strong lensing regime, close to the core of the lens' mass distribution, the assumption of small image distortions does not hold any more. The lens equation becomes nonlinear and therefore multiple images of the same source can form. This happens near the critical line at a given redshift which is defined by the roots of the lensing Jacobian

$$\det \mathcal{A} = (1-\kappa)^2 - \gamma^2. \quad (10)$$

While the weak lensing regime expands over the full cluster field, it does not describe the mass distribution in the center of the cluster. Strong lensing is limited to the inner-most 10″–50″ of the cluster field, which renders the combination of the two regimes the ideal approach for mass reconstruction. One particular limitation of gravitational is the mass-sheet-degeneracy (Falco et al. 1985; Gorenstein et al. 1988). It describes the invariance of many lensing observables under the transformation

$$\kappa(\boldsymbol{\theta}) \rightarrow \kappa'(\boldsymbol{\theta}) = \lambda\kappa(\boldsymbol{\theta}) + (1-\lambda) \quad (11)$$

$$\gamma(\boldsymbol{\theta}) \rightarrow \gamma'(\boldsymbol{\theta}) = \lambda\gamma(\boldsymbol{\theta}) \quad (12)$$

with the free[33] transformation parameter λ. Several ways have been suggested to break the mass-sheet-degeneracy, including the use of magnification constraints (e.g., Broadhurst et al. 1995), which are not invariant under the mass-sheet transformation, and the inclusion of multi-redshift strong-lensing features (Bradač et al. 2004, 2005b). In this work, however, we will folow another route to break the mass-sheet-degeneracy, which is the simple condition that the average convergence at the edge of the reconstruction field goes to zero in the absence of a lensing signal. This assumption is justified once wide-field imaging is used, entailing the full cluster field well-beyond its virial radius and we will present its specific implementation into our reconstruction algorithm in the next section.

[33] The parameter is free up to the limit that the solution for the surface-mass density must be physical in terms of e.g., the dynamics of cluster member galaxies etc.

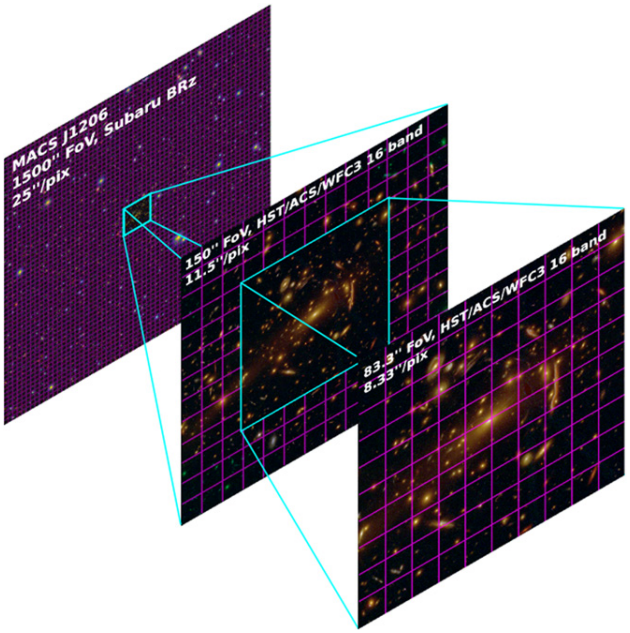

Figure 1. Visualization of our multi-scale approach. While weak lensing data from Subaru allows for a mass reconstruction of a galaxy cluster on a wide field, the achievable resolution is rather low. *HST* weak lensing delivers higher resolution but on a relatively small field. Finally, the strong lensing regime provides a very high resolution, but only in the inner-most cluster core. This figure shows one of our sample clusters, MACS J1206 and the reconstruction grids for all three lensing regimes.

2.2. *Non-parametric Lensing Inversion With* `SaWLens`

The `SaWLens` (Strong -and Weak-lensing) method was developed with two goals in mind. First, it should consistently combine weak and strong lensing. The second goal was to make no a priori assumptions about the underlying mass distribution, but to build solely upon the input data. The initial idea for such a reconstruction algorithm was formulated by Bartelmann et al. (1996) and was further developed by Seitz et al. (1998) and Cacciato et al. (2006). Similar ideas were implemented by Bradač et al. (2005b) with first applications to observations in Bradač et al. (2005a, 2006). Other non-parametric reconstruction algorithms, based on different methdologies, have been presented by Abdelsalam et al. (1998), Bridle et al. (1998), Liesenborgs et al. (2006), Jee et al. (2007), Diego et al. (2007), and Merten (2014). In its current implementation (Merten et al. 2009), `SaWLens` performs a reconstruction of the lensing potential (Equation (5)) on an adaptively refined grid. In this particular study, the method uses three different grid sizes to account for weak lensing on a wide field, such as is provided by ground-based telescopes, weak lensing constraints from the *HST* on a much smaller field of view but with considerably higher spatial resolution, and a fine grained grid to trace strong lensing features near the inner-most core of the cluster. This three-level adaptive grid is illustrated in Figure 1.

SaWLens uses a statistical approach to reconstruct the lensing potential ψ in every pixel of the grid. A χ^2-function, which depends on the lensing potential and includes a weak and a strong-lensing term is defined by

$$\chi^2(\psi) = \chi^2_w(\psi) + \chi^2_s(\psi), \tag{13}$$

and the algorithm minimizes it such that the input data is best described by a pixelized lensing potential ψ_l

$$\frac{\partial \chi^2(\psi)}{\partial \psi_l} \stackrel{!}{=} 0. \tag{14}$$

In Equation (14), l runs over all grid pixels. The weak-lensing term in Equation (13) is derived from Equation (8) with a measured average complex ellipticity of background sources in each grid pixel ϵ

$$\chi^2_{\rm w} = \sum_{i,j} (\epsilon - g(\psi))_i C^{-1}_{ij} (\epsilon - g(\psi))_j. \tag{15}$$

The covariance matrix C is non-diagonal because the algorithm adaptively averages over a number of background-ellipticity measurements in each pixel to account for the intrinsic ellipticity of background sources. Depending on the reconstruction resolution, this number is either defined by all weak-lensing background galaxies that are contained within the area of the current reconstruction pixel, or, if the reconstruction resolution is high, the algorithm searches in progressively larger squares around the center of the reconstruction pixel until at least 10 galaxies are contained in the square area. Due to this averaging scheme, neighboring pixels may share a certain number of background sources and the algorithm keeps track of these correlations between pixels as described in Section 3.2 and especially Equations (14)–(16) of Merten et al. (2009). We do not perform any distance-weighting in our averages since we treat our reconstruction cells as extended square pixels. However, during the averaging process each measured ellipticity is weighted with the inverse-variance of the shape measurement. This approach has been calibrated and is tested by reconstructing numerically simulated lenses in Merten et al. (2009) and Meneghetti et al. (2010b). The connection to the lensing potential is given by Equation (8) which, when inserted into Equation (15), yields

$$\chi^2_{\rm w}(\psi) = \sum_{i,j} \left(\varepsilon - \frac{Z(z)\gamma(\psi)}{1 - Z(z)\kappa(\psi)} \right)_i \times C^{-1}_{ij} \left(\varepsilon - \frac{Z(z)\gamma(\psi)}{1 - Z(z)\kappa(\psi)} \right)_j, \tag{16}$$

where again both indices i and j run over all grid cells. Note that all lensing quantities given by Equation (7) have a redshift dependence introduced by the critical density in Equations (5) and (6). This is taken into account by a cosmological weight function (Bartelmann & Schneider 2001) scaling each pixel to a fiducial redshift of infinity during the reconstruction.

$$Z(z) := \frac{D_\infty D_{\rm ls}}{D_{\rm l\infty} D_{\rm s}} H(z - z_{\rm l}). \tag{17}$$

The Heaviside step function ensures that only sources behind the lens redshift z_l have non-zero weight.

The definition of the strong lensing term in Equation (13) makes use of the fact the position of the lens' critical line at a certain redshift can be inferred from the position of multiple images. It has been shown in Merten et al. (2009) and Meneghetti et al. (2010b) that pixel sizes $>5''$ are large enough to make this simple assumption. Therefore, following Equation (10)

$$\chi^2_{\rm s}(\psi) = \frac{|\det \mathcal{A}(\psi)|^2_i}{\sigma^2_{i,\rm s}} = \frac{|(1 - Z(z)\kappa(\psi))^2 - |Z(z)\gamma(\psi)|^2|^2_i}{\sigma^2_{i,\rm s}}, \tag{18}$$

where this term is only assigned to those grid cells which are part of the critical line at a certain redshift z given the positions of multiple images. The error term σ is then given by the cell size of the grid following

$$\sigma_{\rm s} \approx \left. \frac{\partial \det \mathcal{A}}{\partial \theta} \right|_{\theta_{\rm c}} \delta\theta \approx \frac{\delta\theta}{\theta_{\rm E}}, \tag{19}$$

with $\theta_{\rm E}$ being an estimate of the Einstein radius of the lens.

The missing connection to the lensing potential ψ is given by Equation (7). The numerical technique of finite differencing is then used to express the basic lensing quantities by simple matrix multiplications

$$\kappa_i = \mathcal{K}_{ij}\psi_j \tag{20}$$

$$\gamma^1_i = \mathcal{G}^1_{ij}\psi_j \tag{21}$$

$$\gamma^2_i = \mathcal{G}^2_{ij}\psi_j \tag{22}$$

where $\mathcal{K}_{ij}$, $\mathcal{G}^1_{ij}$, and $\mathcal{G}^2_{ij}$ are sparse matrices representing the finite differencing stamp of the respective differential operator (Seitz et al. 1998; Bradač et al. 2005a; Merten et al. 2009). With these identities in mind it can be shown that Equation (14) takes the form of a linear system of equations, which is solved numerically. There are two important aspects to this method, which we will only mention briefly. First, a two-level iteration scheme is employed to deal with the nonlinear nature of the reduced shear (Schneider & Seitz 1995) and to avoid overfitting of local noise contributions (Merten et al. 2009). Second, a regularization scheme is adapted (Seitz et al. 1998; van Waerbeke 2000) to ensure a smooth transition from one iteration step to the next. In this work we adapt the regularization scheme of Bradač et al. (2005a), with an initial flat convergence prior, which regularizes the initial convergence to zero over the field. This also conveniently implements the way in which we break the mass-sheet-degeneracy, as we have mentioned earlier on. The initial regularization condition ensures a flat and zero convergence field where no significant lensing signal is found in the shear data.

It is important that a complex lensing inversion algorithm is tested thoroughly and under controlled but realistic conditions. Such tests are particular importance for our analysis since we are applying our method to a large set of real clusters of galaxies and we need to know our expected level of systematic error in the determination of masses and concentrations. Also,

we use several techniques which rely on specific assumptions and hence need to be tested for their validity. This includes our way of breaking the mass-sheet degeneracy, the use of critical line estimators in the strong-lensing regime and the two-level iteration with a specific regularization scheme.

These tests were performed in Meneghetti et al. (2010b) with a set of three simulated clusters with masses between 6.8×10^{14}–$1.1 \times 10^{15}\, M_{\odot}/h$. Each of the three simluated clusters was reconstructed in three perpendicular projections, spanning a range of surface-mass densities of fairly round, to elliptical and highly substuctured morphologies. Figure 15 of Meneghetti et al. (2010b) shows that SaWLens determines the masses of this particular set of simulations with an accuracy of 5%–10% at all relevant radii. Other methods relying on either strong -or weak-lensing constraints are limited to either small or large scales and showed less accurate results with errors of ~20%. SaWLens also recovered the concentrations of the simulated halos with errors at the ~5% level. These results on concentrations are summarized in Table 3 of Meneghetti et al. (2010b). We want to emphasize that the quoted errors refer to the results when reconstructing a set of nine projections from three cluster simulations. This number is smaller than the 19 cluster reconstructions shown in this work and the simulated cluster sample was also not explicitly constructed to mimick the CLASH selection. Hence, these tests can only serve as an approximate lead for the accuracy of individual cluster reconstructions of this work, but nevertheless represent an important check of our methodlogy and numerical implementation. Aside from the successful tests on simulated lenses, the SaWLens algorithm has been used in the reconstruction of observed galaxy clusters (Merten et al. 2009, 2011; Umetsu et al. 2012; Medezinski et al. 2013; Patel et al. 2014).

3. THE CLASH DATA SET

Our analysis focuses on the X-ray selected sub-sample of CLASH (Table 1). For each of these clusters a large number of lensing constraints was collected, either from the *HST* CLASH survey (Postman et al. 2012a), the accompanying Subaru/Suprime-Cam (Umetsu et al. 2011; Postman et al. 2012a; Medezinski et al. 2013) or ESO/WFI (Gruen et al. 2013) weak lensing observations, or from the CLASH-Very Large Telescope (VLT) spectroscopic program (Balestra et al. 2013). The data collection includes strong-lensing multiply imaged systems together with accurate spectroscopic or photometric redshifts and weak-lensing shear catalogs on the full cluster field, paired with a reliable background selection of weak lensing sources.

3.1. Strong Lensing in the HST Fields

The Zitrin et al. (2009) method is applied to identify multiple-image systems in each cluster field. The respective strong-lensing mass models for several CLASH clusters have already been published (Zitrin et al. 2011, 2012a, 2012b, 2013; Coe et al. 2012, 2013; Umetsu et al. 2012; Zheng et al. 2012) and the full set of strong-lensing models and multiple-image identifications is presented in Zitrin et al. (2014). Exceptions are the cluster RXC J2248, where the multiple-image identification is based on the Monna et al. (2014) strong-lensing mass model, and RX J1532, where our team was not able to identify any strong-lensing features to date. In this case, we derive the underlying lensing potential from weak lensing only with a significantly coarser resolution in the central region, compared to the strong-lensing clusters.

Table 2
Strong-lensing Constraints

Name	$N_{\rm sys}$ [a]	$N_{\rm spec}$ [b]	$N_{\rm crit}$ [c]	z-range	$\langle d_{\rm crit}\rangle$ [d] [″]
Abell 383	9	5	20[e]	1.01–6.03	17.5 ± 5.7
Abell 209	6	0	5	1.88–3.5	8.5 ± 0.8
Abell 1423	1	0	1	3.5	17.5 ± —
Abell 2261	12	0	18	1.54–4.92	18.1 ± 8.2
RX J2129+0005	4	1	8	0.55–1.965	8.1 ± 3.5
Abell 611	4	3	9	0.908–2.59	13.1 ± 4.5
MS 2137−2353	2	2	6	1.501–1.502	12.2 ± 4.7
RXC J2248−4431	11	10	22	1.0–6.0	27.8 ± 5.6
MACS J1115+0129	2	0	5	2.46–2.64	19.9 ± 9.2
MACS J1931−26	7	0	8	2.6–3.95	29.2 ± 1.3
RX J1532.8+3021	0	0	0	…	…
MACS J1720+3536	7	0	11	0.6–4.6	19.3 ± 8.8
MACS J0429−02	3	0	6	1.6–4.1	11.8 ± 3.6
MACS J1206−08	13	4	33	1.033–5.44	28.1 ± 14.8
MACS J0329−02	6	0	12	1.55–6.18	23.7 ± 5.2
RX J1347−1145	13	1	15	0.7–4.27	31.6 ± 13.3
MACS J1311−03	2	0	4	2.63–6.0	12.9 ± 5.3
MACS J1423+24	5	3	18	1.779–2.84	15.0 ± 5.6
MACS J0744+39	5	0	8	1.15–4.62	31.6 ± 16.2
CL J1226+3332	4	0	9	2.0–4.2	23.2 ± 12.2

[a] The number of multiple-image systems in this cluster field.
[b] The number of spectroscopically confirmed multiple-image systems.
[c] The number of critical line estimators derived from the position of multiple-image systems.
[d] The mean distance and its standard deviation from the cluster center to the critical line estimators.
[e] An illustration of how the critical line estimators for this specific systems were derived is given in Figure 2.

A summary of multiple-image systems found in each cluster is given in Table 2. From the identified multiple images we estimate the locations of critical lines following the approach of Merten et al. (2009). We show this critical line estimation for one concrete example in Figure 2, where we indicate the multiple images identified by Zitrin et al. (2011) in Abell 383 together with the critical lines derived from a detailed strong-lensing model of the cluster. In addition we show our critical line estimation from the multiple-image identifications which is in excellent agreement with the critical lines from the strong-lensing model given the pixel size of our reconstruction. It is not possible to determine the position of the critical line to high accurazy from multiple images only. In fact, only a conservative and coarse resolution in the strong-lensing regime of 5″–10″ renders the positional error in the critical line estimation negligible when compared to the reconstruction resolution. We show this for a concrete example in Figure 2. However, we are not limited by this coarse resolution since we still map the density profile over three decades in radius and since we are not aiming to break the mass-sheet-degeneracy using multi-plane strong-lensing features, as, e.g., shown in Bradač et al. (2005b).

Redshifts for all strong lensing features are either taken from the literature, spectroscopic redshifts from the on-going CLASH VLT-Vimos large program (186.A-0798) (Balestra et al. 2013), or from the CLASH photometry directly using Bayesian photometric redshifts (BPZ, Benítez 2000). CLASH

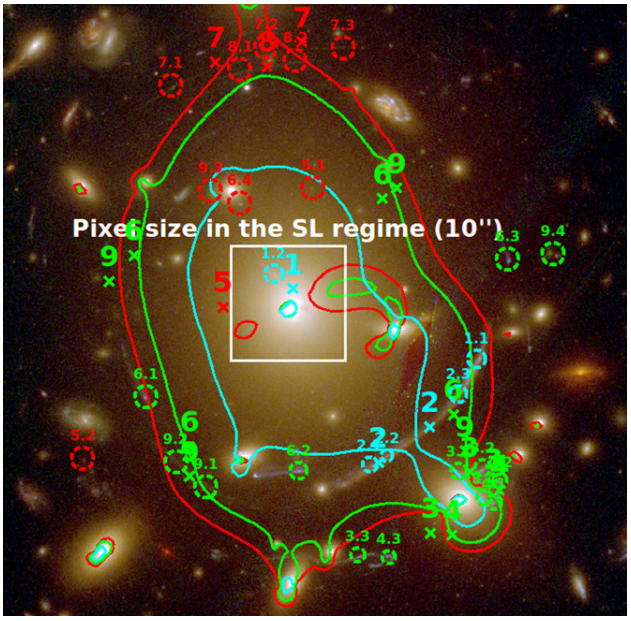

Figure 2. Estimation of the critical line for the SaWLens analysis of Abell 383. Shown by the labeled circles are the different sets of multiple-image systems identified by Zitrin et al. (2011). The three solid lines show the critical lines from their strong lensing model for three different source redshifts (cyan: $z_s = 1.01$, green: $z_s = 2.55$ and red: $z_s = 6.03$). The crosses with integer labels show our critical line estimate for a particular multiple image system with the same ID number. The white box shows the SaWLens pixel size in the strong-lensing regime. The critical line estimates and the multiple-image systems are divided into three groups. Cyan indicates systems at $z_s = 1.01$, green contains systems in a redshift range between $z_s = 2.20$ and $z_s = 3.90$, and red systems in the range from $z_s = 4.55$ to $z_s = 6.03$

has been explicitly designed to deliver accurate photometric redshifts for strong lensing features (Postman et al. 2012a). The accuracy of the CLASH photometric redshifts has been recently evaluated in Jouvel et al. (2014) where we found 3.0%(1+z) precision for strong-lensing arcs and field galaxies.

3.2. Weak Lensing in the HST Fields

For cluster mass reconstruction, the *HST* delivers a four to five times higher density of weakly lensed background galaxies than observations from the ground (e.g., Clowe et al. 2006; Bradač et al. 2006, 2008; Merten et al. 2011; Jee et al. 2012). We measure the shapes of background galaxies in typically seven broad-band Advanced Camera for Surveys (ACS) filters, F435W, F475W, F606W, F625W, F775W, F814W, and F850LP. The full survey design is laid out in detail in Postman et al. (2012a). Where available, the CLASH data is augmented by archival *HST* observations. For the F814W and F850LP filters, two *HST* orbits are allocated for each CLASH cluster, which are split into four different visits with two different *HST* roll angles. The total exposure time in the other filters is one orbit which is split into two separate visits. Each single visit consists of two sequential, dithered expsures. Each of the individiual exposures is corrected for charge-transfer-inefficiency (e.g., Anderson & Bedin 2010; Massey 2010; Jee et al. 2014a) by using the PixCteCorr routine in the STScI Python package. This procedure is based on the pixel-based correction algorithm proposed in Anderson & Bedin (2010). In order to improve the spatial sampling of the PSF and to avoid hot pixels and detector imperfections we do not measure shapes in the individual expsures of each visit but combine the two exposures with a modified version of the MosaicDrizzle pipeline (Koekemoer et al. 2002, 2011) with a drizzle pixel scale of 0.″03. This is possible since the two expsoures in each visit are taken sequentially and the time-dependent variation of the *HST* point-spread function (PSF) is small between the two exposures. In contrast, individual exposures of different visits might be separated by several days, which is why we do not work with the total coadd, based on all visits in a single filter. A final set of bad pixel and cosmic ray masks is provided by the MosaicDrizzle pipeline using all exposures in multiple epochs for a given filter as described in Postman et al. (2012a). For shape measurement and PSF correction we use the RRG package (Rhodes et al. 2000), which implements an *HST* breathing model (Leauthaud et al. 2007; Rhodes et al. 2007) to correct for the thermally induced variation of the *HST* PSF. The method has been used for cosmic shear (Massey et al. 2007) and cluster lensing (Bradač et al. 2008; Merten et al. 2011) applications following testing and calibration on shapelet-based image simulations (Massey et al. 2004) when it was implemented in the context of the COSMOS survey (see Figure 14 of Leauthaud et al. 2007). The shear calibration found an overall multiplicative bias of $1 - 0.86^{+0.07}_{-0.05}$ and RRG applies a correction factor accordingly. To be more precise, the two shear components are multiplied with a factor of $(0.80)^{-1}$ and $(0.92)^{-1}$ for the first and the second shear component, respectively, following the findings of Leauthaud et al. (2007). The additive and quadratic bias was found to be negligible (see Table 5 in Leauthaud et al. 2007). The level of PSF variation was determined from the inspection of stars in the field of each visit (Rhodes et al. 2007) and by cross-comparison with the STScI focus tool[34] (di Nino et al. 2008, and references therein). For the shape measurements in each visit we discard all galaxies with signal-to-noise ratio (S/N) < 10 and every shear catalog is then rotated into a north-up orientation in order to have a unique orientation reference for the directional shape parameters. The individual visit catalogs are finally combined using a S/N weighted average for multiple measurements of the same object. This procedure is applied to each of the seven ACS filters. Catalogs in different filters are combined by using a signal-to-noise weighted average for matching sources. In the case of Abell 611 we did not use F606W and F625W images since the focus tool did not cover the time period when these observations were taken. In the case of RX J2129 additional F555W data is included from archival data. We show the remaining residual PSF in Figure 3, where the two ellipticity components of bright un-saturated stars ($18 \lesssim$ F814W $\lesssim 22$) in the exposures of all clusters and for different filter configurations are shown after PSF correction.

The lensed background sample for each combined catalog was selected using two photo-z criteria. First, the most likely redshift according to the probability distribution of BPZ had to be at least 20% larger than the cluster redshift to ensure a limited contamination by cluster members. Second, the lower bound on the source redshift (based on the BPZ probability distribution) had to be larger or equal to the cluster redshift. A size cut and removal of obvious artifacts finalizes each *HST* weak lensing catalog and the effective lensing redshift of the background distribution is determined from the photometric redshift of each object in the final catalog. All relevant

[34] http://www.stsci.edu/hst/observatory/focus

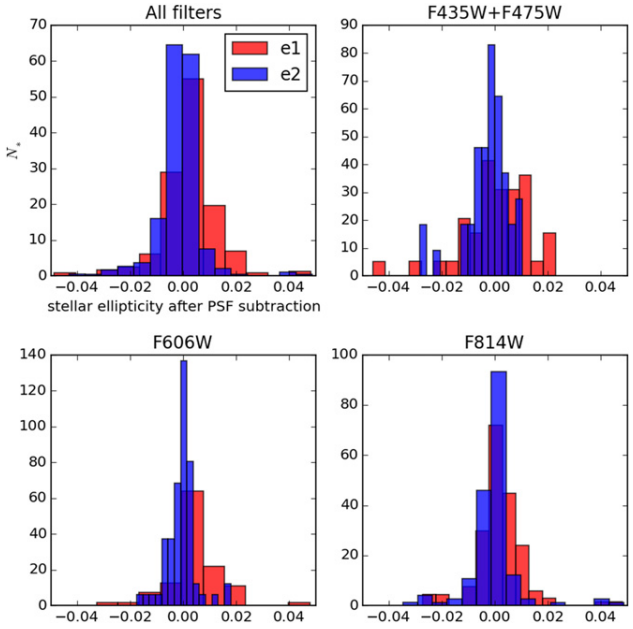

Figure 3. Residual stellar ellipticity after PSF correction with the RRG pipeline. The histograms show both ellipticity components of bright, unsaturated stars ($18 \lesssim$ F814W $\lesssim 22$) in our ACS exposures of all sample clusters. The upper right panel shows the residual ellipticity distribution for a joint catalog using all filters, the other three panels show individual contributions for catalogs in specific filters as indicated by the panel titles.

information about the *HST* weak lensing catalogs is summarized in Table 3.

The cross-shear component was found to be small at all radii. To see this in the case of our *HST* weak lensing we refer to the panels for Abell 1423 and CL J1226 in Figure 5. We also found strong correlations in both ellipticity components between different ACS filter measurements. This is demonstrated for four different filters and four different clusters in Figure 4. As a final cross-check we performed lensing inversions of the *HST* weak lensing data only, as it is shown for the case of Abell 1423 in Figure 15; all of these showed strong correlations with the light distribution in the *HST* fields. Our selection of weak-lensing galaxies in the *HST* fields is finalized by discarding all galaxies which lie within the critical curve of the lens. While doing so, we ensure that Equation (8) holds for all measured reduced shear values in our reconstructed field and we justify this step with the fact that the strong-lensing regime of all our lenses is well-constrained by the strong-lensing features in the field. We determine the position of the critical lines with the strong-lensing models presented in Zitrin et al. (2014).

3.3. Weak Lensing in the Ground-based Fields

The creation of our weak-lensing shear catalogs from ground-based observations is described in detail in Section 4 of Umetsu et al. (2014). For completeness we summarize the properties of these catalogs in Table 4 and list the main steps of our analysis in the following.

The wide-field weak-lensing pipeline of Umetsu et al. (2014) is implemented based on the PSF-correction and shear-calibration procedures outlined in (Umetsu et al. 2010, see Section 3.2) In the course of the CLASH survey, this analysis

Table 3
HST Weak-lensing Constraints

Name	$N_{\rm band}$ [a]	$N_{\rm gal}$ [b]	$\rho_{\rm gal}$ [c] (arcmin^{-2})	$z_{\rm eff}$ [d]
Abell 383	7	796	50.7	0.90
Abell 209	7	832	44.0	0.95
Abell 1423	7	807	50.3	0.92
Abell 2261	7	725	46.7	0.79
RX J2129+0005	8	624	35.8	0.82
Abell 611	5	547	42.3	0.86
MS 2137−2353	7	801	48.3	1.12
RXC J2248−4431	7	598	38.5	1.12
MACS J1115+0129	7	491	37.4	1.03
MACS J1931−26	7	709	59.5	0.82
RX J1532.8+3021	7	508	35.9	1.07
MACS J1720+3536	7	635	40.6	1.11
MACS J0429−02	7	654	42.4	1.08
MACS J1206−08	7	581	51.2	1.13
MACS J0329−02	7	493	35.2	1.18
RX J1347−1145	7	633	45.7	1.13
MACS J1311−03	7	447	33.7	1.03
MACS J1423+24	7	899	75.3	1.04
MACS J0744+39	7	743	61.3	1.32
CL J1226+3332	7	925	32.7	1.66

[a] The number of *HST*/ACS bands from which the final shear catalog was created.
[b] The number of background selected galaxies in the shear catalog.
[c] The surface-number density of background selected galaxies in the field.
[d] The effective redshift of the background sample, derived from their photo-zs and by calculating the average of the $D_{\rm ls}/D_s$ ratio and correcting for the nonlinearity of the reduced shear.

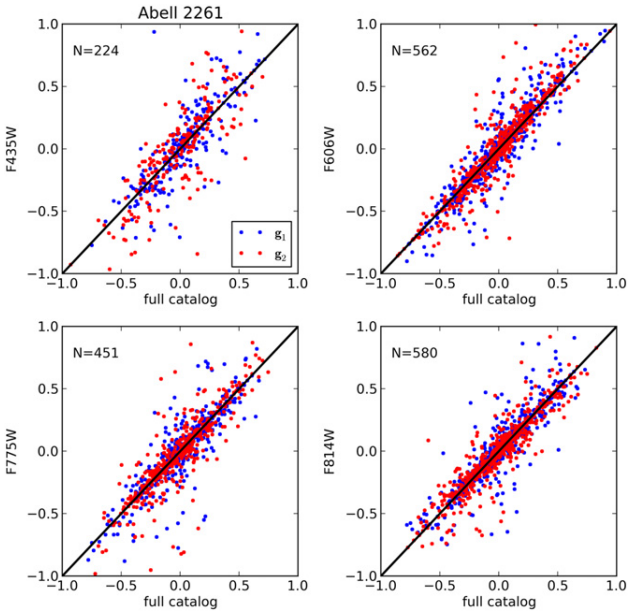

Figure 4. Correlation of shape measurements in different *HST*/ACS filters for the example of Abell 2261. The upper left panel shows the correlation of ellipticities measured in the F435W images compared to the combined *HST*/ACS catalogs. The upper right, lower left, and lower right panels show the same correlation for the F606W, F775W, and F814W catalogs. Also shown in each individual plot is the number of overlapping galaxies in the different catalogs.

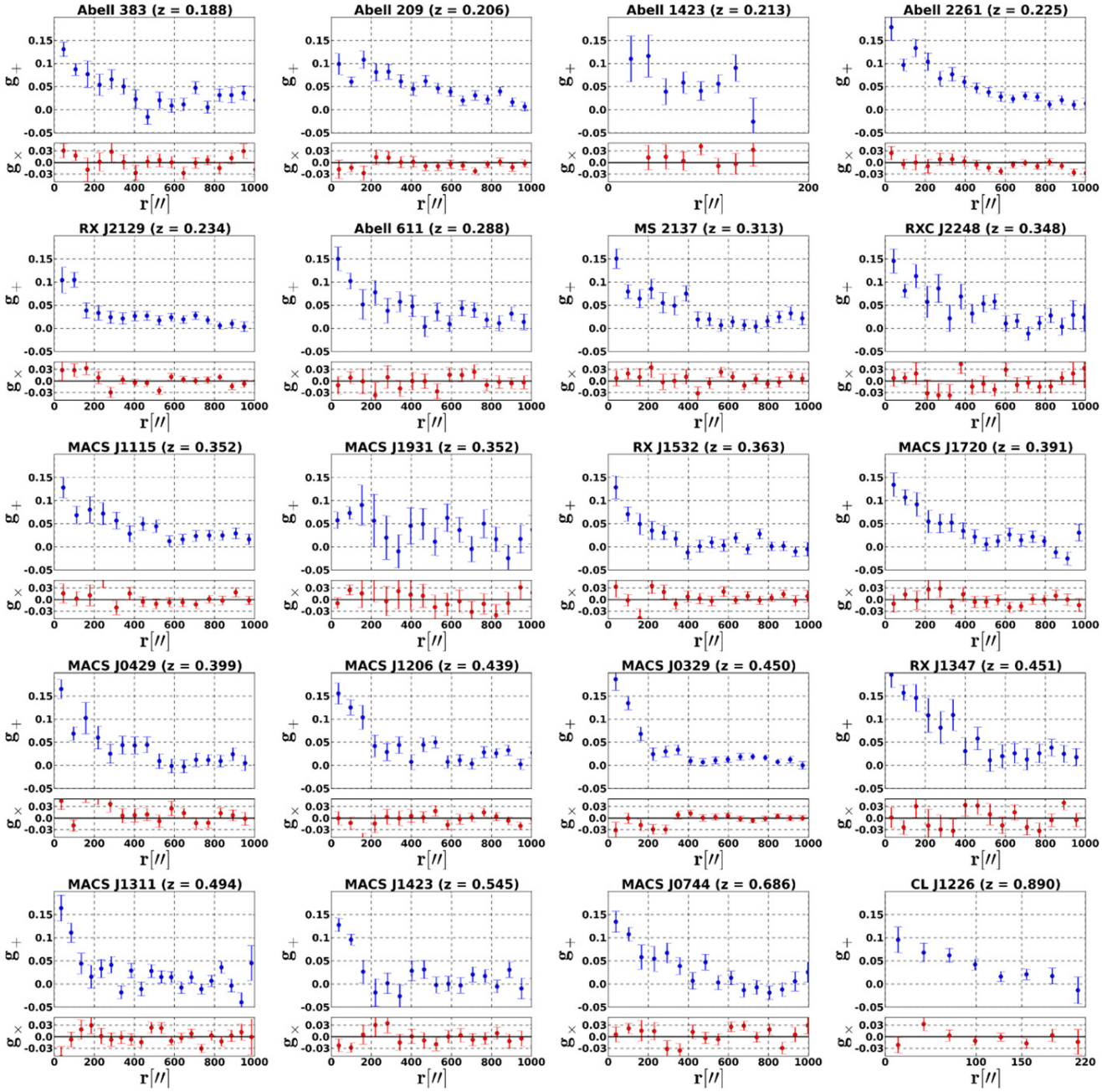

Figure 5. Shear profiles for the final ellipticity catalogs of 20 X-ray selected CLASH clusters. In the case of Abell 1423 and CL J1226 these catalogs derive from *HST*/ACS images only. All other cases show combined *HST*/ACS and Subaru catalogs. The top plot of each panel shows the tangential shear profile, the bottom plot the cross shear profile with respect to the cluster center defined in Table 1. 1σ error bars were derived from 250 bootstrap resamplings of each input catalog.

pipeline has been used in Umetsu et al. (2012), Coe et al. (2012), Medezinski et al. (2013), and Umetsu et al. (2014).

We perform object detection and shape measurements using the IMCAT package developed by N. Kaiser based on the KSB (Kaiser et al. 1995) formalism. After initial object detection, close pairs are carefully identified and rejected to avoid the effects of object crowding on shape measurements (see Section 4.3 of Umetsu et al. 2014). The PSF anisotropy correction is performed according to the Umetsu et al. (2010) KSB+ implementation using bright, un-saturated stars in the respective target fields. Following (Umetsu et al. 2010, see their Section 3.2.3) we calibrate KSB's isotropic correction factor as a function of object size and magnification by using galaxies detected with high significance ($\nu > 30$), in order to minimize the inherent shear calibration bias in the presence of noise. Finally, for each galaxy, shape measurements from different observation epochs and camera orientations are combined according to the prescription provided in Section 4.3 of Umetsu et al. (2014). The pipeline has been thoroughly tested with simulated Subaru/Suprime-Cam images (Massey et al. 2007; Oguri et al. 2012), where a multiplicative shear calibration bias of $|m| \simeq 5\%$ and a residual shear offset of $c \sim 10^{-3}$ were found. We correct individual shear estimates for the residual multiplicative bias as $g \rightarrow g/0.95$.

Table 4
Ground-based Weak-lensing Constraints

Name	Shape-band	$N_{\rm gal}$	$\rho_{\rm gal}$ (arcmin^{-2})	$z_{\rm eff}$
Abell 383	Ip	7062	9.0	1.16
Abell 209	Rc	14,694	16.4	0.94
Abell 1423[a]	…	…	…	…
Abell 2261	Rc	15,429	18.8	0.89
RX J2129+0005	Rc	20,104	24.5	1.16
Abell 611	Rc	7872	8.8	1.13
MS 2137−2353	Rc	9133	11.6	1.23
RXC J2248−4431	WFI R	4008	5.5	1.05
MACS J1115+0129	Rc	13,621	15.1	1.15
MACS J1931−26	Rc	4343	5.3	0.93
RX J1532.8+3021	Rc	13,270	16.6	1.15
MACS J1720+3536	Rc	9855	12.5	1.13
MACS J0429−02	Rc	9990	12.0	1.25
MACS J1206−08	Ic	12,719	13.7	1.13
MACS J0329−02	Rc	25,427	29.5	1.18
RX J1347−1145	Rc	9385	8.9	1.17
MACS J1311−03	Rc	13,748	20.2	1.07
MACS J1423+24	Rc	7470	9.8	0.98
MACS J0744+39	Rc	7561	9.5	1.41
CL J1226+3332[a]	…	…	…	…

Note. These values derive from the comprehensive CLASH weak lensing work by Umetsu et al. (2014). Column explanations are identical to Table 3.
[a] No ground-based data of sufficient data quality in terms of seeing, exposure time and band coverage was available at the time this work was published.

After the catalog with shape measurements has been created, weak-lensing background sources for each cluster are selected following the description in Section 4.4 of Umetsu et al. (2014). Here we shortly summarize the process. The selection is based on the color–color (CC) technique by Medezinski et al. (2010), which uses empircal correlations in CC space, calibrated with evolutionary color tracks of galaxies (Medezinski et al. 2010; Hanami et al. 2012) and with the 30 band photo-z distribution in the COSMOS field (Ilbert et al. 2009). This technique selects a pure sample of background galaxies with negligible contamination by foreground objects and cluster member galaxies. For the selection in CC space we usually use the Subaru/Suprime-Cam $B_J R_C z'$ photometry and our conservative selection criteria usually yield about 12 galaxies arcmin^{-2}.

3.4. Combination of Shear Catalogs

We combine the *HST* and ground-based catalogs into a single weak lensing catalog before the `SaWLens` reconstruction. In order to do so, we first correct for the different redshifts of the background populations in each catalog. We scale the two shear values in the *HST* catalogs with a factor

$$\beta = \frac{D_{\rm lS} D_H}{D_s D_{\rm lH}}, \tag{23}$$

which accounts for the dependence of the shear on the lensing geometry. Here, $D_{\rm lS}$ ($D_{\rm lH}$) is the angular diameter distance between the lens and the ground-based (*HST*) sample and D_s (D_H) is the angular diameter distance between the observer and the ground-based (*HST*) sample. After applying the correction β to the *HST* shapes, we match the two catalogs by calculating the signal-to-noise weighted mean of sources which appear in both catalogs and by concatenating non-matching entries in the two catalogs. As a final cross-check we calculate the tangential (g_+) and cross-shear ($g_\times$) components in azimuthal bins around the cluster center, which we show in Figure 5.

4. DENSITY PROFILES OF CLASH CLUSTERS

Our mass reconstructions with associated error bars are used to fit NFW profiles to the surface-mass density distribution. Mass and concentration parameters for each of the X-ray selected CLASH clusters are the main result of our observational efforts.

4.1. Final `SaWLens` Input and Results

We summarize the basic parameters of each cluster reconstruction in Table 5, including input data, reconstructed field sizes and the refinement levels of the multi-scale grid. For two sample clusters, Abell 1423 and CL J1226, no multi-band wide-field weak lensing data with acceptable seeing and exposure time levels is available. In the case of CL J1226 this is less severe since we have access to a rather wide *HST*/ACS mosaic and, since the cluster resides at high redshift, the angular size of the reconstruction refers to a large physical size of the system. We therefore include CL J1226 in our following mass-concentration analysis, while we drop Abell 1423 from this sample.

The output of the reconstruction is the lensing potential on a multi-scale grid, which is then converted into a convergence or surface-mass density map via Equation (7). The convergence maps on a wide field for all sample clusters are shown in Figure 15. We base our follow-up analysis on these maps, together with a comprehensive assessment of their error budget.

4.2. Error Estimation

Non-parametric methods, especially when they include nonlinear constraints in the strong-lensing regime, do not offer a straight-forward way to analytically describe the error bars attached to reconstructed quantities (van Waerbeke 2000). We therefore follow the route of resampling the input catalogs to obtain error bars on our reconstructed convergence maps. The weak-lensing input is treated by bootstrap resampling the shear catalogs (see, e.g., Bradač et al. 2005a; Merten et al. 2011). For the strong-lensing input, we use two different criteria to re-sample our input catalogs. First, in each realization we radomly turn and off multiple images which were identified as only candidates by the Zitrin et al. (2009) method. The list of candidate system for each cluster has been published in Zitrin et al. (2014). Second, we randomly sample a redshift in the 95% confidence interval of the photo-z estimate of each multiple-image system. Also these redshift intervals are provided in Zitrin et al. (2014). With this strategy of catalog re-sampling in the weak -and the strong-lensing regime, we sequentially repeat the reconstructions and create 1000 realizations for each cluster reconstruction. This number is chosen somewhat arbitrarily but is primarily driven by runtime considerations, due to the high numerical demands of non-parametric reconstruction methods. From the observed scatter in the ensemble of realizations we derive our error bars, e.g., in the form of a covariance matrix for binned convergence profiles, as we describe them in the following section.

Table 5
Reconstruction Properties

Name	Input Data[a]	Ground-based FOV (″ × ″)	*HST* FOV (″ × ″)	Δ_{ground}[b] (″)	Δ_{ACS}[c] (″)	Δ_{SL}[d] (″)	$\#_{masks}$[e]
Abell 383	S, A, H	1500 × 1500	173 × 173	29	12	10	2
Abell 209	S, A, H	1500 × 1500	150 × 150	25	12	8	2
Abell 1423	H	…	200 × 200	…	13	…	…
Abell 2261	S, A, H	1500 × 1500	150 × 150	25	13	8	2
RX J2129+0005	S, A, H	1500 × 1500	150 × 150	25	10	8	3
Abell 611	S, A, H	1400 × 1400	168 × 168	28	10	9	1
MS 2137−2353	S, A, H	1500 × 1500	180 × 180	30	14	10	1
RXC J2248−4431	W, A, H	1500 × 1500	171 × 171	34	12	11	7
MACS J1115+0129	S, A, H	1500 × 1500	150 × 150	25	10	8	2
MACS J1931−26	S, A, H	1500 × 1500	179 × 179	36	10	10	0
RX J1532.8+3021	S, A	1500 × 1500	155 × 155	26	10	…	3
MACS J1720+3536	S, A, H	1500 × 1500	150 × 150	25	9	8	3
MACS J0429−02	S, A, H	1500 × 1500	167 × 167	28	10	9	3
MACS J1206−08	S, A, H	1500 × 1500	150 × 150	25	12	8	0
MACS J0329−02	S, A, H	1500 × 1500	150 × 150	25	9	8	0
RX J1347−1145	S, A, H	1500 × 1500	180 × 180	30	12	10	1
MACS J1311−03	S, A, H	1500 × 1500	150 × 150	25	10	8	6
MACS J1423+24	S, A, H	1500 × 1500	155 × 155	26	8	8	2
MACS J0744+39	S, A, H	1500 × 1500	150 × 150	30	9	7	4
CL J1226+3332	A, H	…	300 × 300	…	8	6	0

[a] "S" stands for Subaru weak lensing data, "W" stands for ESO/WFI weak lensing data, "A" stands for *HST*/ACS weak lensing data and "H" stands for *HST* strong lensing data.
[b] The pixel size of the grid in the Subaru or ESO/WFI weak lensing regime.
[c] The pixel size of the grid in the *HST*/ACS weak lensing regime.
[d] The pixel size of the grid in the strong lensing regime.
[e] The number of masks in the reconstruction grid. There are necessary if bright stars blend large portions of the FOV.

4.3. From Convergence Maps to NFW Profile Parameters

Additional steps are needed to go from non-parametric maps of the surface-mass density distribution to an actual NFW fit of the halo. First, since we are interested in 1D density profiles, we apply an azimuthal binning scheme, with a bin pattern that follows the adaptive resolution of our multi-scale maps. The initial bin is limited by the resolution of the highest refinement level of the convergence grid (compare Table 5) and the outermost bin is set to a physical scale of 2 Mpc/h for each halo. We split the radial range defined by the two thresholds into 15 bins. An example for the cluster MACS J1720 is shown in Figure 6. An exception is CL J1226 with no available wide-field data from the ground, where we were limited to a maximum radius of 1.2 Mpc/h and where we divided the radial range into 11 bins. The center for the radial profile is the dominant peak in the convergence map. We applied this binning scheme to all 1000 convergence realizations for each cluster and derived the covariance matrix for the convergence bins. Both the convergence data points and the convergence matrix are shown in Figure 16.

To the convergence bins and the corresponding covariance matrix we fit a NFW profile given by Equation (1). We numerically project the NFW profile on a sphere along the line-of-sight and thereby introduce the assumption of spherical symmetry in our cluster mass profiles. This is certainly not justified for all sample clusters and may introduce biases. We discuss this issue in further detail in Section 6.

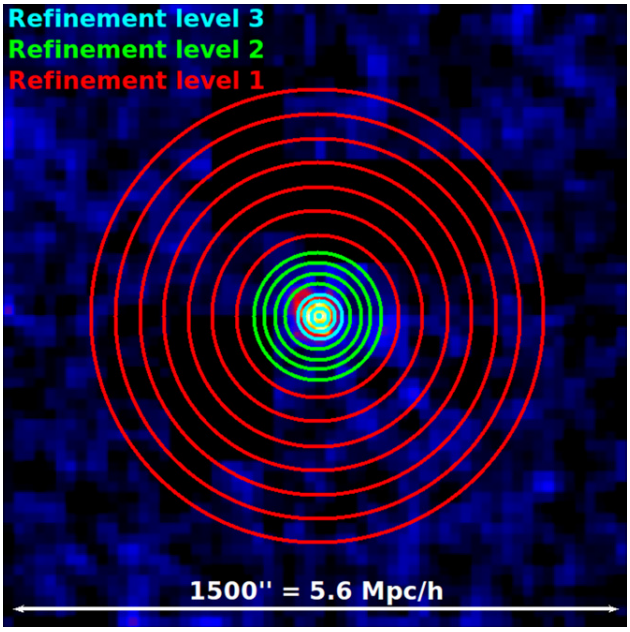

Figure 6. Adaptive binning scheme for the radial convergence profiles. Shown in this figure are the actual bins, overlaid on the cluster's convergence map, used to derive the convergence profile for the cluster MACS J1720 (compare Figure 16). The size of the bins follows the three levels of grid refinement as they are visualized in Figure 1 and listed in Table 5.

Table 6
NFW Fits: General Parameters

Name	$\rho_s \pm \sqrt{\sigma_{\rho_s\rho_s}}$ $\left(10^{15}h^2\ M_\odot\ \mathrm{Mpc}^{-3}\right)$	$r_s \pm \sqrt{\sigma_{r_sr_s}}$ (Mpc/h)	$\sigma_{\rho_s r_s}$ $\left(10^{15}h\ M_\odot\ \mathrm{Mpc}^{-2}\right)$	Δ_{vir}[a]	r_{vir} (Mpc/h)	(χ^2)[b]
Abell 383	2.47 ± 0.59	0.33 ± 0.04	−0.02	111	1.86	2.0
Abell 209	1.14 ± 0.29	0.46 ± 0.07	−0.02	112	1.95	2.9
Abell 1423	…	…	…	113	…	…
Abell 2261	1.07 ± 0.41	0.51 ± 0.11	−0.05	114	2.26	3.7
RX J2129+0005	2.16 ± 0.67	0.30 ± 0.05	−0.04	114	1.65	5.3
Abell 611	1.36 ± 0.32	0.41 ± 0.06	−0.02	118	1.79	4.1
MS 2137−2353	1.14 ± 0.20	0.48 ± 0.05	−0.01	120	1.89	1.5
RXC J2248−4431	1.24 ± 0.34	0.48 ± 0.07	−0.02	122	1.92	1.3
MACS J1115+0129	0.61 ± 0.17	0.62 ± 0.11	−0.02	123	1.78	5.6
MACS J1931−26	1.22 ± 0.31	0.41 ± 0.07	−0.02	123	1.61	4.2
RX J1532.8+3021	1.16 ± 0.52	0.39 ± 0.10	−0.05	123	1.47	6.9
MACS J1720+3536	2.44 ± 0.84	0.31 ± 0.06	−0.05	125	1.61	4.2
MACS J0429−02	1.37 ± 0.57	0.41 ± 0.08	−0.05	126	1.65	1.9
MACS J1206−08	2.60 ± 0.94	0.31 ± 0.06	−0.05	128	1.63	4.9
MACS J0329−02	2.05 ± 0.84	0.33 ± 0.08	−0.06	129	1.54	6.3
RX J1347−1145	2.10 ± 0.90	0.38 ± 0.08	−0.07	129	1.80	3.2
MACS J1311−03	2.97 ± 0.62	0.24 ± 0.03	−0.02	131	1.28	4.0
MACS J1423+24	3.70 ± 1.83	0.24 ± 0.06	−0.11	134	1.34	6.4
MACS J0744+39	3.18 ± 0.71	0.28 ± 0.04	−0.03	141	1.33	3.2
CL J1226+3332	3.72 ± 0.83	0.35 ± 0.05	−0.04	150	1.57	2.7

[a] The virial overdensity at cluster redshift in units of the critical density.
[b] The number of degrees of freedom is 10 in the case of CL J1226 and 14 for all other clusters.

Table 7
NFW Fits: Mass-concentration Parameters

Name	M_{2500c} $(10^{15}\ M_\odot/h)$	c_{2500c}	M_{500c} $(10^{15}\ M_\odot/h)$	c_{500c}	M_{200c} $(10^{15}\ M_\odot/h)$	c_{200c}	M_{vir} $(10^{15}\ M_\odot/h)$	c_{vir}
Abell 383	0.26 ± 0.05	1.3 ± 0.3	0.61 ± 0.07	2.9 ± 0.7	0.87 ± 0.07	4.4 ± 1.0	1.04 ± 0.07	5.6 ± 1.3
Abell 209	0.22 ± 0.05	0.9 ± 0.3	0.63 ± 0.07	2.1 ± 0.6	0.95 ± 0.07	3.3 ± 0.9	1.17 ± 0.07	4.3 ± 1.1
Abell 1423	…	…	…	…	…	…	…	…
Abell 2261	0.34 ± 0.12	0.9 ± 0.4	0.95 ± 0.16	2.2 ± 0.9	1.42 ± 0.17	3.4 ± 1.4	1.76 ± 0.18	4.4 ± 1.8
RX J2129+0005	0.18 ± 0.03	1.2 ± 0.4	0.43 ± 0.04	2.8 ± 0.9	0.61 ± 0.06	4.3 ± 1.4	0.73 ± 0.07	5.6 ± 1.7
Abell 611	0.21 ± 0.04	0.9 ± 0.3	0.57 ± 0.04	2.2 ± 0.6	0.85 ± 0.05	3.4 ± 0.9	1.03 ± 0.07	4.3 ± 1.1
MS 2137−2353	0.23 ± 0.04	0.8 ± 0.2	0.68 ± 0.05	2.0 ± 0.4	1.04 ± 0.06	3.1 ± 0.6	1.26 ± 0.06	4.0 ± 0.7
RXC J2248−4431	0.27 ± 0.07	0.8 ± 0.3	0.76 ± 0.12	2.0 ± 0.6	1.16 ± 0.12	3.2 ± 0.9	1.40 ± 0.12	4.0 ± 1.1
MACS J1115+0129	0.15 ± 0.05	0.5 ± 0.2	0.54 ± 0.08	1.4 ± 0.4	0.90 ± 0.09	2.3 ± 0.7	1.13 ± 0.10	2.9 ± 0.9
MACS J1931−26	0.16 ± 0.03	0.8 ± 0.2	0.45 ± 0.04	2.0 ± 0.6	0.69 ± 0.05	3.2 ± 0.9	0.83 ± 0.06	3.9 ± 1.1
RX J1532.8+3021	0.11 ± 0.05	0.8 ± 0.4	0.34 ± 0.08	1.9 ± 0.9	0.53 ± 0.08	3.0 ± 1.4	0.64 ± 0.09	3.8 ± 1.7
MACS J1720+3536	0.22 ± 0.06	1.2 ± 0.5	0.53 ± 0.08	2.8 ± 1.0	0.75 ± 0.08	4.3 ± 1.4	0.88 ± 0.08	5.2 ± 1.7
MACS J0429−02	0.19 ± 0.11	0.9 ± 0.4	0.53 ± 0.13	2.1 ± 0.9	0.80 ± 0.14	3.3 ± 1.3	0.96 ± 0.14	4.0 ± 1.6
MACS J1206−08	0.25 ± 0.08	1.2 ± 0.5	0.60 ± 0.11	2.8 ± 1.0	0.86 ± 0.11	4.3 ± 1.5	1.00 ± 0.11	5.2 ± 1.7
MACS J0329−02	0.20 ± 0.06	1.1 ± 0.4	0.50 ± 0.09	2.5 ± 1.1	0.73 ± 0.10	3.8 ± 1.6	0.86 ± 0.11	4.7 ± 1.9
RX J1347−1145	0.31 ± 0.13	1.1 ± 0.5	0.79 ± 0.19	2.5 ± 1.1	1.16 ± 0.19	3.9 ± 1.5	1.35 ± 0.19	4.7 ± 1.8
MACS J1311−03	0.14 ± 0.02	1.3 ± 0.3	0.32 ± 0.19	2.9 ± 0.6	0.46 ± 0.03	4.4 ± 1.0	0.53 ± 0.04	5.3 ± 1.1
MACS J1423+24	0.18 ± 0.08	1.4 ± 0.8	0.41 ± 0.06	3.1 ± 0.8	0.57 ± 0.10	4.7 ± 1.2	0.65 ± 0.11	5.7 ± 2.8
MACS J0744+39	0.20 ± 0.03	1.2 ± 0.3	0.49 ± 0.04	2.7 ± 0.6	0.70 ± 0.04	4.1 ± 1.0	0.79 ± 0.04	4.8 ± 1.1
CL J1226+3332	0.43 ± 0.07	1.1 ± 0.3	1.08 ± 0.09	2.6 ± 0.6	1.56 ± 0.10	4.0 ± 0.9	1.72 ± 0.11	4.5 ± 1.1

We perform the profile fitting using the least-squares formalism by minimizing

$$\chi^2(\boldsymbol{p}) = \sum_{i,j=0}^{N_{\mathrm{bin}}} \left(\kappa_{\mathrm{bin}} - \kappa(\boldsymbol{p})\right)_i C_{ij}^{-1} \left(\kappa_{\mathrm{bin}} - \kappa(\boldsymbol{p})\right)_j, \qquad (24)$$

where $\boldsymbol{p} = (\rho_s, r_s)$ and C is the covariance matrix of the binned data. The numerical fitting is performed using the open-source library `levmar`[35] and by making use of the Cholesky decomposition of C^{-1}. The best-fit parameters, the corresponding covariance matrix and the fitting norm is reported in Table 6. We use these values, together with Equations (2) and (3) to find our final mass and concentration values at several different radii. We report this central result of our work in

[35] http://users.ics.forth.gr/lourakis/levmar/

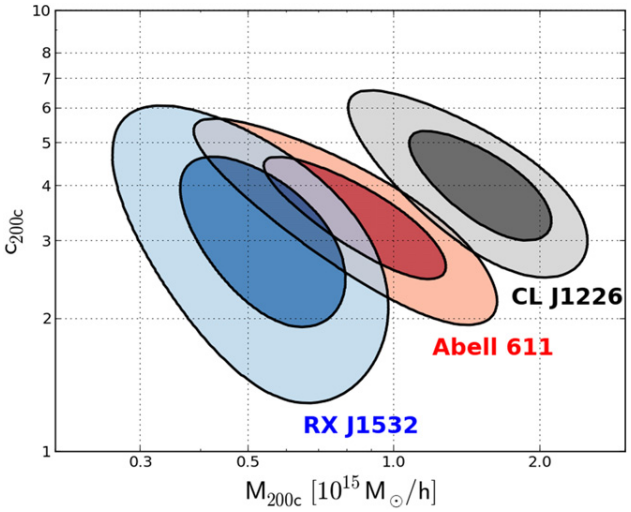

Figure 7. Likelihood of NFW fits in the c–M plane. The cluster Abell 611 represents a typical CLASH cluster at an intermediate redshift with the full set of lensing constraints available. RX J1532 is the only cluster in this c–M analysis without strong lensing constraints and CL J1226 is the only cluster in the sample without available Subaru weak lensing data. The inner and outer contours show the 68% and 95% confidence levels.

Table 7. To visualize degeneracies and to show the information gain when including strong-lensing features into the reconstruction we explore the likelihood in the c–M plane for three CLASH clusters in Figure 7.

4.4. Sources of Systematic Error

Before moving on in our analysis we want to discuss possible sources of systematic error. In the strong-lensing regime there is the possibility of false identification of multiple-image systems. In the case of CLASH, many strong-lensing features have no spectroscopic confirmation. However, CLASH can rely on 16-band *HST* photometry for photo-z determination. Finally, those systems which are only identified as candidates by the Zitrin et al. (2009) method for image identification are considered as such in our extensive bootstrap approach. Another problem for strong lensing is the shift of multiple-image positions by contributions of projected large scale structure. This has been pointed out recently in D'Aloisio & Natarajan (2011), Host (2012). However, as it was shown by the latter authors, the expected shift in image postion is well below our minimum reconstruction pixel scale of 5″–10″ for the different clusters (compare Figure 2).

We address shape scatter in the weak-lensing catalogs with the adaptive-averaging approach of the `SawLens` method and by bootstrapping the weak-lensing input. Foreground contamination of the shear catalogs is another serious concern which will lead to a significant dilution of the weak lensing signal. In the *HST* images this is controlled by reliable photometric redshifts. However, there is the possibility of remaining contamination by cluster members in the crowded fields and by stars falsely identified as galaxies. Background selection in the ground-based catalogs is more difficult due to the smaller number of photometric bands. Hence, we use the Medezinski et al. (2010) method of background selection in color–color space which was optimized to avoid weak lensing dilution.

The aforementioned mass-sheet degeneracy (Equation (11)) is another concern for systematic error. We described the way of breaking this degeneracy in this work and tested the validity of this approach against numerical simulations (Merten et al. 2009; Meneghetti et al. 2010b). However, these simulations represent a much smaller sample and derive from a different selection function than the CLASH sample. Furthermore, the box-sizes of these cluster re-simulations is limited and therefore these tests do not guarantee that our treatment of the mass-sheet degeneracy produces fully unbiased mass estimates.

We have not commented yet on the dominant density peak in the lensing reconstruction as our center choice for the radial density profile. Because of the inclusion of strong lensing constraints, this peak position has an uncertainty of only a few arcsec (e.g., Bradač et al. 2006; Merten et al. 2011), but one might argue that e.g., the position of the cluster's BCG is a more accurate tracer of the potential minimum. However, our pixel resolution is of the order of ∼5″ and BCG position and the peak in the surface-mass density coincide or are offset by one or two pixels.

More important is the effect of uncorrelated large scale structure (e.g., Hoekstra et al. 2011, and references therein) and tri-axial halo shape (Becker & Kravtsov 2011) which is picked up by our lensing reconstruction. Becker & Kravtsov (2011) claim that these effects introduce only small biases in the mass determination but increase the scatter by up to 20% with tri-axial shape being the dominant component. We do not seek to correct for these effects directly but adapt our way of analyzing numerical simulations accordingly (Section 6). In order to quantify our total error budget, we refer to Meneghetti et al. (2010b) where our `SaWLens` approach of mass-modeling underwent a thorough testing procedure in a controlled, simulated environment. Based on these results we report a systematic error between 5%–10%, depending on the level of substructure in the halo of interest.

4.5. Comparison to Other Analyses

As a final consistency check we look into 15 clusters that we have in common with the Weighing the Giants (dubbed as WtG hereafter) project (Applegate et al. 2014; Kelly et al. 2014; von der Linden et al. 2014) and the 16 clusters we have in common with the CLASH shear and magnification study by Umetsu et al. (2014; dubbed as U14 hereafter). For the direct comparison to WtG and U14 we calculate the enclosed mass within 1.5 Mpc of the cluster center following Applegate et al. (2014). This is to have a meaningful comparison at a fixed phyiscal radius and not to have to correct for the different mass apertures. We also used the cosmology of WtG to derive the masses for this comparison and show the mass comparison for the three data sets in Figure 8. We find median values for the ratios $M_{\rm SaWLens}/M_{\rm WtG}$ and $M_{\rm WtG}/M_{\rm SaWLens}$ of $0.88^{+0.10}_{-0.06}$ and $1.12^{+0.06}_{-0.10}$, respectively. The upper and lower bounds derive from the third and first quartile of the ratio sample. For the unweighted geometric mean[36] of these ratios we find 0.94 ± 0.11. The respective numbers for the 16 cluster comparison to U14 are $0.93^{+0.14}_{-0.09}$ and $1.08^{+0.11}_{-0.14}$ for the median of the ratios $M_{\rm SaWLens}/M_{\rm U14}$ and $M_{\rm U14}/M_{\rm SaWLens}$. The geometric mean of the ratios yields 0.95 ± 0.06. Although we see

[36] The geometric mean satisfies $\langle X/Y\rangle = 1/\langle Y/X\rangle$ for the ratio of samples X and Y.

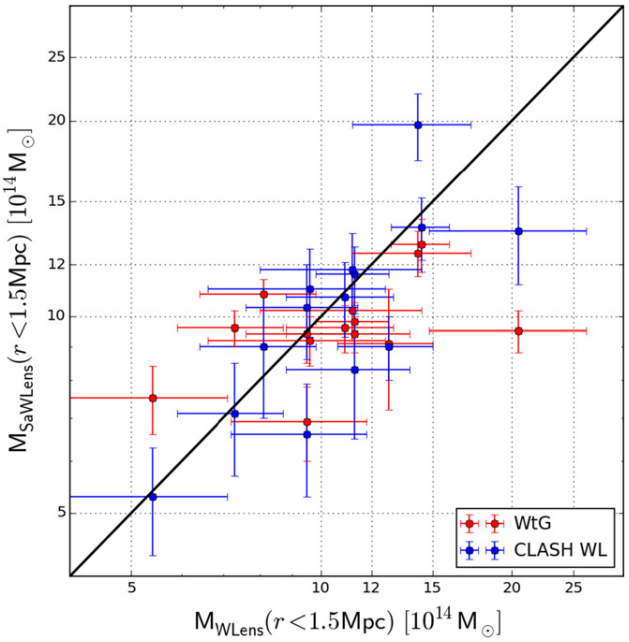

Figure 8. Comparison between our analysis and other weak-lensing studies. The red data points show clusters in common with WtG and the blue data points show the overlap with Umetsu et al. (2014). On the y-axis we plot enclosed `SaWLens` masses within a radius of 1.5Mpc from the cluster center. The x-axis shows equivalent masses from WtG and U14, respectively. The black line indicates a one-to-one agreement.

significant scatter between the different studies, there is general agreement but we have to point out that our analysis and U14 use identical Subaru weak-lensing catalogs. In the following subsections we report these different mass estimates cluster by cluster and also consult other studies of a specific object.

For a comparison of our mass estimates to X-ray masses we want to refer to the recent work by Donahue et al. (2014), where X-ray mass profiles from *Chandra* and *XMM-Newton* were compared to the lensing-derived profiles of U14 and to our profiles reported in Table 6. Donahue et al. (2014) find that *Chandra* masses at 0.5 Mpc, assuming hydrostatic equilibrium, are on average 11% larger than the masses presented in this work for a sample of 10 clusters that the studies have in common. For hydrostatic masses from *XMM-Newton* at 0.5 Mpc, the opposite trend was found, where for a sample of 13 common clusters our lensing masses were 18% higher than the X-ray masses.

4.5.1. Abell 383

This cluster at $z = 0.188$ is one of the first clusters studied by CLASH Zitrin et al. (2011). In the mass comparison with WtG, our value of $M_{1.5\mathrm{Mpc}} = 9.6 \pm 0.6 \times 10^{14} M_\odot$ is larger than $M_{1.5\mathrm{Mpc}} = 7.3 \pm 1.4 \times 10^{14} M_\odot$ of WtG at the $\sim 1.5\sigma$ level, which is consistent with the findings of U14 with $M_{1.5\,\mathrm{Mpc}} = 7.1 \pm 1.4 \times 10^{14} M_\odot$. To have another independent study we refer to Newman et al. (2013) who find $M_{1.7\mathrm{Mpc}} = 6.6^{+1.5}_{-1.1} \times 10^{14} M_\odot$ for this object. The mass from our model at the same radius yields $M_{1.7\,\mathrm{Mpc}} = 10.7 \pm 0.7 \times 10^{14} M_\odot$, which is again in some tension. The reason for this discrepancy is unclear, especially since Abell 383 is thought to be a rather relaxed object. However, the tension is also not very significant.

4.5.2. Abell 209

Our lensing reconstruction of this system at $z = 0.206$ suggests a rather massive but regular system with respect to the morphology in its surface-mass density map. This is supported by our derived mass of $M_{1.5\mathrm{Mpc}} = 9.8 \pm 0.7 \times 10^{14} M_\odot$, which compares well to the findings of U14 with $M_{1.5\mathrm{Mpc}}$=11.6 $\pm$ 1.2 $\times$ $10^{14} M_\odot$ and WtG with $M_{1.5\mathrm{Mpc}} = 11.3 \pm 1.5 \times 10^{14} M_\odot$. An earlier study by Paulin-Henriksson et al. (2007) reports $M_{1.8\mathrm{Mpc}} = 7.7^{+4.3}_{-2.7} \times 10^{14} M_\odot$ and we compare to our result at the same radius and using the same cosmology of $M_{1.8\mathrm{Mpc}} = 11.7 \pm 0.9 \times 10^{14} M_\odot$, which shows no significant tension but a higher mass. We would expect such a result since the background selection of weak-lensing galaxies in Paulin-Henriksson et al. (2007) was based on single-band data which is plagued by severe dilution effects (Medezinski et al. 2007, 2008).

4.5.3. Abell 2261

Abell 2261 at $z = 0.225$ is one of the most massive clusters in our sample with one of the largest BCGs observed (Postman et al. 2012b). Our mass estimate of $M_{1.5\mathrm{Mpc}} = 12.9 \pm 1.2 \times 10^{14} M_\odot$ is in excellent agreement with $M_{1.5\mathrm{Mpc}} = 13.7 \pm 1.5 \times 10^{14} M_\odot$ by U14 and $M_{1.5\mathrm{Mpc}} = 14.4 \pm 1.5 \times 10^{14} M_\odot$ by WtG. An earlier CLASH study by Coe et al. (2012) derived a virial mass of $M_{\mathrm{vir}} = 22.1^{+2.5}_{2.3} \times 10^{14} M_\odot$, which compares well to our virial mass estimate of $M_{\mathrm{vir}} = 25.1 \pm 2.5 \times 10^{14} M_\odot$.

4.5.4. RXJ 2129

This low-mass system at $z = 0.234$ shows some interesting morphology in the surface-mass density map of its core (see Figure 15). Since our fitting range starts at smaller radii, this might explain why our mass of $M_{1.5\mathrm{Mpc}} = 7.5 \pm 0.9 \times 10^{14} M_\odot$ is larger, although insignificantly, than $M_{1.5\mathrm{Mpc}} = 5.4 \pm 1.7 \times 10^{14} M_\odot$ by WtG and shows some more tension with $M_{1.5\mathrm{Mpc}} = 5.3 \pm 1.0 \times 10^{14} M_\odot$ by U14.

4.5.5. Abell 611

Also Abell 611 at $z = 0.288$ was studied by Newman et al. (2013) where a mass of $M_{1.76\mathrm{Mpc}} = 8.3^{+1.5}_{-1.2} \times 10^{14} M_\odot$ is reported. At this radius we find $M_{1.76\mathrm{Mpc}} = 10.9 \pm 1.1 \times 10^{14} M_\odot$, in good agreement with this former study, and also our value of $M_{1.5\mathrm{Mpc}} = 9.4 \pm 0.9 \times 10^{14} M_\odot$ is in agreement with $M_{1.5\mathrm{Mpc}} = 9.5 \pm 1.9 \times 10^{14} M_\odot$ by WtG. This picture is further confirmed by U14 with $M_{1.5\mathrm{Mpc}} = 10.3 \pm 1.7 \times 10^{14} M_\odot$.

4.5.6. MS 2137

MS 2137 is a well-studied cluster at $z = 0.313$ for which we find a rather high mass of $M_{1.5\mathrm{Mpc}} = 10.8 \pm 0.6 \times 10^{14} M_\odot$, compared to $M_{1.5\mathrm{Mpc}} = 8.1 \pm 1.7 \times 10^{14} M_\odot$ by WtG and $M_{1.5\mathrm{Mpc}} = 9.0 \pm 2.0 \times 10^{14} M_\odot$ by U14. Also Newman et al. (2013) looked at this system and found $M_{1.32\mathrm{Mpc}} = 3.6^{+1.3}_{-0.8} \times 10^{14} M_\odot$. For this aperture however, we find

$M_{1.32\mathrm{Mpc}} = 6.4 \pm 0.4 \times 10^{14}\,M_\odot$, indicating a significantly higher mass from our reconstruction.

4.5.7. RXCJ 2248

This clusters is another very massive system at $z = 0.348$ and part of the *HST* Frontier Fields initiative.[37] RXCJ 2248 is not part of the WtG program but our mass of $M_{1.5\mathrm{Mpc}} = 11.8 \pm 0.7 \times 10^{14}\,M_\odot$ agrees well with U14's $M_{1.5\mathrm{Mpc}} = 12.0 \pm 2.0 \times 10^{14}\,M_\odot$ and as an independent cross-check we refer to Melchior et al. (2015) presenting a cluster study of the Science Verification Data of the Dark Energy Survey (The Dark Energy Survey Collaboration 2005). Although they do not provide the exact radius of their mass-measurement aperture, they report $M_{200c} = 17.6 \pm 4.5 \times 10^{14}\,M_\odot$, which is in good agreement with our value of $M_{200c} = 16.6 \pm 1.7 \times 10^{14}\,M_\odot$, when assuming that the enclosed-mass apertures are similar. With the same assumption we finally quote another recent mass estimate by Gruen et al. (2013), which yields $M_{200c} = 22.8^{+6.6}_{-4.7} \times 10^{14}\,M_\odot$, also in agreement with the other mass estimates, although it has to be noted that the Gruen et al. (2013) result is based on the same imaging data as our work.

4.5.8. MACS J1115

For this system at $z = 0.352$ we also find excellent agreement between all mass measurements. Our mass of $M_{1.5\mathrm{Mpc}} = 9.6 \pm 0.8 \times 10^{14}\,M_\odot$ compares to $M_{1.5\mathrm{Mpc}} = 10.9 \pm 2.1 \times 10^{14}\,M_\odot$ by WtG and $M_{1.5\mathrm{Mpc}} = 10.7 \pm 1.4 \times 10^{14}\,M_\odot$ by U14.

4.5.9. MACS J1931

For this cluster at $z = 0.352$ we have no overlap with the WtG progam but U14 find $M_{1.5\mathrm{Mpc}} = 11.0 \pm 2.9 \times 10^{14}\,M_\odot$, which is consistent with our value $M_{1.5\mathrm{Mpc}} = 8.3 \pm 1.0 \times 10^{14}\,M_\odot$ within the large uncertainties. This is due to a low number of useable background galaxies in the MACS J1931 field at a low Galactic latitude (see Section 4.4 of Umetsu et al. 2014).

4.5.10. RXJ 1532

Situated at $z = 0.363$, this is another low-mass system for which we find $M_{1.5\mathrm{Mpc}} = 6.9 \pm 0.9 \times 10^{14}\,M_\odot$, in good agreement with U14 who quote $M_{1.5\mathrm{Mpc}} = 6.6 \pm 1.3 \times 10^{14}\,M_\odot$ and consistent with the WtG value $M_{1.5\mathrm{Mpc}} = 9.5 \pm 2.3 \times 10^{14}\,M_\odot$.

4.5.11. MACS J1720

MACS J1720 at $z = 0.391$ shows good agreement between the mass from WtG with $M_{1.5\mathrm{Mpc}} = 9.6 \pm 3.0 \times 10^{14}\,M_\odot$, U14 with $M_{1.5\mathrm{Mpc}} = 11.0 \pm 1.7 \times 10^{14}\,M_\odot$ and our value of $M_{1.5\mathrm{Mpc}} = 9.2 \pm 0.8 \times 10^{14}\,M_\odot$.

4.5.12. MACS J0429

For MACS J0429 at $z = 0.399$ we find a higher mass of $M_{1.5\mathrm{Mpc}} = 9.4 \pm 0.6 \times 10^{14}\,M_\odot$ than U14 with $M_{1.5\mathrm{Mpc}} = 8.3 \pm 1.8 \times 10^{14}\,M_\odot$, but a lower mass than WtG with $M_{1.5\mathrm{Mpc}} = 11.3 \pm 2.5 \times 10^{14}\,M_\odot$. All quoted values are in agreement within their 68% confidence interval error bars.

[37] http://www.stsci.edu/hst/campaigns/frontier-fields/

4.5.13. MACS J1206

The well-studied CLASH cluster MACS J1206 at $z = 0.439$ was the first cluster analyzed with our new CLASH Subaru weak-lensing pipeline in Umetsu et al. (2012). In this earlier work we report a virial mass of $M_{\mathrm{vir}} = 16.4^{+4.9}_{-4.0} \times 10^{14}\,M_\odot$, which is in good agreement with our vitial mass $M_{\mathrm{vir}} = 14.3 \pm 1.6 \times 10^{14}\,M_\odot$. The same is true when comparing to the analysis of Biviano et al. (2013) which is based on the dynamics of cluster member galaxies and yields $M_{2.0\mathrm{Mpc}} = 14.0 \pm 2.0 \times 10^{14}\,M_\odot$ in excellent agreement with our value of $M_{2.0\mathrm{Mpc}} = 12.9 \pm 1.3 \times 10^{14}\,M_\odot$, after we adopt the background cosmology of Biviano et al. (2013). When comparing to the more recent analysis of U14 and WtG at smaller radius, we find $M_{1.5\mathrm{Mpc}} = 10.2 \pm 1.0 \times 10^{14}\,M_\odot$ for our work, $M_{1.5\mathrm{Mpc}} = 11.8 \pm 1.6 \times 10^{14}\,M_\odot$ for U14 and $M_{1.5\mathrm{Mpc}} = 11.2 \pm 3.2 \times 10^{14}\,M_\odot$ for WtG, respectively.

4.5.14. MACS J0329

This cluster at $z = 0.450$ shows quite some interesting morphology in its central surface-mass density map, with a very broad and flat inner core, which was already reported in Zitrin et al. (2012a). This might explain the somewhat lower mass from our NFW fit which yields $M_{1.5\mathrm{Mpc}} = 9.1 \pm 1.9 \times 10^{14}\,M_\odot$ compared to $M_{1.5\mathrm{Mpc}} = 12.8 \pm 2.2 \times 10^{14}\,M_\odot$ from WtG. However, U14 find $M_{1.5\mathrm{Mpc}} = 9.1 \pm 1.0 \times 10^{14}\,M_\odot$, which is in excellent agreement with our result.

4.5.15. RXJ 1347

This well-known cluster at $z = 0.451$ was subject to many strong-lensing studies (e.g., Bradač et al. 2005a; Halkola et al. 2008, and references therein) at small radii. In order to compare our estimate for the total mass, for which we find $M_{1.5\mathrm{Mpc}} = 12.5 \pm 1.0 \times 10^{14}\,M_\odot$, we quote the number by WtG $M_{1.5\mathrm{Mpc}} = 14.2 \pm 3.0 \times 10^{14}\,M_\odot$, which is in good agreement. However, U14 find a much larger value of $M_{1.5\mathrm{Mpc}} = 19.7 \pm 2.3 \times 10^{14}\,M_\odot$. In an ealier study, Broadhurst et al. (2008) quote a virial mass of $M_{\mathrm{vir}} = 14.7^{+2.6}_{-2.3} \times 10^{14}\,M_\odot$, which is interestingly enough smaller than our estimate of $M_{\mathrm{vir}} = 19.3 \pm 2.7 \times 10^{14}\,M_\odot$. The reason for this inconsistently diverting mass estimates is not entirely clear to us, but we suspect that the different fitting ranges for the NFW fits might play a crucial role in the mass estimates for disturbed systems such as RX J1347.

4.5.16. MACS J1423

For this system at $z = 0.545$ we only have the comparison to the WtG analysis. Depending on the method of weak-lensing background selection, they report quite different mass estimates in Applegate et al. (2014). For a color-selected background selection they find $M_{1.5\mathrm{Mpc}} = 3.7 \pm 2.8 \times 10^{14}\,M_\odot$, while for a selection based on the full photo-z distribution function they quote $M_{1.5\mathrm{Mpc}} = 8.8 \pm 3.6 \times 10^{14}\,M_\odot$. Our value of $M_{1.5\mathrm{Mpc}} =$

$7.9 \pm 1.2 \times 10^{14}\,M_\odot$, agrees well with the photo-z selected mass by WtG.

4.5.17. MACS J0744

This cluster at a fairly high redshift of $z = 0.686$ shows very different mass estimates, which might again be related to the extreme dynamical state this cluster is in. Korngut et al. (2011) report a very disturbed morphology for the matter distribution in the core based on high-resolution SZ and X-ray observations. We find a mass of $M_{1.5\mathrm{Mpc}} = 9.5 \pm 0.7 \times 10^{14}\,M_\odot$, which is significantly lower than $M_{1.5\mathrm{Mpc}} = 20.5 \pm 5.7 \times 10^{14}\,M_\odot$ by WtG and $M_{1.5\mathrm{Mpc}} = 13.5 \pm 2.3 \times 10^{14}\,M_\odot$ by U14. A recent study by Sereno et al. (2015) finds $M_{200c} = 13.6 \pm 3.3 \times 10^{14}\,M_\odot$ in marginal agreement with our finding of $M_{200c} = 10.0 \pm 0.6 \times 10^{14}\,M_\odot$. Although the Sereno et al. (2015) analysis differs in the way the NFW fit was performed, it is not independent of our analysis since it uses the radial shear profile reported in U14 and an estimate on the critical curve of the system from our Table 2. The largely different mass estimates for this interesting cluster render it as ideal target for further multi-wavelength studies.

4.5.18. CLJ 1226

For the highest-redshift system in our sample at $z = 0.89$ we compare to the study by Jee & Tyson (2009) who report a total mass of the system of $M_{1.12\mathrm{Mpc}} = 14.0 \pm 2.0 \times 10^{14}\,M_\odot$. Using their cosmological background model and deriving the enclosed mass for the same aperture radius we find $M_{1.12\mathrm{Mpc}} = 18.9 \pm 1.5 \times 10^{14}\,M_\odot$. This 35% larger mass is in mild tension with the previous study. However, as stated in Jee & Tyson (2009) and confirmed by Korngut et al. (2011), also this system seems to be in a disturbed, merging state. As we have seen for the examples of RX J1347 and MACS J0744, such systems are prone to differing mass estimates, especially if different fitting ranges were used, which renders also this system as an interesting candidate for additional, independent studies.

5. GENERAL C–M ANALYSIS

We now derive a c–M relation from our 19 X-ray selected CLASH clusters and compare the observed values to the theoretical expectations from the literature. In the following, we will quote mass and concentration values which refer to a halo radius of r_{200c}.

5.1. The c–M Relation from CLASH

In Figure 9 we visualize the CLASH data points from Table 7 in the c–M plane. A general statistical summary of the data is shown in Table 10. In order to derive a c–M relation, we choose a parametrization following Duffy et al. (2008), but with pivot mass and redshift matched to our sample,

$$c_{200c}\left(M_{200c}, z\right) = A \times \left(\frac{1.37}{1+z}\right)^{B} \times \left(\frac{M_{200c}}{8 \times 10^{14}\,M_\odot/h}\right)^{C}. \quad (25)$$

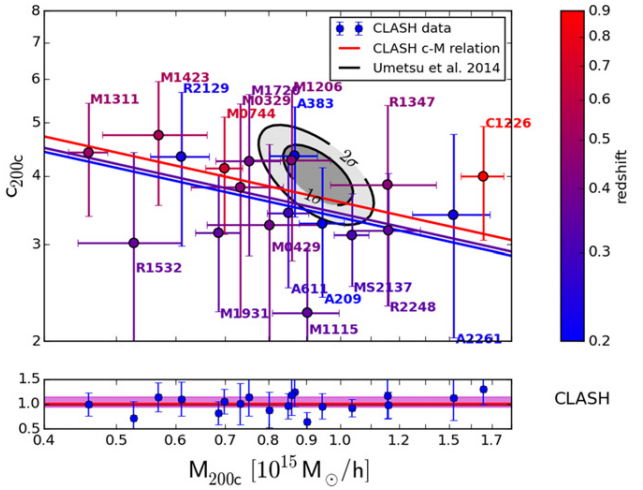

Figure 9. Concentrations and masses from CLASH. The labeled data points in the top panel show each CLASH cluster in the $M_{200c} - c_{200c}$ plane. The solid lines show the best-fit c–M relation to the CLASH data for $z = 0.2$ (blue), $z = 0.35$ (purple) and $z = 0.9$ (red). The color of data points and lines encodes the redshift of the CLASH clusters or the c–M relation. Overplotted with the gray contours is the concentration–mass analysis of Umetsu et al. (2014) for a redshift of $z \simeq 0.35$. The contour lines encircle the 68% and 95% confidence levels, respectively. The bottom panel shows the ratio between the observed concentration value and the value predicted by the CLASH-derived c–M relation for each CLASH cluster. The red line shows the median of this ratio for all clusters and the pink area defines the interval between its first and third quartile.

Here, A is the concentration of a halo at the pivot mass and redshift, B the redshift dependence of the concentration and C the dependence on halo mass.

Our data used in the fit contain errors in both mass and concentration, and we expect an intrinsic scatter about the mean relation. Despite this, unbiased estimates of the parameters of the relation can be determined using a likelihood method (e.g., Kelly 2007). In analogy to Hoekstra et al. (2012) and Gruen et al. (2013), we write the likelihood with an additional term that includes the intrinsic scatter as

$$-2 \ln \mathcal{L} = \sum_i \ln\left(s_i^2\right) + \left(\frac{\ln(c_i) - \ln\left(c\left(M_i, z_i\right)\right)}{s_i}\right)^2$$
$$s_i^2 = C^2 \sigma_{\ln M,i}^2 + \sigma_{\ln c,i}^2 + \sigma_{\ln c,\mathrm{int}}^2, \quad (26)$$

where we use the single-parameter ln-normal measurement uncertainties of mass and concentration $\sigma_{\ln M,i}$ and $\sigma_{\ln c,i}$, an intrinsic ln-normal scatter of concentration $\sigma_{\ln c,\mathrm{int}}$ and Equation (25) as $c\left(M_i, z_i\right)$, with a sum over all clusters i. The likelihood is a function of both the parameters A, B, C and $\sigma_{\ln c,\mathrm{int}}$. For our measurements, it is maximized by $A = 3.66 \pm 0.16$, $B = -0.14 \pm 0.52$, and $C = -0.32 \pm 0.18$, where the errors are close to uncorrelated. The intrinsic scatter is consistent with zero at a 1σ upper limit of $\sigma_{\ln c,\mathrm{int}} = 0.07$.

The results can be summarized as follows.

1. The concentration at the mean mass and redshift of the CLASH sample is constrained at the 5% level. We detect an indication of a negative slope of concentration with mass. The sign of this slope is in agreement with theoretical expectations (Duffy et al. 2008; Bhattacharya

et al. 2013), although one has to keep in mind that our measurement has a very low significance of $\sim 1.5\sigma$ due to our limited dynamic range in mass.

2. Due to the limited dynamic range, our data allow no conclusion on the dependence of concentration on redshift. The theoretical expectation here is to find a negative dependence on redshift from the combined effect of density at the formation time and mass growth (e.g Navarro et al. 1997; Duffy et al. 2008).

To confirm our result with another c–M analysis, which is of course not fully independent but different in its methodology, we overplot in Figure 9 the c–M contours at the 68% and 95% confidence levels from Umetsu et al. (2014). These contours derive from the stacked weak-shear analysis of 16 CLASH X-ray selected clusters. Although the stacked result, which refers to a redshift of $z \simeq 0.35$, lies slightly above the value from our relation, it is in excellent agreement with our results given the uncertainties in both analyses.

5.2. Comparison with Results from the Literature

We choose the relations of Duffy et al. (2008) (hereafter D08) and Bhattacharya et al. (2013) (hereafter B13) for our comparison to the CLASH data.

D08 used a set of three N-body simulation runs with a co-moving box size of 25, 100, and 400 Mpc/h, respectively. All runs adopted a WMAP5 cosmology (Komatsu et al. 2009) and provided a total mass-range of 10^{11}–$10^{15}\,M_{\odot}/h$. In addition, D08 also defined a relaxed sub-sample, with the criterion that the separation between the most bound halo particle and the center of mass of the halo is smaller than $0.07 r_{\rm vir}$, which was formerly identified as one efficient way of selecting relaxed halos (Neto et al. 2007).

B13 worked with a set of four cosmological boxes ranging in co-moving box size from 128–2000 Mpc/h. Also B13 splits their sample into a full and a relaxed subset, where the relaxed one is defined by the same criterion as in D08. Apart from the larger cosmological boxes, the main difference between D08 and B13 is the cosmological background model, which resembled a WMAP7 (Komatsu et al. 2011) cosmology in the case of B13 and the larger box size.

5.2.1. c–M Relation of the Full Samples

First, we compare the CLASH data set to the full sample c–M relations of D08 and B13. As one can see from visual inspection of Figure 10 already, there is good agreement between the CLASH data and the theoretical c–M relations derived from the simulations.

To statistically quantify the agreement we calculate the ratio $c_{\rm obs}/c_{\rm sim}$ as a function of cluster redshift. This ratio for each data point is shown in the bottom panel of Figure 10. Next, we calculate the mean, standard deviation, first, second (median) and third quartiles of all these ratios and report them in Table 8. The median is also shown as horizontal pink line in the bottom panel of Figure 10 with the error range defined by the first and third quartiles. As a last test we perform a Pearson's χ^2 test, with the null hypothesis that the theoretical c–M relation is a good fit to our data and report the p-value in Table 8. All the analysis components, described in this paragraph shall serve as the prototype for all following comparisons between our data and c–M relations from simulations. To quantify how well we can expect the data and c–M relation to agree, we show in the very top of Table 8 the comparison to the c–M relation which we derived in Section 5.1 from the CLASH data itself.

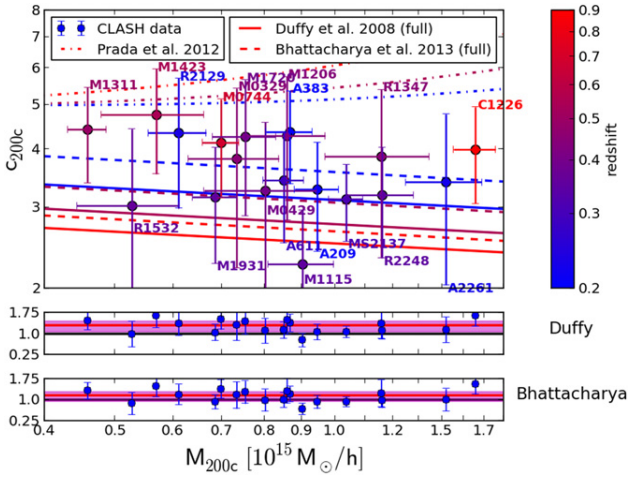

Figure 10. Comparison between CLASH clusters and c–M relations from the literature. This figure is identical in its structure to Figure 9. The lines indicate the c–M relations for the full samples of D08, B13, and P12. The bottom panels show the ratio of the observed and the simulation-based concentration, together with the sample median of this ratio and its quartiles.

Table 8
Goodness-of-fit: CLASH Compared to Literature Samples

Reference	$\langle c_{\rm obs}/c_{\rm sim}\rangle$[a]	Q_2[b]	Q_1[c]	Q_3[d]	χ^2	p-value
CLASH c–M	1.02 ± 0.17	1.01	0.94	1.14	7.6	0.94
D08 (full)	1.26 ± 0.24	1.31	1.07	1.45	15.3	0.43
B13 (full)	1.12 ± 0.23	1.16	0.94	1.29	11.4	0.72
D08 (relaxed)	1.11 ± 0.21	1.15	0.95	1.27	10.1	0.81
B13 (relaxed)	1.08 ± 0.23	1.12	0.91	1.24	11.3	0.73

[a] The mean of $c_{\rm obs}/c_{\rm sim}$ for the full cluster sample.
[b] The second quartile or median.
[c] The first quartile (25%).
[d] The third quartile (75%).

Finally, Figure 10 also shows the c–M relation of Prada et al. (2012) since it is widely used in the literature. One can easily see that there is a discrepancy between this relation and the CLASH results, especially when the good agreement with the D08 and B13 relations is considered. However, we refer to Meneghetti & Rasia (2013) which argues that a direct comparison in the c–M plane is not a meaningful comparison in the case of the Prada et al. (2012) relation.

5.2.2. c–M Relation for the Relaxed Samples

Since the CLASH clusters were selected to represent a more relaxed sample of clusters than former studies, we expect a much higher level of agreement when comparing to the relaxed subsets of the simulations. The visual comparison is shown in Figure 11, together with the statistical assessment in Table 8. We indeed find that in the case of D08 a 31% difference between simulation and observation is reduced to 15%, although the two comparisons agree within their error bars as also eported in Table 8. Note that the change from the full to the relaxed sample c–M relation in the work of B13 is only marginal (from 16% difference to 12%), although the same relaxation criterion was applied as in D08. This might either be caused by the different cosmology used in the two simulations

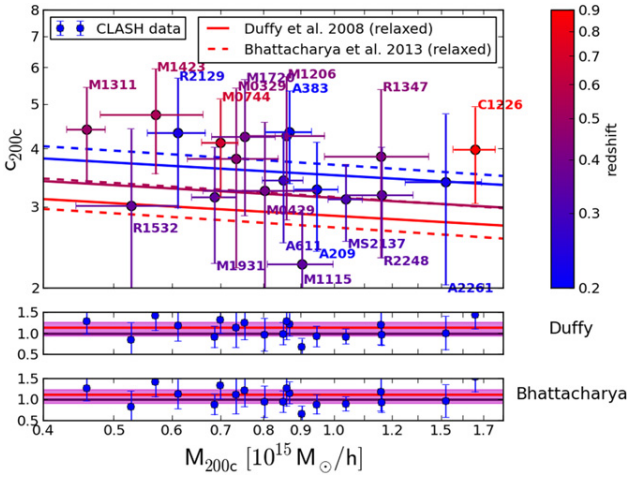

Figure 11. This figure is identical to Figure 10 but shows the c–M relations derived from the relaxed samples of D08 and B13.

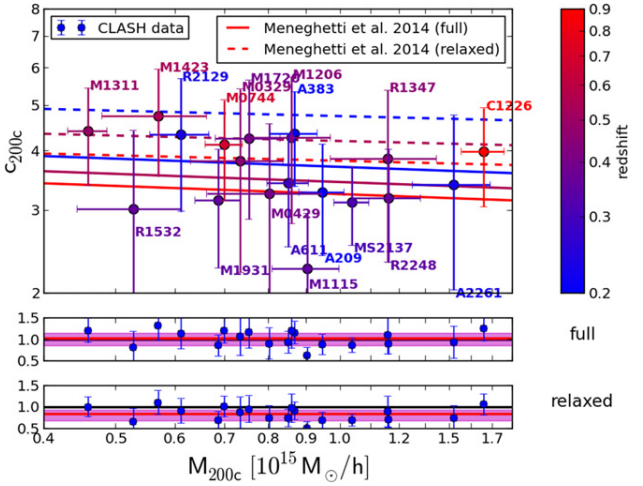

Figure 12. Comparison between CLASH and a tailored set of c–M relations from numerical simulations. This figure is identical in its structure to Figure 10 and shows the comparison between the CLASH data and the analysis of the simulations by M14 in 3D.

or might relate to the much bigger set of clusters in B13 and the increased statistical power of the sample.

6. C–M ANALYSIS WITH A TAILORED SET OF SIMULATIONS

In the preceding analysis we ignored the fact that we derive our NFW fits from a lensing reconstruction which sees the clusters in projection and we have not properly accounted for the CLASH selection function. We aim at eliminate these shortcomings by using our own set of simulations, where we have full control over the selection of our halo sample and the way in which masses and concentrations are derived from the simulations.

In our companion paper Meneghetti et al. (2014) (hereafter M14) we use a set of 1419 cluster-sized halos from the MUSIC-2 sample (Sembolini et al. 2013). These halos were found in the 1 Gpc MultiDark cosmological simulation (Klypin et al. 2011; Riebe et al. 2013) which was run with a best-fit WMAP7+BAO+SNI cosmology ($\Omega_M = 0.27$, $\Omega_\Lambda = 0.73$ $h = 0.7$). Starting from the large cosmological box with coarse particle mass resolution, the zoom-technique (Klypin et al. 2001) was applied to run re-simulations of the halos of interest with added non-radiative gas physics. This comprehensive set of clusters spans a mass-range between $2 \times 10^{14}\, M_\odot/h$ –$2 \times 10^{15}\, M_\odot/h$ at $z = 0$ and is available at four different redshifts $(0.25, 0.33, 0.43, 0.67)$. More details on this set of numerically simulated clusters are given in M14 and J. Vega et al. (2014, in preparation).

6.1. Analysis in 3D

We measure masses and concentrations of the halos in our simulated sample in a standard way by counting particles in radial bins around the halo center and by assigning a mean density to each bin. The innermost radial bin in this scheme is defined by the spatial resolution of the underlying zoom simulations and the outermost radial bin refers to r_{200c} of the halo. We fit a NFW profile to the decadic logarithm of the density as described in more detail in Ludlow et al. (2014) and M14. To the measured masses and concentrations of each halo and at all available redshifts we fit a c–M relation following the parametrization of Duffy et al. (2008), adapted to the mass and redshift range of the simulations.

Table 9
Goodness-of-fit: Meneghetti et al. 2014

Sample	$\langle c_{obs}/c_{sim} \rangle$	Q_2	Q_1	Q_3	χ^2	p-value
3D full	1.00 ± 0.18	1.03	0.86	1.15	9.5	0.85
3D relaxed	0.80 ± 0.16	0.84	0.68	0.93	29.4	0.01
2D full	1.03 ± 0.19	1.06	0.89	1.09	9.2	0.87
2D relaxed	0.86 ± 0.16	0.88	0.73	0.98	32.1	0.01
2D SL	0.91 ± 0.19	0.93	0.78	1.03	18.0	0.26
2D X-ray	0.94 ± 0.20	0.96	0.80	1.06	16.1	0.38

Note. The column explanations are identical to Table 8.

To define a limiting case we construct a strictly relaxed subset[38] of our simulated sample, by applying all three relaxation criteria of Neto et al. (2007). In addition to the already mentioned ratio of center of mass and virial radius, this includes also a constraint on the halo's substructure mass fraction $f_{sub} < 0.1$ and the restriction that the virial ratio must obey $2\,T/|U| < 1.35$. For complete definitions of f_{sub}, T and U see Neto et al. (2007). This selection reduces the number of halos in this strictly relaxed subset to 15% of the original full sample. Please note that this relaxation criterion is indeed more restrictive than the one used by D08 and B13 which only obeyed the center of mass constraint. The c–M relations for both the full and the relaxed sample are shown in Figure 12.

We summarize the quantitative comparison to our observed CLASH results in Table 9. We find excellent agreement between our observed data and the full sample of M14, very similar to the findings of B13. It is indeed reassuring that our baseline c–M relation derived from the full set of simulated clusters and analyzed with standard profile-fitting techniques gives a very similar result to B13 since most of our sample clusters were selected from the same parent cosmological box. The picture changes however, when we turn our attention to the strictly relaxed sample of M14, as can be seen in Figure 12 and Table 9. On average, the concentrations of the CLASH sample

[38] This is defined as the "super-relaxed" sample in M14.

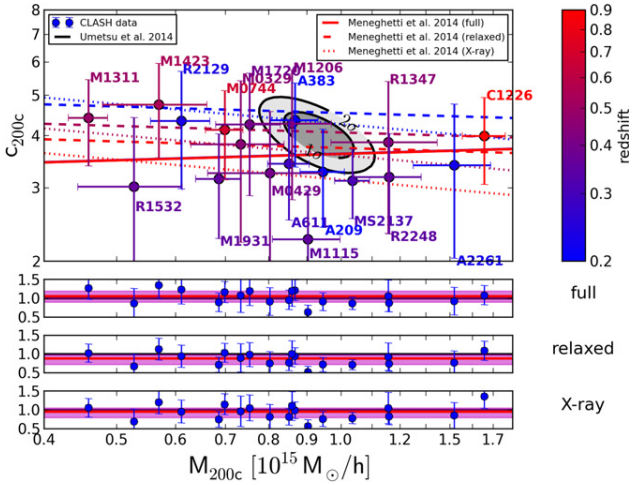

Figure 13. c–M comparison in 2D. This figure is identical to Figure 12, but shows the comparison between different c–M relations, based on different halo subsets from M14 in 2D. In addition, we overlay again the c–M likelihood contours from Umetsu et al. (2014).

are underestimated by about 15% and the associated p-value drops from 0.85 in the full to about 0.01 in the relaxed sample. This is in some tension with the results seen for D08 and B13, but we remind the reader that the selection criteria we adopt differ from those in D08 and B13. Specifically, we adopt all three criteria as used by Neto et al. (2007) to create the limiting case of a strictly relaxed sample, while D08 and B13 used a less strict definition of relaxation based on only one of these criteria.

6.2. Analysis in 2D

One aspect of our analysis may introduce substantial biases, namely that we assume spherical symmetry while fitting a 3D radial profile to our projected data coming from a lensing reconstruction. Several solutions to work around this issue have been proposed, e.g., by using X-ray and SZ data to gain information on the 3D shape of the density profile (see, e.g., Mahdavi et al. 2007; Corless et al. 2009; Morandi et al. 2010, 2012; Sereno et al. 2013). In this work we choose a different approach by also analyzing our simulated data in projection and by making the same assumption of spherical symmetry when deriving the density profiles of the simulated halos.

We perform the projection for each of our halos in the full sample by projecting all simulation particles in a box with 6 Mpc/h sides around the halo center. We chose 100 randomly selected lines of sight to obtain many realizations of the same halo, thereby increasing the statistical power of our sample. From the projected particle density we derive convergence maps, bin them azimuthally around the halo center and fit a NFW profile to the binned data under the assumption of spherical symmetry. For more details we refer the interested reader to M14 and Vega et al. (2014, in preparation). Also for this 2D case, we define a strictly relaxed sample as limiting case following the criteria outlined in Section 6.1.

The results of the comparison to these 2D c–M relations with the CLASH data can be seen in Figure 13. By applying the same statistical tests we find an excellent agreement with the full 2D sample of M14. When evaluating the median of the ratio between the two, the observed concentrations are only 6% higher than in the simulated sample which is now free of the projection bias, although the scatter is large. However, when restricting ourselves to the strictly relaxed clusters the 2D c–M relation is in tension with observations. The p-value drops from 0.87 to 0.01 and the difference in the median concentration ratio increases to 12%. The situation improves significantly to only 7% overestimation in the concentration ratio and a p-value of 0.26 once we pick only those simulated clusters which are able to produce strong-lensing features by demanding that the cluster produces a critical line (comp. Equation (10)). This selection is appropriate since all but one CLASH cluster allowed us to identify strong lensing features. However, the observational data is clearly in tension with a simulated cluster sample selected after the three relaxation criteria of Neto et al. (2007) and which is analyzed in 2D. This highlights the importance of halo selection and the necessity to properly account for the CLASH selection function.

6.2.1. X-Ray Selection of CLASH Clusters

As is pointed out in Postman et al. (2012a), the CLASH X-ray selected sample was designed to have a mostly regular X-ray morphology. Therefore, we perform yet another selection from our M14 cluster sample, mimicking the CLASH X-ray selection. As pointed out in Section 6 of M14, the selection based on X-ray regularity is related to but not identical to a selection based on halo relaxation. The X-ray selection is possible with the help of the X-MAS simulator (Rasia et al. 2008; Meneghetti et al. 2010b; Rasia et al. 2012) which produces simulated X-ray observations from a numerically simulated halo. We conFigure X-MAS to reproduce the X-ray observations (Ebeling et al. 2007; Allen et al. 2008; Cavagnolo et al. 2008; Maughan et al. 2008; Mantz et al. 2010) according to which the CLASH clusters were selected. Using this set of simulated X-ray images we apply the very same selection criteria which were used to select the CLASH X-ray selected clusters. For a more detailed description of these criteria and the selection process see M14.

This CLASH-like, X-ray selected sample in 2D is the one simulated sample which comes closest to the real CLASH clusters, both with respect to the selection criteria and the analysis method. The comparison between the c–M relation of this sample and the observed CLASH clusters shows indeed significant improvement over the limiting case of the fully relaxed sample in the last section. The qualitative agreement between the data points and the X-ray selected c–M relation in Figure 13 is quite obvious. The median concentration ratio shows that the observed CLASH concentrations are only 4% lower than the ones from the X-ray selected simulation sample and the p-value 0.38 indicates no strong tension between the two samples (compare Table 9). Finally, we calculate the $\Delta\chi^2$ value for the fits of the CLASH c–M relation from Section 5.1 and the X-ray selected c–M relation and find that the two relations agree at the 90% confidence level.

6.3. Individual CLASH Clusters in Our Simulated Sample

As the final analysis in this work we now select close matches to individual CLASH clusters out of our 2D set of simulated halos. We do this in order to gather additional confirmation that our specific way of selecting CLASH clusters from a numerical simulation is sufficiently accurate to characterize the CLASH selection function. We find simulated

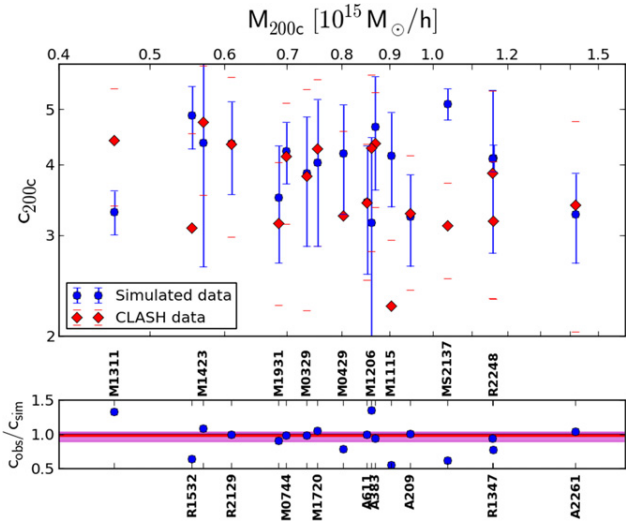

Figure 14. Distribution of observed and simulated concentrations for 18 X-ray selected CLASH clusters. The blue points show the expected concentration for each CLASH cluster as it is derived from all halo projections which fulfill our CLASH X-ray selection criteria for that specific halo. The red points show the observational equivalent. In the bottom panel we show the ratio between the two concentration values, together with the median of the ratio sample in red. The pink error band is defined by the first and third quartile of this sample.

counterparts to individual CLASH clusters by means of a regularity metric defined in Section 4 of M14. After all matching projections have been found for a single CLASH cluster, we calculated the expected concentration by a weighted average over the concentrations of these projections (see Section 7 of M14 for details). In the course of this analysis we had to drop CL J1226 because no match was found in our simulated set. The system is very massive and sits at high redshift which would require a larger simulation to find an equivalent.[39] We show the findings of the remaining 18 systems in Figure 14, where we compare the expected concentration for each individual simulated CLASH-like cluster with the findings from observations. All but two points overlap within the 1σ error bars and the ratio between observed and simulated concentrations for all CLASH clusters is close to a perfect match with the median of $c_{\rm obs}/c_{\rm sim}$ $Q_2 = 0.99^{+0.05}_{-0.09}$ where the error margins are defined by the first and third quartiles of the sample. The fact that the selection of individual CLASH clusters shows good agreement between predicted and observed concentrations gives us some confidence that we are indeed able to characterize the CLASH selection function by means of X-ray morphology.

We provide a general statistical summary of the distribution of simulated concentrations in Table 10 and we conclude our comparison to the simulations of M14 with a two-sample statistical analysis. We perform a Kolmogorov-Smirnov test and find a p-value of 0.75, again showing no indication for tension in the null hypothesis that the observed and simulated data have the same parent distribution of c–M values.

7. CONCLUSIONS

The *HST* multi-cycle treasury program CLASH was in part designed to shed light on the dark matter density profile of galaxy clusters by combining the enormous resolving power of the *HST* with wide-field Subaru imaging. The CLASH X-ray selected sample of galaxy clusters was specifically selected to have a mostly undisturbed X-ray morphology, suggesting that this sub-sample represents an undisturbed and unbiased set of clusters in terms of their density profile. This choice was made since former studies of lensing clusters with exquisite data quality were inconsistent with the predictions of ΛCDM, and selection effects were thought to be a possible cause of this disagreement.

In this work we applied advanced lensing reconstruction techniques to this CLASH data set. Our reconstructions combines weak and strong lensing to fully exploit the lensing data provided by the CLASH program. With the help of adaptively refined grids, we achieve a non-parametric reconstruction of the lensing potential over a wide range of scales, from the inner-most strong-lensing core of the system at scales ∼10 kpc out to the virial radius at ∼2 Mpc. This is the first time that such a multi-scale reconstruction using weak and strong lensing has been performed for such a large sample of clusters. Fits to the surface-mass density profiles provide masses and concentrations for 19 massive galaxy clusters.

In order to have full control over the selection function of halos and in order to avoid possible biases introduced by the tri-axial structure of high-mass halos, we also derive c–M relations from a new, unique set of simulated halos. These simulations allow us to make specific choices in our selection and analysis, providing a much closer match to real observations. While simulations are usually analyzed in 3D we perform a purely 2D analysis in projection, as this is the only option for the observed lensing data. We apply different selection functions to the simulations, including a selection based on the X-ray morphology of realistic X-ray images of our hydro-simulations. This sample obeys the selection criteria of CLASH. This is of great importance since the selection of a cluster from a numerical simulation based on X-ray regularity, like in the case of CLASH, relates to but is not identical to a selection based on relaxation parameters only. The details of this selection function are studied in much more detail in another CLASH paper by Meneghetti et al. (2014). For the X-ray selected 2D sample we find excellent agreement between simulations and observations. Observed concentration are on average only 4% lower than in simulations and we find no statistical indication for tension between the simulated and observed data set. This detailed comparison between observations and simulations in 2D, with full consideration of the underlying selection function is unique and gives us great confidence in the results, which are a confirmation of the ΛCDM paradigm, at least in the context of a c–M relation of cluster-sized halos.

From fitting a c–M relation to the CLASH data directly we find our concentrations distributed around a central value of $c_{200c} \simeq 3.7$ with a mild negative slope in mass at the 1σ-level.

Table 10
General Properties of Concentration Samples

Sample	Mean	SD	Q_2	Q_1	Q_3	Min	Max
Observed data	3.65	0.65	3.43	3.18	4.26	2.26	4.75
Simulated data	3.87	0.61	3.76	3.62	3.93	3.07	5.68

Note. The column explanations are identical to Table 8.

[39] An even more massive system at similar redshift has been observed (e.g., Menanteau et al. 2012; Jee et al. 2014b).

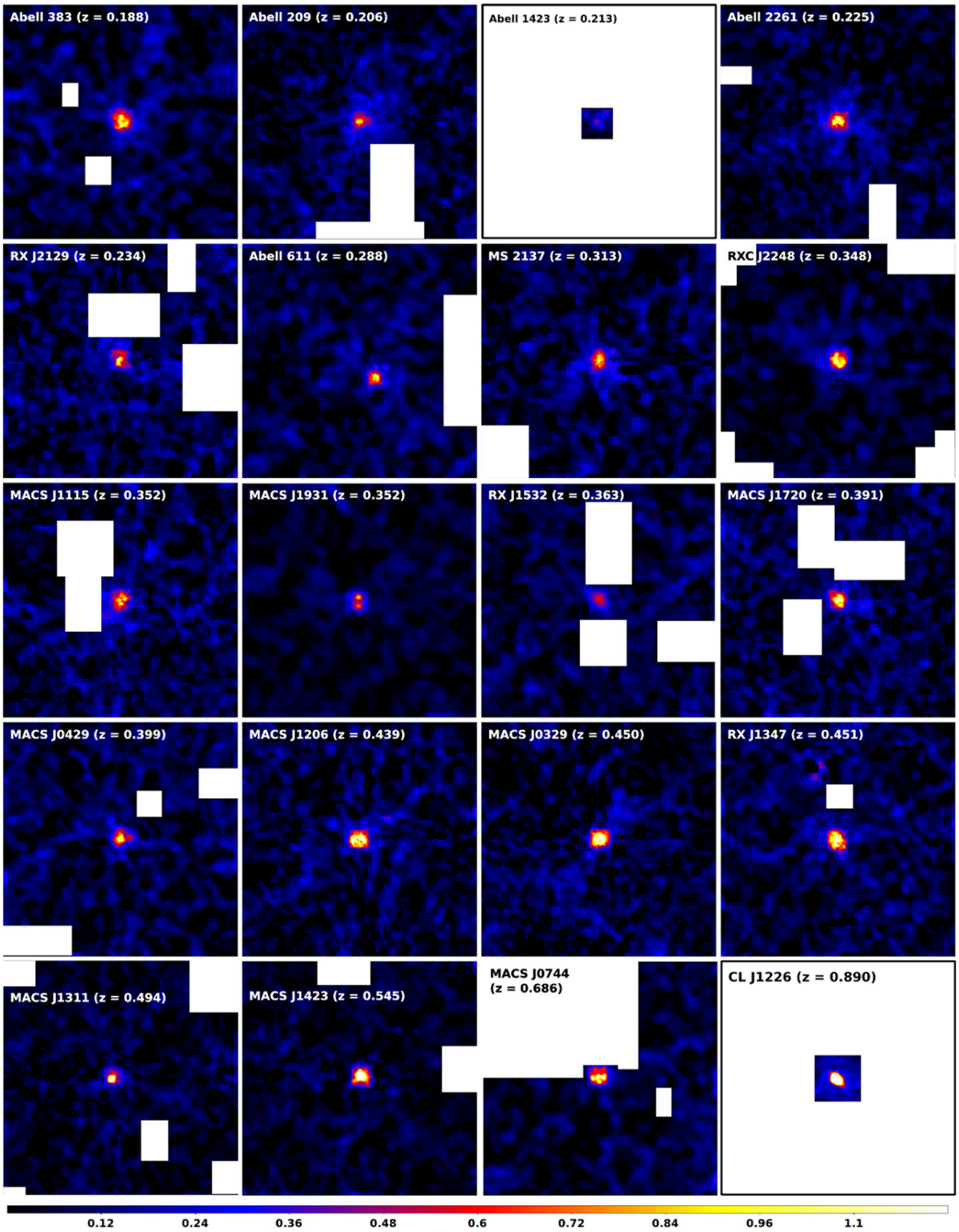

Figure 15. Convergence maps for 20 X-ray selected CLASH clusters. The field size for the map of Abell 1423 is 200″, for CL J1226 it is 300″, and for Abell 611 it is 1400″. For all other clusters the field size is 1500″. The color coding, together with the colorbar shows the lensing convergence, scaled to a redshift of $z = 20{,}000$. Extended white patches in the convergence maps indicate field masks, usually at the position of bright foreground stars. The orientation of all maps is north is up.

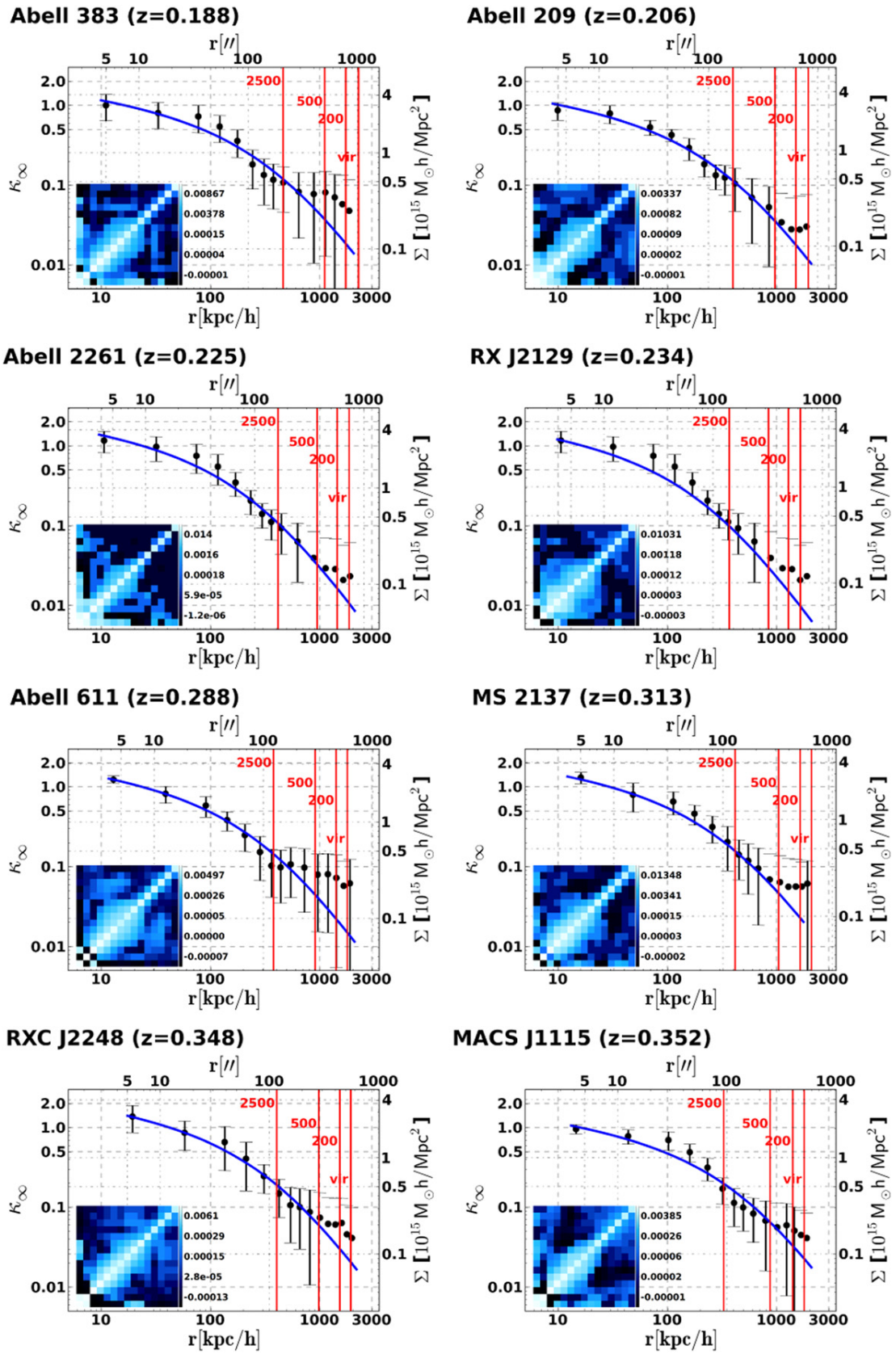

Figure 16. Convergence/surface-mass density profiles for 19 X-ray selected CLASH clusters. The black data points show the mean convergence in each bin. The square inset in the bottom left of each panel is the covariance matrix of the binned data and the error bars attached to each black data point show the square root of the diagonal elements of this matrix. Shown by the blue line is the best-fit NFW profile to the data. All radii refer to the peak in the dark matter density distribution of each halo as a center. Drawn in red are r_{2500}, r_{500}, and r_{200} and the virial radius of the halo. The convergence values are scaled to a source redshift of $z = 20{,}000$.

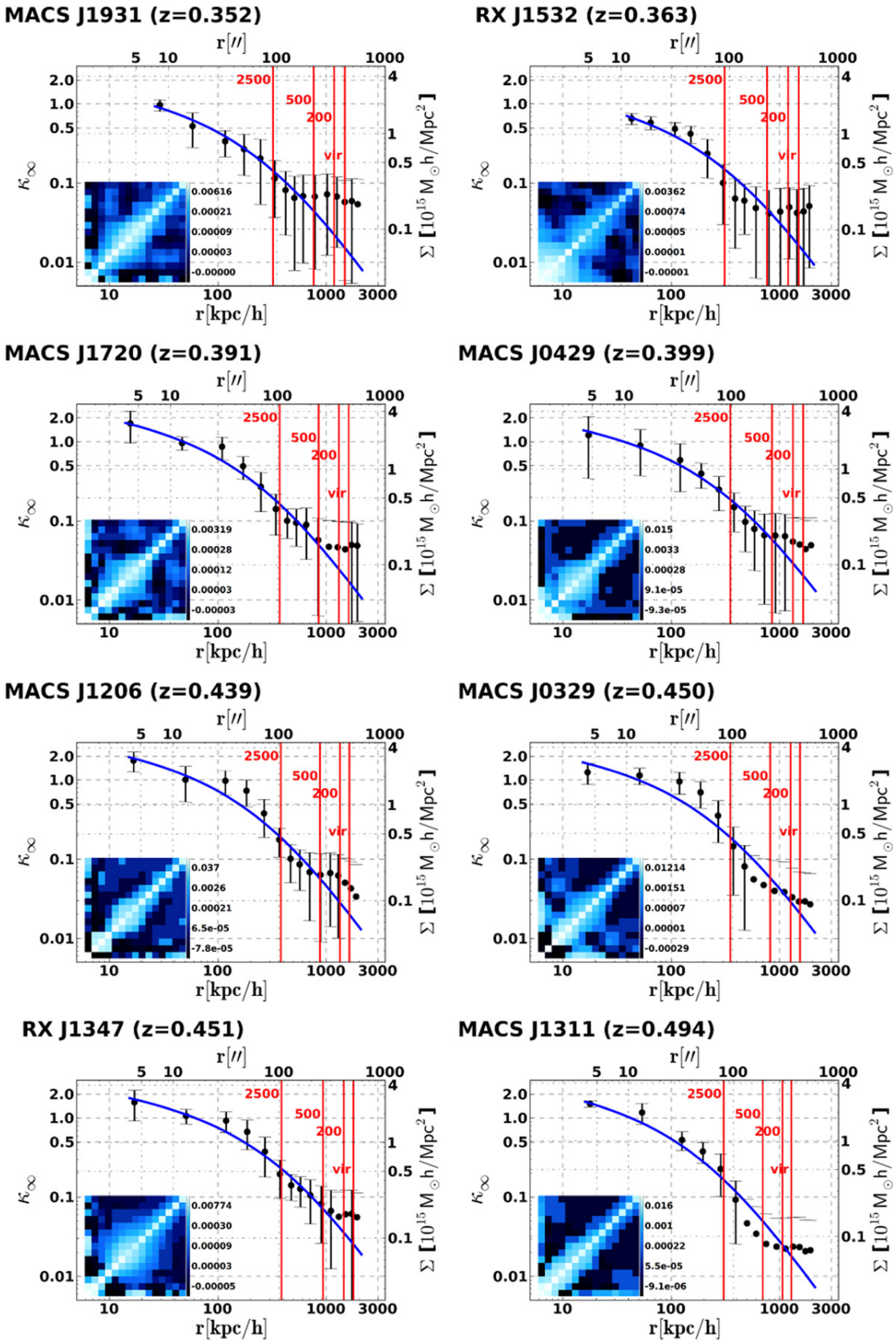

Figure 16. (Continued.)

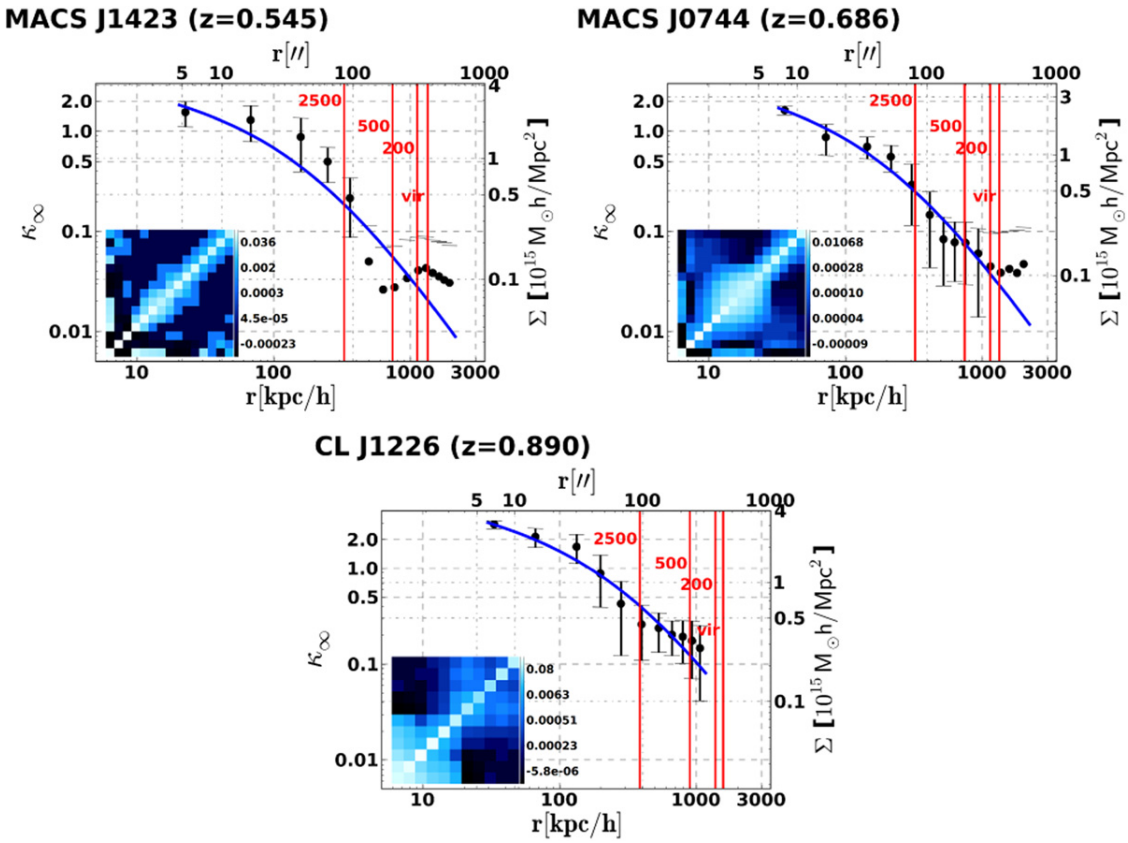

Figure 16. (Continued.)

This c–M relation derived from the CLASH data directly agrees with the c–M relation of simulated X-ray selected halos analyzed in projection at the 90% confidence level. Our comprehensive likelihood analysis shows that we are insensitive to any possible redshift dependence of the c–M relation. A larger leverage in redshift would be needed to probe this trend which is suggested by numerical simulations.

We want to highlight the complementary work on CLASH weak lensing and magnification measurements by Umetsu et al. (2014) and the full characterization of the CLASH simulations by Meneghetti et al. (2014). However, due to the exquisite quality of the lensing data used for this analysis, further and more advanced studies will be possible. Ongoing analyses include additional functional forms describing the dark matter distribution, like the generalized NFW or Einasto profiles. Particularly the analysis of inner slopes of the CLASH clusters and the intrinsic scatter of c–M relations derived from these profiles will give interesting insights into the physics of dark matter and the role of baryons on cluster scales. Ultimately, one would like to go away from 1D, radial density profiles and describe the full morphology and shape of the dark matter distributions in observations and simulations. Such techniques might indeed prove more powerful in, e.g., distinguishing different particle models of dark matter. The CLASH clusters are clearly the ideal data set to perform such analyses.

The research was in part carried out at the Jet Propulsion Laboratory, California Institute of Technology, under a contract with the National Aeronautics and Space Administration. J. M. has received funding from the People Programme (Marie Curie Actions) of the European Union's Seventh Framework Programme (FP7/2007–2013) under REA grant agreement number 627288. M. M. thanks ORAU and NASA for supporting his research at JPL and acknowledges support from the contract ASI/INAF I/023/12/0, INFN/PD51, and the PRIN MIUR 20102011 "The dark universe and the cosmic evolution of baryons: from current surveys to Euclid." K. U. acknowledges support from the National Science Council of Taiwan (grant NSC100-2112-M-001-008-MY3) and from the Academia Sinica Career Development Award. Support for A. Z. is provided by NASA through Hubble Fellowship grant #*HST*-HF-51334.01 A awarded by STScI. D. G., S. S. and P. R. were supported by SFB Transregio 33 "The Dark universe" by the Deutsche Forschungsgemeinschaft (DFG) and the DFG cluster of excellence "Origin and Structure of the universe." This work was supported in part by contract research "Internationale Spitzenforschung II/2-6" of the Baden Württemberg Stiftung. The Dark Cosmology Centre is funded by the DNRF. J. S. was supported by NSF/AST1313447, NASA/NNX11AB07G, and the Norris Foundation CCAT Postdoctoral Fellowship. E.R. acknowledges support from the National Science Foundation AST-1210973, SAO TM3-14008X (issued under NASA Contract No. NAS8-03060)

REFERENCES

Abdelsalam, H. M., Saha, P., & Williams, L. L. R. 1998, MNRAS, 294, 734
Abell, G. O. 1958, ApJS, 3, 211
Abell, G. O., Corwin, H. G., Jr., & Olowin, R. P. 1989, ApJS, 70, 1
Allen, S. W., Rapetti, D. A., Schmidt, R. W., et al. 2008, MNRAS, 383, 879
Anderson, J., & Bedin, L. R. 2010, PASP, 122, 1035

Anderson, L., Aubourg, E., Bailey, S., et al. 2012, MNRAS, 427, 3435
Applegate, D. E., von der Linden, A., Kelly, P. L., et al. 2014, MNRAS, 439, 48
Bacon, D. J., Goldberg, D. M., Rowe, B. T. P., & Taylor, A. N. 2006, MNRAS, 365, 414
Balestra, I., Vanzella, E., Rosati, P., et al. 2013, A&A, 559, L9
Bartelmann, M. 2010, CQGra, 27, 233001
Bartelmann, M., Narayan, R., Seitz, S., & Schneider, P. 1996, ApJL, 464, L115+
Bartelmann, M., & Schneider, P. 2001, PhR, 340, 291
Becker, M. R., & Kravtsov, A. V. 2011, ApJ, 740, 25
Benítez, N. 2000, ApJ, 536, 571
Bhattacharya, S., Habib, S., Heitmann, K., & Vikhlinin, A. 2013, ApJ, 766, 32
Biviano, A., Rosati, P., Balestra, I., et al. 2013, A&A, 558, A1
Borgani, S., & Kravtsov, A. 2011, ASL, 4, 204
Boylan-Kolchin, M., Bullock, J. S., & Kaplinghat, M. 2012, MNRAS, 422, 1203
Bradač, M., Allen, S. W., Treu, T., et al. 2008, ApJ, 687, 959
Bradač, M., Clowe, D., Gonzalez, A. H., et al. 2006, ApJ, 652, 937
Bradač, M., Erben, T., Schneider, P., et al. 2005a, A&A, 437, 49
Bradač, M., Lombardi, M., & Schneider, P. 2004, A&A, 424, 13
Bradač, M., Schneider, P., Lombardi, M., & Erben, T. 2005b, A&A, 437, 39
Bridle, S. L., Hobson, M. P., Lasenby, A. N., & Saunders, R. 1998, MNRAS, 299, 895
Broadhurst, T., Benítez, N., Coe, D., et al. 2005, ApJ, 621, 53
Broadhurst, T., Umetsu, K., Medezinski, E., Oguri, M., & Rephaeli, Y. 2008, ApJL, 685, L9
Broadhurst, T. J., & Barkana, R. 2008, MNRAS, 390, 1647
Broadhurst, T. J., Taylor, A. N., & Peacock, J. A. 1995, ApJ, 438, 49
Bullock, J. S., Kolatt, T. S., Sigad, Y., et al. 2001, MNRAS, 321, 559
Buote, D. A., Gastaldello, F., Humphrey, P. J., et al. 2007, ApJ, 664, 123
Cacciato, M., Bartelmann, M., Meneghetti, M., & Moscardini, L. 2006, A&A, 458, 349
Cavagnolo, K. W., Donahue, M., Voit, G. M., & Sun, M. 2008, ApJ, 682, 821
Clowe, D., Bradač, M., Gonzalez, A. H., et al. 2006, ApJL, 648, L109
Coe, D., Umetsu, K., Zitrin, A., et al. 2012, ApJ, 757, 22
Coe, D., Zitrin, A., Carrasco, M., et al. 2013, ApJ, 762, 32
Comerford, J. M., & Natarajan, P. 2007, MNRAS, 379, 190
Corless, V. L., King, L. J., & Clowe, D. 2009, MNRAS, 393, 1235
D'Aloisio, A., & Natarajan, P. 2011, MNRAS, 411, 1628
di Nino, D., Makidon, R. B., Lallo, M., et al. 2008, *HST* Focus Variations with Temperature, Tech. Rep. 2008-03
Diego, J. M., Tegmark, M., Protopapas, P., & Sandvik, H. B. 2007, MNRAS, 375, 958
Donahue, M., Voit, G. M., Mahdavi, A., et al. 2014, ApJ, 794, 136
Duffy, A. R., Schaye, J., Kay, S. T., & Dalla Vecchia, C. 2008, MNRAS, 390, L64
Ebeling, H., Barrett, E., Donovan, D., et al. 2007, ApJL, 661, L33
Ebeling, H., Edge, A. C., & Henry, J. P. 2001, ApJ, 553, 668
Ebeling, H., Edge, A. C., Mantz, A., et al. 2010, MNRAS, 407, 83
Eke, V. R., Navarro, J. F., & Steinmetz, M. 2001, ApJ, 554, 114
Ettori, S., Donnarumma, A., Pointecouteau, E., et al. 2013, SSRv, 177, 119
Ettori, S., Gastaldello, F., Leccardi, A., et al. 2010, A&A, 524, A68
Falco, E. E., Gorenstein, M. V., & Shapiro, I. I. 1985, ApJL, 289, L1
Fedeli, C. 2012, MNRAS, 424, 1244
Fedeli, C., & Bartelmann, M. 2007, A&A, 461, 49
Francis, M. J., Lewis, G. F., & Linder, E. V. 2009, MNRAS, 394, 605
Gao, L., Navarro, J. F., Cole, S., et al. 2008, MNRAS, 387, 536
Gorenstein, M. V., Shapiro, I. I., & Falco, E. E. 1988, ApJ, 327, 693
Grossi, M., & Springel, V. 2009, MNRAS, 394, 1559
Gruen, D., Brimioulle, F., Seitz, S., et al. 2013, MNRAS, 432, 1455
Halkola, A., Hildebrandt, H., Schrabback, T., et al. 2008, A&A, 481, 65
Hanami, H., Ishigaki, T., Fujishiro, N., et al. 2012, PASJ, 64, 70
Hennawi, J. F., Dalal, N., Bode, P., & Ostriker, J. P. 2007, ApJ, 654, 714
Hoekstra, H., Hartlap, J., Hilbert, S., & van Uitert, E. 2011, MNRAS, 412, 2095
Hoekstra, H., Mahdavi, A., Babul, A., & Bildfell, C. 2012, MNRAS, 427, 1298
Host, O. 2012, MNRAS, 420, L18
Ilbert, O., Capak, P., Salvato, M., et al. 2009, ApJ, 690, 1236
Jee, M. J., Ford, H. C., Illingworth, G. D., et al. 2007, ApJ, 661, 728
Jee, M. J., Hoekstra, H., Mahdavi, A., & Babul, A. 2014a, ApJ, 783, 78
Jee, M. J., Hughes, J. P., Menanteau, F., et al. 2014b, ApJ, 785, 20
Jee, M. J., Mahdavi, A., Hoekstra, H., et al. 2012, ApJ, 747, 96
Jee, M. J., & Tyson, J. A. 2009, ApJ, 691, 1337
Jouvel, S., Host, O., Lahav, O., et al. 2014, A&A, 562, A86
Kaiser, N., Squires, G., & Broadhurst, T. 1995, ApJ, 449, 460
Kelly, B. C. 2007, ApJ, 665, 1489
Kelly, P. L., von der Linden, A., Applegate, D. E., et al. 2014, MNRAS, 439, 28
Killedar, M., Borgani, S., Meneghetti, M., et al. 2012, MNRAS, 427, 533
Kitching, T. D., Balan, S. T., Bridle, S., et al. 2012, MNRAS, 423, 3163
Klypin, A., Kravtsov, A. V., Bullock, J. S., & Primack, J. R. 2001, ApJ, 554, 903
Klypin, A. A., Trujillo-Gomez, S., & Primack, J. 2011, ApJ, 740, 102
Koekemoer, A. M., Faber, S. M., Ferguson, H. C., et al. 2011, ApJS, 197, 36
Koekemoer, A. M., Fruchter, A. S., Hook, R. N., & Hack, W. 2002, in Proc. of the 2002 HST Calibration Workshop, ed. S. Arribas, A. Koekemoer, & B. Whitmore (Baltimore, MD: STScI), 337
Komatsu, E., Dunkley, J., Nolta, M. R., et al. 2009, ApJS, 180, 330
Komatsu, E., Smith, K. M., Dunkley, J., et al. 2011, ApJS, 192, 18
Korngut, P. M., Dicker, S. R., Reese, E. D., et al. 2011, ApJ, 734, 10
Leauthaud, A., Massey, R., Kneib, J., et al. 2007, ApJS, 172, 219
Lemze, D., Broadhurst, T., Rephaeli, Y., Barkana, R., & Umetsu, K. 2009, ApJ, 701, 1336
Liesenborgs, J., de Rijcke, S., & Dejonghe, H. 2006, MNRAS, 367, 1209
Ludlow, A. D., Navarro, J. F., Angulo, R. E., et al. 2014, MNRAS, 441, 378
Mahdavi, A., Hoekstra, H., Babul, A., Balam, D. D., & Capak, P. L. 2007, ApJ, 668, 806
Mandelbaum, R., Rowe, B., Bosch, J., et al. 2014, ApJS, 212, 5
Mantz, A., Allen, S. W., Rapetti, D., & Ebeling, H. 2010, MNRAS, 406, 1759
Massey, R. 2010, MNRAS, 409, L109
Massey, R., & Goldberg, D. M. 2008, ApJL, 673, L111
Massey, R., Hoekstra, H., Kitching, T., et al. 2013, MNRAS, 429, 661
Massey, R., Refregier, A., Conselice, C. J., David, J., & Bacon, J. 2004, MNRAS, 348, 214
Massey, R., Rhodes, J., Ellis, R., et al. 2007, Natur, 445, 286
Maughan, B. J., Jones, C., Forman, W., & van Speybroeck, L. 2008, ApJS, 174, 117
Medezinski, E., Broadhurst, T., Umetsu, K., & Coe, D. 2008, MPLA, 23, 1521
Medezinski, E., Broadhurst, T., Umetsu, K., et al. 2007, ApJ, 663, 717
Medezinski, E., Broadhurst, T., Umetsu, K., et al. 2010, MNRAS, 405, 257
Medezinski, E., Umetsu, K., Nonino, M., et al. 2013, ApJ, 777, 43
Melchior, P., Suchyta, E., Huff, E., et al. 2015, MNRAS, 449, 2219
Menanteau, F., Hughes, J. P., Sifón, C., et al. 2012, ApJ, 748, 7
Meneghetti, M., Fedeli, C., Pace, F., Gottlöber, S., & Yepes, G. 2010a, A&A, 519, A90
Meneghetti, M., Fedeli, C., Zitrin, A., et al. 2011, A&A, 530, A17
Meneghetti, M., & Rasia, E. 2013, arXiv:1303.6158
Meneghetti, M., Rasia, E., Merten, J., et al. 2010b, A&A, 514, A93
Meneghetti, M., Rasia, E., Vega, J., et al. 2014, ApJ, 797, 34
Merten, J. 2014, arXiv:1412.5186
Merten, J., Cacciato, M., Meneghetti, M., Mignone, C., & Bartelmann, M. 2009, A&A, 500, 681
Merten, J., Coe, D., Dupke, R., et al. 2011, MNRAS, 417, 333
Monna, A., Seitz, S., Greisel, N., et al. 2014, MNRAS, 438, 1417
Morandi, A., Limousin, M., Sayers, J., et al. 2012, MNRAS, 425, 2069
Morandi, A., Pedersen, K., & Limousin, M. 2010, ApJ, 713, 491
Navarro, J. F., Frenk, C. S., & White, S. D. M. 1996, ApJ, 462, 563
Navarro, J. F., Frenk, C. S., & White, S. D. M. 1997, ApJ, 490, 493
Neto, A. F., Gao, L., Bett, P., et al. 2007, MNRAS, 381, 1450
Newman, A. B., Treu, T., Ellis, R. S., et al. 2013, ApJ, 765, 24
Oguri, M., Bayliss, M. B., Dahle, H., et al. 2012, MNRAS, 420, 3213
Okabe, N., Smith, G. P., Umetsu, K., Takada, M., & Futamase, T. 2013, ApJL, 769, L35
Patel, B., McCully, C., Jha, S. W., et al. 2014, ApJ, 786, 9
Paulin-Henriksson, S., Antonuccio-Delogu, V., Haines, C. P., et al. 2007, A&A, 467, 427
Peng, E.-H., Andersson, K., Bautz, M. W., & Garmire, G. P. 2009, ApJ, 701, 1283
Planck Collaboration Ade, P. A. R., Aghanim, N., Armitage-Caplan, C., et al. 2014, A&A, 571, A16
Postman, M., Coe, D., Benítez, N., et al. 2012a, ApJS, 199, 25
Postman, M., Lauer, T. R., Donahue, M., et al. 2012b, ApJ, 756, 159
Prada, F., Klypin, A. A., Cuesta, A. J., Betancort-Rijo, J. E., & Primack, J. 2012, MNRAS, 423, 3018
Rasia, E., Mazzotta, P., Bourdin, H., et al. 2008, ApJ, 674, 728
Rasia, E., Meneghetti, M., Martino, R., et al. 2012, NJPh, 14, 055018
Rhodes, J., Refregier, A., & Groth, E. J. 2000, ApJ, 536, 79
Rhodes, J. D., Massey, R. J., Albert, J., et al. 2007, ApJS, 172, 203
Riebe, K., Partl, A. M., Enke, H., et al. 2013, AN, 334, 691
Rosati, P., Borgani, S., & Norman, C. 2002, ARA&A, 40, 539

Sadeh, S., & Rephaeli, Y. 2008, MNRAS, 388, 1759
Sand, D. J., Treu, T., & Ellis, R. S. 2002, ApJL, 574, L129
Schmidt, R. W., & Allen, S. W. 2007, MNRAS, 379, 209
Schneider, P., & Er, X. 2008, A&A, 485, 363
Schneider, P., & Seitz, C. 1995, A&A, 294, 411
Seitz, S., Schneider, P., & Bartelmann, M. 1998, A&A, 337, 325
Sembolini, F., Yepes, G., de Petris, M., et al. 2013, MNRAS, 429, 323
Sereno, M., Giocoli, C., Ettori, S., & Moscardini, L. 2015, MNRAS, 449, 2024
Sereno, M., Umetsu, K., Ettori, S., & Baldi, A. 2013, AN, 334, 445
The Dark Energy Survey Collaboration. 2005, arXiv:0510346
Umetsu, K., Broadhurst, T., Zitrin, A., Medezinski, E., & Hsu, L.-Y. 2011, ApJ, 729, 127
Umetsu, K., Medezinski, E., Broadhurst, T., et al. 2010, ApJ, 714, 1470
Umetsu, K., Medezinski, E., Nonino, M., et al. 2014, ApJ, 795, 163
Umetsu, K., Medezinski, E., Nonino, M., et al. 2012, ApJ, 755, 56
van Waerbeke, L. 2000, MNRAS, 313, 524
Voit, G. M. 2005, RvMP, 77, 207
von der Linden, A., Allen, M. T., Applegate, D. E., et al. 2014, MNRAS, 439, 2
Walker, M. G., & Peñarrubia, J. 2011, ApJ, 742, 20
Wojtak, R., & Łokas, E. L. 2010, MNRAS, 408, 2442
Zhao, D. H., Jing, Y. P., Mo, H. J., & Börner, G. 2003, ApJL, 597, L9
Zheng, W., Postman, M., Zitrin, A., et al. 2012, Natur, 489, 406
Zitrin, A., Broadhurst, T., Coe, D., et al. 2011, ApJ, 742, 117
Zitrin, A., Broadhurst, T., Umetsu, K., et al. 2009, MNRAS, 396, 1985
Zitrin, A., Broadhurst, T., Umetsu, K., et al. 2010, MNRAS, 408, 1916
Zitrin, A., Fabris, A., Merten, J., et al. 2014, arXiv:1411.1414
Zitrin, A., Meneghetti, M., Umetsu, K., et al. 2013, ApJL, 762, L30
Zitrin, A., Moustakas, J., Bradley, L., et al. 2012a, ApJL, 747, L9
Zitrin, A., Rosati, P., Nonino, M., et al. 2012b, ApJ, 749, 97

The Astrophysical Journal, 797:34 (21pp), 2014 December 10 doi:10.1088/0004-637X/797/1/34

THE MUSIC OF CLASH: PREDICTIONS ON THE CONCENTRATION–MASS RELATION

M. Meneghetti[1,2,3], E. Rasia[4], J. Vega[5,6], J. Merten[2,7], M. Postman[8], G. Yepes[5], F. Sembolini[5], M. Donahue[9], S. Ettori[2,3], K. Umetsu[10], I. Balestra[11,12], M. Bartelmann[13], N. Benítez[14], A. Biviano[12], R. Bouwens[15], L. Bradley[16], T. Broadhurst[17,18], D. Coe[8], N. Czakon[10], M. De Petris[19], H. Ford[16], C. Giocoli[20], S. Gottlöber[21], C. Grillo[22], L. Infante[23], S. Jouvel[24,25], D. Kelson[26], A. Koekemoer[7], O. Lahav[25], D. Lemze[16], E. Medezinski[16], P. Melchior[27], A. Mercurio[11], A. Molino[14], L. Moscardini[20], A. Monna[28,29], J. Moustakas[30], L. A. Moustakas[2], M. Nonino[12], J. Rhodes[1,7], P. Rosati[31], J. Sayers[7], S. Seitz[28], W. Zheng[8], and A. Zitrin[7,33]

[1] INAF, Osservatorio Astronomico di Bologna, via Ranzani 1, I-40127 Bologna, Italy
[2] Jet Propulsion Laboratory, California Institute of Technology, 4800 Oak Grove Drive, Pasadena, CA 91109, USA
[3] INFN, Sezione di Bologna, Viale Berti Pichat 6/2, I-40127 Bologna, Italy
[4] Physics Department, University of Michigan, 450 Church Avenue, Ann Arbor, MI 48109, USA
[5] Departamento de Fsica Terica, Universidad Autnoma de Madrid, Cantoblanco, E-28049 Madrid, Spain
[6] LERMA, CNRS UMR 8112, Observatoire de Paris, 61 Avenue de l'Observatoire, F-75014 Paris, France
[7] California Institute of Technology, MC 249-17, Pasadena, CA 91125, USA
[8] Space Telescope Science Institute, 3700 San Martin Drive, Baltimore, MD 21208, USA
[9] Department of Physics and Astronomy, Michigan State University, East Lansing, MI 48824, USA
[10] Institute of Astronomy and Astrophysics, Academia Sinica, PO Box 23-141, Taipei 10617, Taiwan
[11] INAF-Osservatorio Astronomico di Capodimonte, Via Moiariello 16, I-80131 Napoli, Italy
[12] INAF/Osservatorio Astronomico di Trieste, via G. B. Tiepolo 11, I-34143 Trieste, Italy
[13] Institut fur Theoretische Astrophysik, Universität Heidelberg, Zentrum für Astronomie, Philosophenweg 12, D-69120 Heidelberg, Germany
[14] Instituto de Astrofísica de Andalucía (CSIC), E-18080 Granada, Spain
[15] Leiden Observatory, Leiden University, PO Box 9513, NL-2333 Leiden, The Netherlands
[16] Department of Physics and Astronomy, The Johns Hopkins University, 3400 North Charles Street, Baltimore, MD 21218, USA
[17] Department of Theoretical Physics and History of Science, University of the Basque Country UPV/EHU, PO Box 644, E-48080 Bilbao, Spain
[18] Ikerbasque, Basque Foundation for Science, Alameda Urquijo, 36-5 Plaza Bizkaia, E-48011 Bilbao, Spain
[19] Dipartimento di Fisica, Sapienza Universit di Roma, Piazzale Aldo Moro 5, I-00185 Roma, Italy
[20] Dipartimento di Fisica e Astronomia, Università di Bologna, Via Ranzani 2, 40127, Bologna
[21] Leibniz-Institut für Astrophysik, An der Sternwarte 16, D-14482 Potsdam, Germany
[22] Dark Cosmology Centre, Niels Bohr Institute, University of Copenhagen, Juliane Maries Vej 30, DK-2100 Copenhagen, Denmark
[23] Centro de Astro-Ingeniería, Departamento de Astronomía y Astrofísica, Pontificia Universidad Catolica de Chile, V. Mackenna 4860, Santiago, Chile
[24] Institut de Ciéncies de l'Espai (IEEC-CSIC), E-08193 Bellaterra (Barcelona), Spain
[25] Department of Physics and Astronomy, University College London, London WC1E 6BT, UK
[26] Observatories of the Carnegie Institution of Washington, Pasadena, CA 91101, USA
[27] Center for Cosmology and Astro-Particle Physics and Department of Physics, The Ohio State University, Columbus, OH 43210, USA
[28] Universitäts-Sternwarte München, Scheinerstr. 1, D-81679 München, Germany
[29] Max Planck Institute for Extraterrestrial Physics, Giessenbachstrasse, D-85748 Garching, Germany
[30] Department of Physics and Astronomy, Siena College, 515 Loudon Road, Loudonville, NY 12211, USA
[31] Dipartimento di Fisica e Scienze della Terra, Università degli Studi di Ferrara, Via Saragat 1, I-44122 Ferrara, Italy
[32] Institute for Computational Cosmology, Durham University, South Road, Durham DH1 3LE, UK
Received 2014 April 10; accepted 2014 September 25; published 2014 November 21

ABSTRACT

We present an analysis of the MUSIC-2 *N*-body/hydrodynamical simulations aimed at estimating the expected concentration–mass relation for the CLASH (*Cluster Lensing and Supernova Survey with Hubble*) cluster sample. We study nearly 1,400 halos simulated at high spatial and mass resolution. We study the shape of both their density and surface-density profiles and fit them with a variety of radial functions, including the Navarro–Frenk–White (NFW), the generalized NFW, and the Einasto density profiles. We derive concentrations and masses from these fits. We produce simulated *Chandra* observations of the halos, and we use them to identify objects resembling the X-ray morphologies and masses of the clusters in the CLASH X-ray-selected sample. We also derive a concentration–mass relation for strong-lensing clusters. We find that the sample of simulated halos that resembles the X-ray morphology of the CLASH clusters is composed mainly of relaxed halos, but it also contains a significant fraction of unrelaxed systems. For such a heterogeneous sample we measure an average two-dimensional concentration that is ∼11% higher than is found for the full sample of simulated halos. After accounting for projection and selection effects, the average NFW concentrations of CLASH clusters are expected to be intermediate between those predicted in three dimensions for relaxed and super-relaxed halos. Matching the simulations to the individual CLASH clusters on the basis of the X-ray morphology, we expect that the NFW concentrations recovered from the lensing analysis of the CLASH clusters are in the range [3–6], with an average value of 3.87 and a standard deviation of 0.61.

Key words: dark matter – galaxies: clusters: general – gravitation lensing: weak – gravitational lensing: strong

Online-only material: color figures

1. INTRODUCTION

Gravitational lensing is one the most powerful methods of investigating the distribution of matter (either dark or baryonic) in galaxy clusters. It is well known that this class of objects is particularly important in cosmology for several reasons. First, in a hierarchical model of structure formation, galaxy clusters are the most recent bound structures to form in the universe. They are often captured in the middle of violent dynamical processes like mergers between smaller structures, allowing us to study in detail how structure formation proceeds. Second, each of them is a miniature universe; their composition closely reflects the matter composition of the universe at large. Last but not least, they trace the exponential tail of the structure mass function. Tiny variations of the cosmological parameters are reflected in dramatic changes in the mass function and its evolution.

The lensing effects produced by galaxy clusters are sometimes spectacular. The light emitted by galaxies in the background of these objects interacts with the immense gravitational fields of these large cosmic structures and is deflected. Occasionally, if a background galaxy lies at a small angular distance from the cluster center, the lensing effects are highly nonlinear, leading to the formation of *giant* arcs and multiple-image systems. This regime is often called *strong lensing*. However, even at large angular distances, the light feels the gravitational pull of the cluster. In this case, where the lensing distortion changes on scales much larger than the size of the sources, the shape of the distant galaxies is only weakly distorted. In this *weak lensing* regime, the lensing effects are described by means of an additional image ellipticity.

Every cluster produces a weak lensing signal, but strong lensing events are rare and are often observed only in the cores of the most massive clusters or in systems with enhanced shear fields. Hennawi et al. (2007) and Meneghetti et al. (2010a) illustrated with the help of numerical simulations how peculiar the population of strong lensing clusters is. Clusters forming in the context of cold dark matter (CDM) typically have oblate, triaxial dark matter halos (Frenk et al. 1988; Dubinski & Carlberg 1991; Muñoz-Cuartas et al. 2011; Limousin et al. 2013; Lemze et al. 2012; Despali et al. 2013), and, among them, strong lenses tend to have their major axes preferentially oriented along the line of sight. Additionally, as described in Torri et al. (2004), the cluster's ability to produce strong lensing features is boosted by dynamical events such as mergers or, more generally, by substructures orbiting around their host halo and occasionally crossing the cluster cores in projection (Bayliss et al. 2014).

For these reasons, the selection of clusters based on their ability to produce strong lensing events is likely to generate a sample affected by biases. Because lensing is sensitive to the total mass projected onto the lens plane, the halo structural parameters inferred from the lensing analysis of clusters affected by an orientation bias will be biased as well. In particular, for clusters elongated along the line of sight, we expect to measure higher masses and concentrations (see, e.g., Oguri et al. 2009; Oguri & Blandford 2009; Hennawi et al. 2007; Meneghetti et al. 2010a; Gralla et al. 2011), and the opposite is expected for clusters whose major axes are perpendicular to the line of sight.

To avoid these issues, a selection based on the cluster X-ray morphology is often advocated. The thermal X-ray emission by galaxy clusters originates in the intracluster medium (ICM), which is ionized gas heated to temperatures up to ∼20 keV emitting in the X-ray via thermal bremsstrahlung radiation (e.g., Sarazin 1986). In the absence of processes inducing nonthermal pressure contributions, for example perturbations induced by dynamical events like mergers or ICM turbulence, we do expect the ICM to be nearly in hydrostatic equilibrium with the cluster gravitational potential. As an indication for such equilibrium, or *relaxation*, the X-ray surface brightness is expected to be symmetric and its isocontours "round" and concentric (see, e.g., Rasia et al. 2013b). Following this philosophy, a Cluster Lensing and Supernova Survey with Hubble (CLASH) cluster sample (Postman et al. 2012) has been constructed by selecting 20 massive clusters from X-ray-based compilations of massive relaxed clusters. The relaxation state has been established on the basis of X-ray morphological estimators applied to *Chandra X-ray Observatory* images.

Are these selection criteria really leading to a sample that is unbiased in terms of lensing masses and concentrations? Giocoli et al. (2012a) have recently pointed out that for randomly selected cluster samples, the concentration–mass relation derived from a two-dimensional (2D) lensing analysis is expected to have a lower amplitude compared to the intrinsic three-dimensional (3D) concentration–mass relation. The reason is identified in the prolate triaxial shape of the cluster halos. Because of their prolateness, the probability of observing them elongated on the plane of the sky is higher than the probability of viewing them with their major axes pointing toward the observer (some examples are shown in Figure 10 of Gao et al. 2012). Rasia et al. (2013a) showed that selecting clusters according to their X-ray luminosity not only increases the normalization of the c–M relation with respect to a control sample but also returns a steeper slope. This behavior is explained by the fact that at fixed mass, the most luminous clusters are also the most concentrated.

In this paper, we aim to use a set of numerical simulations of galaxy clustersized halos, the `MUSIC-2` simulation set, to better understand the expected properties of a sample of clusters having X-ray morphologies similar to the CLASH sample. In particular, we wish to quantify the possible residual biases on the mass and on the concentration estimates that are due to the CLASH selection function. This work has two companion papers[34]: the strong lensing and weak shear study of CLASH clusters by Merten et al. (2014) and the weak lensing and magnification study of CLASH clusters by Umetsu et al. (2014), where a comparison between our results and the observational analysis of the CLASH sample is presented.

The paper is structured as follows. In Section 2, we introduce the simulation set used in our analysis, and we describe the methods used to measure the shape of density profiles in simulated halos. In Section 3, we introduce the CLASH cluster sample to which the simulations will be compared. In Section 4, we describe the morphological parameters used to construct a sample of X-ray-selected clusters resembling the properties of the CLASH clusters. In Section 5, we describe the general properties of the halos in the simulated set and discuss their concentration–mass relation. In Section 6, we discuss the concentration–mass relation of strong lensing and X-ray-selected halos. In Section 7, we use the X-ray morphology of the simulated clusters to predict the concentrations of the individual CLASH clusters. Finally, Section 8 contains our summary and conclusions.

[33] Hubble Fellow.

[34] To appear on arXiv/astro-ph the same day as this work.

2. SIMULATIONS

2.1. The MUSIC-2 Sample

The MUSIC-2 sample (Sembolini et al. 2013a, 2013b; Biffi et al. 2014) consists of a mass-limited sample of resimulated halos selected from the MultiDark cosmological simulation. This simulation is dark matter only and contains 2048^3 (almost 9 billion) particles in a $(1\ h^{-1}\ \mathrm{Gpc})^3$ cube. It was performed in 2010 using ART (Kravtsov et al. 1997) at the NASA Ames Research Center. All of the data of this simulation are accessible from the online *MultiDark database*.[35] The run was done using the best-fitting cosmological parameters to WMPA7+BAO+SNI ($\Omega_M = 0.27$, $\Omega_b = 0.0469$, $\Omega_\Lambda = 0.73$, $\sigma_8 = 0.82$, $n = 0.95$, $h = 0.7$). This is the reference cosmological model used in the rest of the paper.

The halo sample was originally constructed by selecting all of the objects in the simulation box that are more massive than $10^{15}\ h^{-1}\ M_\odot$ at redshift $z = 0$. In total, 282 objects were found above this mass limit. All of these massive clusters were resimulated both with and without radiative physics. The zooming technique described in Klypin et al. (2001) was used to produce the initial conditions for the resimulations. All particles within a sphere of 6 Mpc radius around the center of each selected object at $z = 0$ were found in a low-resolution version (256^3 particles) of the MultiDark volume. This set of particles was then mapped back to the initial conditions to identify the Lagrangian region corresponding to a $6\ h^{-1}$ Mpc radius sphere centered at the cluster center of mass at $z = 0$. The initial conditions of the original simulations were generated in a finer mesh of size 4096^3. By doing so, the mass resolution of the resimulated objects was improved by a factor of eight with respect to the original simulations. The parallel TREEPM+SPH GADGET code (Springel 2005) was used to run all of the resimulations. We stress that during the resimulation process, we make sure that all of the clusters that have been included in the MUSIC database are free from contamination by low-resolution particles that are outside the Lagrangian region of the resimulated area. If an object is formed close to the boundary of the high-resolution region, it might be very likely affected by the presence of particles with different spatial and mass resolution. In this case, we exclude this object from our analysis because it is not properly simulated. All of the MUSIC objects used in the analysis thus have their Lagrangian regions well inside the high-resolution regions defined by the $6\ h^{-1}$ Mpc spheres at $z = 0$.

The MUSIC-2 sample exists in two flavors. In a first set of resimulations, baryons were added to the dark matter distributions extracted from the parent cosmological box, and their physics was simulated via smoothed particle hydrodynamics (SPH) techniques, without including radiative processes. A second set of resimulations accounts for the effects of radiative cooling, UV photoionization, star formation, and supernova feedback, including the effects of strong winds from supernovae.

In this paper, we focus our analysis on the nonradiative version of these simulations. Our choice is based on the fact that radiative simulations without a proper description of energy feedback from active galactic nuclei (AGNs) generally produce unrealistically dense cores because of the well-known overcooling problem (see, e.g., Borgani & Kravtsov 2011). More recent simulations show that this problem is mitigated in simulations that simulate energy feedback from AGNs (Duffy et al. 2010; McCarthy et al. 2011; Planelles et al. 2014; Rasia et al. 2013a; Planelles et al. 2014). This physical ingredient is not yet included in the MUSIC-2 sample. Moreover, our intention is to correlate the profile measurements with the strong lensing efficiency of the simulated halos. Killedar et al. (2012), comparing simulations with different treatments of baryonic processes, find that the addition of gas in nonradiative simulations does not significantly change the strong lensing predictions. However, gas cooling and star formation together significantly increase the number of expected giant arcs and the Einstein radii by a nonrealistic amount, particularly for lower redshift clusters and lower source redshifts. Further inclusion of AGN feedback, however, reduces the predicted strong lensing efficiencies such that the lensing cross sections become closer to those obtained for simulations including only dark matter or nonradiative gas. The main requirements for this study are (1) a large number of highly resolved halos to accurately measure the profiles and determine the dependence of concentration on mass, and (2) the presence of gas in the simulations in order to allow their X-ray analysis (see Section 4). For these reasons, we choose to use the nonradiative version of the MUSIC-2 sample.

Table 1
Completeness Mass Limits and Number of Halos above the Completeness Mass Limits in the MUSIC-2 Sample

Redshift	Mass Limit ($M_{\rm vir}$) ($h^{-1}\ M_\odot$)	Mass Limit (M_{200}) ($h^{-1}\ M_\odot$)	No. of Halos
0.250	6.3×10^{14}	4.3×10^{14}	128
0.333	6.4×10^{14}	5.1×10^{14}	97
0.429	6.0×10^{14}	5.0×10^{14}	80
0.667	3.9×10^{14}	4.0×10^{14}	89

The mass resolution for these simulations corresponds to $m_{\rm DM} = 9.01 \times 10^8\ h^{-1}\ M_\odot$ and to $m_{\rm SPH} = 1.9 \times 10^8\ h^{-1}\ M_\odot$. The gravitational softening was set to $6\ h^{-1}$ kpc for the SPH and dark-matter particles in the high-resolution areas. Several low-mass clusters have been found close to the large ones and not overlapping with them. Thus, the total number of resimulated objects is considerably larger than originally identified in the parent cosmological box. In total, there are 535 clusters with $M > 10^{14}\ h^{-1}\ M_\odot$ at $z = 0$ and more than 2000 group-like objects with masses in the range $10^{13}\ h^{-1}\ M_\odot < M_{\rm vir} < 10^{14}\ h^{-1}\ M_\odot$. In this study, we use a subsample of these halos, as explained below.

We have stored snapshots for 15 different redshifts in the range $0 \leqslant z \leqslant 9$ for each resimulated object. The snapshots that overlap with the redshifts of the CLASH clusters are at $z = 0.250$, 0.333, 0.429, and 0.667.

The sample is complete above the mass thresholds given in Table 1. To extend our analysis toward smaller masses and to be able to constrain the concentration–mass relation over a wider mass range, we also analyze halos with masses below the completeness limits. In particular, we use all halos with mass $M_{\rm vir} > 2 \times 10^{14}\ h^{-1}\ M_\odot$. Therefore, we investigate a total of 1,419 halos, summing all halos at different redshifts.

2.2. Density Profiles

2.2.1. Generalities

Navarro et al. (1996) argued that the density profiles of numerically simulated dark matter halos can be well fitted by an appropriate scaling of a "universal" function over a wide range of masses. The function suggested to fit these profiles was

[35] www.MultiDark.org

later dubbed the Navarro–Frenk–White density profile (NFW hereafter) and is given by

$$\rho(r) = \frac{\rho_s}{(r/r_s)(1+r/r_s)^2}, \quad (1)$$

where ρ_s and r_s are the characteristic density and the scale radius of the halo. The profile is characterized by a logarithmic slope that is shallower than isothermal for $r \ll r_s$ and steeper than isothermal for $r \gg r_s$.

Subsequent numerical studies (see e.g., Navarro et al. 1997) confirmed that the NFW function is appropriate to describe the profiles of *equilibrium* halos, i.e., of systems that are close to being in virial equilibrium, and is now widely used to characterize the shape of cluster-sized halos both in observations and in simulations.

Along with the definition of the NFW density profile came that of the halo *concentration*, $c_\Delta = r_\Delta/r_s$, which is the ratio of the size of the halo, here defined as the radius enclosing a certain mean overdensity Δ above the critical density of the universe, $\rho_{\rm crit}(z)$. The most appropriate value to describe the size of an equilibrium halo is its virial radius, i.e., the radius within which the halo particles are gravitationally bound and settled into equilibrium orbits. In this case the virial overdensity, $\Delta_{\rm vir}$, is a function of cosmology and redshift (Bryan & Norman 1998; Nakamura & Suto 1997). To avoid this cosmological dependence, Navarro et al. (1996) adopted the round number of $\Delta = 200$, which is commonly used in the literature independently of the assumed cosmological model. In this paper, we will also define the size of the halos as r_{200}, which is the radius enclosing a mean density $\overline{\rho} = 200\rho_{\rm crit}(z)$. Diemer & Kravtsov (2014) recently showed that rescaling clusters to this radius returns a self-similar inner density profile.

Despite the fact that the profiles of equilibrium halos are well described by the NFW function, a large fraction of halos formed in a cosmological box are far from having reached virial equilibrium (Ludlow et al. 2012; Meneghetti & Rasia 2013). Balmès et al. (2014) discussed the dependence of this fraction on cosmology, finding that it is particularly sensitive to dark energy. The reason is simply understood: dark energy affects the formation and the growth of the cosmic structures. In the case of nonequilibrium halos, the NFW function gives a poorer description of the shape of the density profiles, and other functions involving a larger flexibility (i.e., additional free parameters) may yield a preferable result. One example is the generalized NFW profile (gNFW; Zhao 1996), which is given by

$$\rho(r) = \frac{\rho_s}{(r/r_s)^\beta(1+r/r_s)^{3-\beta}}. \quad (2)$$

Compared to the NFW model, this profile is characterized by an additional parameter, namely the logarithmic inner slope β,

$$-\frac{d\ln\rho}{d\ln r} = \beta, \quad (3)$$

which is radius-independent.

A strong debate exists in the literature about the inner slope of the density profile of simulated halos (see e.g., Moore et al. 1998; Newman et al. 2011). The advent of modern supercomputers allows us to push the mass and the spatial resolution of numerical simulations to unprecedented limits, and the new results indicate that there is a systematic deviation of the dark matter halo profiles from the form proposed by NFW (Merritt et al. 2006; Navarro et al. 2010). The function that best fits such profiles is the Einasto function (Einasto & Haud 1989; Retana-Montenegro et al. 2012),

$$\rho(r) = \rho_{-2}\exp\left\{-2n\left[\left(\frac{r}{r_{-2}}\right)^{1/n} - 1\right]\right\}, \quad (4)$$

which is characterized by a running logarithmic slope,

$$-\frac{d\ln\rho}{d\ln r} \propto r^{1/n}, \quad (5)$$

parameterized in terms of the index n. The amplitude of the profile is set by the density ρ_{-2}, which is the density at the radius r_{-2}, i.e., at the radius where the logarithmic slope of the density profile is -2.

2.2.2. *The Density Profiles of the* MUSIC-2 *Halos*

To describe the structural properties of the MUSIC-2 halos, we perform an analysis of their three-dimensional density profiles based on the functional forms introduced in this section. This analysis is done by fitting the Equations (1), (2), and (4) to the azimuthally averaged density profiles of the simulated halos. The code used to perform this analysis is the same used in another CLASH paper by Merten et al. (2014).[36] As is common practice in the literature (e.g., Ludlow et al. 2013), we minimize the function

$$R^2_{3D} = \frac{1}{N_{\rm dof}}\sum_i [\log_{10}\rho_i - \log_{10}\rho(r_i, \boldsymbol{p})]^2, \quad (6)$$

where ρ_i is the density measured in the ith radial shell and $\boldsymbol{p}$ is the vector of parameters that are adjusted to derive the best-fitting function $\rho(r)$. In the case of the NFW profile, $\boldsymbol{p} = [\rho_s, r_s]$, and in the cases of the gNFW or Einasto profiles, $\boldsymbol{p} = [\rho_s, r_s, \beta]$ and $\boldsymbol{p} = [\rho_s, r_s, n]$, respectively. The variable $N_{\rm dof}$ is the number of degrees of freedom, i.e., the number of radii at which the profiles are evaluated minus the number of free parameters in the fit.

When analyzing these three-dimensional density profiles, we perform the fit over the radial range $[\tilde{r}_{\rm min}, \tilde{r}_{200}]$, where $\tilde{r}_{\rm min} = 0.02R_{\rm vir}$, and $\tilde{r}_{200}$ is the true r_{200} of the halo. Of course, the choice of the radial range over which the fit is performed is important because substructures located within this range can affect the result of the fit (Meneghetti & Rasia 2013).

A similar analysis is performed on the two-dimensional profiles, i.e., on the azimuthally averaged surface-density profile, Σ_i, corresponding to an arbitrary line of sight to the halo. The details of this analysis are discussed in the paper by J. Vega et al. (in preparation). In this case, the fitting functions are the projections of the functions in Equations (1), (2), and (4):

$$\Sigma(R) = 2\int_0^{r_t}\rho(r = \sqrt{R^2+\xi^2})d\xi, \quad (7)$$

where ξ indicates the spatial coordinate along the line of sight, and R is the projected radius. In the formula above, r_t is a truncation radius, which is introduced to take into account that our halos are at the center of a cube with side length $r_t = 6\,h^{-1}$ Mpc comoving. The figure-of-merit function to be minimized in this case is

$$R^2_{2D} = \frac{1}{N_{\rm dof}}\sum_i [\log_{10}\Sigma_i - \log_{10}\Sigma(R_i, \boldsymbol{p})]^2\,. \quad (8)$$

[36] Based on the open-source library Levmar, http://users.ics.forth.gr/lourakis/levmar/.

In order to be consistent with the analysis done on the CLASH clusters, we perform the two-dimensional fits over the radial range $[20\,h^{-1}\,\mathrm{kpc}, R_{\rm vir}]$.

When projecting the cubes within which the halo particles are distributed, we expect that in particular for the smallest systems, there will be a two-halo contribution, which is not properly taken into account in the fitting procedure. To estimate if this may bias our conclusions, we repeat the fit using only the particles inside spheres with radius $R_{\rm vir}$. The average concentrations do not change significantly, even at low masses, so we conclude that the two-halo contribution is a minor perturbation relative to the one-halo term for the radial scales we are probing ($R_{2D} < R_{\rm vir}$).

For both the three- and the two-dimensional analyses, the best-fit parameters are used to compute the masses and the concentrations of the simulated halos. In the following, we identify the quantities estimated from these two analyses with the labels 3D and 2D, respectively. The best-fit masses are obviously obtained by integrating the best-fit density profiles,

$$M = 4\pi \int_0^{r_{200}} \rho(r, \boldsymbol{p}_{\rm best}) r^2 dr. \tag{9}$$

The value of r_{200} used here is derived by solving the equation

$$\frac{\int_0^{r_{200}} \rho(r, \boldsymbol{p}_{\rm best}) r^2 dr}{r_{200}^3} = \frac{200}{3} \times \rho_{\rm crit}(z). \tag{10}$$

Using its original definition (NFW), the concentration is the ratio between r_{200} and the scale radius, r_s. For the NFW profile, the scale radius corresponds to the radius where

$$-\frac{d\ln\rho}{d\ln r} = 2, \tag{11}$$

that is, where the density profile has an isothermal slope. In the rest of the paper, we adopt the same definition also for the gNFW and Einasto profiles,

$$c_{200} \equiv \frac{r_{200}}{r_{-2}}. \tag{12}$$

Note that for the gNFW the following relation holds between r_{-2}, the scale radius r_s, and the inner slope β:

$$r_{-2} = (2-\beta) r_s. \tag{13}$$

2.3. Lensing Analysis

The lensing analysis of the MUSIC-2 halos is described in detail in Vega et al. (in preparation). For the purpose of this paper, we use their estimates of the Einstein radii over a large number of projections per cluster. We also use their convergence profiles, properly rescaled into surface-density profiles, and their mass and concentrations based on the fits of the surface-density profiles. The masses M_{2D} and the concentrations c_{2D} are equivalent to the values derived from a comprehensive lensing analysis of real observations. Hence, we compare M_{2D} and c_{2D} to Merten et al. (2014) and Umetsu et al. (2014).

For this work, we use our consolidated lensing simulation pipeline (see, e.g., Meneghetti et al. 2010a and references therein). Briefly, the following steps are involved.

1. We project the particles belonging to each individual halo along the desired line of sight on the *lens plane*.
2. Starting from the position of the virtual observer, we trace a bundle of light rays through a regular grid of 2048×2048 covering a region of $1.5 \times 1.5\ h^{-1}$ Mpc around the halo center on the lens plane.
3. Using our code RayShoot (Meneghetti et al. 2010b), we compute the deflection $\boldsymbol{\alpha}(\boldsymbol{x})$ at each light-ray position $\boldsymbol{x}$, accounting for the contributions from all particles on the lens plane.
4. The resulting deflection field is used to derive several relevant lensing quantities. In particular, we use the spatial derivatives of $\boldsymbol{\alpha}(\boldsymbol{x})$ to construct the convergence, $\kappa(\boldsymbol{x})$, and the shear, $\boldsymbol{\gamma} = (\gamma_1, \gamma_2)$, maps. These are defined as

$$\kappa(\boldsymbol{x}) = \frac{1}{2}\left(\frac{\partial\alpha_1}{\partial x_1} + \frac{\partial\alpha_2}{\partial x_2}\right), \tag{14}$$

$$\gamma_1(\boldsymbol{x}) = \frac{1}{2}\left(\frac{\partial\alpha_1}{\partial x_1} - \frac{\partial\alpha_2}{\partial x_2}\right), \tag{15}$$

$$\gamma_2(\boldsymbol{x}) = \frac{\partial\alpha_1}{\partial x_2} = \frac{\partial\alpha_2}{\partial x_1}. \tag{16}$$

5. The lens critical lines are defined as the curves along which the determinant of the lensing Jacobian is zero (e.g., Schneider et al. 1992):

$$\det A = (1-\kappa-|\gamma|)(1-\kappa+|\gamma|) = 0. \tag{17}$$

In particular, the *tangential* critical line is defined by the condition $(1-\kappa-|\gamma|) = 0$, whereas the *radial* critical line corresponds to the line along which $(1-\kappa+|\gamma|) = 0$. In the following sections, we will often use the term *Einstein radius* to refer to the size of the tangential critical line. As discussed in Meneghetti et al. (2013), there are several possible definitions for the Einstein radius. In this paper, we adopt the *effective* Einstein radius definition (see also Redlich et al. 2012),

$$\theta_E \equiv \frac{1}{d_{\rm L}}\sqrt{\frac{S}{\pi}}, \tag{18}$$

where S is the area enclosed by the tangential critical line and $d_{\rm L}$ is the angular diameter distance to the lens plane.

All of the lensing quantities are computed for a source redshift $z_{\rm s} = 2$.

In order to increase the statistics and to take into account possible projection effects, J. Vega et al. (in preparation) study each halo under a large number of lines of sight. More precisely, they investigate 100 lines of sight for the halos above the mass completeness limits and 30 projections for those below the completeness limit. This implies that for each halo, we have a catalog containing at least 30 measurements of the Einstein radius, projected mass, and projected concentration.

2.4. X-Ray Analysis

We build a mock X-ray catalog by producing for each simulated cluster three *Chandra* event files corresponding to orthogonal projections aligned with the Cartesian axes of the simulation. Because of excessive computational demand, we cannot investigate all of the lines of sight considered in J. Vega et al. (in preparation). The images are created by the X-ray

MAp Simulator (X-MAS; Gardini et al. 2004), in which we utilize the ancillary response function and redistribution matrix function proper of the ACIS-S3 detector (for a complementary X-ray analysis of the MUSIC-2 sample, we refer the reader to Biffi et al. 2014). The field of view (FOV) covers (16 arcmin)^2. For the cosmology and redshifts analyzed, the FOV size is equivalent to the following physical scales: 5.43 h^{-1} Mpc at $z = 0.250$, 6.57 h^{-1} Mpc at $z = 0.333$, 7.71 h^{-1} Mpc at $z = 0.429$, and 9.57 h^{-1} Mpc at $z = 0.667$. The spectral emission is generated by adopting the MEKAL model in which we fix the redshift to the simulation's value and the metallicity to a constant value equal to 0.3 times the solar metallicity as tabulated by Anders & Grevesse (1989). Finally, the contribution of the galactic absorption is introduced through a WABS model with $N_{\rm H} = 5 \times 10^{20}$ cm^{-2} (see e.g., Lemze et al. 2009). The exposure time is set to 100 ks, allowing a fair comparison with observations.

3. THE CLASH CLUSTER SAMPLE

The Cluster Lensing and Supernova Survey with Hubble (CLASH) is a Multi-Cycle Treasury program with the *Hubble Space Telescope* (*HST*). During *HST* cycles 18–20, 524 orbits were dedicated to observing 25 massive galaxy clusters. Among the goals of the program is to use the gravitational lensing properties of these objects to accurately constrain their mass distributions. In particular, one of the key objectives is to establish the degree of concentration of dark matter in the cluster cores, a key prediction of structure formation models. The survey is described in detail in Postman et al. (2012).

The targets of the CLASH program were selected to minimize the lensing-based selection that favors systems with overly dense cores. Specifically, 20 CLASH clusters are solely X-ray selected. The X-ray-selected clusters are massive ($kT > 5$ keV) and, in most cases, they appear to have a regular X-ray morphology. Five additional clusters are included for their lensing strength. These clusters have large Einstein radii ($\theta_E > 35''$) and were included to optimize the likelihood of finding highly magnified high-z ($z > 7$) galaxies. Using galaxy clusters as gravitational telescopes is another of the key objectives of CLASH, and the program has provided an extraordinary contribution to this field of research (Zheng et al. 2012; Bouwens et al. 2014; Bradley et al. 2014; Smit et al. 2013; Coe et al. 2013).

For each CLASH cluster, a large number of lensing constraints were collected, either from the *HST*, Subaru (e.g., Medezinski et al. 2013), or ESO/WFI (Gruen et al. 2013) telescopes or from the CLASH-VLT spectroscopic program (Balestra et al. 2013). Using these data of unprecedented quality, mass models for several CLASH targets have been published over the last few years employing different methods of reconstruction (Zitrin et al. 2011, 2012a, 2012b, 2013; Umetsu et al. 2012; Coe et al. 2012; Medezinski et al. 2013). These techniques are based on strong, weak, or a combination of strong and weak lensing.

In two companion papers, Merten et al. (2014) and Umetsu et al. (2014) focus on the analysis of the X-ray-selected subsample of CLASH clusters. In Merten et al. (2014), a well-tested reconstruction method (Merten et al. 2009, 2011; Meneghetti et al. 2010b; Rasia et al. 2012) is used to combine weak and strong lensing constraints and derive the convergence maps of these clusters. Fitting the surface-density profiles extracted from the maps, they measure the masses and concentrations of the CLASH clusters. As stated, the X-ray-selected CLASH clusters are ideal for this density profile analysis. In this paper, we analyze the MUSIC-2 halo sample with the intent of deriving theoretical expectations to compare to the results of the observational analysis of Merten et al. (2014) and Umetsu et al. (2014).

4. X-RAY SELECTION

4.1. X-Ray Morphological Parameters

One of the goals of this paper is to identify halos in the MUSIC-2 sample that closely resemble the X-ray properties of the clusters in the CLASH X-ray-selected sample. Because this sample was selected to have a high degree of regularity in the X-ray morphology, we try to find equivalents in the simulations that mimic these X-ray characteristics.

We use five parameters to measure the X-ray morphology in the soft-energy band ([0.5–2] keV) images of our halos. These morphological parameters are evaluated within a physical radius $R_{\rm max} = 500$ kpc following the same procedure adopted in the X-ray analysis of the CLASH clusters. The results of this analysis will be presented in detail in a forthcoming paper by Donahue et al. (2014). The five parameters are:

1. the centroid-shift, w, which assesses how much the centroid of the X-ray surface brightness moves when the aperture radius used to compute it decreases from $R_{\rm max}$ to smaller values. It is defined as
$$w = \frac{1}{R_{\rm max}} \times \sqrt{\frac{\Sigma(\Delta_i - \langle\Delta\rangle)^2}{N-1}}, \quad (19)$$
where N is the total number of apertures considered and Δ_i is the separation of the centroids computed within $R_{\rm max}$ and within the ith aperture;
2. the ellipticity, $e = 1 - b/a$, where the axial ratio is equal to the ratio of the square root of the eigenvalues obtained by diagonalizing the inertia tensor of the X-ray surface brightness evaluated within $R_{\rm max}$ (Buote & Canizares 1992);
3. the X-ray-brightness concentration, which is the ratio between the integral of the surface brightness S within two apertures with radii 100 kpc and $R_{\rm max}$,
$$c_X = \frac{S(r < 100\ {\rm kpc})}{S(r < R_{\rm max})} \quad (20)$$
Cassano et al. (2010);
4. and 5. the third- and fourth-order power ratios, P_3 and P_4. These are the third- and fourth-order multipoles of the surface-brightness distribution within an aperture of radius $R_{\rm ap} = R_{\rm max}$. The generic m-order power ratio ($m > 0$) is defined as P_m/P_0 with
$$P_m = \frac{1}{2m^2 R_{\rm ap}^{2m}}\left(a_m^2 + b_m^2\right) \quad \text{and} \quad P_0 = a_0 \ln(R_{\rm ap}), \quad (21)$$
where a_0 is the total intensity within the aperture radius Buote & Tsai (1996). The generic moments a_m and b_m are expressed in polar coordinates, R' and ϕ', and given by
$$a_m(r) = \int_{R' \leqslant R_{\rm ap}} S(x') R' \cos(m\phi') d^2x', \quad (22)$$
and
$$b_m(r) = \int_{R' \leqslant R_{\rm ap}} S(x') R' \sin(m\phi') d^2x'. \quad (23)$$

For a review of X-ray morphological parameters, we refer to Rasia et al. (2013b).

The five morphological parameters introduced above are combined to define a global degree of X-ray regularity. Such a quantity is measured with respect to the mean of the simulated sample. Note that with reference to the X-ray appearance, we use the term "regular" to indicate halos with unperturbed surface brightness distributions (Rasia et al. 2012). Very often, these halos are called "relaxed." We do not use this term to differentiate from the classification discussed in Section 5.2. Regular halos have small centroid shift, ellipticity, and power ratios. In addition, they have large surface-brightness concentrations. Thus, we define the regularity parameter

$$M = \left(\frac{\log_{10}(w) - \langle\log_{10}(w)\rangle}{\sigma_{\log_{10} w}}\right) + \left(\frac{e - \langle e\rangle}{\sigma_e}\right) + \left(\frac{\log_{10}(1/c_X) - \langle\log_{10}(1/c_X)\rangle}{\sigma_{\log_{10} 1/c_X}}\right) + \left(\frac{\log_{10}(P_3) - \langle\log_{10}(P_3)\rangle}{\sigma_{\log_{10} P_3}}\right) + \left(\frac{\log_{10}(P_4) - \langle\log_{10}(P_4)\rangle}{\sigma_{\log_{10} P_4}}\right) \quad (24)$$

similarly to the M parameter derived in Rasia et al. (2013b). In the formula above, each morphological parameter, p_i, is compared to its mean over the simulated halos, $\langle p_i\rangle$, and rescaled by the standard deviation of its distribution, σ_{p_i}.

By plugging the parameters $p_{\mathrm{CLASH},i}$ measured on the X-ray images of the CLASH clusters into Equation (24), we use the M parameter to quantify the regularity of the CLASH clusters with respect to the simulations. The M parameters of the CLASH X-ray-selected clusters are listed in Table 3. To construct a sample of CLASH-like clusters, we select the simulated halos having a regularity parameter similar to the observed clusters.

For the purpose of matching simulated halos to each individual CLASH cluster, we define the parameter C_X, which is defined as the distance, in parameter space, between each CLASH cluster and the simulated halos:

$$C_X = \sum_{i=1,5} \left(\frac{p_i - p_{\mathrm{CLASH},i}}{\sigma_{p_i}}\right)^2, \quad (25)$$

where $p_i = [\log_{10}(w), e, -\log_{10}(c_X), \log_{10} P_3, \log_{10} P_4]$ are the morphological parameters discussed above and σ_{p_i} their standard deviations. As a result, the sample constructed via the M parameter has an X-ray regularity similar to the CLASH sample. When we match halos using C_X, we identify only the simulated halos closest to each individual CLASH cluster in the morphological parameter space.

4.2. Nonradiative versus Radiative Simulations

While our choice to use the nonradiative version of the MUSIC-2 halos is motivated by the need to avoid biases caused by overcooling, it is well known that hydrodynamical simulations like those employed here poorly describe several X-ray properties of real clusters (Borgani & Kravtsov 2011; Kravtsov & Borgani 2012). For this reason, we do not use gas temperatures or X-ray luminosities to match the CLASH clusters in our simulations. Our comparison is based solely on the X-ray morphology.

To evaluate how the morphological parameters used in this work are influenced by the treatment of the gas, we use the hydrodynamical simulations described in Fabjan et al. (2010) and in Bonafede et al. (2011; see also Killedar et al. 2012; Planelles et al. 2014). These simulations, performed in the framework of a cosmological setting similar to that of the MUSIC-2 simulations, exist both in nonradiative and radiative versions. Contrary to the MUSIC-2 simulations, the effects of AGN feedback are also included in the radiative case. The sample is significantly smaller, though. Seventy of these halos were recently processed with the X-MAS simulator, both in the nonradiative and radiative versions. We use this analysis to quantify the impact of radiative processes on the morphological parameters.

The distributions derived from the two simulated sets are consistent for all morphological parameters computed within 500 kpc, with the exception of the light concentration, which is lower in the radiative simulation because part of the central gas is turned into star and contributes less to the X-ray central emission. Applying the selection method based on the parameter C_X on the halos in these two data sets for a few CLASH clusters, we obtained identical matches. Therefore, we can assume that our X-ray selection method can safely be used on the nonradiative simulations.

Notice that the two samples are characterized by similar concentration distributions, as shown in Rasia et al. (2013a). In particular, that paper found the following results: (1) the c–M relations have similar slopes independent of the physics, and (2) the normalization of the c–M relation in radiative simulations with no AGN feedback is ∼20% higher than that of the nonradiative simulations; the c–M relation from simulations including AGN feedback has a normalization similar to that of the nonradiative simulations.

4.3. Example of a Regular Cluster: A383

To illustrate how our selection based on the X-ray morphology performs, we discuss the case of A383 (Allen et al. 2008), which is the first cluster observed in the framework of the CLASH program. A383 is a galaxy cluster at redshift $z = 0.189$ (see, e.g., Zitrin et al. 2011). In the X-ray, it exhibits a very regular morphology, with nearly circular surface brightness contours (ellipticity ∼0.04; Postman et al. 2012). An X-ray image taken from the Archive of Chandra Cluster Entropy Profile Tables (ACCEPT) is shown in the small inset at the center of Figure 1. The image subtends ∼3.′45.

The four largest panels of Figure 1 show a sequence of simulated *Chandra* observations of MUSIC-2 halos corresponding to increasing values of C_X, which are annotated on the images. The top left panel shows the X-ray morphology of the halo that best matches A383 ($C_X = 0.2$). The X-ray morphology is indeed very similar to that of the observed cluster. As C_X increases, the differences between the simulated and the true X-ray morphologies become more significant. On the basis of this and other visual inspections, we verified that $C_X \sim 0.4$ represents a good limit to select the halos "similar" to the true cluster.

4.4. Example of Disturbed Cluster: MACSJ 1149

Our selection successfully identifies simulated halos that also closely resemble more perturbed clusters. For example, this is the case for MACSJ 1149 (Ebeling et al. 2007), which is one of the CLASH clusters identified as *high-magnification clusters*, i.e., not included in the X-ray-selected sample. A comparison

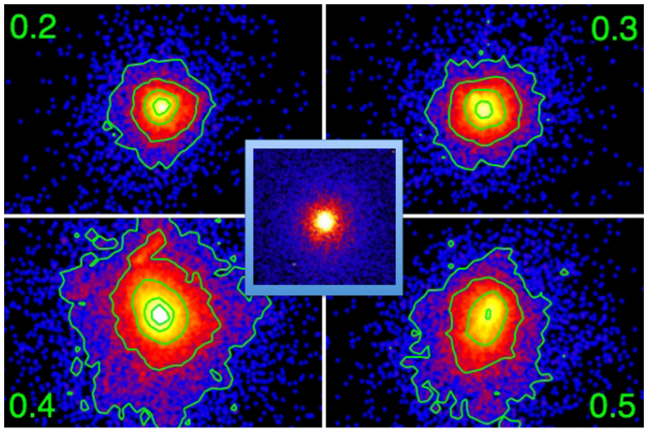

Figure 1. Examples of simulated clusters that match the CLASH cluster A383 (shown in the small inset) with four increasing values of C_X.
(A color version of this figure is available in the online journal.)

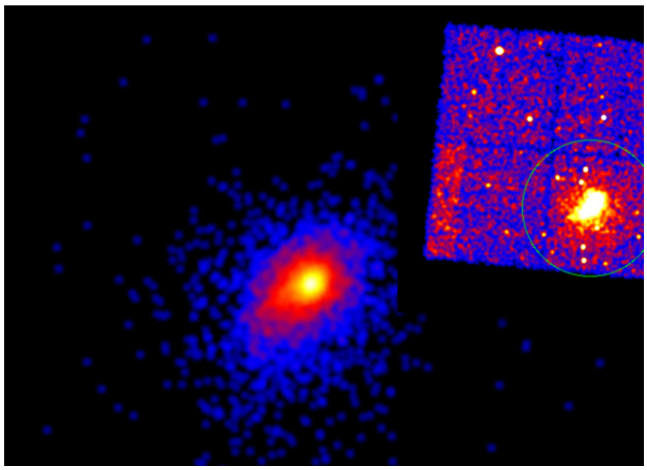

Figure 2. Best match to the morphologically disturbed cluster MACSJ 1149. The real X-ray image of the cluster is shown in the small inset on the right.
(A color version of this figure is available in the online journal.)

between the true X-ray morphology and that of a simulated halo with $C_X = 0.18$ is shown in Figure 2, where we show the true *Chandra* image of the cluster in the smaller inset on the right.

Clearly, the degree of asymmetry and of elongation of the surface-brightness distribution in the simulated observation matches very closely that of MACSJ 1149.

5. RESULTS

In this section, we discuss the results of our analyses on cluster mass profiles. First, we focus on the intrinsic properties of the whole sample, i.e., we do not apply any selection method to match the properties of the CLASH clusters. We compare to existing studies in the literature to verify the consistency of our and previous results. Then we apply the selection based on the X-ray selection and perform a one-to-one comparison between the simulated halos and each CLASH cluster.

5.1. Relaxed and Unrelaxed Halos

In this section we differentiate between relaxed and unrelaxed halos on the basis of a few criteria that are commonly used in the literature. Following the most restrictive approach proposed by Neto et al. (2007), we classify as strictly relaxed (or super-relaxed, as we dub them later in the paper) those objects satisfying the following properties.

1. Their center of mass displacement, defined as the offset between the center of mass (determined using all of the particles within the virial radius) and the minimum of the potential, in units of the virial radius, is $s = (\boldsymbol{r}_{\rm cm} - \boldsymbol{r}_{\phi})/r_{\rm vir} < 0.07$.
2. Their virial ratio is $\eta = 2T/|U| < 1.35$, where T is the kinetic energy and U is the gravitational energy, computed using the particles within the virial radius.
3. Their substructure mass fraction, computed as the mass in resolved substructures within the virial radius, is $f_{\rm sub} < 0.1$.

Applying these selection criteria to the MUSIC-2 halos results in a fraction of relaxed halos of about 14.9% at redshift $z = 0.25$. The fraction is reduced to 11.7% at redshift 0.333, and it further drops to 10.4% and 8.9% at redshifts 0.429 and 0.667, respectively.

Other authors use less restrictive or alternative criteria to identify the relaxed systems (e.g., Skibba & Macciò 2011; Skibba et al. 2011). For example, Bhattacharya et al. (2013) only use the center-of-mass displacement. In their paper, they report that the addition of the two other conditions on η and $f_{\rm sub}$ does not significantly affect the selection. On the contrary, we find that using only the center-of-mass displacement we end up with a significantly higher fraction of halos being classified as relaxed. This fraction amounts to ∼60% at $z = 0.250$ and decreases to ∼51% at $z = 0.667$. Such fractions are compatible with those quoted by Bhattacharya et al. (2013) (see also Biffi et al. 2014). Sembolini et al. (2013a) recently used the center-of-mass displacement in combination with the virial ratio to identify relaxed systems in simulations. They report that the relation between η and s becomes flat for $s \lesssim 0.1$, thus indicating that η does not impact severely on the selection of relaxed systems. For our sample, the combination of s and η yields a fraction of relaxed halos corresponding to 47% at $z = 0.250$, which decreases to 29% at $z = 0.667$.

In the following sections, we will study the properties of the MUSIC-2 halos, dividing them into three subsamples. First, we will consider all halos, regardless of their relaxation state. Second, we will set the limit defined above on the center-of-mass displacement to construct the subsample of *relaxed* halos. Third, we will further downsize the sample by using all three criteria described above to identify the *super-relaxed* halos.

5.2. Density Profiles

As explained in Section 2.2, we fit the density profiles of the MUSIC-2 halos using the functions in Equations (1), (2), and (4). In Figure 3, we show the results of the fitting procedure. We quantify the goodness of fit by means of the residuals given in Equations (6) and (8).

The upper left panel shows the distributions of the fit residuals for the entire MUSIC-2 sample. When all halos are considered, regardless of their relaxation state, the NFW profile is the worst-fitting model, i.e., the one with the largest residuals (see also Meneghetti & Rasia 2013). This is not surprising given that the NFW model has one free parameter less than the gNFW or the Einasto profiles. However, this result highlights the difficulty of fitting all profiles with a universal law. Because the gNFW and the Einasto functions generally provide better fits to the profiles, we may use the statistical distributions of their residuals to identify the halos deviating significantly from the NFW form.

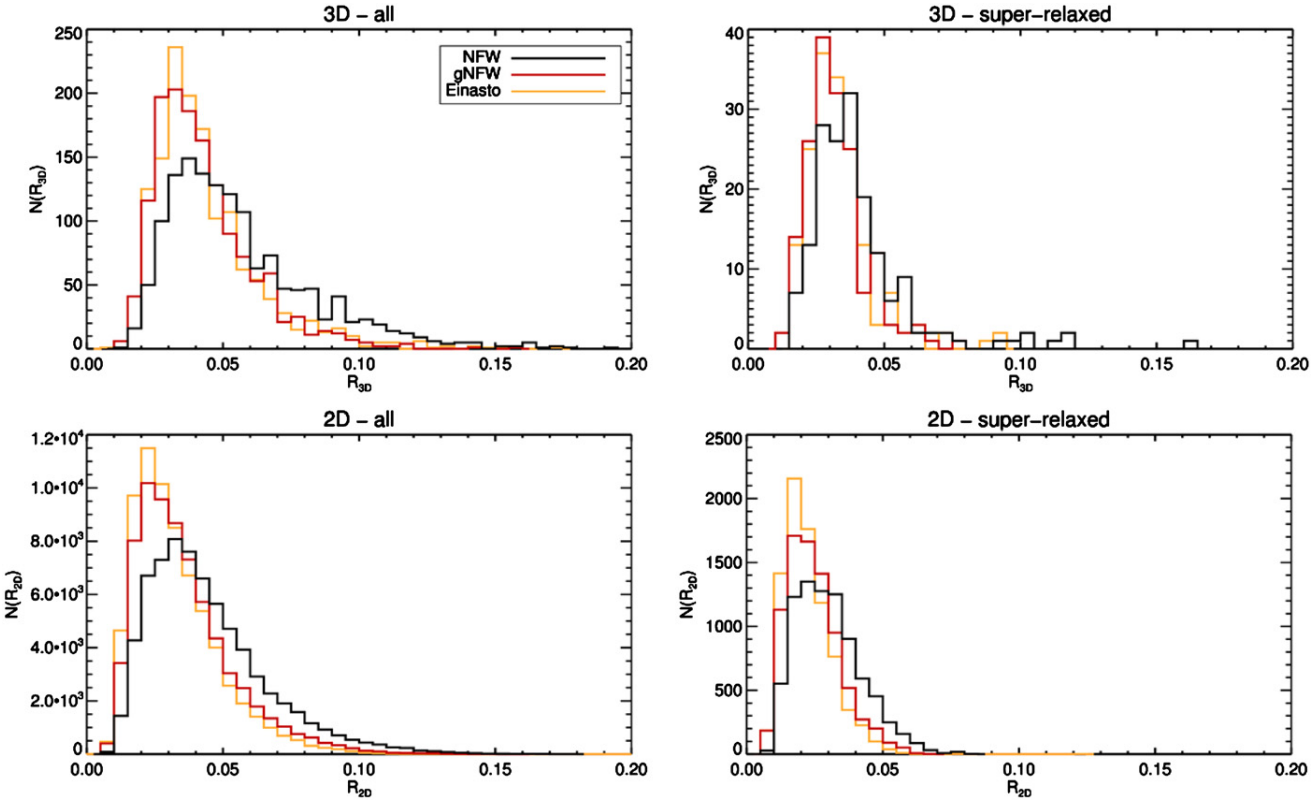

Figure 3. Distributions of the fit residuals. Results are shown for the fits of the density (upper panels) and of the surface-density profiles (bottom panels). The left and the right panels refer to the whole sample and to the subsample of super-relaxed halos, respectively. The black, red, and yellow histograms show the results for the NFW, gNFW, and Einasto models.

(A color version of this figure is available in the online journal.)

As can be seen from Figure 3, such distributions are nearly log-normal, which suggests that halos having too-large NFW residuals compared to the Einasto and gNFW models may be identified via their deviation $\delta = \ln R_{3D,\mathrm{NFW}} - \langle \ln R_{3D,x} \rangle$, where $\langle \ln R_{3D,x} \rangle$ is the mean value of $\ln R_{3D}$ for either the Einasto or the gNFW model. Using this criterion, we find that about 40% of the halos have NFW fits resulting in too-large residuals compared to what is typically found by fitting with more flexible profiles.

This fraction drops to ∼19% and ∼6% if only relaxed and super-relaxed halos are considered. The distributions of the fit residuals for the super-relaxed subsample are shown in the upper right panel of Figure 3. For these halos, the NFW model is only a slightly worse fit compared to the gNFW and Einasto models.

In Figure 4 we see that the profiles that most deviate from the NFW form have inner slopes β (resulting from the gNFW fits) that significantly differ from unity: their profiles are steeper or shallower than the NFW model. There is a slight indication for preferring a steep over a shallow slope (see also Figure 5). Indeed, the mean value of the inner slope β, measured for the whole sample, is $\langle \beta \rangle = 1.03 \pm 0.31$, where the error is the rms in the sample. We also find that the goodness of the gNFW fit is not correlated with the inner slope β, i.e., shallow or steep inner slopes are not systematically the result of a bad gNFW fit.

When fitting the surface-density profiles, we find again that the NFW model is generally the worst-fitting function among the three models employed in this work. This is shown in the bottom left panel of Figure 3. Again, we find that restricting the analysis to the relaxed halos reduces the differences between the residual

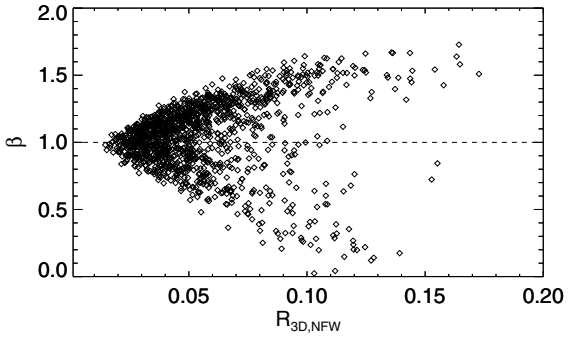

Figure 4. Inner slopes as they result from fitting the halo density profiles with gNFW models vs. the residuals of the NFW fits.

distributions of the NFW and gNFW or Einasto fits. However, from the results shown in the bottom right panel of Figure 3, it appears that a fraction of halos that are well fitted by NFW models in 3D are not NFW-like in projection. This result must be caused by the halo triaxiality and by the effects of substructures and additional matter along the line of sight. The work of J. Vega et al. (in preparation), from which the 2D analysis shown here is taken, investigates the effects of triaxiality on the shape of the surface-density profiles of the CLASH clusters. We refer the reader to that paper for more details. We note that the halo surface-density profiles were derived by using all of the particles in a cylinder centered on the halo and with depth $6\,h^{-1}$ Mpc.

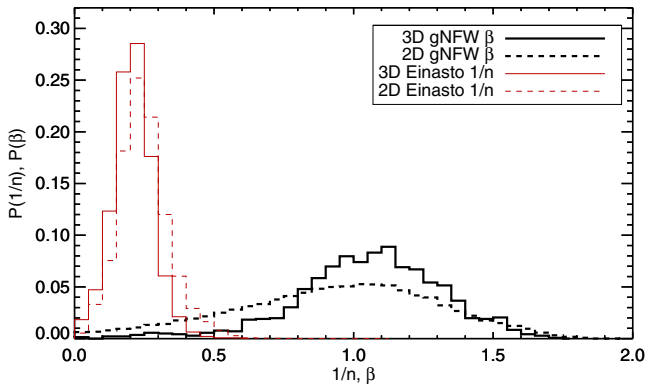

Figure 5. Distributions of the inner slopes obtained from the gNFW fits (β) and of the Einasto index $1/n$ derived from the analysis of the density (solid histograms) and of the surface-density profiles (dashed histograms) of the MUSIC-2 halos, as they result from fitting the halo density profiles with gNFW models vs. the residuals of the NFW fits.

(A color version of this figure is available in the online journal.)

The distributions of the inner slopes obtained from the gNFW fits of the surface-density profiles are shown in Figure 5 (thick histograms). We find that a large number of halos have rather flat profiles in 2D. The mean value of β is $\langle\beta\rangle = 0.89 \pm 0.47$. About 33% (15%) of the halo projections are fitted with $\beta \leqslant 0.8$ ($\leqslant$0.5). The red histograms show the distributions of the Einasto indexes $1/n$. The indexes obtained from the fit of the density profiles are slightly smaller than what are obtained from the fit of the surface-density profiles. The smaller the $1/n$, the steeper the inner profile. The mean values are $\langle 1/n\rangle = 0.21 \pm 0.07$ and $\langle 1/n\rangle = 0.24 \pm 0.09$ for the 3D and 2D distributions, respectively. Such Einasto slopes appear to be in excellent agreement with the recent results of Dutton & Macciò (2014).

To summarize, the halos in the MUSIC-2 sample span a wide range of structural parameters. As expected, the density profiles can differ significantly from the NFW form, and their shape can be better described with more flexible functions, such as the Einasto or gNFW models. When projecting the mass distributions, the scatter in the profile parameters and the deviation from the NFW model become even larger.

5.3. Cluster Masses

Having determined the level of diversity among density and surface-density profiles of the MUSIC-2 halos, we consider now how precisely the halo masses are derived from the profile fits. We consider both the cases of 2D and 3D masses, the former being the masses derived by deprojecting the best-fit models of the surface-density profiles under the assumption of spherical symmetry, and the latter those derived from the fits of the density profiles. Note that when measuring the 2D masses, we are not simulating any lensing analysis at this stage. In particular, we are not considering additional sources of systematics that may depend on the particular method to derive the mass from the weak and the strong lensing signals. Other works have shown that different methods of analysis may introduce systematic errors that are due, for example, to the presence of substructures inside and outside the clusters (Meneghetti et al. 2010b; Becker & Kravtsov 2011; Rasia et al. 2012) and to the Bright Central Galaxy (Giocoli et al. 2013). Nevertheless, this exercise gives us important information on the intrinsic limits of the mass measurements based on the analyses of azimuthally averaged density or surface-density profiles.

We begin with the 3D masses. The distributions of the ratios between such masses and the true halo masses are shown in the left panel of Figure 6. The results are shown for the three fitting functions employed in this work (black, red, and orange histograms). We find that the masses recovered from the azimuthal fits of the density profiles are generally in good agreement with the true masses. The best agreement is obtained with the Einasto and gNFW profiles, with a slight preference for the first. These fits provide ratios around unity with rms = 0.06 and 0.05, respectively. The masses estimated through the NFW fits are also in good agreement with the true masses. In this case, the median (mean) ratio is 0.98 (0.97) and the distribution is twice as broad as in the two previous cases. The purple histogram is constructed by choosing, for each cluster, the mass estimate derived from the fitting function leading to the smallest residuals. In other words, we choose the most reliable mass estimate among those obtained with the three fitting functions. In most cases, the best model is the Einasto profile. Thus, the purple and the orange histograms are nearly coincident.

The histograms shown here refer to the whole halo sample, regardless of the relaxation state. As shown in the previous section, the density profiles of the relaxed halos are generally equally well fitted by NFW, gNFW, or Einasto models. Indeed, restricting the analysis to these halos, we find smaller rms for all three kinds of fit ($\lesssim$0.03), with mean and median ratios very close to unity. Despite the fact that the fraction of relaxed halos varies with redshift, we find that the mean mass ratios and their scatter remain constant as a function of redshift.

Even when fitting the surface-density profiles, the mass estimates (M_{2D}) deviate only slightly from the true masses. The 2D masses appear to be underestimated by $\sim$5% on average, with the NFW and gNFW fits being slightly more biased than the Einasto fits. However, the scatter is much larger ($\sim$13%–14%) than for the 3D masses. The larger scatter is expected, given that the masses are derived under the assumption of spherical symmetry. Halos are generally triaxial, and projection effects can easily cause the mass to be over- or underestimated by a significant amount, depending on the halo orientation (see, e.g., Meneghetti et al. 2010b). As reported by Giocoli et al. (2012a), the halo prolateness may also cause a systematic underestimation of the mass derived from the 2D analysis. Assuming the triaxial model of Jing & Suto (2002), they estimate this bias to be of order $\sim$10%.

As in the left panel, the purple histogram in the right panel of Figure 6 shows the distribution of the ratios between the best 2D mass estimate and the true mass. Again, the distribution is close to that obtained by fitting with the Einasto profile.

On the basis of this result, we conclude that we should expect a modest negative bias of $\sim$5% on the mass estimates obtained by fitting the surface-density (or the convergence) profiles of galaxy clusters. This is due to the prolate shape of the halos, which are more frequently elongated on the plane of the sky than along the line of sight. The choice of the NFW or gNFW models to fit the halos tend to slightly increase the bias, and the opposite occurs with the Einasto profile.

If we repeat this analysis on the samples of relaxed and super-relaxed halos, we find that the mass bias tends to become smaller. In fact, the 2D masses deviate from the true masses by only $\sim$1%–2% in these cases. If the bias originates from halo triaxiality, this suggests that the most relaxed systems must generally be more spherical. In Figure 7, we show the distribution of the axis ratios b/a and c/a of all of the MUSIC-2 halos (color map). Here a, b, and c are the semi-axes of the

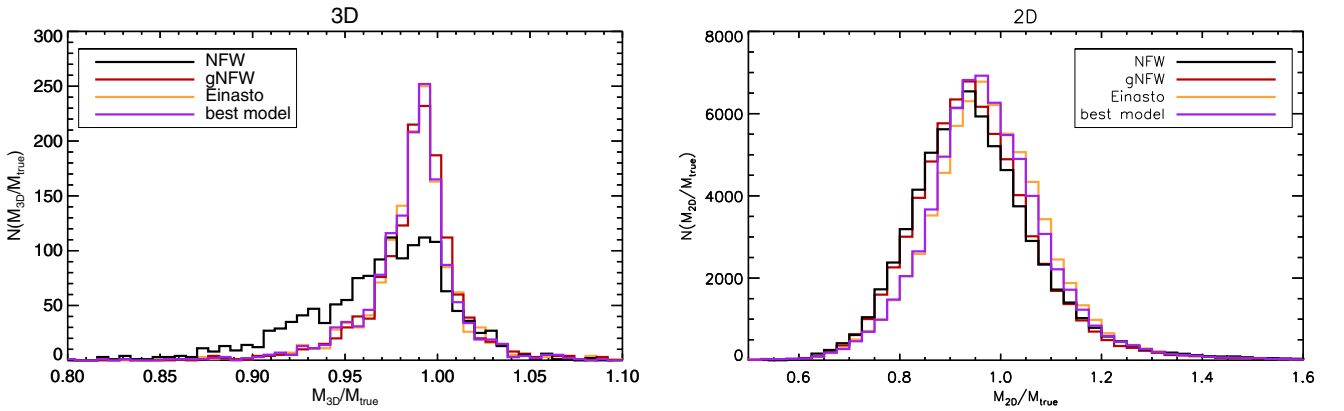

Figure 6. Distributions of the ratios between 3D and true masses (left panel) and between 2D and true masses (right panel). The results are shown for the three fitting functions employed in this work: NFW (black), gNFW (red), and Einasto (yellow). We also show the distributions obtained for the mass estimates given by the model with the lowest residuals.

(A color version of this figure is available in the online journal.)

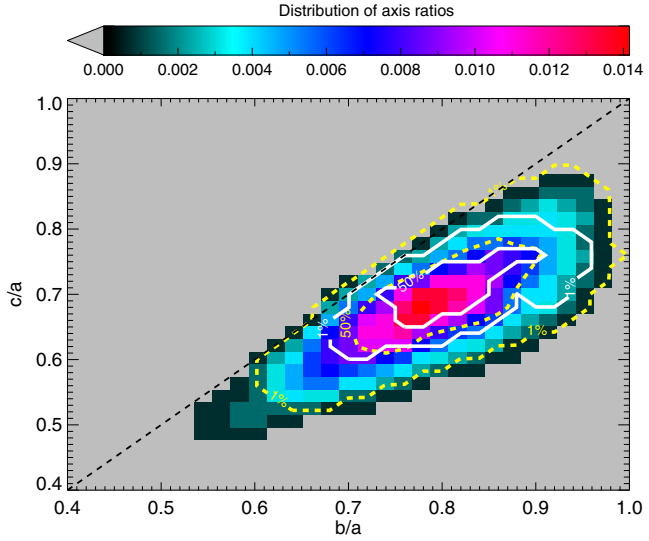

Figure 7. Color map shows the distribution of the axis ratios b/a and c/a of all of the MUSIC-2 halos. The dashed and solid contours indicate the levels corresponding to 1% and 50% of the peaks of the distributions for the relaxed and super-relaxed halos.

(A color version of this figure is available in the online journal.)

inertial ellipsoid fitting the mass distribution of the halos with $a > b > c$. This fit is done using all particles within the virial radius. It is clear from this plot that the relaxed (yellow dashed contours) and super-relaxed systems (white contours) generally have higher values of both b/a and c/a. Thus, their shape is closer to spherical than that of nonrelaxed halos, in agreement with Lemze et al. (2012).

5.4. Concentration–mass Relation

The concentration–mass ($c - M - z$) relation is derived by means of nonlinear least-squares fitting using a Levenberg–Marquardt algorithm. The fitting function we employ is

$$c(M, z) = A \left(\frac{1.34}{1+z}\right)^{B} \left(\frac{M}{8 \times 10^{14}\, h^{-1}\, M_{\odot}}\right)^{C}, \qquad (26)$$

which was also used by Duffy et al. (2008) and De Boni et al. (2013), although using a different pivot mass and redshift. We perform this analysis for the three fitting models considered and report the corresponding best-fit parameters and errors in Table 2. The results are reported for the full sample as well as for the subsamples of relaxed and super-relaxed halos. We use Equation (26) to fit the c–M–z relations derived from the analyses of the density profiles.

5.4.1. Comparison between Fitting Models

In the following, we consider the concentrations obtained from the NFW fit of the density profiles as a reference when making comparisons with the concentrations derived from the gNFW and Einasto fits. The yellow and green histograms in the upper panel of Figure 8 show the the distributions of the ratios $c_{\rm 3D,gNFW}/c_{\rm 3D,NFW}$ and $c_{\rm 3D,Einasto}/c_{\rm 3D,NFW}$ obtained from our analysis. In both cases, we find that the distributions peak at values around ∼0.9–0.95, with the Einasto concentrations being generally smaller than the NFW ones. This result is in agreement with the recent findings of Dutton & Macciò (2014), who also find that the Einasto concentrations are ∼10–15% smaller than the NFW concentrations on the mass scale of the MUSIC-2 halos. The halos with the smallest concentrations are of course the unrelaxed systems, for which we already pointed out that the NFW model is generally a bad fit. An example of such profiles is shown in the bottom panel of Figure 8. In this case, the best-fit NFW concentration is $c_{\rm 3D,NFW} = 2.5$, and the gNFW and Einasto concentrations are $c_{\rm 3D,gNFW} = 10^{-2}$ and $c_{\rm 3D,Einasto} = 0.1$, respectively. Considering only the relaxed or the super-relaxed halos, the ratios between fitted and true concentrations are much closer to unity. For example, the mean ratios of $c_{\rm 3D,gNFW}/c_{\rm 3D,NFW}$ and $c_{\rm 3D,Einasto}/c_{\rm 3D,NFW}$ for the super-relaxed systems are 1.0 and 0.99, respectively. We want to stress that the concentration of the Einasto profile being smaller than the NFW does not imply necessarily that the halos are less concentrated. For the Einasto profile, the mass inside the scale radius also depends on the $1/n$ parameter. A halo with the same mass ratio between two radii as given by the NFW model can be fitted with a smaller concentration and a larger n.

In Figure 9, we show the c–M relations obtained from fitting the density profiles of the MUSIC-2 with the NFW, gNFW, and Einasto models (upper, middle, and bottom panels, respectively). The results are displayed for the halos at the

Table 2
Best-Fit Parameters for the 3D and 2D c–M–z Relations

Fitting Func.	3D/2D	Relax.	A	B	C	Sel. Func.
NFW	3D	all	3.757 ± 0.054	0.288 ± 0.077	-0.058 ± 0.017	ext
NFW	3D	rel	4.051 ± 0.067	0.197 ± 0.093	-0.084 ± 0.020	ext
NFW	3D	srel	4.704 ± 0.151	0.519 ± 0.187	-0.054 ± 0.039	ext
NFW	2D	all	3.580 ± 0.040	0.003 ± 0.053	0.051 ± 0.013	ext
NFW	2D	rel	3.813 ± 0.050	0.108 ± 0.064	-0.032 ± 0.015	ext
NFW	2D	srel	4.380 ± 0.113	0.420 ± 0.137	-0.052 ± 0.030	ext
gNFW	3D	all	3.671 ± 0.055	0.050 ± 0.086	0.101 ± 0.019	ext
gNFW	3D	rel	4.091 ± 0.068	0.057 ± 0.098	0.018 ± 0.021	ext
gNFW	3D	srel	4.646 ± 0.152	0.457 ± 0.195	-0.023 ± 0.040	ext
gNFW	2D	all	4.088 ± 0.047	-0.228 ± 0.055	0.164 ± 0.014	ext
gNFW	2D	rel	4.261 ± 0.055	-0.159 ± 0.063	0.071 ± 0.015	ext
gNFW	2D	srel	4.660 ± 0.117	0.138 ± 0.129	0.022 ± 0.029	ext
Einasto	3D	all	3.407 ± 0.055	0.040 ± 0.092	0.088 ± 0.020	ext
Einasto	3D	rel	3.805 ± 0.068	0.088 ± 0.104	-0.007 ± 0.022	ext
Einasto	3D	srel	4.366 ± 0.151	0.470 ± 0.204	-0.046 ± 0.043	ext
Einasto	2D	all	3.617 ± 0.034	0.070 ± 0.049	0.103 ± 0.012	ext
Einasto	2D	rel	3.729 ± 0.041	0.020 ± 0.060	0.028 ± 0.014	ext
Einasto	2D	srel	4.151 ± 0.096	0.352 ± 0.126	0.012 ± 0.028	ext
NFW	2D	all	3.978 ± 0.055	0.651 ± 0.073	-0.214 ± 0.018	sl
NFW	2D	rel	4.200 ± 0.068	0.593 ± 0.090	-0.185 ± 0.021	sl
NFW	2D	srel	4.658 ± 0.150	0.781 ± 0.189	-0.124 ± 0.041	sl
gNFW	2D	all	4.338 ± 0.056	0.276 ± 0.073	-0.060 ± 0.018	sl
gNFW	2D	rel	4.571 ± 0.069	0.310 ± 0.089	-0.053 ± 0.020	sl
gNFW	2D	srel	4.892 ± 0.152	0.558 ± 0.187	-0.059 ± 0.041	sl
Einasto	2D	all	3.774 ± 0.053	0.465 ± 0.080	-0.128 ± 0.019	sl
Einasto	2D	rel	3.961 ± 0.066	0.489 ± 0.098	-0.128 ± 0.022	sl
Einasto	2D	srel	4.317 ± 0.147	0.684 ± 0.208	-0.102 ± 0.045	sl
NFW	2D	all	4.105 ± 0.100	0.668 ± 0.341	-0.160 ± 0.108	xray
gNFW	2D	all	4.228 ± 0.138	0.376 ± 0.458	-0.080 ± 0.145	xray
Einasto	2D	all	3.880 ± 0.119	-0.017 ± 0.425	-0.035 ± 0.137	xray

Notes. The results are listed for the concentration–mass measurements based on the NFW, gNFW, and Einasto models. First column: fitting model; second column: 3D or 2D analysis; third column: relaxation state (all = full sample; rel = relaxed; srel = super-relaxed); columns 3, 4, 5: c–M–z parameters (see Equation (26)); column 6: selection function (ext = extended sample, no selection applied except that based on the relaxation state; sl = strong lensing selection; xray = X-ray selection). The parameters of the 2D c–M–z relation for the extended sample are taken from J. Vega et al. (in preparation).

lowest redshift investigated in this work ($z = 0.250$). Each circle corresponds to a halo, and the solid, dashed, and dotted lines indicate the best-fit c–M–z relations for the full, relaxed, and super-relaxed samples. At fixed mass, the distribution of NFW halo concentrations is reasonably well fitted by a log-normal distribution and have a standard deviation $\sigma_c \sim 0.25$, compatible with the findings of several previous works (see e.g., Dolag et al. 2004). The concentrations derived from the gNFW and Einasto fits are characterized by a larger scatter. In all cases we find that the dependence of the concentration on mass is very shallow. For the NFW profile, $c \propto M^{-0.057\pm0.017}$ for the full sample. Instead, for the gNFW and the Einasto profiles, the logarithmic slope of the c–M relation is slightly positive. For the relaxed and super-relaxed halos, all of the c–M relations have logarithmic slopes that are negative or consistent with zero. As expected, we find that the more relaxed the halos are, the higher their concentrations (Zhao et al. 2009; Giocoli et al. 2012b). This result holds regardless of the fitting function. At the lowest masses, the relative change in typical concentrations between the full and the relaxed (or super-relaxed) samples is larger for the gNFW and Einasto fits. In fact, we find that a larger fraction of small-mass unrelaxed halos are fitted with lower concentrations using these two fitting models than with the NFW profile. These halos are responsible for the positive logarithmic slope of the c–M relation when fitting with the gNFW or Einasto profiles.

As can be seen from the B parameters listed in Table 2, the normalization of the 3D c–M relation has an almost negligible redshift dependence for the full sample. For example, in the case of the NFW profile, $c \propto (1+z)^{-0.29\pm0.08}$. For the gNFW and Einasto profiles, the redshift evolution is even shallower. We notice, however, that the dependence of the concentration on redshift appears to be stronger for the most relaxed systems. In particular, for the super-relaxed halos, we find $B \sim 0.52$, regardless of the fitting function.

5.4.2. The NFW Concentration–Mass Relation

There are several parameterizations of the c–M relation in the literature, mostly derived from fitting simulated halos using NFW profiles. In the upper panel of Figure 10, we show the NFW c–M–z relation derived from the 3D analysis for the whole sample of `MUSIC-2` halos (solid lines). We use different colors to show how the relation evolves with redshift. We find a rather shallow dependence of the concentrations on mass and redshift. Over the mass range $[4\text{–}12 \times 10^{14}\, h^{-1}\, M_\odot]$, the concentrations vary by less than 10%, decreasing as a function of mass as $M^{-0.058\pm0.017}$. The amplitude of the c–M relation scales with redshifts as $(1+z)^{-0.29\pm0.08}$. Other authors find that the c–M relation of massive halos is rather flat. For example, Zhao et al. (2009), studying an ensemble of numerical simulations in the context of various cosmological models, find that the

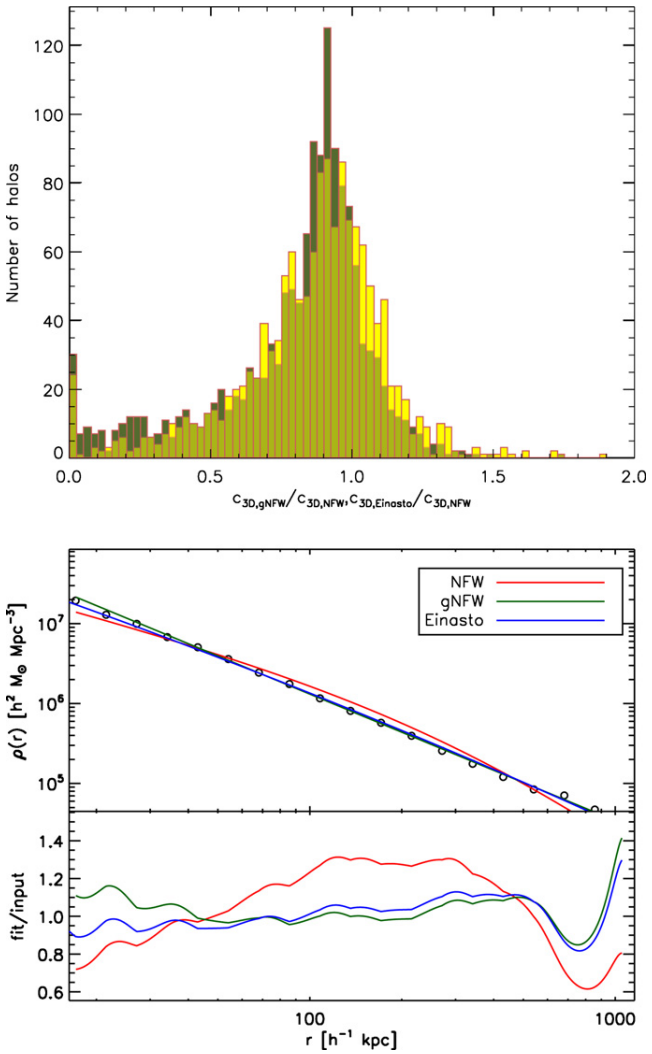

Figure 8. Upper panel: distributions of concentration ratios $c_{3D,gNFW}/c_{3D,NFW}$ (yellow histogram) and $c_{3D,Einasto}/c_{3D,NFW}$ (green histogram). Bottom panel: example of a density profile for which the Einasto and gNFW concentrations are nearly zero. The halo profile is indicated by the open circles, and the best-fit NFW, gNFW, and Einasto profiles are given by the red, green, and blue lines, respectively. In the lower subpanel we show the ratio between the best fit and the input profiles.

(A color version of this figure is available in the online journal.)

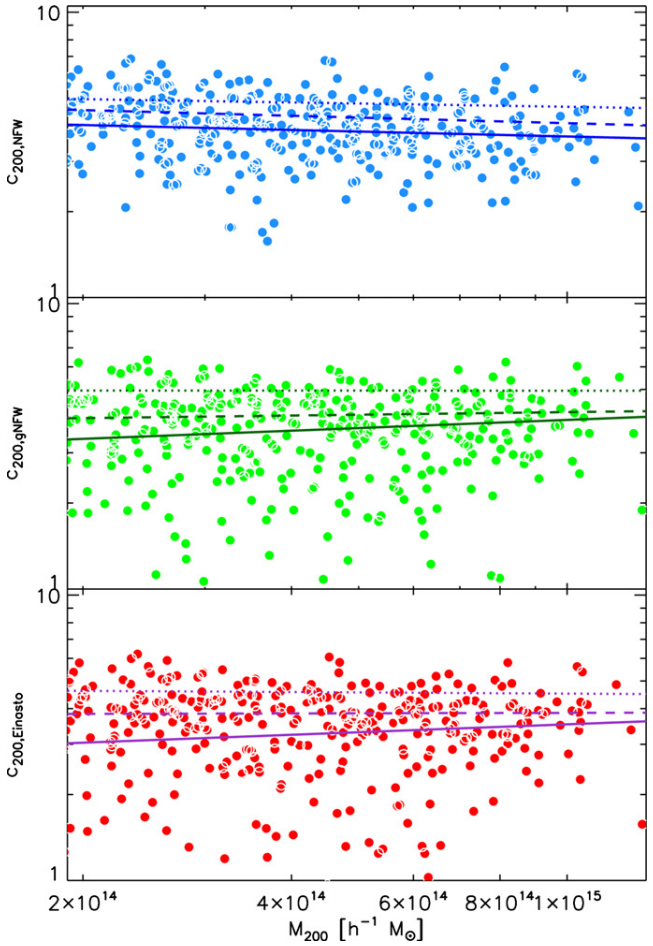

Figure 9. Concentration–mass measurements at $z = 0.250$. The results are shown for the full sample (filled circles). The upper, middle, and bottom panels refer to the NFW, gNFW, and Einasto fits, respectively. In each panel, we show the best-fit c–M–z relations for the full, relaxed, and super-relaxed samples (solid, dashed, and dotted lines, respectively).

(A color version of this figure is available in the online journal.)

concentration is strongly correlated with the age of the universe when the halo progenitor on the mass accretion history first reaches 4% of its current mass. According to this correlation, they find that the concentration is nearly constant for halos with mass $M \gtrsim 10^{14}\,h^{-1}\,M_\odot$. They also predict a very shallow redshift evolution of the c–M relation. In a recent work, De Boni et al. (2013) also find concentrations that scale with mass and redshift, similar to our results. Their concentrations scale with mass and redshift as $M^{-0.07}$ and $(1+z)^{-0.26}$, respectively.

The normalization of our c–M–z relation is higher than that found by some other authors, like De Boni et al. (2013; dot-dashed lines in the upper panel of Figure 10) or Duffy et al. (2008). In these cases, the differences can be explained in terms of different cosmological settings. For example, De Boni et al. (2013) analyze halos evolved in the framework of a WMAP3 cosmological model and adopt a rather small normalization of the matter power spectrum, $\sigma_8 = 0.72$. If we consider other analyses in the literature in the context of WMAP7 normalized cosmologies, the agreement is much better. For example, the c–M relation that best fits our data at low redshift is in rather good agreement with the results of Bhattacharya et al. (2013) for nonrelaxed halos. For comparison, their c–M relation is overplotted in the upper panel of Figure 10 (dashed lines). At $z = 0.250$, the concentrations we measure at a given mass are only $\lesssim$6% higher than found by Bhattacharya et al. (2013). However, their c–M relation has a stronger redshift evolution. Between $z = 0.250$ and $z = 0.667$, their concentrations at a fixed mass decrease by ∼17%, while ours vary only by ∼10%.

Potentially important differences between this work and Bhattacharya et al. (2013) are (1) our simulations include baryons, while the halos studied by Bhattacharya et al. (2013) are made only of dark matter; (2) our analysis focuses on a limited mass range, and the volume we sample is smaller than in the simulations employed by Bhattacharya et al. (2013); (3) the mass resolution of our simulations is roughly two orders of magnitude better; (4) Bhattacharya et al. (2013) fit their halos over a different radial range, $[0.1–1r_{vir}]$ versus $[0.02–1r_{200}]$; and, finally, (5) Bhattacharya et al. (2013) fit the mass profiles instead of the density profiles, as we do. Given that our simulations are nonradiative, it is unlikely that the

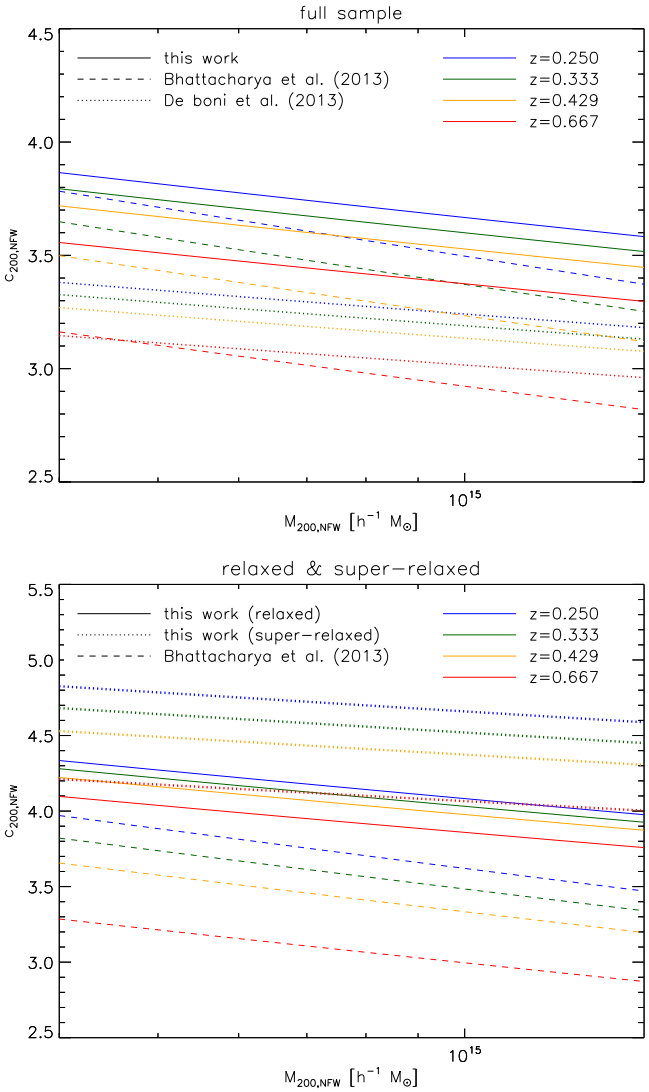

Figure 10. Concentration–mass relation and its redshift evolution as obtained from fitting the halo density profiles with the NFW model. The results of this analysis are compared with the recent work of Bhattacharya et al. (2013; dashed lines) and De Boni et al. (dotted lines in the upper panel). The redshift evolution is illustrated by different colors. The upper and bottom panels show the results for the whole sample and for the subsamples of relaxed and super-relaxed halos. Note that Bhattacharya et al. (2013) only distinguish between relaxed and unrelaxed halos.

(A color version of this figure is available in the online journal.)

differences between the c–M relations arise from baryonic effects. De Boni et al. (2013) show that concentrations are higher by 5%–15% in radiative simulations compared to dark matter-only simulations. This result, however, was obtained using hydrodynamical simulations that are known to suffer from the overcooling problem. It has been shown by other authors that halos in adiabatic simulations develop density profiles pretty similar to those of pure dark matter halos (Killedar et al. 2012). The different mass range, volume, and resolution of the simulations may have a larger impact on the results. Because our halos are sampled with a larger number of particles, the profiles are better resolved. Thus, the measurements of the individual concentrations should be more robust and allow us to resolve smaller radial scales. On the other hand, because their volume is bigger, Bhattacharya et al. (2013) have a larger number of massive halos to constrain the c–M relation at the cluster scales. In contrast, Bhattacharya et al. (2013) fit halos over three orders of magnitude in mass. It may be possible that the strong redshift evolution of their c–M relation is driven by the smallest halos. Overall, it is likely that the higher normalization of our c–M is largely due to the better resolution of the MUSIC-2 sample compared to the simulation sets used in Bhattacharya et al. (2013).

The bottom panel in Figure 10 shows another comparison between our best-fit NFW c–M–z relation and the results of Bhattacharya et al. (2013). The solid and the dotted lines show our relations for relaxed and the super-relaxed samples, respectively. The most striking difference from Bhattacharya et al. (2013) (dashed lines) is that we find a much stronger dependence of concentration on the halo dynamical state. While the normalization of our c–M–z relation increases by $\sim$10% between the full and relaxed samples, Bhattacharya et al. (2013) find that concentrations of relaxed halos increase only by $\sim$3%.

5.4.3. The c–M Relation and Temperature Selection

The CLASH relaxed sample is composed of clusters with X-ray temperatures larger than 5 keV. Even if the observational sample is not complete, it is interesting to check whether a selection based on temperature may lead to a biased concentration–mass relation. Once more, we stress that the description of the gas physical processes is not sufficiently accurate in these nonradiative simulations to reproduce several observed X-ray properties of clusters. Thus, we do not aim to draw quantitative conclusions here. Rather, we are interested in understanding in which directions a temperature selection would change the results.

Under the assumption of self-similarity, expected in the case that cluster properties and correlations between them are determined by gravity alone and that clusters are in virial equilibrium, the mass should scale as $\propto T^{2/3}$, thus implying that both selections based on mass and temperature should lead to the same samples. Unfortunately, as we discussed earlier, a large fraction of halos is still far from being in equilibrium. As a result, the scatter around the M–T relation is large (see, e.g., Rasia et al. 2011). At fixed mass, the halos with the lowest temperatures are also less concentrated, implying that in introducing a temperature cut we would exclude the least concentrated halos, thus increasing the average concentration of the sample.

In Figure 12, we illustrate the effects of the selection by showing the distributions of the halos at $z = 0.250$ in the c–M plane. The upper panel refers to all halos in the MUSIC-2 sample. The red circles indicate those halos that have a mass-weighted temperature $T_{\rm mw} > 5$ keV. As expected, the hottest halos are the most massive in the sample. At the largest masses, almost all halos pass the temperature cut. However, if we consider less-massive objects, we notice that there is an increasing fraction of halos that are not hot enough to be selected. The halos that do not pass the cut have likely experienced a recent merger and are therefore characterized by small concentrations. The accretion of a smaller (and colder) object decreases temporally the measured temperature before the shock heats the intracluster medium. This implies that the small-mass halos in the temperature-selected sample have concentrations above the average of the full sample. Given that it affects the sample composition in a way that depends on the mass, the temperature selection thus changes the overall slope of the c–M relation. The best linear fits to the data in

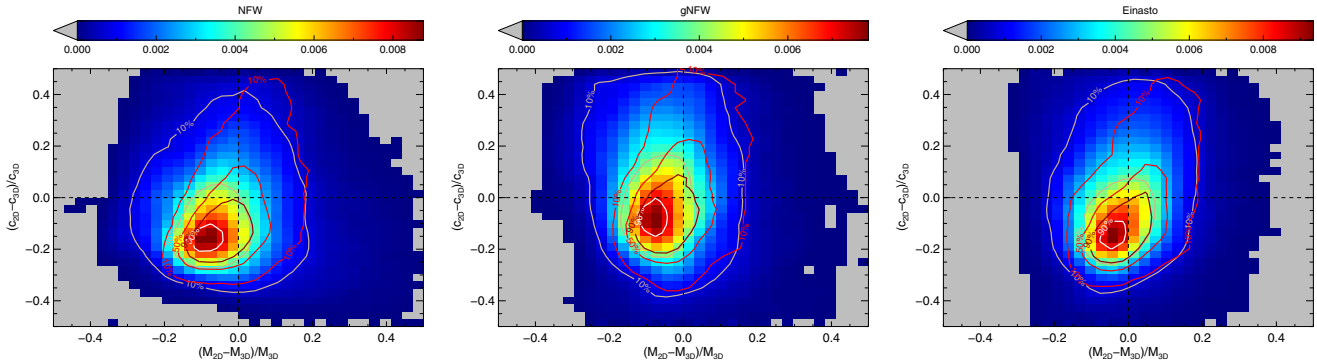

Figure 11. Distributions of MUSIC-2 halos in the plane $(c_{2D} - c_{3D})/c_{3D}$ vs. $(M_{2D} - M_{3D})/M_{3D}$. Results are shown for the NFW, gNFW, and Einasto fits (left, central, and right panels, respectively). The two-dimensional histograms refer to the whole sample. The gray and white contours overlaid on the image show the intensity levels corresponding to 10%, 50%, and 90% of the probability peak. The red contours correspond to the same levels for the distributions of the relaxed halos.

(A color version of this figure is available in the online journal.)

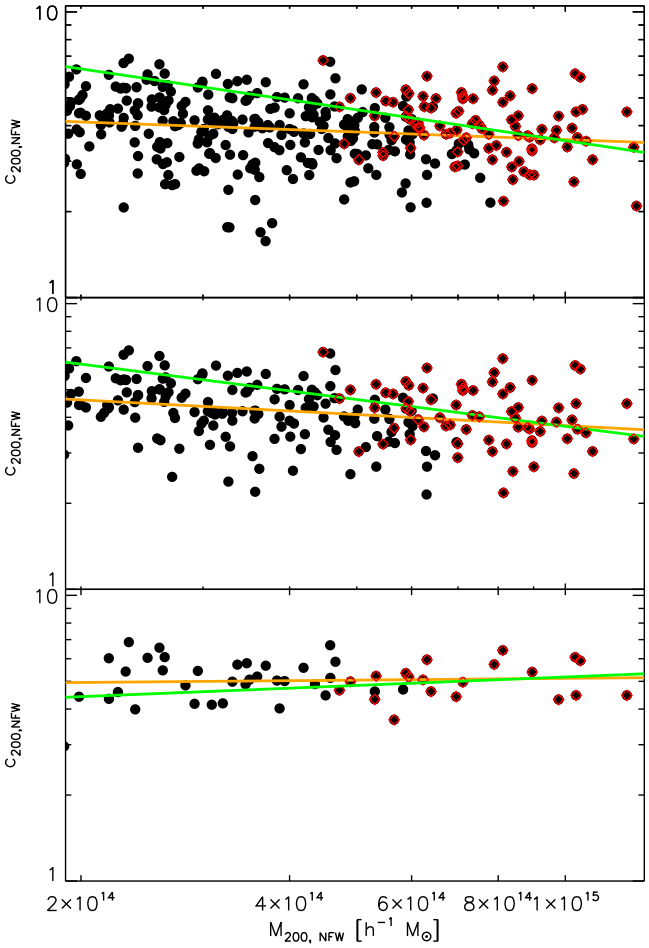

Figure 12. Effects of temperature selection on the c–M relation. The black data points show the NFW 3D concentrations vs. masses for all halos in the MUSIC-2 sample at $z = 0.250$. The red circled data points indicate the halos with mass-weighted temperature $T > 5$ keV. While all (relaxed and unrelaxed) halos are used in the upper panel, the middle and the bottom panels show the results for the relaxed and super-relaxed halos only. The orange and green solid lines are the best-fit c–M relations to the data points before and after applying the temperature cut.

(A color version of this figure is available in the online journal.)

the log M–log c space are given by the orange and green lines, which refer to the samples without and with temperature cuts applied.

However, the differences between the c–M relations of mass- and temperature-selected samples become negligible when additional filtering is applied based on the relaxation state. Given that the temperature selection mainly affects the fraction of unrelaxed halos in the sample, there are not significant differences between the mass and temperature selections when the unrelaxed halos are discarded a priori. Thus, the c–M relations of relaxed and super-relaxed halos are less sensitive to the temperature selection. This is shown in the middle and in the bottom panels of Figure 12, which refer to the relaxed and super-relaxed halos, respectively.

5.4.4. The Concentration–Mass Relation in 2D

The 2D concentration–mass relation of the MUSIC-2 halos will be discussed in detail in an upcoming paper (J. Vega et al., in preparation). We briefly summarize some properties of this c–M relation that are relevant for the following discussion. Projection effects do affect concentrations, which are generally found to be smaller than in 3D. This effect of triaxiality, also discussed in Giocoli et al. (2012a), is illustrated in Figure 11, where we show the distribution of the MUSIC-2 halos in the $(c_{2D} - c_{3D})/c_{3D}$ versus $(M_{2D} - M_{3D})/M_{3D}$ plane. The 2D histograms show that regardless of the fitting model, the masses and concentrations derived from fitting the surface-density profiles tend to be smaller than measured from fitting the density profiles. The trend is in qualitative agreement with the findings of Giocoli et al. (2012a), although the amplitude of both the concentration and mass biases found here is smaller. The white contours overlaid on the 2D histograms show the intensity levels corresponding to 10%, 50%, and 90% of the peaks of the distributions. The red contours indicate the same intensity levels for the subsample of super-relaxed halos. As explained in Section 5.3, the bias is reduced for the relaxed halos because these systems are typically more spherical than the unrelaxed halos.

The best-fit parameters of the 2D c–M–z relation are listed in Table 2. The relations for halos at $z = 0.250$ are given by the solid lines in Figure 13. Interestingly, the c–M relation is very flat and characterized by an inverted slope compared to the c–M relation in 3D. This suggests that the 2D concentrations underestimate the 3D ones more significantly at the lowest than at the highest masses. One possible explanation is that the halo triaxiality is somehow biased below the completeness limits

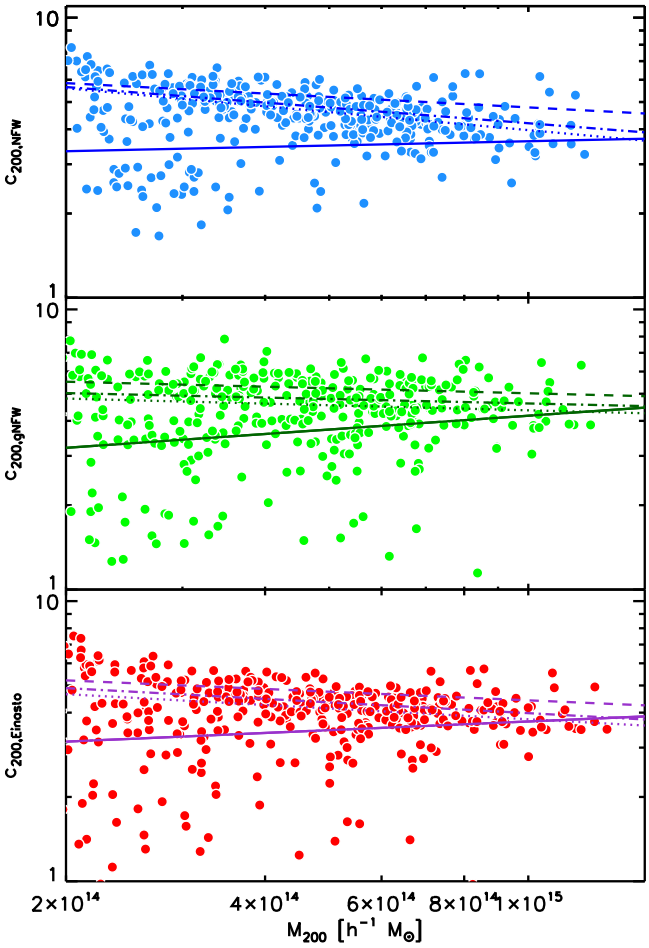

Figure 13. Concentration–mass relation for strong-lensing halos at $z = 0.250$. The lines indicate the results obtained for the halos in the full, relaxed, and super-relaxed samples (dotted, dot–dashed, and dashed lines, respectively). For comparison, the 2D c–M relation derived for the full sample including nonstrong lenses is shown by the solid line. The colored circles correspond to the projections capable of producing critical lines for $z_s = 2$. The upper, middle, and bottom panels refer to the NFW, gNFW, and Einasto fits.

(A color version of this figure is available in the online journal.)

listed in Table 1. However, we checked that the c–M relation obtained only from halos above the completeness limits does not differ significantly from what we obtain using the extended sample. However, the constraints on its slope are obviously weakened. In addition, we notice that Giocoli et al. (2012a) also find indications for a 2D concentration bias that decreases as a function of mass. This will be discussed in J. Vega et al. (in preparation).

6. THE CONCENTRATION–MASS RELATION OF CLASH-LIKE CLUSTERS

We can now discuss how different cluster selection methods impact the c–M–z relation. We will start with the c–M–z relation of strong-lensing (SL) galaxy clusters. Then we investigate the c–M–z relation obtained by selecting halos on the basis of their X-ray morphology. The results of this analysis are compared to the observations in Merten et al. (2014) and Umetsu et al. (2014).

6.1. The c–M–z Relation of Strong-lensing Halos

As explained above, the CLASH cluster sample is composed of 25 galaxy clusters, of which only five were selected on the basis of their SL strength. The remaining 20 clusters are not SL selected, and they were chosen on the basis of their X-ray morphology. We will discuss this selection method in the next section. Nevertheless, SL features (multiple images and arcs) have been securely detected in all CLASH clusters except RXJ 1532.8+3021. The analyses of these SL features have allowed the creation of detailed lens models and the measurement of their Einstein radii (Zitrin et al. 2014). The Einstein radii for sources at redshift $z_s = 2$ are within the range 5–55 arcsec.

We construct the c–M–z relation of SL galaxy clusters by selecting those projections where we measure an Einstein radius compatible with those measured in the CLASH sample ($\theta_E > 5''$). As explained, the Einstein radius is defined as in Equation (18).

In Figure 13, we show the concentration–mass relations at $z = 0.250$ derived from SL halos in the MUSIC-2 sample. The relations are displayed for the NFW, gNFW, and Einasto models (upper, middle, and bottom panels). The corresponding parameters are listed in Table 2. The dotted, dashed, and dot–dashed lines indicate the relations obtained for the full, the relaxed, and the super-relaxed samples, respectively. For comparison, we show also the c–M relation for the full sample, including also the nonstrong lenses, as discussed in Section 5.4.4. By requiring that the halos are strong lenses in their projections, we remove a large fraction of halos with low concentrations, obtaining relations characterized by a larger normalization. In particular, an increasingly larger number of halos of small mass are unable to produce an appreciable SL signal. By removing them from the initial catalog, we restore the negative logarithmic slope of the c–M relation. Because of this selection, the concentration scales with mass as $c \propto M^{-0.214\pm0.018}$. This result is in very good agreement with the theoretical predictions of Giocoli et al. (2013) and Oguri et al. (2012), who estimated the lensing bias of the c–M via semianalytic calculations employing triaxial halos. For the gNFW and Einasto models, the concentration–mass relations are slightly flatter.

Even for the SL halos, the normalization of the c–M–z relation depends on the relaxation state. The most relaxed systems have the largest concentrations. The differences between the c–M–z relations of relaxed and unrelaxed halos are smaller than found earlier for the whole sample including nonstrong lenses, though. This is because in the SL-selected sample the fraction of relaxed and super-relaxed halos is pretty high. At $z = 0.250$, about 75% of the SL projections belong to relaxed halos. The fraction of super-relaxed halos in this sample is ∼27%. At $z = 0.667$ the fractions of relaxed and super-relaxed halos are ∼60% and ∼13%, respectively.

Finally, we find that the redshift evolution of the $c-M$ relation of SL halos is stronger than for non-SL halos. The values for the B parameters listed in Table 2 are in the range [0.48–0.64] for the three fitting models.

6.2. The c–M–z Relation of X-ray-selected Halos

We discuss now the impact of the X-ray selection on the concentration–mass relation. In particular, we discuss the expectations for halos selected so as to resemble the X-ray morphologies of the clusters in the CLASH X-ray-selected sample. The results shown here are based on the analysis of three

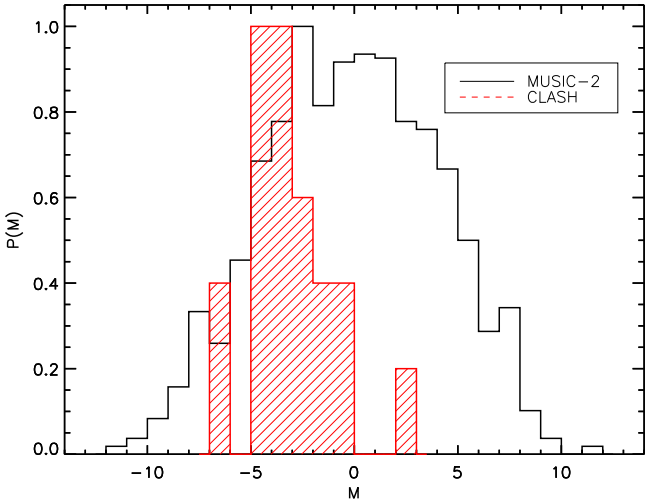

Figure 14. Distributions of regularity parameters M in the MUSIC-2 (black histogram) and in the CLASH sample (red histogram).

(A color version of this figure is available in the online journal.)

projections per halo, and the halos considered are those with 3D mass above the completeness limits given in Table 1. The restriction of the analysis to this smaller sample of simulated halos was dictated by the large computational time required to produce the X-ray-simulated observations. The mass range covered by these simulations is however representative of the mass range of the CLASH clusters (see both Merten et al. 2014 and Umetsu et al. 2014).

As explained in Section 4.1, the X-ray morphology is measured by means of five morphological parameters. They can be combined to quantify the degree of regularity of the halos, as shown in Equation (24). The regularity parameters of the CLASH clusters, as measured in their X-ray images, are listed in Table 3. In Figure 14, we show their distribution (red histogram), and we compare it to the distribution of the regularity parameters in the MUSIC-2 sample (black histogram). The histograms have been normalized to have the same peak value. As it emerges from these distributions, the CLASH clusters have quite typical regularity parameters in the simulations. With the exception of MACSJ 1206.2-0847, the clusters in the CLASH X-ray-selected sample have negative M parameters, indicating that they are more regular than the mean of the simulations. Even in the case of MACSJ 1206.2-0847, other works based on different analyses find that this system is not likely to be perturbed by significant substructures (Lemze et al. 2013; Biviano et al. 2013). This is expected given that these clusters were selected on the basis of their X-ray regularity. On the other hand, the comparison shows that their regularity is not extreme, in the sense that there are several simulated halos with regularity parameters exceeding the values for the CLASH clusters. In fact, the simulated sample has a tail of low M values extending well beyond those of the CLASH clusters.

In the upper panel of Figure 15, we show that the concentration inferred from the analysis of the 2D mass distributions is correlated with the regularity parameter M. The red, green, and blue circles refer to unrelaxed, relaxed, and super-relaxed halos. The correlation was evaluated by measuring the linear Pearson correlation coefficient P between the $\log_{10} c_{200,2D}$ and the M values. It is stronger for the super-relaxed halos, for which we measure $P = -0.67$. For the relaxed and the full samples,

Table 3
Comparison between CLASH Clusters and X-Ray-Selected Halos

Cluster	$z_{\rm sim}$	z	M	$M_{200,X}$ ($10^{14}\ h^{-1}\ M_\odot$)	$c_{200,X}$
A383	0.250	0.188	−6.49	8.52 ± 1.47	3.46 ± 1.09
A209	0.250	0.206	−0.87	9.43 ± 1.76	4.09 ± 0.94
A1423	0.250	0.213	−3.11	7.00 ± 1.80	4.60 ± 1.12
A2261	0.250	0.225	−3.93	9.98 ± 2.03	3.76 ± 1.00
RXJ2129+0005	0.250	0.234	−3.70	6.12 ± 2.71	3.69 ± 1.01
A611	0.250	0.288	−4.27	8.50 ± 1.59	3.12 ± 1.43
MS2137−2353	0.333	0.313	−5.00	10.41 ± 2.65	4.38 ± 1.11
RXJ1532.8+3021	0.333	0.345	−6.27	6.19 ± 2.65	3.73 ± 1.11
RXCJ2248−4431	0.333	0.348	−1.56	11.50 ± 3.33	3.62 ± 1.09
MACSJ1115+0129	0.333	0.352	−2.87	9.00 ± 1.80	3.07 ± 1.45
MACSJ1931−26	0.333	0.352	−4.37	6.92 ± 2.31	3.91 ± 1.05
MACSJ1720+3536	0.429	0.391	−4.12	7.50 ± 1.92	5.68 ± 1.81
MACSJ0429−02	0.429	0.399	−3.50	8.05 ± 1.81	3.74 ± 1.10
MACSJ1206−08	0.429	0.439	2.29	8.62 ± 1.96	3.14 ± 1.43
MACSJ0329−02	0.429	0.450	−2.90	7.31 ± 1.89	3.82 ± 1.09
RXJ1347−1145	0.429	0.451	−2.79	11.47 ± 4.20	3.62 ± 1.16
MACSJ1311−03	0.429	0.494	−3.44	6.09 ± 2.31	3.90 ± 1.02
MACSJ1423+24	0.667	0.545	−4.10	5.71 ± 2.49	3.93 ± 1.07
MACSJ0744+39	0.667	0.686	−1.56	7.00 ± 1.93	4.58 ± 1.22

Notes. Column 1: cluster name; column 2: reference redshift in the simulations; column 3: true redshift of the CLASH cluster; column 4: regularity parameter M; column 5: mass range of X-ray-selected clusters in the simulation; column 6: mean NFW concentration of selected halos.

we obtain $P = -0.46$ and $P = -0.39$, respectively. The best linear fit between the two parameters is

$$\log_{10} c_{200,2D} = (0.598 \pm 0.009) - (0.019 \pm 0.002) \times M. \quad (27)$$

If we refer to the average of all halos in the simulations ($M = 0$ by construction), for negative values of M we expect a positive concentration bias. Because the median value of the M parameters of the CLASH clusters is $M_{\rm CLASH} = -3.44$, on the basis of Equation (27), we can give an estimate of the expected concentration bias for the CLASH X-ray-selected sample, which is

$$\frac{c_{200,\rm CLASH}}{c_{200,2D}(M=0)} = 1.11 \pm 0.03. \quad (28)$$

An interesting question is whether this concentration excess compared to the full sample arises from the selection of purely relaxed halos. The answer is already contained in the upper panel of Figure 15: a selection based on the M regularity parameter does not lead to the construction of a purely relaxed sample. Indeed, the left side of the diagram contains several red circles, indicating that unrelaxed halos can have $M < 0$. The composition of samples selected by means of the M parameter is shown in the bottom panel of Figure 15. The curves show the fractions of relaxed (R), nonrelaxed (NR), and super-relaxed (SR) halos in the samples with regularity parameter smaller than M. As indicated by the dotted and the solid black lines (R and NR halos), the fraction of relaxed and unrelaxed halos is nearly constant as a function of M. Thus, there is no strong correlation between X-ray regularity and halo relaxation. In particular, we find that only ∼70% of the halos among those with $M < 0$ are relaxed.[37] The remainder ∼30% of the halos are unrelaxed. As stated, this composition is very similar to that of the full sample.

[37] We remind that relaxed halos are identified by means of the criteria described in Section 5.2. By definition, super-relaxed halos are also included in this category.

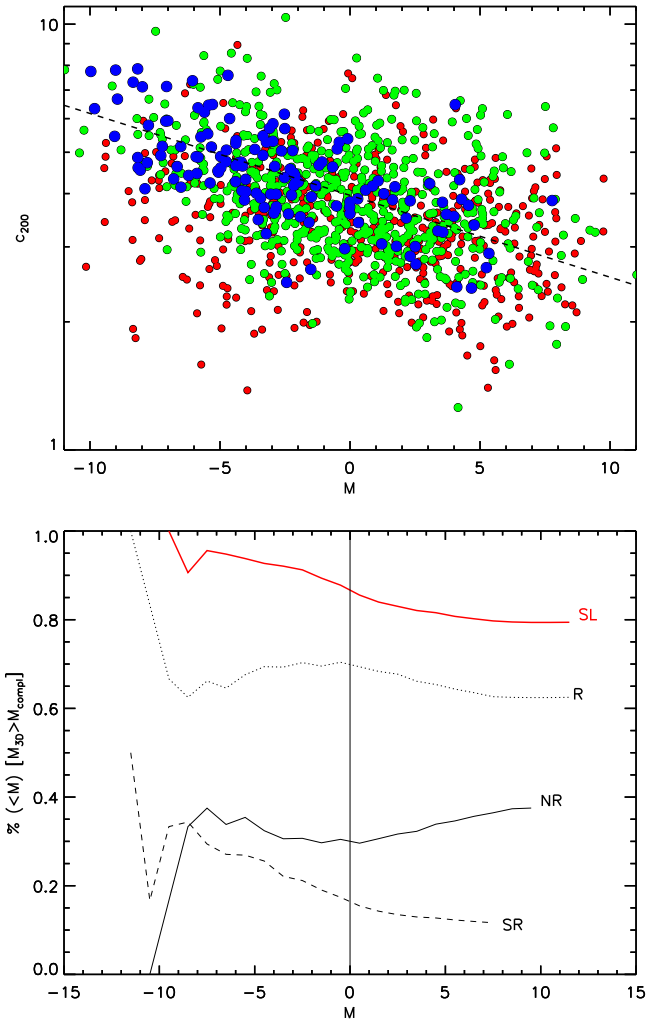

Figure 15. Upper panel: correlation between projected concentration and regularity parameter M. The red, green, and blue circles indicate the unrelaxed, relaxed, and super-relaxed halos, respectively. The dashed line shows the best linear fit between $\log_{10}(c_{200})$ and M, obtained using all of the data points and given in Equation (27). Bottom panel: fraction of strong lensing (SL), unrelaxed (NR), relaxed (R), and super-relaxed (SR) halos in samples selected by means of the M parameter.

(A color version of this figure is available in the online journal.)

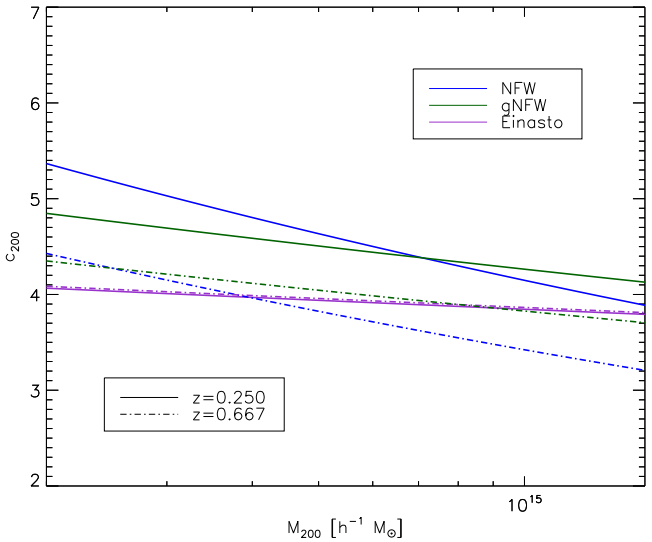

Figure 16. Concentration–mass relation at $z = 0.250$ and $z = 0.667$ for X-ray-selected halos (solid and dot–dashed lines, respectively). The results are shown for the NFW, gNFW, and Einasto fitting models.

(A color version of this figure is available in the online journal.)

In contrast, as indicated by the dashed line, the fraction of super-relaxed halos decreases as a function of M. Thus, in samples of clusters selected to have regular X-ray morphologies, we expect to have a larger fraction of super-relaxed halos. Because these typically have larger concentrations, we expect that the average concentration in an M-selected sample is higher than in the full sample.

The red solid line shows that the fraction of strong lensing (SL) halos in M-selected samples also decreases as a function of M. This trend reflects the correlation between concentration and regularity parameter. Because the halos are more concentrated, they more easily act as strong lenses. However, we notice that a correlation exists also between the concentrations and the M parameters of the unrelaxed halos, although this is weaker than for the relaxed and super-relaxed halos. For unrelaxed halos, the linear Pearson coefficient is $P = -0.22$, indicating also that among these halos, those with a small M parameter tend to have larger concentrations. In part, the classification of unrelaxed halos as regular is due to the different radial scales over which the relaxation and the regularity are evaluated. Whereas the former is measured using all particles inside the virial radius, the second is meant to quantify the morphology of the cluster cores, within 500 kpc. A fraction of halos with regular X-ray morphologies have significant substructures outside 500 kpc, which implies that they are classified as unrelaxed. These substructures explain the low concentrations of those unrelaxed halos that have small M. However, for ∼42% of the unrelaxed halos with $M < 0$, we do not find evidence for substructures outside the region where we carry over the X-ray morphological classification. These halos generally have 2D concentrations higher than the average of the sample, indicating that the selection based on X-ray morphology may lead to the inclusion of unrelaxed objects that are elongated along the line of sight. Such a sample would then be affected by a small orientation bias.

We use the M parameters to create a sample of X-ray-selected halos. These halos are drawn from the full MUSIC-2 sample so as to reproduce the distribution of the M parameters found for the CLASH clusters. In doing so, we take into account the masses and redshifts of the CLASH clusters. The masses are taken from Merten et al. (2014). A halo is selected if it has a suitable M parameter and if the mass inferred from the 2D analysis is within 3σ of the mass measured by CLASH. To account for the redshift distribution, given that the halos available for this analysis are simulated only at four redshifts, we create a match between each CLASH cluster and the nearest simulated redshift. The matches are listed in Table 3.

As explained earlier in the paper, the X-ray analysis is limited to three orthogonal lines of sight per halo. Given that many more projections are available in the 2D analysis of the MUSIC-2 halos, we can improve our statistical power by increasing the number of projections used. To do so, we identify the projections whose lines of sight are within 20 deg of those selected in the X-ray analysis.

Using the concentrations and masses inferred from the 2D analysis of the X-ray-selected projections, we fit the c–M–z relation for our X-ray-selected sample. The relation is shown in Figure 16 for all of the fitting models employed in this study. The best-fit parameters are listed in Table 2. Overall, the

c–M–z relation for X-ray-selected halos is in good agreement with the SL c–M–z relation for a sample composed of both relaxed and unrelaxed halos. This is not surprising given that X-ray-selected halos are frequently efficient strong lenses, with only ∼8% of them not having an extended critical line for sources at $z = 2$. About 70% of the selected projections belong to relaxed halos. About 18% of them correspond to halos classified as super-relaxed. For the NFW model, we find that the concentrations scale with mass as $c \propto M^{-0.16\pm0.11}$, resulting in average concentrations that are intermediate between those predicted in 3D for relaxed and super-relaxed halos in the mass range $2 \times 10^{14} \lesssim M_{200} \lesssim 10^{15}\, h^{-1}\, M_\odot$.

Some differences between the fitting models are found with regards to the redshift evolution of the concentration–mass relation. For the NFW model, the c–M–z relation is evolving strongly. The redshift dependence is shallower in the case of the gNFW model, and it is consistent with zero evolution for the Einasto profile.

7. PREDICTIONS FOR INDIVIDUAL CLASH CLUSTERS

Finally, we use the MUSIC-2 halos and their X-ray morphology to predict the concentrations of each individual CLASH cluster. As explained in Section 4.1, this is done using the parameter C_X, which measures the distance of each simulated halo from a given CLASH cluster in the multidimensional space defined by the X-ray morphological parameters. We select projections with $C_X < 0.4$ to create the match.

Again, for each of the matched X-ray images, we include in our analysis the projections from nearby lines of sight. To be associated with a specific CLASH cluster, the halos must also have compatible masses and redshifts. For all of the CLASH clusters except CLJ 1226+3332, we could create associations with ∼10–200 projections. CLJ 1226+3332 turned out not to have any counterpart in the simulated set. For this cluster, Merten et al. (2014) measured a large mass, $M_{200} \sim 1.5 \times 10^{15}$. The cluster is also at high redshift ($z = 0.89$), and because of the limited volume of the MultiDark cosmological box, there are too few massive systems at such a large redshift to make a fair comparison based on the X-ray morphology.

Having built the associations between simulated and real clusters, we estimate the concentrations by averaging over the selected projections. The results are listed in the sixth column of Table 3 for the NFW model. In the fifth column, we report the mass range of the selected halos. On the basis of these results, we find that CLASH-like clusters have concentrations in the range ∼[3–6]. These measurements are shown in Figure 17. The different colors allow one to discriminate between the redshifts of the simulations. For comparison, we also show the c–M–z relation previously determined using the larger sample of X-ray-selected halos.

The X-ray morphology may reflect the orientation of the cluster. Clusters may appear to have round X-ray isophotes if they have prolate three-dimensional shapes and have their major axis aligned with the line of sight. Knowing the shapes and orientation of the MUSIC-2 halos, we can estimate whether a sample constructed to resemble the morphology of the CLASH clusters is likely to be affected by a large orientation bias. On the basis of the associations we made between real and simulated clusters, we find that the mean angle between the major axes of the simulated halos and the line of sight is ∼54 deg. This indicates that the orientation bias is modest because the expected angle for a distribution of random orientations is ∼57 deg.

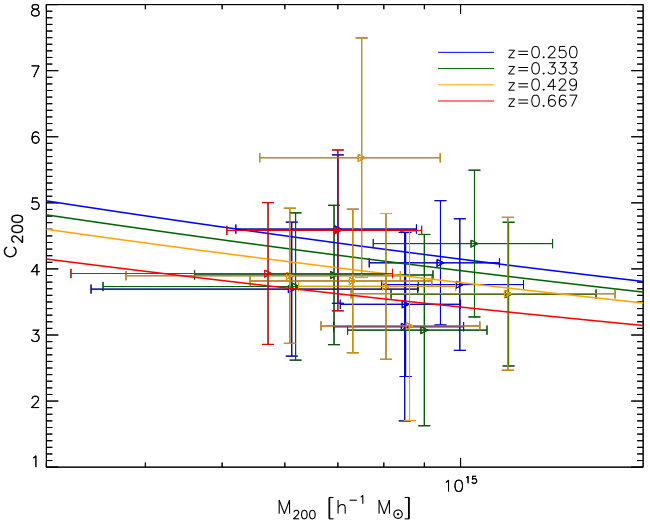

Figure 17. NFW concentrations and masses of MUSIC-2 halos matching the X-ray morphologies of the CLASH X-ray-selected clusters. The error bars reflect the scatter in the masses and concentrations of the halos matching each CLASH cluster. The data points have different colors depending on the redshift of the simulations. For comparison, we also show the c–M–z relation derived from the simulated X-ray-selected sample, whose parameters are given in Table 2 (solid lines).

(A color version of this figure is available in the online journal.)

8. SUMMARY AND CONCLUSIONS

In this paper, we used a large set of 1,419 cluster-sized halos evolved in N-body/hydrodynamical simulations and distributed over the redshift range $0.25 \leqslant z \leqslant 0.67$ to make predictions about several properties of the clusters included in the CLASH sample (Postman et al. 2012). The simulations used here, which are taken from the MUSIC-2 sample (Sembolini et al. 2013b), intentionally do not include radiative physics in order to avoid an artificial boost of the halo concentrations due to the well-known overcooling problem.

First, we characterized the halos by studying their total density profiles. We fitted the profiles using three fitting models: the NFW, the gNFW, and the Einasto profiles. We derived concentration–mass relations and we quantified their dependence on the degree of relaxation. By fitting with the gNFW and Einasto profiles, we could also investigate the distribution of the inner slopes and of the shape parameters of the density profiles.

We combined our work with the measurements of concentrations and masses taken from J. Vega et al. (in preparation). These measurements were obtained by fitting the surface-density profiles extracted from hundreds of projections of the MUSIC-2 halos. The fits were performed with the same codes used to measure the surface-density profiles recovered from the strong and weak lensing analyses of the CLASH cluster sample, as described in Merten et al. (2014). The radial ranges over which the fits were performed are compatible with those used in the observational analysis.

Using the X-MAS code (Gardini et al. 2004; Rasia et al. 2011), we produced simulated *Chandra* observations for three orthogonal lines of sight to each halo above the MUSIC-2 mass completeness limit. These simulated observations were processed using the same routines employed in Donahue et al. (2014) to carry out the X-ray morphological analysis of the CLASH clusters. The X-ray morphology of the simulated halos

was quantified by means of five morphological parameters, which we combined to define a global regularity parameter.

Using the concentrations and masses derived from the analysis of the surface-density profiles, we derived lensing-like concentration–mass relations, including the effects of selection functions aimed at reproducing some observational properties of the CLASH clusters. In particular, we focused on their ability to produce strong lensing effects and their X-ray regularity. For this purpose, we created two subsamples of MUSIC-2 halos. The first includes halos with Einstein radii in the range of those of the CLASH clusters. The second is constructed so as to reproduce the distribution of X-ray regularity parameters of the CLASH clusters.

Our results can be summarized as follows.

1. We find that a large fraction of MUSIC-2 halos has density profiles that are better fitted by gNFW and Einasto profiles than by NFW profiles. Not surprisingly, the halos that most deviate from the NFW model are the least relaxed. For these halos, more flexible profiles are needed to better reproduce the shape of the density profiles. The analysis based on the gNFW model shows that the inner slopes of these profiles are distributed over a wide range of values. On average, the logarithmic inner slope is largely consistent with the NFW slope, though. The Einasto profile fits the halos slightly better than does the gNFW model.
2. When seen in projection, the distribution of the inner slopes widens further, and a large fraction of halos is fitted with profiles that are flatter than the NFW at small radii. On average, the inner logarithmic slopes derived from the gNFW fits of the surface-density profiles are ∼15% smaller than found fitting the density profiles. About 15% of the halos have inner logarithmic slopes smaller than 0.5.
3. The masses derived from the fits of the density profiles match quite well with the true masses of the halos, with a scatter of only a few percent. When they are recovered from the projected mass distributions, mimicking the results obtainable from the analysis of surface-density fields reconstructed via lensing, the masses are smaller than the true masses by less than 5% on average. As discussed in Giocoli et al. (2012a), a mass bias is expected for randomly oriented, prolated triaxial halos. However, the amplitude of the bias for this sample is ∼50% smaller than expected from semianalytical calculations. The bias is even smaller for relaxed halos because their shapes are more spherical.
4. The concentrations derived from the fits of the density profiles with different models are rather similar. However, we find that Einasto concentrations are smaller by 10–15% compared to the NFW and gNFW concentrations.
5. We find that the MUSIC-2 halos follow an intrinsic concentration–mass relation characterized by a slightly larger normalization compared to other concentration–mass relations recently proposed in the literature for the NFW model. The redshift evolution is rather weak.
6. When we mimic the selection of clusters on the basis of their strong lensing signal, we find that the concentration–mass relation derived from the analysis of the projected mass distributions is considerably steeper than expected for nonstrong lenses. It also has a larger normalization. This result holds for all of the fitting models used in this work.
7. Using the X-ray regularity parameter M to select halos with regular X-ray morphologies leads to the inclusion of both relaxed and unrelaxed halos in the sample. Therefore, the X-ray morphology, especially if evaluated in a relatively small region around the cluster center, is not ideal for identifying relaxed halos.
8. The parameter M is correlated with the halo 2D concentration. The most regular halos have higher mass concentrations compared to the full sample of simulated halos because they could be measured from a lensing analysis. The excess of concentration is explained in terms of (1) the higher fraction of super-relaxed objects in the X-ray-selected sample and (2) the presence, among the selected halos, of unrelaxed systems that happen to be well aligned with the line of sight. For a regularity parameter M equal to the median value measured for the CLASH sample, we expect that the concentration will be higher than the average of all halos in the simulated set by $\sim 11\% \pm 3\%$.
9. Measuring the concentration–mass relation and its redshift evolution in a subsample of MUSIC-2 halos that reproduces the distribution of X-ray regularity parameters of the clusters in the CLASH X-ray-selected sample, we find that this has an amplitude and mass dependence similar to those of the concentration–mass relation of strong lensing clusters. We verified that the sample of X-ray-selected halos is largely composed of strong lensing clusters and contains a fraction of only 8% of halos that do not have extended critical lines for sources at $z \sim 2$.
10. The sample of X-ray-selected halos is in large part composed of relaxed halos. These amount to ∼70% of the sample.

These results suggest that the CLASH clusters are prevalently relaxed and likely to be modestly affected by strong lensing bias. Once accounting for projection and selection effects, their NFW concentrations are expected to scale with mass as $c \propto M^{-0.16\pm0.11}$ for the NFW model, resulting in average concentrations that are intermediate between those predicted in 3D for relaxed and super-relaxed halos in the mass range $2 \times 10^{14} \lesssim M_{200} \lesssim 10^{15}\, h^{-1}\, M_{\odot}$. Matching the simulations to the individual CLASH clusters on the basis of the X-ray morphology, we expect that the NFW concentrations recovered from the lensing analysis of the CLASH clusters are in the range [3–6], with an average value of 3.87 and a standard deviation of 0.61. The median value of the concentrations in the simulated sample is 3.76, and the first and third quartiles of the concentration distribution are 3.62 and 3.93, respectively. As shown in Meneghetti et al. (2010a) and in Hennawi et al. (2008), strong lensing clusters are expected to be frequently elongated along the line of sight. For the simulated CLASH sample, the median angle between the major axis of the halos and the lines of sight selected from the X-ray analysis is 54 deg. This indicates that the orientation bias is very modest. It is consistent with the results based on the analysis of the halos from the MareNostrum Universe presented in Meneghetti et al. (2010a).

The research was in part carried out at the Jet Propulsion Laboratory, California Institute of Technology, under a contract with the National Aeronautics and Space Administration. M.M. thanks ORAU and NASA for supporting his research at JPL. M.M., C.G., and L.M. acknowledge support from the contracts ASI/INAF I/023/12/0, INFN/PD51, and the PRIN MIUR 2010–2011 "The dark universe and the cosmic evolution of baryons: From current surveys to Euclid." E.R. acknowledges support from the National Science Foundation AST-1210973, SAO TM3-14008X (issued under NASA Contract No. NAS8-03060). C.G.'s research is part of the project GLENCO, funded under the European Seventh Framework Programme, Ideas,

grant agreement No. 259349. K.U. acknowledges support from the National Science Council of Taiwan (grant NSC100-2112-M-001-008-MY3) and from the Academia Sinica Career Development Award. Support for A.Z. is provided by NASA through Hubble Fellowship grant #HST-HF-51334.01-A awarded by STScI. D.G., S.S., and P.R. were supported by SFBTransregio 33 The Dark Universe by the Deutsche Forschungsgemeinschaft (DFG) and the DFG cluster of excellence Origin and Structure of the Universe. This work was supported in part by contract research "Internationale Spitzenforschung II/2-6" of the Baden Württemberg Stiftung. The Dark Cosmology Centre is funded by the DNRF. J.S. was supported by NSF/AST1313447, NASA/NNX11AB07G, and the Norris Foundation CCAT Postdoctoral Fellowship. The MUSIC simulations were performed at the Barcelona Supercomputing Center (BSC), and the initial conditions were done at the Leibniz Rechenzentrum Munich (LRZ). G.Y. and F.S. acknowledge support from MINECO under research grants AYA2012-31101, FPA2012-34694, and MultiDark CSD2009-00064. We thank Stefano Borgani and the whole computational astrophysics group at the University of Trieste and at INAF-OATS for giving us access to their set of hydrodynamical simulations.

REFERENCES

Allen, S. W., Rapetti, D. A., Schmidt, R. W., et al. 2008, MNRAS, 383, 879
Anders, E., & Grevesse, N. 1989, GeCoA, 53, 197
Balestra, I., Vanzella, E., Rosati, P., et al. 2013, A&A, 559, L9
Balmès, I., Rasera, Y., Corasaniti, P.-S., & Alimi, J.-M. 2014, MNRAS, 437, 2328
Bayliss, M. B., Johnson, T., Gladders, M. D., Sharon, K., & Oguri, M. 2014, ApJ, 783, 41
Becker, M. R., & Kravtsov, A. V. 2011, ApJ, 740, 25
Bhattacharya, S., Habib, S., Heitmann, K., & Vikhlinin, A. 2013, ApJ, 766, 32
Biffi, V., Sembolini, F., De Petris, M., et al. 2014, MNRAS, 439, 588
Biviano, A., Rosati, P., Balestra, I., et al. 2013, A&A, 558, A1
Bonafede, A., Dolag, K., Stasyszyn, F., Murante, G., & Borgani, S. 2011, MNRAS, 418, 2234
Borgani, S., & Kravtsov, A. 2011, ASL, 4, 204
Bouwens, R., Bradley, L., Zitrin, A., et al. 2014, ApJ, 795, 126
Bradley, L. D., Zitrin, A., Coe, D., et al. 2014, ApJ, 792, 76
Bryan, G. L., & Norman, M. L. 1998, ApJ, 495, 80
Buote, D. A., & Canizares, C. R. 1992, ApJ, 400, 385
Buote, D. A., & Tsai, J. C. 1996, ApJ, 458, 27
Cassano, R., Ettori, S., Giacintucci, S., et al. 2010, ApJL, 721, L82
Coe, D., Umetsu, K., Zitrin, A., et al. 2012, ApJ, 757, 22
Coe, D., Zitrin, A., Carrasco, M., et al. 2013, ApJ, 762, 32
De Boni, C., Ettori, S., Dolag, K., & Moscardini, L. 2013, MNRAS, 428, 2921
Despali, G., Tormen, G., & Sheth, R. K. 2013, MNRAS, 431, 1143
Diemer, B., & Kravtsov, A. V. 2014, arXiv:1407.4730
Dolag, K., Bartelmann, M., Perrotta, F., et al. 2004, A&A, 416, 853
Donahue, M., Voit, G., Mark, M. A., et al. 2014, ApJ, 794, 136
Dubinski, J., & Carlberg, R. G. 1991, ApJ, 378, 496
Duffy, A. R., Schaye, J., Kay, S. T., & Dalla Vecchia, C. 2008, MNRAS, 390, L64
Duffy, A. R., Schaye, J., Kay, S. T., et al. 2010, MNRAS, 405, 2161
Dutton, A. A., & Macciò, A. V. 2014, arXiv:1402.7073
Ebeling, H., Barrett, E., Donovan, D., et al. 2007, ApJL, 661, L33
Einasto, J., & Haud, U. 1989, A&A, 223, 89
Fabjan, D., Borgani, S., Tornatore, L., et al. 2010, MNRAS, 401, 1670
Frenk, C. S., White, S. D. M., Davis, M., & Efstathiou, G. 1988, ApJ, 327, 507
Gao, L., Navarro, J. F., Frenk, C. S., et al. 2012, MNRAS, 425, 2169
Gardini, A., Rasia, E., Mazzotta, P., et al. 2004, MNRAS, 351, 505
Giocoli, C., Meneghetti, M., Ettori, S., & Moscardini, L. 2012a, MNRAS, 426, 1558
Giocoli, C., Meneghetti, M., Metcalf, R. B., Ettori, S., & Moscardini, L. 2013, arXiv:1311.1205
Giocoli, C., Tormen, G., & Sheth, R. K. 2012b, MNRAS, 422, 185
Gralla, M. B., Sharon, K., Gladders, M. D., et al. 2011, ApJ, 737, 74
Gruen, D., Brimioulle, F., Seitz, S., et al. 2013, MNRAS, 432, 1455
Hennawi, J. F., Dalal, N., Bode, P., & Ostriker, J. P. 2007, ApJ, 654, 714
Hennawi, J. F., Gladders, M. D., Oguri, M., et al. 2008, AJ, 135, 664
Jing, Y., & Suto, Y. 2002, ApJ, 574, 538
Killedar, M., Borgani, S., Meneghetti, M., et al. 2012, MNRAS, 427, 533
Klypin, A., Kravtsov, A. V., Bullock, J. S., & Primack, J. R. 2001, ApJ, 554, 903
Kravtsov, A., & Borgani, S. 2012, arXiv:1205.5556
Kravtsov, A. V., Klypin, A. A., & Khokhlov, A. M. 1997, ApJS, 111, 73
Lemze, D., Postman, M., Genel, S., et al. 2013, ApJ, 776, 91
Lemze, D., Sadeh, S., & Rephaeli, Y. 2009, MNRAS, 397, 1876
Lemze, D., Wagner, R., Rephaeli, Y., et al. 2012, ApJ, 752, 141
Limousin, M., Morandi, A., Sereno, M., et al. 2013, SSRv, 177, 155
Ludlow, A. D., Navarro, J. F., Angulo, R. E., et al. 2013, arXiv:1312.0945
Ludlow, A. D., Navarro, J. F., Li, M., et al. 2012, arXiv:1206.1049
McCarthy, I. G., Schaye, J., Bower, R. G., et al. 2011, MNRAS, 412, 1965
Medezinski, E., Umetsu, K., Nonino, M., et al. 2013, ApJ, 777, 43
Meneghetti, M., Bartelmann, M., Dahle, H., & Limousin, M. 2013, SSRv, 177, 31
Meneghetti, M., Fedeli, C., Pace, F., Gottlöber, S., & Yepes, G. 2010a, A&A, 519, A90
Meneghetti, M., & Rasia, E. 2013, arXiv:1303.6158
Meneghetti, M., Rasia, E., Merten, J., et al. 2010b, A&A, 514, A93
Merritt, D., Graham, A. W., Moore, B., Diemand, J., & Terzić, B. 2006, AJ, 132, 2685
Merten, J., Cacciato, M., Meneghetti, M., Mignone, C., & Bartelmann, M. 2009, A&A, 500, 681
Merten, J., Coe, D., Dupke, R., et al. 2011, MNRAS, 417, 333
Merten, J., Meneghetti, M., Postman, M., et al. 2014, arXiv:1404.1376
Moore, B., Governato, F., Quinn, T., Stadel, J., & Lake, G. 1998, ApJL, 499, L5
Muñoz-Cuartas, J. C., Macciò, A. V., Gottlöber, S., & Dutton, A. A. 2011, MNRAS, 411, 584
Nakamura, T. T., & Suto, Y. 1997, PThPh, 97, 49
Navarro, J. F., Frenk, C., & White, S. 1996, ApJ, 462, 563
Navarro, J. F., Frenk, C., & White, S. 1997, ApJ, 490, 493
Navarro, J. F., Ludlow, A., Springel, V., et al. 2010, MNRAS, 402, 21
Neto, A. F., Gao, L., Bett, P., et al. 2007, MNRAS, 381, 1450
Newman, A. B., Treu, T., Ellis, R. S., & Sand, D. J. 2011, ApJL, 728, L39
Oguri, M., Bayliss, M. B., Dahle, H., et al. 2012, MNRAS, 420, 3213
Oguri, M., & Blandford, R. D. 2009, MNRAS, 392, 930
Oguri, M., Hennawi, J. F., Gladders, M. D., et al. 2009, ApJ, 699, 1038
Planelles, S., Borgani, S., Fabjan, D., et al. 2014, MNRAS, 438, 195
Postman, M., Coe, D., Benítez, N., et al. 2012, ApJS, 199, 25
Rasia, E., Borgani, S., Ettori, S., Mazzotta, P., & Meneghetti, M. 2013a, ApJ, 776, 39
Rasia, E., Mazzotta, P., Evrard, A., et al. 2011, ApJ, 729, 45
Rasia, E., Meneghetti, M., & Ettori, S. 2013b, AstRv, 8, 010000
Rasia, E., Meneghetti, M., Martino, R., et al. 2012, NJPh, 14, 055018
Redlich, M., Bartelmann, M., Waizmann, J.-C., & Fedeli, C. 2012, A&A, 547, A66
Retana-Montenegro, E., van Hese, E., Gentile, G., Baes, M., & Frutos-Alfaro, F. 2012, A&A, 540, A70
Sarazin, C. L. 1986, RvMP, 58, 1
Schneider, P., Ehlers, J., & Falco, E. E. 1992, Gravitational Lenses (Berlin: Springer)
Sembolini, F., De Petris, M., Yepes, G., et al. 2013a, arXiv:1309.5387
Sembolini, F., Yepes, G., De Petris, M., et al. 2013b, MNRAS, 429, 323
Skibba, R. A., & Macciò, A. V. 2011, MNRAS, 416, 2388
Skibba, R. A., van den Bosch, F. C., Yang, X., et al. 2011, MNRAS, 410, 417
Smit, R., Bouwens, R. J., Labbe, I., et al. 2013, arXiv:1307.5847
Springel, V. 2005, MNRAS, 364, 1105
Torri, E., Meneghetti, M., Bartelmann, M., et al. 2004, MNRAS, 349, 476
Umetsu, K., Medezinski, E., Nonino, M., et al. 2012, ApJ, 755, 56
Umetsu, K., Medezinski, E., Nonino, M., et al. 2014, arXiv:1404.1375
Zhao, D. H., Jing, Y. P., Mo, H. J., & Börner, G. 2009, ApJ, 707, 354
Zhao, H. 1996, MNRAS, 278, 488
Zheng, W., Postman, M., Zitrin, A., et al. 2012, Natur, 489, 406
Zitrin, A., Broadhurst, T., Coe, D., et al. 2011, ApJ, 742, 117
Zitrin, A., Fabris, A., Merten, J., et al. 2014, arXiv:1411.1414
Zitrin, A., Meneghetti, M., Umetsu, K., et al. 2013, ApJL, 762, L30
Zitrin, A., Moustakas, J., Bradley, L., et al. 2012a, ApJL, 747, L9
Zitrin, A., Rosati, P., Nonino, M., et al. 2012b, ApJ, 749, 97

The Astrophysical Journal Letters, 762:L30 (6pp), 2013 January 10 doi:10.1088/2041-8205/762/2/L30

CLASH: THE ENHANCED LENSING EFFICIENCY OF THE HIGHLY ELONGATED MERGING CLUSTER MACS J0416.1−2403

A. Zitrin[1,21], M. Meneghetti[2], K. Umetsu[3], T. Broadhurst[4,5], M. Bartelmann[1], R. Bouwens[6], L. Bradley[7], M. Carrasco[1,8], D. Coe[7], H. Ford[9], D. Kelson[10], A. M. Koekemoer[7], E. Medezinski[9], J. Moustakas[11], L. A. Moustakas[12], M. Nonino[13], M. Postman[7], P. Rosati[14], G. Seidel[15], S. Seitz[16,17], I. Sendra[4], X. Shu[18], J. Vega[19,20], and W. Zheng[9]
[1] Institut für Theoretische Astrophysik, Zentrum für Astronomie, Universität Heidelberg, Philosophenweg 12, D-69120 Heidelberg, Germany; adizitrin@gmail.com
[2] INAF, Osservatorio Astronomico di Bologna, & INFN, Sezione di Bologna; Via Ranzani 1, I-40127 Bologna, Italy
[3] Institute of Astronomy and Astrophysics, Academia Sinica, P.O. Box 23-141, Taipei 10617, Taiwan
[4] Department of Theoretical Physics, University of Basque Country UPV/EHU, P.O. Box 644, E-48080 Bilbao, Spain
[5] IKERBASQUE, Basque Foundation for Science, Alameda Urquijo 36-5, E-48008 Bilbao, Spain
[6] Leiden Observatory, Leiden University, NL-2300 RA Leiden, The Netherlands
[7] Space Telescope Science Institute, 3700 San Martin Drive, Baltimore, MD 21208, USA
[8] Department of Astronomy and Astrophysics, AIUC, Pontificia Universidad Católica de Chile, Santiago, Chile
[9] Department of Physics and Astronomy, The Johns Hopkins University, 3400 North Charles Street, Baltimore, MD 21218, USA
[10] Observatories of the Carnegie Institution of Washington, Pasadena, CA 91101, USA
[11] Department of Physics & Astronomy, Siena College, Loudonville, NY 12211, USA
[12] Jet Propulsion Laboratory, California Institute of Technology, MS 169-327, Pasadena, CA 91109, USA
[13] INAF-Osservatorio Astronomico di Trieste, via G.B. Tiepolo 11, I-40131 Trieste, Italy
[14] ESO-European Southern Observatory, D-85748 Garching bei München, Germany
[15] Max-Planck-Institute for Astronomy, Königstuhl 17, D-69117 Heidelberg, Germany
[16] University Observatory Munich, Scheinerstrasse 1, D-81679 München, Germany
[17] Max-Planck-Institut für extraterrestrische Physik, Postfach 1312, Giessenbachstr., D-85741 Garching, Germany
[18] Department of Astronomy, University of Science and Technology of China, Hefei, Anhui, 230026, China
[19] Departamento de Física Teórica, Módulo C-15, Facultad de Ciencias, Universidad Autónoma de Madrid, E-28049 Cantoblanco, Madrid, Spain
[20] LERMA, UMR CNRS 8112, Observatoire de Paris, 61 Avenue de l'Observatoire, F-75014 Paris, France
Received 2012 November 8; accepted 2012 December 1; published 2012 December 20

ABSTRACT

We perform a strong lensing analysis of the merging galaxy cluster MACS J0416.1−2403 (M0416; $z = 0.42$) in recent CLASH/*HST* observations. We identify 70 new multiple images and candidates of 23 background sources in the range $0.7 \lesssim z_{\rm phot} \lesssim 6.14$ including two probable high-redshift dropouts, revealing a highly elongated lens with axis ratio ≃5:1, and a major axis of ∼100″ ($z_s \sim 2$). Compared to other well-studied clusters, M0416 shows an enhanced lensing efficiency. Although the critical area is not particularly large (≃0.6 □′; $z_s \sim 2$), the number of multiple images, per critical area, is anomalously high. We calculate that the observed elongation boosts the number of multiple images, *per critical area*, by a factor of ∼2.5×, due to the increased ratio of the caustic area relative to the critical area. Additionally, we find that the observed separation between the two main mass components enlarges the critical area by a factor of ∼2. These geometrical effects can account for the high number (density) of multiple images observed. We find in numerical simulations that only ∼4% of the clusters (with $M_{\rm vir} \geqslant 6 \times 10^{14}\, h^{-1}\, M_{\odot}$) exhibit critical curves as elongated as in M0416.

Key words: dark matter – galaxies: clusters: general – galaxies: clusters: individual (MACS J0416.1−2403) – galaxies: high-redshift – gravitational lensing: strong

Online-only material: color figures, machine-readable table

1. INTRODUCTION

Due to their high projected surface mass densities, galaxy clusters magnify and distort background objects, forming natural gravitational lenses in the sky. The lensing and magnification effects generally increase toward the central region of the cluster, where the projected mass density is often high enough to form multiple images of the same background source, depending also on the angular diameter distances involved (for reviews, see Bartelmann 2010; Kneib & Natarajan 2011).

The lensing efficiency of galaxy clusters (e.g., the number of multiple images generated) is also related to other factors, such as the ellipticity, amount of substructure and its distance from the center, and degree of relaxation or merger (e.g., Meneghetti et al. 2003). For example, the critical area grows with the concentration of the cluster (e.g., Sadeh & Rephaeli 2008), so it is clear that massive and more concentrated clusters should show more multiple images. The "overconcentration" problem in which lensing-selected clusters are found to have high concentrations (and large Einstein radii; e.g., Comerford & Natarajan 2007; Broadhurst et al. 2008; Broadhurst & Barkana 2008) is often attributed to a lensing selection bias toward higher concentrations of triaxial clusters preferentially aligned with the line of sight (see also Hennawi et al. 2007; Sereno et al. 2010; Oguri et al. 2012a; Okabe et al. 2010, and references therein).

On the other hand, recent efforts show that there exists a second class of prominent strong lenses. Sereno & Zitrin (2012) showed that in a triaxial lensing analysis, the 12 MAssive Cluster Survey (MACS) clusters at $z > 0.5$ (Ebeling et al. 2007) have relatively low concentrations, despite the many multiple images uncovered in their fields. They suggested that since most of these

[21] Mass models are publicly available at: ftp://wise-ftp.tau.ac.il/pub/adiz/M0416/.

clusters are not yet relaxed, the amount of substructure in their centers as well as their higher redshift than most previously known lenses turns them into highly magnifying lenses. The critical curves of several subclumps are merged together into a bigger lens, whose overall mass profile in the central part is often shallower, thus boosting the magnification.

Indeed, various clusters around $z \sim 0.5$ show prominent lensing features (giant arcs and many multiple images; Zitrin et al. 2012a, 2012b). Interestingly, the largest gravitational lens, MACS J0717.5+3745 ($z = 0.55$; Zitrin et al. 2009a), is formed by several merging clumps possibly at the tip of a filament (Limousin et al. 2012; Jauzac et al. 2012). Zitrin & Broadhurst (2009) showed that MACS J1149.5+2223 ($z = 0.54$) is an excellent "magnifying glass" in the sky due to its shallow inner mass profile. This cluster is now known to magnify a galaxy at $z \sim 10$ (Zheng et al. 2012). Recently, Coe et al. (2012) uncovered the highest redshift galaxy known to date at $z \sim 10.8$, multiply imaged by MACS J0647.7+7015 ($z = 0.59$), another complex cluster expected to be highly magnifying (Zitrin et al. 2011; Postman et al. 2012).

Meneghetti et al. (2003) found that the cluster lensing cross section for giant arcs grows rapidly with ellipticity. A typical ellipticity of $e = 1 - b/a = 0.3$ entails an order of magnitude increase in the lensing cross section (see also Torri et al. 2004), for example, because with increasing ellipticity the caustics stretch, develop cusps, and enclose a growing area. Meneghetti et al. (2003) also found that approaching subclumps boost the lensing cross sections. Meneghetti et al. (2007) examined the arc sensitivity to cluster ellipticity, asymmetries, and substructures, and found that these contribute, respectively, ∼40%, ∼10%, and ∼30%, to the lensing cross section. Recently, Redlich et al. (2012) found that cluster mergers can enhance the lensing cross section by typically ∼30%–50%. It is therefore expected that merging, substructured, and elongated clusters should also constitute prominent strong lenses.

Here, we present the lensing analysis (Section 2) of the merging cluster MACS J0416.1−2403 (hereafter M0416; Mann & Ebeling 2012), performed on recent *Hubble Space Telescope* (*HST*) imaging in 16 bands from the UV to the near-IR to a total depth of ∼20 orbits, as part of the Cluster Lensing And Supernova survey with Hubble (CLASH) program (see Postman et al. 2012). The CLASH pipeline uses the 16-band observations to derive photometric redshifts for each arc, via the Bayesian Photometric Redshifts (BPZ) program (Benítez et al. 2004; Coe et al. 2006), used here to constrain the model. As we shall see, the cluster exhibits high elongation, in part as a result of the possible merger. We test, by a simple semi-analytical simulation (Section 3), the expected increase in lensing efficiency with ellipticity and merger stage to see if these may account for the many multiple images in M0416, per its critical area. For this work, we define the *lensing efficiency* simply as *the number of multiple images per critical area*, which we also refer to as *the number density* of multiple images. This ratio, naturally, scales with the ratio of the caustic area and the critical area.

M0416 was listed as a MACS cluster (see Ebeling et al. 2010) due to its X-ray brightness. Mann & Ebeling (2012) classified it as merging based on the double-peaked X-ray structure, where the southern peak is offset by a few arcseconds from the corresponding (second) brightest cluster galaxy (BCG), as expected in mergers (e.g., Bradač et al. 2006; Merten et al. 2011). Based also on its predicted Einstein radius, M0416 was designated as one of the five "high-magnification" CLASH clusters (where 20 clusters are X-ray selected to be dynamically relaxed). We found no record of a published strong lensing (SL) analysis of M0416, but Christensen et al. (2012) published a measured spectroscopic redshift for the giant arc north of the BCG (systems 1 and 2 here), $z_s = 1.896$, which we use in our analysis.

Throughout we adopt a ΛCDM cosmology with ($\Omega_{m0} = 0.3$, $\Omega_{\Lambda 0} = 0.7$, $h = 0.7$), where $1'' = 5.53$ kpc at the redshift for M0416, $z = 0.42$ (Christensen et al. 2012).

2. STRONG LENSING ANALYSIS OF M0416

We use two complementary modeling techniques to construct mass models for M0416. These are then compared to each other and to our new weak lensing (WL) analysis.

Method 1. The first method we use follows the prescription of Zitrin et al. (2009b), with several modifications recently implemented for speed and a wider choice of priors. First, instead of power-law profiles traditionally used to represent the galaxies in our method (Broadhurst et al. 2005; Zitrin et al. 2009b), we model each galaxy with a pseudo-isothermal elliptical mass distribution (PIEMD; Kassiola & Kovner 1993), adopting the exact formulation from Jullo et al. (2007):

$$\begin{cases} \sigma_0 = \sigma_0^\star \left(\dfrac{L}{L^\star}\right)^{1/4} , \\ r_{\rm core} = r_{\rm core}^\star \left(\dfrac{L}{L^\star}\right)^{1/2} , \\ r_{\rm cut} = r_{\rm cut}^\star \left(\dfrac{L}{L^\star}\right)^{\alpha} , \end{cases} \quad (1)$$

where $r_{\rm core}$ is the core radius, $r_{\rm cut}$ the cutoff radius, and σ_0 the velocity dispersion. The total mass of a subhalo then scales as

$$M = (\pi/G)(\sigma_0^\star)^2 r_{\rm cut}^\star (L/L^\star)^{1/2+\alpha} , \quad (2)$$

where $L^\star$ is the typical luminosity of a galaxy at the cluster redshift, and $r_{\rm cut}^\star$, $r_{\rm core}^\star$, and $\sigma_0^\star$ are its PIEMD parameters (Jullo et al. 2007).

The PIEMD representation is used in many modeling methods (e.g., Halkola et al. 2006; Jullo et al. 2007; Richard et al. 2010; Oguri et al. 2012b), and eases the comparison to the second method we implement here. As a second change, this mass distribution is now smoothed with an *elliptical Gaussian* (eGaussian), instead of our traditional smoothing by a two-dimensional polynomial spline, and therefore eliminates the need for an external shear as the ellipticity is now directly introduced into the mass distribution. The superposed galaxies' contribution and its eGaussian-smoothed map are then added with a relative weight that is a free parameter. This method therefore includes six free basic parameters: $r_{\rm cut}^*$, σ_0^* for the PIEMD galaxy models (Equations (1) and (2)); $\sigma_{\rm MJA}$ and $\sigma_{\rm MNA}$, the widths of the eGaussian kernel along the major and minor axes; ϕ, the angle of the major axis in the eGaussian kernel; and the relative fraction of the galaxies' component from the total mass (the remaining fraction is contributed by the smooth dark matter (DM) component).

Method 2. The second method we use adopts the following parameterization. Galaxies are each modeled as PIEMD scaled by its light as above (method 1; Equation (1)). To represent the DM, we implement an elliptical Navarro–Frenk–White (eNFW) halo. Since M0416 is clearly a complex, likely merging system, the first few modeling attempts introduced the need to add a second eNFW halo to the model. In total, then,

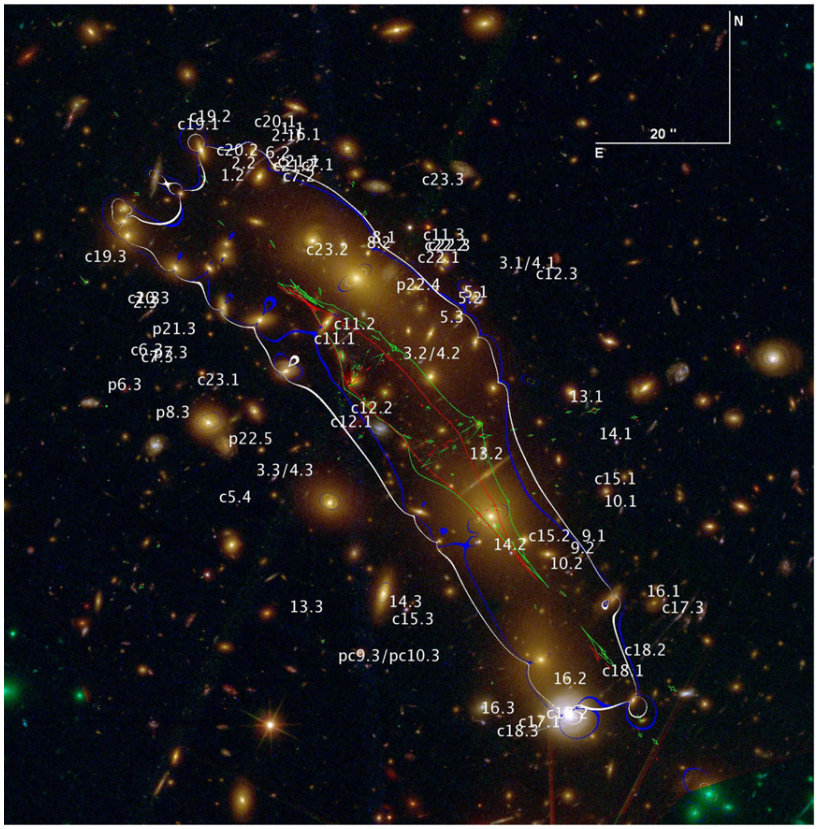

Figure 1. CLASH/*HST* 16-band color-composite image of M0416, with multiple images numbered. Lensed candidates are marked with "c," and "p" stands for predicted location. Overlaid in blue (white) is the critical curve for $z_s = 1.896$, corresponding to the giant arc (systems 1 and 2), from the eNFW (eGaussian) based model (see Section 2). In red (green) we plot the corresponding caustics.

(A color version of this figure is available in the online journal.)

the model includes the galaxy component described by the superposition of all PIEMD representations, and two eNFW halos (where the ellipticity, defined here throughout as $e = (\mathrm{MJA} - \mathrm{MNA})/(\mathrm{MJA} + \mathrm{MNA})$, is directly introduced into the NFW mass distribution via the transformation $r \rightarrow r_e = \sqrt{[x/(1+e)]^2 + [y/(1-e)]^2}$). We maintain the eNFW halos centered on the first and second brightest cluster members, respectively. This keeps the number of free parameters as low as possible and yields an excellent fit. Note that we tried to construct a model while allowing the (southern halo) center to vary but did not find a significantly better solution. This parameterization therefore consists of 10 free basic parameters: r^*_{cut}, σ^*_0 for the PIEMD galaxy models; the scale radius r_s and the concentration parameter c_{vir}, as well as the ellipticity and its position angle, for each of the two eNFW halos.

Using a preliminary model with the Zitrin et al. (2009b) method, and the two iteratively improved models above, along with a complementary examination by eye, we iteratively matched together multiply imaged systems. The best-fit solution in both methods is obtained via a long (several dozens of thousand steps) Monte Carlo Markov Chain (MCMC) minimization, using several chains. We note that in some chains, including the final ones used here, the redshifts of some of the multiple systems were left as free parameters (with flat priors) to be optimized. Also, in both final chains for methods 1 and 2, we left the three BCGs to be freely weighted and optimized by the MCMC. For the two main BCGs, we fix the ellipticity and position angle to the parameters derived using SExtractor (Bertin & Arnouts 1996). Throughout, we fix for the PIEMD, $r^*_{\mathrm{core}} = 0.3$ kpc, use an L^* value equivalent to an absolute magnitude of $M^*_{\mathrm{F814W}} = -20.113$, and assume a constant mass-to-light ratio ($\alpha = 0.5$; Equation (2)). The F814W−F475W color was used to extract the red sequence, where we used the 122 brightest (F814W) members.

2.1. Results and Comparison of the Two Models

In total, we found 70 multiple images and candidates of 23 background sources (Table 1 and Figure 1). All images *not* marked as *candidates* were used as constraints for the model: 34 images of 13 sources. For seven of these, the redshifts were left to be optimized by the models. Two of the multiply imaged sources seem to be high-redshift "dropouts": system 6 at $z \sim 6.5$, and candidate system 20 at $z \sim 5$, although the redshift constraints on the latter are poor. We leave the detailed examination of these two objects for future work.

Both models yield very similar critical curves, except for a small region of a few arcsecond discrepancy where there are only systems that were not used as constraints (or their redshifts left free). In addition, the mass profiles (centered on the midpoint between the first and second brightest members, R.A.$_{\mathrm{J2000}} = 04{:}16{:}08.38$, decl.$_{\mathrm{J2000}} = -24{:}04{:}20.80$) of the two models are almost identical throughout the range where multiple images are observed ($r < 1'$); see Figure 2. The two models are also in excellent agreement with independent, color–color-selected background galaxies' (Medezinski et al. 2010) WL measurements from BR_cz' Subaru data (Figure 2), using the Bayesian method of Umetsu et al. (2011a, 2011b) that combines tangential-distortion and magnification-bias measurements in a

Table 1
Multiple-image Systems and Candidates

Arc ID	R.A.(J2000.0)	Decl.(J2000.0)	Phot-z [$z_{\rm min}$-$z_{\rm max}$]	$z_{\rm NFW}$	Δ NFW (arcsec)	$z_{\rm Gauss}$	Δ Gauss (arcsec)	Comments
1.1	04:16:09.780	−24:03:41.73	1.788 [1.541–1.879]	2.01 [1.66–2.69]	1.6	2.10 [1.67–2.17]	1.5	Sys fixed to $z_{\rm spec} = 1.896$
1.2	04:16:10.435	−24:03:48.75	2.482 [2.379–2.560]	”	0.9	”	2.3	Nearby part $z_{\rm phot} \sim 1.9$
1.3	04:16:11.365	−24:04:07.21	2.555 [2.442–2.675]	”	0.3	”	0.9	Nearby part $z_{\rm phot} \sim 1.9$
2.1	04:16:09.884	−24:03:42.77	1.788 [1.541–1.879]	2.00 [1.71–2.13]	1	2.24 [1.73–2.24]	0.5	
2.2	04:16:10.321	−24:03:46.93	1.846 [1.796–1.998]	”	0.5	”	1.2	
2.3	04:16:11.394	−24:04:07.86	1.928 [1.806–2.239]	”	0.7	”	1.4	
3.1	04:16:07.388	−24:04:01.62	2.149 [2.130–2.323]	2.00 [1.61–3.74]	1.1	2.14 [1.59–3.97]	0.9	
3.2	04:16:08.461	−24:04:15.53	2.324 [2.166–2.369]	”	0.5	”	2.3	Blended with 4.2
3.3	04:16:10.036	−24:04:32.56	2.778 [2.759–2.814]	”	0.6	”	3	
4.1	04:16:07.398	−24:04:02.01	2.199 [1.182–2.819]	1.99 [1.60–3.54]	0.4	1.81 [1.58–4.03]	2.3	
4.2	04:16:08.437	−24:04:15.53	2.324 [2.166–2.369]	”	1	”	0.7	Blended with 3.2
4.3	04:16:10.051	−24:04:33.08	2.244 [2.140–2.325]	”	0.5	”	0.9	

Notes. Column 1: arc ID. “c” stands for candidate and “p” for predicted location. For candidates the photo-z distribution, or identification by eye, was ambiguous; Columns 2 and 3: R.A. and Decl. in J2000.0; Column 4: photometric redshift and 95% C.L.; Column 5: predicted and 95% C.L. redshift by the eNFW model ; Column 6: reproduction distance of image from the observed location in the eNFW model; Column 7: predicted and 95% C.L. redshift by the eGaussian model; Column 8: reproduction distance of image from the observed location in the eGaussian model; Column 9: comments.

(This table is available in its entirety in a machine-readable form in the online journal. A portion is shown here for guidance regarding its form and content.)

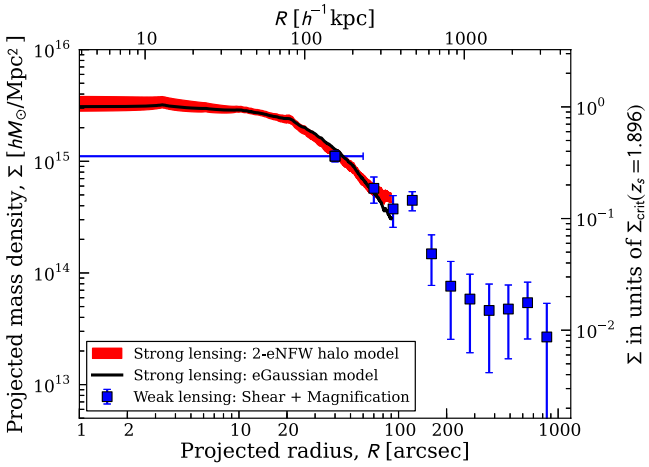

Figure 2. Projected mass density profile of M0416. The red curve shows the resulting profile and 1σ errors from the two eNFW halo model; the black curve shows the resulting profile from the eGaussian-smoothing model (see Section 2 for details). The two models are similar in the range where multiple-image constraints are available ($<1'$), and highly consistent with independent Subaru WL analysis data (blue squares and error bars).

(A color version of this figure is available in the online journal.)

model-independent manner, effectively breaking the mass-sheet degeneracy. The WL analysis pipeline is described in Umetsu et al. (2012).

The image-plane reproduction rms(χ^2) is $1\farcs89(56.67)$ and $1\farcs37(29.67)$ for the eGaussian and eNFW models, respectively. The rms increases slightly to $2\farcs40$ and $2\farcs11$, respectively, when including all images and candidates and not only those used as constraints. For the χ^2 we used a positional error of $\sigma_{\rm pos} = 1\farcs4$, which was found to be a reasonable value accounting for large-scale structure and matter along the line of sight (see Zitrin et al. 2012b and references therein). The multiple-image input comprises 35 constraints, where the number of degrees of freedom (dof) is 26 and 22 for the eGaussian and eNFW models, respectively, yielding, correspondingly, $\chi^2/{\rm dof} = 2.18$ and $\chi^2/{\rm dof} = 1.35$. Both models show a critical area (A) with an effective Einstein radius of $\theta_e = \sqrt{A/\pi} \simeq 26'' \pm 2$ ($z_s = 1.896$), enclosing $M(< \theta_e) = 1.25 \pm 0.09 \times 10^{14}\, M_\odot$. Comparing the two methods, the eNFW model has a somewhat better fit to the data—and higher flexibility to match it. The eGaussian smoothed model fit is somewhat worse, following more rigorously the light-traces-mass assumption, but the fact that it physically matches multiple images a priori (without needing to accurately constrain the fit first) is remarkable evidence for its credibility.

The number density of multiple images and candidates uncovered, i.e., number per the given critical area (70 images of 23 sources over $\simeq 0.6\ \square'$ for $z_s \sim 2$), is a few times higher than other prominent known lensing clusters (for similar background redshifts). A1689 ($z = 0.19$), for example, one of the largest lenses known, shows 135 images of 42 sources, over a critical area of $\simeq 1.8\ \square'$ (Coe et al. 2010). A1703 ($z = 0.28$) has more than 50 multiple images of 17 sources known, and a critical area of $\simeq 0.8\ \square'$ (Richard et al. 2009). MACS J0717.5+3745 ($z = 0.55$), the largest gravitational lens (Zitrin et al. 2009a), has about 60 multiple images known from 18 sources (see also Limousin et al. 2012), and a critical area of $\simeq 2.64\ \square'$.

3. EXPECTED EFFECT OF ELLIPTICITY AND MERGER

We now wish to test the effects of ellipticity and merger on the observed number of multiple images.

We start by producing a fiducial eNFW model at $z = 0.42$, with point sources planted behind it ($z_s = 2$), every 45 kpc on a grid. We then increase the ellipticity ($e = ({\rm MJA} - {\rm MNA})/({\rm MJA} + {\rm MNA})$) from 0.0 to 0.8 and count the number of multiple images generated. Note that throughout we always count *all* multiple images formed. For each configuration we also measure the critical area for normalization, so the effect of ellipticity can be extracted per given critical area.

In Figure 3 we plot the resulting increase in the number of multiple images with lens ellipticity, per critical area, for various combinations of NFW parameters. A clear correlation is observed, so larger numbers of multiple images are generated by higher ellipticities (but the amplitude may vary with masses and distances). To assess the effect in M0416 (for a fixed axis ratio of $\simeq 5.1$), we choose different combinations of c_{200} and r_s that yield comparable critical area to that of M0416. The

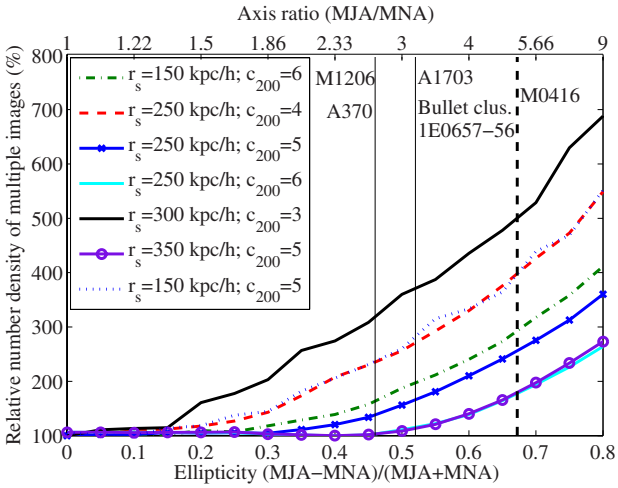

Figure 3. Number density of multiple images as a function of lens ellipticity (normalized to the circular case), for different concentration and scale-radius parameters. In all cases probed, higher ellipticity boosts the lensing efficiency, generating more multiple images *per critical area*. We mark on the figure the measured effective ellipticity of M0416 and other (less) elongated clusters. Choosing those combinations of c_{200} and r_s that yield comparable critical area to that of M0416, we obtain that the number density of multiple images observed in M0416 is $\sim$2.5$\times$ higher due to its elongation.

(A color version of this figure is available in the online journal.)

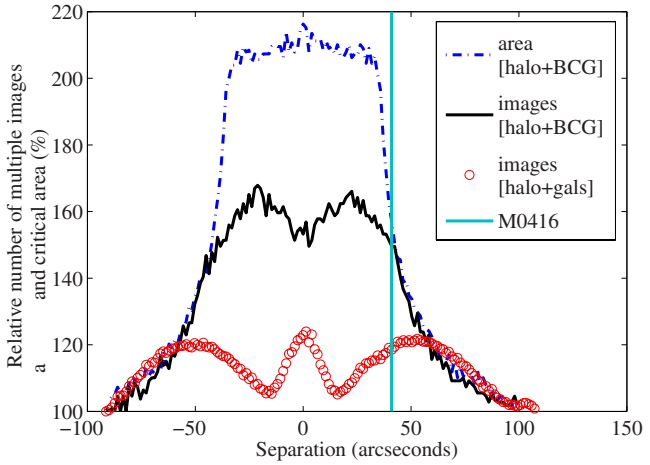

Figure 4. Critical area (blue dash-dotted line) and number of multiple images vs. the displacement between the two halos, normalized to a large-separation case. The black curve shows the behavior when accounting only for the DM halos and BCGs, while the red circle curve shows the same scenario but with more massive halos to account for the missing galaxies mass. In either case, it is clear that the merger contributes a boost of $\sim$20%–60% to the number of multiple images observed.

(A color version of this figure is available in the online journal.)

observed elongation results in a $\sim$2.5$\times$ increase in the number of multiple images compared with the circular case, for the given critical area. Therefore, the observed elongation explains why M0416 has a few times higher multiple-image number density than other typical lensing clusters (in comparable *HST* imaging). In reality, the increase in the number density of multiple images with ellipticity is of course a more complex function and the exact number depends also on the luminosity function and observational depth, and on the mass shape parameters. However, our goal here was to merely show that such a correlation exists and assess its order of magnitude.

To test the effect of merger in M0416, we simulate two eNFW halos with similar parameters as in the resulting mass model including also the BCGs in their centers, approaching each other on the line connecting them (Figure 4). The observed separation between the two halos entails a $\sim$20%–60%(120)% increase in the total number of multiple images (critical area), compared to the "far-away" initial position where each halo comprised its own (unmerged) critical curve. The exact amount is dependent on the true mass of each halo, including the true contribution of the galaxies (Figure 4). Note that as the two halos continue approaching each other, although the total number of multiple images may increase, the number of multiple images *per critical area* will decrease.

To assess how extreme the elongation of the critical curves is, we compare to Multidark/MUSIC 2 numerical simulations (Sembolini et al. 2012). We used the 80 clusters at $z \simeq 0.42$ above the completeness mass limit $M_{\rm vir} = 6 \times 10^{14} h^{-1} M_{\odot}$ in a volume of $1\,h^{-3}$ Gpc^3. Each cluster was projected along 100 lines of sight. We searched for those projections where the critical lines both exceed 50″ in at least one direction and exhibit high elongations (axis ratio > 5). These conditions are satisfied in $\sim$4% of the 8000 lens planes.

4. SUMMARY

We presented an SL study of M0416, in which we uncovered 70 multiple images and candidates of 23 background sources. We constructed mass models using two independent methods—both yield similar critical curves and mass profiles, in agreement also with independent larger-scale WL analysis. Compared to other well-known lensing clusters, M0416 exhibits a high number of multiple images for its critical area ($\simeq$0.6 □′).

We simulated the effects of ellipticity and merger on the lensing efficiency, and showed that (1) the *number density* of multiple images increases with ellipticity (the source-plane caustics get bigger, generating more multiple images *for the same critical area*), and (2) the critical area and correspondingly *total number* of multiple images increase with lower separations between two merging clumps, peaking when the two halos are either on top of each other or a few dozen arcseconds away, depending on their mass and shape.

We conclude that the observed critical area size can be attributed to the merger, which boosts the mass in the center. For this given critical area, the high multiple-image number density can be explained by the observed elongation, which boosts the lensing efficiency by $\sim$2.5$\times$. Background cosmic variance, estimated typically at a $\sim$20% level (Somerville et al. 2004) or double for $z > 5$ (Trenti & Stiavelli 2008), is likely to play only a small role in the increased number of multiple images, which are spread over a wide redshift range.

This cluster shows once more that there exists a class of prominent lenses at redshifts around $z \sim 0.4$–0.5 (and higher), probably due to their merging state, and thus level of substructure and ellipticity, which as we have shown, boost the SL properties.

We thank the anonymous reviewer of this work for very valuable comments. A.Z. is supported by contract research "Internationale Spitzenforschung II/2-6" of the Baden Württemberg Stiftung. P.R. acknowledges partial support by the DFG cluster of excellence Origin and Structure of the Universe. K.U. acknowledges partial support from the National Science Council of Taiwan (grant NSC100-2112-M-001-008-MY3) and from the Academia Sinica Career Development Award. The work of L.A.M. was carried out at Jet Propulsion Laboratory,

California Institute of Technology, under a contract with NASA. ACS was developed under NASA contract NAS 5-32865. Results are based on observations made with the NASA/ESA *Hubble Space Telescope*, obtained from the data archive at the Space Telescope Science Institute. STScI is operated by the Association of Universities for Research in Astronomy, Inc. under NASA contract NAS 5-26555. This work is based in part on data collected at the Subaru Telescope, which is operated by the National Astronomical Society of Japan.

REFERENCES

Bartelmann, M. 2010, CQGra, 27, 233001
Benítez, N., Ford, H., Bouwens, R., et al. 2004, ApJS, 150, 1
Bertin, E., & Arnouts, S. 1996, A&AS, 117, 393
Bradač, M., Clowe, D., Gonzalez, A. H., et al. 2006, ApJ, 652, 937
Broadhurst, T., Benítez, N., Coe, D., et al. 2005, ApJ, 621, 53
Broadhurst, T., Umetsu, K., Medezinski, E., Oguri, M., & Rephaeli, Y. 2008, ApJL, 685, 9
Broadhurst, T. J., & Barkana, R. 2008, MNRAS, 390, 1647
Christensen, L., Richard, J., Hjorth, J., et al. 2012, arXiv:1209.0767
Coe, D., Benítez, N., Broadhurst, T., & Moustakas, L. A. 2010, ApJ, 723, 1678
Coe, D., Benítez, N., Sánchez, S. F., et al. 2006, AJ, 132, 926
Coe, D., Zitrin, A., Carrasco, M., et al. 2012, ApJ, 762, 32
Comerford, J. M., & Natarajan, P. 2007, MNRAS, 379, 190
Ebeling, H., Barrett, E., Donovan, D., et al. 2007, ApJL, 661, 33
Ebeling, H., Edge, A. C., Mantz, A., et al. 2010, MNRAS, 407, 83
Halkola, A., Seitz, S., & Pannella, M. 2006, MNRAS, 372, 1425
Hennawi, J. F., Dalal, N., Bode, P., & Ostriker, J. P. 2007, ApJ, 654, 714
Jauzac, M., Jullo, E., Kneib, J.-P., et al. 2012, MNRAS, 426, 3369
Jullo, E., Kneib, J.-P., Limousin, M., et al. 2007, NJPh, 9, 447
Kassiola, A., & Kovner, I. 1993, ApJ, 417, 450
Kneib, J.-P., & Natarajan, P. 2011, A&ARv, 19, 47
Limousin, M., Ebeling, H., Richard, J., et al. 2012, A&A, 544, A71
Mann, A. W., & Ebeling, H. 2012, MNRAS, 420, 2120
Medezinski, E., Broadhurst, T., Umetsu, K., et al. 2010, MNRAS, 405, 257
Meneghetti, M., Argazzi, R., Pace, F., et al. 2007, A&A, 461, 25
Meneghetti, M., Bartelmann, M., & Moscardini, L. 2003, MNRAS, 346, 67
Merten, J., Coe, D., Dupke, R., et al. 2011, MNRAS, 417, 333
Oguri, M., Bayliss, M. B., Dahle, H., et al. 2012a, MNRAS, 420, 3213
Oguri, M., Schrabback, T., Jullo, E., et al. 2012b, MNRAS
Okabe, N., Takada, M., Umetsu, K., Futamase, T., & Smith, G. P. 2010, PASJ, 62, 811
Postman, M., Coe, D., Benítez, N., et al. 2012, ApJS, 199, 25
Redlich, M., Bartelmann, M., Waizmann, J.-C., & Fedeli, C. 2012, A&A, 547, A66
Richard, J., Kneib, J.-P., Limousin, M., Edge, A., & Jullo, E. 2010, MNRAS, 402, L44
Richard, J., Pei, L., Limousin, M., Jullo, E., & Kneib, J. P. 2009, A&A, 498, 37
Sadeh, S., & Rephaeli, Y. 2008, MNRAS, 388, 1759
Sembolini, F., Yepes, G., De Petris, M., et al. 2012, MNRAS
Sereno, M., Jetzer, P., & Lubini, M. 2010, MNRAS, 403, 2077
Sereno, M., & Zitrin, A. 2012, MNRAS, 419, 3280
Somerville, R. S., Lee, K., Ferguson, H. C., et al. 2004, ApJL, 600, 171
Torri, E., Meneghetti, M., Bartelmann, M., et al. 2004, MNRAS, 349, 476
Trenti, M., & Stiavelli, M. 2008, ApJ, 676, 767
Umetsu, K., Broadhurst, T., Zitrin, A., Medezinski, E., & Hsu, L. 2011a, ApJ, 729, 127
Umetsu, K., Broadhurst, T., Zitrin, A., et al. 2011b, ApJ, 738, 41
Umetsu, K., Medezinski, E., Nonino, M., et al. 2012, ApJ, 755, 56
Zheng, W., Postman, M., Zitrin, A., et al. 2012, Natur, 489, 406
Zitrin, A., & Broadhurst, T. 2009, ApJL, 703, 132
Zitrin, A., Broadhurst, T., Barkana, R., Rephaeli, Y., & Benítez, N. 2011, MNRAS, 410, 1939
Zitrin, A., Broadhurst, T., Rephaeli, Y., & Sadeh, S. 2009a, ApJL, 707, 102
Zitrin, A., Broadhurst, T., Umetsu, K., et al. 2009b, MNRAS, 396, 1985
Zitrin, A., Moustakas, J., Bradley, L., et al. 2012a, ApJL, 747, 9
Zitrin, A., Rosati, P., Nonino, M., et al. 2012b, ApJ, 749, 97

Bibliography

Abdelsalam, H. M., Saha, P., & Williams, L. L. R. 1998, MNRAS, 294, 734, astro-ph/9707207

Abell, G. O. 1958, ApJS, 3, 211

Abell, G. O., Corwin, Jr., H. G., & Olowin, R. P. 1989, ApJS, 70, 1

Allen, S. W. 1998, MNRAS, 296, 392, astro-ph/9710217

Allen, S. W., Evrard, A. E., & Mantz, A. B. 2011, ARA&A, 49, 409, 1103.4829

Allgood, B., Flores, R. A., Primack, J. R., Kravtsov, A. V., Wechsler, R. H., Faltenbacher, A., & Bullock, J. S. 2006, MNRAS, 367, 1781, astro-ph/0508497

Bailin, J., & Steinmetz, M. 2005, ApJ, 627, 647, astro-ph/0408163

Barkana, R., & Loeb, A. 2010, MNRAS, 405, 1969, 0907.1102

Bartelmann, M. 1995, A&A, 299, 11, astro-ph/9410076

Bartelmann, M. 1996, Astron.Astrophys., 313, 697, astro-ph/9602053

Bartelmann, M. 2010, Classical and Quantum Gravity, 27, 233001, 1010.3829

Bartelmann, M., Huss, A., Colberg, J. M., Jenkins, A., & Pearce, F. R. 1998, Astron.Astrophys., 330, 1, astro-ph/9707167

Bartelmann, M., Huss, A., Colberg, J. M., Jenkins, A., & Pearce, F. R. 1998, A&A, 330, 1, astro-ph/9707167

Bartelmann, M., & Meneghetti, M. 2004, A&A, 418, 413, astro-ph/0312011

Bartelmann, M., Meneghetti, M., Perrotta, F., Baccigalupi, C., & Moscardini, L. 2003, A&A, 409, 449, astro-ph/0210066

Bartelmann, M., & Steinmetz, M. 1996, MNRAS, 283, 431, astro-ph/9603101

Bartlett, J. G., Chamballu, A., Melin, J.-B., Arnaud, M., & Members of the Planck Working Group 5. 2008, Astronomische Nachrichten, 329, 147

Bayliss, M. B., Gladders, M. D., Oguri, M., Hennawi, J. F., Sharon, K., Koester, B. P., & Dahle, H. 2011, ApJ, 727, L26+, 1010.6060

Bayliss, M. B., Johnson, T., Gladders, M. D., Sharon, K., & Oguri, M. 2014, ApJ, 783, 41, 1312.3637

Behroozi, P., Wechsler, R., & Wu, H.-Y. 2012, Rockstar: Phase-space halo finder, Astrophysics Source Code Library, 1210.008

Bergmann, A. G., Petrosian, V., & Lynds, R. 1990, ApJ, 350, 23

Bhattacharya, S., Habib, S., Heitmann, K., & Vikhlinin, A. 2013, ApJ, 766, 32, 1112.5479

Böhringer, H. et al. 2004, A&A, 425, 367, astro-ph/0405546

Bonamigo, M., Despali, G., Limousin, M., Angulo, R., Giocoli, C., & Soucail, G. 2015, MNRAS, 449, 3171, 1410.0015

Borgani, S., & Guzzo, L. 2001, Nat, 409, 39, astro-ph/0012439

Borgani, S., & Kravtsov, A. 2011, Advanced Science Letters, 4, 204, 0906.4370

Borgani, S. et al. 2004, MNRAS, 348, 1078, astro-ph/0310794

Bradac, M. et al. 2006, ApJ, 652, 937, astro-ph/0608408

Bradac, M., Erben, T., Schneider, P., Hildebrandt, H., Lombardi, M., Schirmer, M., Miralles, J. M., & Clowe, D. 2005, A&A, 437, 49

Bradac, M. et al. 2008, ApJ, 681, 187, 0711.4850

Bradac, M., Treu, T., Applegate, D., Gonzalez, A. H., Clowe, D., Forman, W., & Jones, C. 2009, ApJ, 706, 1201, 0910.2708

Broadhurst, T. et al. 2005a, ApJ, 621, 53, astro-ph/0409132

Broadhurst, T., Takada, M., Umetsu, K., Kong, X., Arimoto, N., & Chiba, M. 2005b, ApJ, 619, L143, astro-ph/0412192

Broadhurst, T., Takada, M., Umetsu, K., Kong, X., Arimoto, N., Chiba, M., & Futamase, T. 2005c, ApJ, 619, L143, astro-ph/0412192

Broadhurst, T., Umetsu, K., Medezinski, E., Oguri, M., & Rephaeli, Y. 2008, ApJ, 685, L9, 0805.2617

Broadhurst, T. J., & Barkana, R. 2008, MNRAS, 390, 1647, 0801.1875

Bryan, G. L. 2000, ApJ, 544, L1, astro-ph/0009286

Bryan, G. L., Cen, R., Norman, M. L., Ostriker, J. P., & Stone, J. M. 1994, ApJ, 428, 405

Bryan, G. L., & Norman, M. L. 1998, ApJ, 495, 80, astro-ph/9710107

Bryan, G. L., & Voit, G. M. 2001, ApJ, 556, 590, astro-ph/0101467

Cacciato, M., Bartelmann, M., Meneghetti, M., & Moscardini, L. 2006, A&A, 458, 349, astro-ph/0511694

Carlstrom, J. E. et al. 2011, PASP, 123, 568, 0907.4445

Carlstrom, J. E., Holder, G. P., & Reese, E. D. 2002, ARA&A, 40, 643, astro-ph/0208192

Cavaliere, A. G., Gursky, H., & Tucker, W. H. 1971, Nat, 231, 437

Coe, D., Benítez, N., Broadhurst, T., & Moustakas, L. A. 2010, ApJ, 723, 1678, 1005.0398

Coe, D., Fuselier, E., Benítez, N., Broadhurst, T., Frye, B., & Ford, H. 2008, ApJ, 681, 814, 0803.1199

Coe, D. et al. 2012, ApJ, 757, 22, 1201.1616

Colberg, J. M., White, S. D. M., Jenkins, A., & Pearce, F. R. 1999, MNRAS, 308, 593

Cole, S., & Lacey, C. 1996, MNRAS, 281, 716, astro-ph/9510147

Comerford, J. M., & Natarajan, P. 2007, MNRAS, 379, 190, astro-ph/0703126

Dalal, N., Holder, G., & Hennawi, J. F. 2004, ApJ, 609, 50, astro-ph/0310306

Davis, M., & Peebles, P. J. E. 1983, ApJ, 267, 465

De Boni, C., Ettori, S., Dolag, K., & Moscardini, L. 2013, MNRAS, 428, 2921, 1205.3163

Deb, S., Goldberg, D. M., & Ramdass, V. J. 2008, ApJ, 687, 39, 0802.0004

Diego, J. M., Protopapas, P., Sandvik, H. B., & Tegmark, M. 2005a, MNRAS, 360, 477, astro-ph/0408418

Diego, J. M., Sandvik, H. B., Protopapas, P., Tegmark, M., Benítez, N., & Broadhurst, T. 2005b, MNRAS, 362, 1247, astro-ph/0412191

Diego, J. M., Tegmark, M., Protopapas, P., & Sandvik, H. B. 2007, MNRAS, 375, 958, astro-ph/0509103

Diemer, B., & Kravtsov, A. V. 2014, ApJ, 789, 1, 1401.1216

Dolag, K., Bartelmann, M., Perrotta, F., Baccigalupi, C., Moscardini, L., Meneghetti, M., & Tormen, G. 2004, A&A, 416, 853, astro-ph/0309771

Donnarumma, A., Ettori, S., Meneghetti, M., & Moscardini, L. 2009, MNRAS, 398, 438, 0902.4051

Dubinski, J., & Carlberg, R. G. 1991, ApJ, 378, 496

Duffy, A. R., Schaye, J., Kay, S. T., & Dalla Vecchia, C. 2008, MNRAS, 390, L64, 0804.2486

Duffy, A. R., Schaye, J., Kay, S. T., Dalla Vecchia, C., Battye, R. A., & Booth, C. M. 2010, MNRAS, 405, 2161, 1001.3447

Duong, T. 2007, Journal of Statistical Software, 21, 1

Ebeling, H., Barrett, E., Donovan, D., Ma, C.-J., Edge, A. C., & van Speybroeck, L. 2007, ApJ, 661, L33, astro-ph/0703394

Ebeling, H., Edge, A. C., Bohringer, H., Allen, S. W., Crawford, C. S., Fabian, A. C., Voges, W., & Huchra, J. P. 1998, MNRAS, 301, 881, astro-ph/9812394

Ebeling, H., Edge, A. C., & Henry, J. P. 2001, ApJ, 553, 668, astro-ph/0009101

Ebeling, H., Edge, A. C., Mantz, A., Barrett, E., Henry, J. P., Ma, C. J., & van Speybroeck, L. 2010, MNRAS, 407, 83, 1004.4683

Ebeling, H., Ma, C. J., Kneib, J.-P., Jullo, E., Courtney, N. J. D., Barrett, E., Edge, A. C., & Le Borgne, J.-F. 2009, MNRAS, 395, 1213, 0901.2144

Edge, A. C., Stewart, G. C., Fabian, A. C., & Arnaud, K. A. 1990, MNRAS, 245, 559

Einasto, J., & Haud, U. 1989, A&A, 223, 89

Eisenstein, D. J., & Hu, W. 1999, ApJ, 511, 5, astro-ph/9710252

Eke, V. R., Cole, S., & Frenk, C. S. 1996, MNRAS, 282, 263, astro-ph/9601088

Eke, V. R., Cole, S., Frenk, C. S., & Patrick Henry, J. 1998, MNRAS, 298, 1145, astro-ph/9802350

Evrard, A. E. 1988, MNRAS, 235, 911

Evrard, A. E., & Henry, J. P. 1991, ApJ, 383, 95

Fabjan, D., Borgani, S., Rasia, E., Bonafede, A., Dolag, K., Murante, G., & Tornatore, L. 2011, MNRAS, 416, 801, 1102.2903

Fedeli, C. 2012, MNRAS, 424, 1244, 1111.5780

Fedeli, C., Bartelmann, M., Meneghetti, M., & Moscardini, L. 2008, A&A, 486, 35, 0803.0656

Fisher, R. A., & Tippett, L. H. C. 1928, Proceedings of the Cambridge Philosophical Society, 24, 180

Forman, W., Kellogg, E., Gursky, H., Tananbaum, H., & Giacconi, R. 1972, ApJ, 178, 309

Frenk, C. S. et al. 1999, ApJ, 525, 554, astro-ph/9906160

Frenk, C. S., White, S. D. M., Davis, M., & Efstathiou, G. 1988, ApJ, 327, 507

Frye, B., & Broadhurst, T. 1998, ApJ, 499, L115, astro-ph/9712111

Gao, L., Navarro, J. F., Cole, S., Frenk, C. S., White, S. D. M., Springel, V., Jenkins, A., & Neto, A. F. 2008, MNRAS, 387, 536, 0711.0746

Gao, L., White, S. D. M., Jenkins, A., Stoehr, F., & Springel, V. 2004, MNRAS, 355, 819, astro-ph/0404589

Gavazzi, R. 2005, A&A, 443, 793, astro-ph/0503696

Gavazzi, R., Fort, B., Mellier, Y., Pelló, R., & Dantel-Fort, M. 2003, A&A, 403, 11, astro-ph/0212214

Gill, S. P. D., Knebe, A., & Gibson, B. K. 2004, MNRAS, 351, 399, astro-ph/0404258

Gingold, R. A., & Monaghan, J. J. 1977, MNRAS, 181, 375

Giocoli, C., Meneghetti, M., Bartelmann, M., Moscardini, L., & Boldrin, M. 2012a, MNRAS, 421, 3343

Giocoli, C., Meneghetti, M., Ettori, S., & Moscardini, L. 2012b, MNRAS, 426, 1558, 1205.2375

Giocoli, C., Meneghetti, M., Metcalf, R. B., Ettori, S., & Moscardini, L. 2014, MNRAS, 440, 1899, 1311.1205

Gitti, M., Piffaretti, R., & Schindler, S. 2007, A&A, 472, 383, 0706.3001

Gladders, M. D., & Yee, H. K. C. 2005, ApJS, 157, 1, astro-ph/0411075

Gladders, M. D., Yee, H. K. C., Majumdar, S., Barrientos, L. F., Hoekstra, H., Hall, P. B., & Infante, L. 2007, ApJ, 655, 128, astro-ph/0603588

Gnedenko, B. 1943, Annals of Mathematics, 44, pp. 423

Gonzalez, A. H., Zaritsky, D., & Zabludoff, A. I. 2007, ApJ, 666, 147, 0705.1726

Gottlöber, S., & Yepes, G. 2007, ApJ, 664, 117

Grillo, C. et al. 2015, ApJ, 800, 38, 1407.7866

Gumbel, E. 2004, Statistics of extremes (Mineola, N.Y: Dover Publications)

Gursky, H., Kellogg, E., Murray, S., Leong, C., Tananbaum, H., & Giacconi, R. 1971, ApJ, 167, L81

Halkola, A., Hildebrandt, H., Schrabback, T., Lombardi, M., Bradac, M., Erben, T., Schneider, P., & Wuttke, D. 2008, A&A, 481, 65, 0801.1795

Hao, J. et al. 2010, ApJS, 191, 254, 1010.5503

Harrison, E. R. 1970, Phys. Rev. D, 1, 2726

Hasinger, G. et al. 1998, A&A, 340, L27, astro-ph/9810347

Hennawi, J. F., Dalal, N., Bode, P., & Ostriker, J. P. 2007, ApJ, 654, 714, astro-ph/0506171

Hennawi, J. F. et al. 2008, AJ, 135, 664

Hockney, R. W., & Eastwood, J. W. 1981, Computer Simulation Using Particles

Hockney, R. W., Goel, S. P., & Eastwood, J. W. 1974, Journal of Computational Physics, 14, 148

Hogg, D. W. 1999, ArXiv Astrophysics e-prints, astro-ph/9905116

Israel, H. et al. 2010, A&A, 520, A58, 0911.3111

Jansen, F. et al. 2001, A&A, 365, L1

Jauzac, M. et al. 2014a, MNRAS, 443, 1549, 1405.3582

Jauzac, M., Richard, J., Jullo, E., Clément, B., Limousin, M., & Kneib, J.-P. 2014b, ArXiv e-prints, 1409.8663

Jenkins, A., Frenk, C. S., White, S. D. M., Colberg, J. M., Cole, S., Evrard, A. E., Couchman, H. M. P., & Yoshida, N. 2001, MNRAS, 321, 372, astro-ph/0005260

Jing, Y. P., & Suto, Y. 2002, ApJ, 574, 538, astro-ph/0202064

Jullo, E., & Kneib, J.-P. 2009, MNRAS, 395, 1319, 0901.3792

Jullo, E., Kneib, J.-P., Limousin, M., Elíasdóttir, Á., Marshall, P. J., & Verdugo, T. 2007, New Journal of Physics, 9, 447, 0706.0048

Kaiser, N. 1991, ApJ, 383, 104

Kasun, S. F., & Evrard, A. E. 2005, ApJ, 629, 781, astro-ph/0408056

Katz, N., & White, S. D. M. 1993, ApJ, 412, 455

Kellogg, E., Gursky, H., Tananbaum, H., Giacconi, R., & Pounds, K. 1972, ApJ, 174, L65

Killedar, M., Borgani, S., Meneghetti, M., Dolag, K., Fabjan, D., & Tornatore, L. 2012, MNRAS, 427, 533, 1208.5770

Klypin, A., Kravtsov, A. V., Bullock, J. S., & Primack, J. R. 2001, ApJ, 554, 903, astro-ph/0006343

Klypin, A., Yepes, G., Gottlober, S., Prada, F., & Hess, S. 2014, ArXiv e-prints, 1411.4001

Knebe, A. et al. 2011, MNRAS, 415, 2293, 1104.0949

Kneib, J.-P., Ellis, R. S., Santos, M. R., & Richard, J. 2004, ApJ, 607, 697, astro-ph/0402319

Kneib, J.-P., Ellis, R. S., Smail, I., Couch, W. J., & Sharples, R. M. 1996, ApJ, 471, 643, astro-ph/9511015

Kneib, J.-P. et al. 2003, ApJ, 598, 804, astro-ph/0307299

Kneib, J.-P., & Natarajan, P. 2011, A&A Rev., 19, 47, 1202.0185

Knollmann, S. R., & Knebe, A. 2009, ApJS, 182, 608, 0904.3662

Koester, B. P. et al. 2007, ApJ, 660, 239, astro-ph/0701265

Komatsu, E., Smith, K. M., & Dunkley, e. a. 2011, ApJS, 192, 18, 1001.4538

Kosowsky, A. 2006, New Astron. Rev., 50, 969, astro-ph/0608549

Kovner, I. 1987, ApJ, 318, L1

Kravtsov, A. V., Klypin, A. A., & Khokhlov, A. M. 1997, ApJS, 111, 73, astro-ph/9701195

Lacey, C., & Cole, S. 1993, MNRAS, 262, 627

Lahav, O., Fabian, A. C., Edge, A. C., & Putney, A. 1989, MNRAS, 238, 881

Le Fevre, O., Hammer, F., Angonin, M. C., Gioia, I. M., & Luppino, G. A. 1994, ApJ, 422, L5

Li, G.-L., Mao, S., Jing, Y. P., Bartelmann, M., Kang, X., & Meneghetti, M. 2005, ApJ, 635, 795, astro-ph/0503172

Liesenborgs, J., de Rijcke, S., Dejonghe, H., & Bekaert, P. 2009, MNRAS, 397, 341, 0904.2382

Limousin, M., Morandi, A., Sereno, M., Meneghetti, M., Ettori, S., Bartelmann, M., & Verdugo, T. 2013, Space Sci. Rev., 177, 155, 1210.3067

Lucy, L. B. 1977, AJ, 82, 1013

Ludlow, A. D., Navarro, J. F., Angulo, R. E., Boylan-Kolchin, M., Springel, V., Frenk, C., & White, S. D. M. 2014, MNRAS, 441, 378, 1312.0945

Ludlow, A. D., Navarro, J. F., Li, M., Angulo, R. E., Boylan-Kolchin, M., & Bett, P. E. 2012, MNRAS, 427, 1322, 1206.1049

Luppino, G. A., Gioia, I. M., Hammer, F., Le Fèvre, O., & Annis, J. A. 1999, A&A Supp., 136, 117, astro-ph/9812355

Lynds, R., & Petrosian, V. 1986, in Bulletin of the American Astronomical Society, Vol. 18, Bulletin of the American Astronomical Society, 1014

Macciò, A. V. 2005, MNRAS, 361, 1250, astro-ph/0402657

Marriage, T. A. et al. 2011, ApJ, 737, 61, 1010.1065

McCarthy, I. G., Schaye, J., Bower, R. G., Ponman, T. J., Booth, C. M., Dalla Vecchia, C., & Springel, V. 2011, MNRAS, 412, 1965, 1008.4799

McNamara, B. R., & Nulsen, P. E. J. 2007, ARA&A, 45, 117, 0709.2152

Meekins, J. F., Fritz, G., Chubb, T. A., & Friedman, H. 1971, Nat, 231, 107

Meneghetti, M., Argazzi, R., Pace, F., Moscardini, L., Dolag, K., Bartelmann, M., Li, G., & Oguri, M. 2007, A&A, 461, 25, astro-ph/0606006

Meneghetti, M., Bartelmann, M., Dahle, H., & Limousin, M. 2013, Space Sci. Rev., 177, 31, 1303.3363

Meneghetti, M., Bartelmann, M., Dolag, K., Moscardini, L., Perrotta, F., Baccigalupi, C., & Tormen, G. 2005, A&A, 442, 413

Meneghetti, M., Bartelmann, M., & Moscardini, L. 2003, MNRAS, 346, 67, astro-ph/0302603

Meneghetti, M., Bolzonella, M., Bartelmann, M., Moscardini, L., & Tormen, G. 2000, MNRAS, 314, 338, astro-ph/9907324

Meneghetti, M., Fedeli, C., Pace, F., Gottlöber, S., & Yepes, G. 2010a, A&A, 519, A90, 1003.4544

Meneghetti, M., Fedeli, C., Zitrin, A., Bartelmann, M., Broadhurst, T., Gottlöber, S., Moscardini, L., & Yepes, G. 2011, A&A, 530, A17, 1103.0044

Meneghetti, M., & Rasia, E. 2013, ArXiv e-prints, 1303.6158

Meneghetti, M., Rasia, E., Merten, J., Bellagamba, F., Ettori, S., Mazzotta, P., Dolag, K., & Marri, S. 2010b, A&A, 514, A93, 0912.1343

Meneghetti, M. et al. 2014, The Astrophysical Journal, 797, 34

Meneghetti, M., Yoshida, N., Bartelmann, M., Moscardini, L., Springel, V., Tormen, G., & White, S. D. M. 2001, MNRAS, 325, 435, astro-ph/0011405

Merritt, D., Navarro, J. F., Ludlow, A., & Jenkins, A. 2005, ApJ, 624, L85, astro-ph/0502515

Merten, J., Cacciato, M., Meneghetti, M., Mignone, C., & Bartelmann, M. 2009, A&A, 500, 681, 0806.1967

Merten, J. et al. 2015, ApJ, 806, 4, 1404.1376

Metzler, C. A., & Evrard, A. E. 1994, ApJ, 437, 564, astro-ph/9309050

Miralda-Escude, J. 1995, ApJ, 438, 514

Miranda, M., Sereno, M., de Filippis, E., & Paolillo, M. 2008, MNRAS, 385, 511, 0801.1429

Mohr, J. J., & Evrard, A. E. 1997, ApJ, 491, 38, astro-ph/9707184

Moore, B., Quinn, T., Governato, F., Stadel, J., & Lake, G. 1999, MNRAS, 310, 1147, astro-ph/9903164

Murray, S. G., Power, C., & Robotham, A. S. G. 2013, Astronomy and Computing, 3, 23, 1306.6721

Natarajan, P., & Kneib, J.-P. 1997, MNRAS, 287, 833, astro-ph/9609008

Navarro, J. F., Frenk, C. S., & White, S. D. M. 1995, MNRAS, 275, 720, astro-ph/9408069

Navarro, J. F., Frenk, C. S., & White, S. D. M. 1996, ApJ, 462, 563, astro-ph/9508025

Navarro, J. F., Frenk, C. S., & White, S. D. M. 1997, ApJ, 490, 493, astro-ph/9611107

Navarro, J. F. et al. 2010, MNRAS, 402, 21, 0810.1522

Nelder, J. A., & Mead, R. 1965, The Computer Journal, 7, 308, http://comjnl.oxfordjournals.org/content/7/4/308.full.pdf+html

Neto, A. F. et al. 2007, MNRAS, 381, 1450, 0706.2919

Oguri, M., Bayliss, M. B., Dahle, H., Sharon, K., Gladders, M. D., Natarajan, P., Hennawi, J. F., & Koester, B. P. 2012, MNRAS, 420, 3213, 1109.2594

Oguri, M., & Blandford, R. D. 2009, MNRAS, 392, 930, 0808.0192

Oguri, M. et al. 2009, ApJ, 699, 1038, 0901.4372

Oguri, M., Lee, J., & Suto, Y. 2004, ApJ, 608, 1175

Oguri, M., Takada, M., Umetsu, K., & Broadhurst, T. 2005, ApJ, 632, 841, astro-ph/0505452

Peebles, P. J. E. 1970, AJ, 75, 13

Pelló, R. et al. 1999, A&A, 346, 359, astro-ph/9810390

Pelló, R., Schaerer, D., Richard, J., Le Borgne, J.-F., & Kneib, J.-P. 2004, A&A, 416, L35, astro-ph/0403025

Planck Collaboration et al. 2011, A&A, 536, A1, 1101.2022

Planck Collaboration et al. 2015, ArXiv e-prints, 1502.01589

Planelles, S., Borgani, S., Dolag, K., Ettori, S., Fabjan, D., Murante, G., & Tornatore, L. 2013, MNRAS, 431, 1487, 1209.5058

Planelles, S., Borgani, S., Fabjan, D., Killedar, M., Murante, G., Granato, G. L., Ragone-Figueroa, C., & Dolag, K. 2014, MNRAS, 438, 195, 1311.0818

Postman, M. et al. 2012, ApJS, 199, 25, 1106.3328

Power, C., Read, J. I., & Hobbs, A. 2014, MNRAS, 440, 3243, 1307.0668

Prada, F., Klypin, A. A., Cuesta, A. J., Betancort-Rijo, J. E., & Primack, J. 2012, MNRAS, 423, 3018, 1104.5130

Pratt, G. W., Böhringer, H., & Finoguenov, A. 2005, A&A, 433, 777, astro-ph/0502322

Press, W. H., & Schechter, P. 1974, ApJ, 187, 425

Puchwein, E., Bartelmann, M., Dolag, K., & Meneghetti, M. 2005, A&A, 442, 405, astro-ph/0504206

Puchwein, E., & Hilbert, S. 2009, MNRAS, 398, 1298, 0904.0253

Ragone-Figueroa, C., Granato, G. L., Murante, G., Borgani, S., & Cui, W. 2013, MNRAS, 436, 1750, 1308.3246

Rasia, E., Borgani, S., Ettori, S., Mazzotta, P., & Meneghetti, M. 2013, ApJ, 776, 39, 1301.7476

Rasia, E. et al. 2006, MNRAS, 369, 2013, astro-ph/0602434

Read, J. I., Hayfield, T., & Agertz, O. 2010, MNRAS, 405, 1513, 0906.0774

Redlich, M., Bartelmann, M., Waizmann, J.-C., & Fedeli, C. 2012, A&A, 547, A66, 1205.6906

Redlich, M., Waizmann, J.-C., & Bartelmann, M. 2014, A&A, 569, A34, 1408.2720

Reiprich, T. H., & Böhringer, H. 2002, ApJ, 567, 716, astro-ph/0111285

Retana-Montenegro, E., van Hese, E., Gentile, G., Baes, M., & Frutos-Alfaro, F. 2012, A&A, 540, A70, 1202.5242

Richard, J. et al. 2010, MNRAS, 404, 325, 0911.3302

Richard, J., Stark, D. P., Ellis, R. S., George, M. R., Egami, E., Kneib, J.-P., & Smith, G. P. 2008, ApJ, 685, 705, 0803.4391

Rozo, E., Nagai, D., Keeton, C., & Kravtsov, A. 2008, ApJ, 687, 22, astro-ph/0609621

Rzepecki, J., Lombardi, M., Rosati, P., Bignamini, A., & Tozzi, P. 2007, A&A, 471, 743, 0706.2992

Saha, P., & Williams, L. L. R. 1997, MNRAS, 292, 148, astro-ph/9707346

Sand, D. J., Treu, T., Ellis, R. S., & Smith, G. P. 2005, ApJ, 627, 32, astro-ph/0502528

Sembolini, F., De Petris, M., Yepes, G., Foschi, E., Lamagna, L., & Gottlöber, S. 2014, MNRAS, 440, 3520, 1309.5387

Sembolini, F., Yepes, G., De Petris, M., Gottlöber, S., Lamagna, L., & Comis, B. 2013a, Astronomische Nachrichten, 334, 441

Sembolini, F., Yepes, G., De Petris, M., Gottlöber, S., Lamagna, L., & Comis, B. 2013b, MNRAS, 429, 323, 1207.4438

Sembolini, F. et al. 2015, ArXiv e-prints, 1503.06065

Sereno, M., Fedeli, C., & Moscardini, L. 2015a, ArXiv e-prints, 1504.05183

Sereno, M., Giocoli, C., Ettori, S., & Moscardini, L. 2015b, MNRAS, 449, 2024, 1410.4568

Sereno, M., Jetzer, P., & Lubini, M. 2010, MNRAS, 403, 2077, 1001.1696

Sereno, M., & Zitrin, A. 2012, MNRAS, 419, 3280, 1110.2854

Sheth, R. K., & Tormen, G. 1999, MNRAS, 308, 119, astro-ph/9901122

Smail, I. et al. 2007, ApJ, 654, L33, astro-ph/0611486

Smith, G. P., Kneib, J.-P., Ebeling, H., Czoske, O., & Smail, I. 2001, ApJ, 552, 493, astro-ph/0008315

Smith, G. P., Kneib, J.-P., Smail, I., Mazzotta, P., Ebeling, H., & Czoske, O. 2005, MNRAS, 359, 417, astro-ph/0403588

Soucail, G., Fort, B., Mellier, Y., & Picat, J. P. 1987, A&A, 172, L14

Springel, V. 2005, MNRAS, 364, 1105, astro-ph/0505010

Springel, V. 2010, MNRAS, 401, 791, 0901.4107

Springel, V., Di Matteo, T., & Hernquist, L. 2005, MNRAS, 361, 776, astro-ph/0411108

Stark, D. P., Ellis, R. S., Richard, J., Kneib, J.-P., Smith, G. P., & Santos, M. R. 2007, ApJ, 663, 10, astro-ph/0701279

Sunyaev, R. A., & Zeldovich, Y. B. 1970, Ap&SS, 7, 3

Swinbank, A. M., Bower, R. G., Smith, G. P., Smail, I., Kneib, J.-P., Ellis, R. S., Stark, D. P., & Bunker, A. J. 2006, MNRAS, 368, 1631, astro-ph/0603042

Swinbank, A. M., Bower, R. G., Smith, G. P., Wilman, R. J., Smail, I., Ellis, R. S., Morris, S. L., & Kneib, J.-P. 2007, MNRAS, 376, 479, astro-ph/0701221

Tasitsiomi, A., Kravtsov, A. V., Gottlöber, S., & Klypin, A. A. 2004, ApJ, 607, 125, astro-ph/0311062

Teyssier, R. 2002, A&A, 385, 337, astro-ph/0111367

Thomas, P. A., & Couchman, H. M. P. 1992, MNRAS, 257, 11

Tinker, J., Kravtsov, A. V., Klypin, A., Abazajian, K., Warren, M., Yepes, G., Gottlöber, S., & Holz, D. E. 2008, ApJ, 688, 709, 0803.2706

Torri, E., Meneghetti, M., Bartelmann, M., Moscardini, L., Rasia, E., & Tormen, G. 2004, MNRAS, 349, 476, astro-ph/0310898

Umetsu, K., & Broadhurst, T. 2008, ApJ, 684, 177, 0712.3441

Umetsu, K., Broadhurst, T., Zitrin, A., Medezinski, E., Coe, D., & Postman, M. 2011, ApJ, 738, 41, 1105.0444

Umetsu, K., Medezinski, E., Broadhurst, T., Zitrin, A., Okabe, N., Hsieh, B.-C., & Molnar, S. M. 2010, ApJ, 714, 1470, 0908.0069

Umetsu, K. et al. 2014, ApJ, 795, 163, 1404.1375

Umetsu, K., Medezinski, E., Nonino, M., Merten, J., & Zitrin, A. 2012, ApJ, 755, 56, 1204.3630

Vanderlinde, K. et al. 2010, ApJ, 722, 1180, 1003.0003

Viana, P. T. P., & Liddle, A. R. 1996, MNRAS, 281, 323, astro-ph/9511007

Voges, W. et al. 1999, A&A, 349, 389, astro-ph/9909315

Voit, G. M. 2005, Advances in Space Research, 36, 701

Voit, G. M. 2005, Reviews of Modern Physics, 77, 207, astro-ph/0410173

Waizmann, J.-C., Redlich, M., & Bartelmann, M. 2012, A&A, 547, A67, 1207.0801

Waizmann, J.-C., Redlich, M., Meneghetti, M., & Bartelmann, M. 2014, A&A, 565, A28, 1403.4573

Wambsganss, J., Bode, P., & Ostriker, J. P. 2004, ApJ, 606, L93, astro-ph/0306088

Weinberg, S. 1972, Gravitation and Cosmology: Principles and Applications of the General Theory of Relativity

Wen, Z. L., Han, J. L., & Liu, F. S. 2009, ApJS, 183, 197, 0906.0803

Wu, X.-P. 2000, MNRAS, 316, 299, astro-ph/0006124

Yepes, G. 1997, in Astronomical Society of the Pacific Conference Series, Vol. 126, From Quantum Fluctuations to Cosmological Structures, ed. D. Valls-Gabaud, M. A. Hendry, P. Molaro, & K. Chamcham, 279

York, D. G. et al. 2000, AJ, 120, 1579, astro-ph/0006396

Zhao, H. 1996, MNRAS, 278, 488, astro-ph/9509122

Zitrin, A., Broadhurst, T., Barkana, R., Rephaeli, Y., & Benítez, N. 2011, MNRAS, 410, 1939, 1002.0521

Zitrin, A., Broadhurst, T., Bartelmann, M., Rephaeli, Y., Oguri, M., Benítez, N., Hao, J., & Umetsu, K. 2012a, MNRAS, 423, 2308, 1105.2295

Zitrin, A. et al. 2009, MNRAS, 396, 1985, 0902.3971

——. 2015, ApJ, 801, 44, 1411.1414

Zitrin, A. et al. 2013, The Astrophysical Journal Letters, 762, L30

Zitrin, A. et al. 2012b, ApJ, 749, 97, 1107.2649

Zitrin A. et al. 2010, MNRAS, 408, 1916, 1004.4660